UNIVERSITAT POLITÈCNICA DE VALÈNCIA

DOCTORAL PROGRAM IN ENGINEERING AND INDUSTRIAL PRODUCTION

DOCTORAL THESIS

"Development of hydrated calcium silicates by hydrothermal treatments"

Author

Felipe Martí Montava

Supervisors

Prof. Dr. David García Sanoguera (UPV)
Dr. Octavio Ángel Fenollar Gimeno (UPV)
Dr. Ann Opsommer (PRTC/Etex Group)

October 2022

This research work has been fully funded by Promat Research and Technology Centre NV, an Etex Group Company.

The PhD student has been hired by the company to perform this doctoral thesis for industrial purposes. During a 3-yearly Immersion Professional Agreement, the candidate has joined the materials and technologies department located in Tisselt (Belgium).

“If I have seen further, it is by standing on the shoulders of giants.”
-Isaac Newton-

A mis padres, Ana y José Vicente
A mis tíos, Isabel y Paco
A Olivia

ACKNOWLEDGEMENTS

Before starting to name people, institutions and entities that have made possible this doctoral thesis, I would like to say that without having the vocation and passion for research, this work would have been unthinkable. So, first of all, it is my own will to which I must be grateful for this enormous effort done.

As a PhD is a collective work, I have to thank a number of people who contributed very significantly for achieving my thesis.

Firstly, I would like to thank my university supervisors David and Tayo who have given me the possibility to carry out a PhD, opening their door in order to allow me starting a scientific career. During all this time, they have shared their knowledge and they have guided my work with a good dedication. On the one hand, David has supported and helped me from bureaucratic point of view. He has dedicated hours and hours talking and discussing about the different aspects of this thesis. And he has always been encouraging mostly in my worst moments. I am really grateful to him, since he has made me open my eyes in situations of frustration, he has paved my way forward. Whilst Tayo has been a strong technical and scientific support during the running of my experiments. Not even the fever was an obstacle during his useful microscopy training sessions on the analysis of my samples.

Special thanks for Ann Opsommer, she has been my scientific mother throughout my 3 years at Promat Research and Technology Centre, in Tisselt (Belgium). She was the person who struggled to get my funding as well as the chance to perform an industrial-oriented PhD project in a well-known company focused on building materials for thermal insulation and passive fire protection. We have fought together in the good times and the bad times, but she has never let me down the cliff. Despite our differences and small disputes along this PhD, she has been one of the most important pillars as long as I was working in this study of investigation.

Many thanks to Promat Research and Technology Centre, specially to Berg Berge as the Head of materials and technologies department as well as the Human Resources department for the approval of this PhD proposal. Without their consent and financial support this would not have come true. Also, I would like to thank my colleagues of department, Dr. Oras Abdul-Khader, Dr. Xiao Wu, Dr. Emmanuel Annerel, Dr. Karim Van Maele, Dr. Paulo Borges, Patrick Vanleuven, Kevin Hart and Ilse Van Balart for their collaboration and advice. I would like to make special mention to the laboratory technicians, Davy Flament, Tim Nijs, Tim Michiels, Luc Colman and laboratory manager, Eddy Ceulemans for their continuous dedication in my experimental part. What I would have done without those moments of good mood at the lab. They have repeatedly been my saviors when there was a mechanical, electrical or computer problem in any equipment, tool o software. Thank you, guys, for all your patience and kindness.

I cannot forget the people of Redco (other Innovation Centre of Etex Group), it has been a pleasure to do research with you. Thanks to Dr. Radim Skapa and Dr. Wim Saenen for his interest on my work. The long scientific conversations about my investigation were very useful and they inspired me to understand better some concepts. Many thanks to Ajsa Dalifi, her great technical support for the microscopy measurements was so important that I am still very grateful. Moreover, I do not forget the rest of engineers and

technicians have contributed on my work. Thanks to Gertie, Hannelore, Véronique and Eddy. Heel erg bedankt allemaal!

The completion of the experimental part of my thesis at the Institute of Earth Sciences (ISTerre) in Grenoble was really the perfect complement. So, I must thank to Dr. Alejandro Fernández and Dr. Germán Montes for giving me this possibility and accept my research collaboration proposal. The fact I joined their team, the geochemistry goup, during my international research stay was a big opportunity to grow as scientist and learn from talented people. Thanks, Alex, for your collaboration and your strong support. As expert in high energy synchrotron-based x-ray diffraction techniques, we could explore the formation mechanism of some hydrated calcium silicates under hydrothermal conditions. Indeed, the most critical and complex part of my PhD. Understanding this, now we are able to control much better the process. Notwithstanding my short period in Grenoble, I have learnt a lot from you, and you have been a fabulous scientific advisor. Many thanks for your measurements at the Advanced Photon Source at Argon National Laboratory in the USA. I would also like to thank Germán as a scientist has always clarified my doubts. He has helped me from a much more engineering point of view. When I was concerned about something and a bit sad, he has given me enough strength and energy in order to solve the issues. I really miss your Mexican mood and your jokes. Thanks again for all. I shall remark the essential collaboration of Dr. Anne-Line, with her very useful work by High Resolution-Transmission Electron Microscopy in Marseille. Besides, I want to add that I met there wonderful and nice people such us researchers, engineers, post-docs, PhD students and master students. Thereupon, I will never forget you.

Thanks also to the Nuclear Magnetic Resonance Unit of the University of Alicante (UA) for the characterization of my samples done using solid state NMR ^{29}Si-MAS.

Secondly, I would like to thank the external evaluators for my PhD assessment and the members of the tribunal who have valued and recognized my work and effort. They are going to attend for my defense and thus close this investigation properly.

Acknowledgments to my great family, especially my parents Ana and José Vicente. Although the distance has been a physical barrier throughout my 3 years out of my city, this has not taken me away from you all the time and your constant encourage has been vital to get my target. What important were your messages, calls and videocalls many evenings after my long day at the laboratory. I really appreciate your love and affection. But, if someone has been by my side all the time, she is my girlfriend, Olivia. She has strengthened me with her words of encouragement, and she has also pulled me a smile in the moments I just needed. Olivia has been my psychologist during my thesis holding my complaints, tantrums and listening my reasoning and talks about my scientific topic. Thank you so much my love. To my aunty and my uncle, Isa and Paco, many thanks for the warm support you have given me. You know Paco pretty well what a PhD means. Also, I would like to thank my cousins, aunts and uncles, other relatives and friends who have pushed me to achieve this.

Finally, I have reserved the last lines to thank all the scientists, PhD students and postdocs I had the opportunity to meet in different events since our talks, conversations and discussions have come up a lot in my thesis.

TABLE OF CONTENT

LIST OF TABLES

LIST OF FIGURES

RESUMEN

Los silicatos de calcio hidratados son materiales que empezaron a estudiarse desde el año 1920, principalmente para ser empleados como elementos de aislamiento a altas temperaturas en el sector construcción y en otros sectores industriales. El grupo Etex empezó con la producción y comercialización de silicatos de calcio para aplicaciones de aislamiento térmico y protección pasiva contra incendios en la empresa Promat (Alemania) en 1958. A finales de los años 70, esta compañía introdujo una nueva tecnología en el desarrollo de estos productos. Esta nueva tecnología consistió en el desarrollo de una serie de fases minerales basadas en silicatos de calcio hidratados sintéticos más estables, la xonotlita y la tobermorita, mediante el uso de reacciones hidrotermales con sistema de agitación. Este proceso se denomina en inglés "stirred reactor autoclave", es una tecnología que consiste en el empleo de una autoclave vertical con un sistema de agitación controlada. Con esta tecnología se obtiene una matriz mineral, siendo posible el control del crecimiento de cristales de xonotlita y tobermorita. Esto permite la formación de diferentes texturas optimizadas para diferentes aplicaciones a altas temperaturas.

En el proceso de producción implantando en Promat (Tisselt, Bélgica), la xonotlita y la tobermorita se obtienen al hacer reaccionar una mezcla de óxido de calcio y sílice cristalina en medio acuoso con una relación CaO/SiO_2 cercana a 1, y en condiciones hidrotermales, a una temperatura de 200°C y a una presión de vapor de 17 bar. De este modo, en estas condiciones se forman esas fases cristalinas (xonotlita y tobermorita); partículas específicas de baja densidad que se utilizan como componentes principales de varios productos y nuevas aplicaciones que se han desarrollado en las últimas décadas en el centro de Investigación y Tecnología de Promat, perteneciente al Grupo Etex. Este proceso da lugar a la obtención de productos de alta calidad, aunque se requiere de una mejor comprensión para poder optimizar y controlar aún más este tipo de materiales, y así reducir costes energéticos en la tecnología empleada.

En este proyecto de doctorado industrial, se pretende alcanzar tres objetivos principales:

1. Desarrollar una nueva tecnología para la obtención de silicatos de calcio hidratados, mediante la síntesis inicial de gel C-S-H para controlar la densidad del producto final. Éste es un proceso que lo emplean algunos competidores de Promat y que denominamos en esta tesis como tecnología 'Gel Tank'. También se pretende llevar a cabo un profundo estudio de los parámetros clave que influyen en el proceso. Además, se pretende investigar la viabilidad de producir silicatos de calcio hidratados con diferentes densidades y comparar las propiedades de éstos con los obtenidos mediante tecnologías existentes. Con el empleo de esta nueva tecnología, la idea es utilizar menor cantidad de agua que en los procesos convencionales, y con ello reducir el gasto energético, minimizando el impacto medioambiental.
2. Ampliar el conocimiento de la tecnología basada en tratamiento hidrotermal mediante agitación e investigar la posibilidad de mejorar el carácter endotérmico de los materiales obtenidos a través de esta tecnología.
3. Desarrollar una nueva generación de productos libres de contenido en cuarzo residual (< 0,1% en peso) mediante el uso de la denominada tecnología "double autoclaving".

La primera parte de esta tesis se centra en la investigación experimental de la síntesis de silicatos de calcio hidratados de baja y media densidad, utilizando la tecnología Gel Tank, una tecnología completamente nueva para Etex. Este proceso se compone de 4 etapas: formación de una suspensión a base de gel C-S-H mediante la reacción de una sílice amorfa reactiva con cal hidratada a alrededor de 90 °C (etapa de gelificación), mezcla de la suspensión de gel C-S-H con componentes adicionales (fibras de refuerzo y minerales funcionales), prensado de la mezcla para obtener placas y, finalmente, tratamiento hidrotermal de esas placas para convertir la fase gel C-S-H en fases más estables, como xonotlita y tobermorita.

El gel C-S-H formado en la etapa inicial (gelificación), tiene una densidad baja y permite alcanzar presiones específicas requeridas durante el prensado para obtener placas con suficiente resistencia mecánica inicial para resistir al posterior tratamiento hidrotérmico en el que el gel C-S-H se transforma en tobermorita y/o xonotlita. La cantidad requerida de gel C-S-H depende de la densidad final deseada del producto a obtener y va disminuyendo conforme se requieren densidades mayores. Para productos de 300 Kg/m^3 de densidad, se utiliza como fuente de silicio, sílice amorfa, en este caso sílice de humo. Mientras que para productos de 600-700 Kg/m^3, se emplea una combinación de sílice amorfa y cristalina (cuarzo) en la formulación inicial, siendo sólo el 25% del total del contenido de sílice, sílice de humo.

La cantidad de gel C-S-H se controla principalmente variando la proporción inicial de sílice amorfa y cristalina. Pero también se ha estudiado la influencia de diferentes parámetros (tiempo de gelificación, temperatura de gelificación, condiciones de agitación) en la síntesis del gel C-S-H. Además, se ha analizado el uso de aditivos específicos y se han determinado las propiedades finales de los correspondientes productos obtenidos. La caracterización del gel C-S-H, incluye la determinación de las fases mineralógicas mediante difracción de rayos X mediante análisis Rietveld; medida de la distribución del tamaño de partícula por difracción láser; medida del área específica superficial y porosidad mediante los métodos BET y BJH; análisis morfológico mediante SEM y determinación de especies químicas mediante espectroscopía FTIR. Los geles C-S-H sintetizados mediante la tecnología Gel Tank, tienen estructuras mesoporosas con poros de 2-50 nm.

Se probaron también diferentes grados de sílice de humo en la formulación, y se caracterizaron mediante varias técnicas de análisis, como XRF, XRD y análisis de difracción láser para determinar el tamaño de partícula. Estos análisis determinaron que la sílice de humo debe ser de alta pureza y debe contener un bajo contenido de Fe_2O_3 para evitar un impacto negativo en la estabilidad térmica del producto final y un bajo contenido de Al_2O_3 para maximizar la formación de xonotlita. Es importante también que la sílice de humo posea un tamaño de partícula muy pequeño, así nos aseguramos una mayor reactividad. La sílice de humo normalmente está presente en forma de partículas aglomeradas que se forman por un proceso de maduración de Oswald; y es de gran importancia para un buen desarrollo de gel C-S-H que estos agregados se rompan mediante la aplicación de un tratamiento mecánico/químico y que se formen partículas primarias de sílice de humo con un diámetro inferior a 10 μm. Si se cumplen las condiciones de pequeño tamaño de partícula y alta pureza en la sílice de humo, y además se mantiene una relación inicial C/S cercana a 1, se asegura la formación de geles C-S-H de baja densidad. Posteriormente, en el tratamiento hidrotermal esto geles se convierten en xonotlita. Para conseguir una buena estabilidad térmica e integridad del producto final, se requieren altos contenidos de xonotlita (típicamente por encima del 70%).

La cantidad y las propiedades del gel C-S-H necesarias para el producto final de densidad dada también son importantes para obtener unas buenas propiedades mecánicas,

prestando especial atención a la tenacidad a la fractura. Por tanto, es requisito primordial el contar con una cantidad mínima de gel C-S-H para tener una mínima resistencia mecánica inicial necesaria para evitar el agrietamiento durante el tratamiento hidrotermal en autoclave de las placas prensadas, aunque también se deben evitar contenidos demasiado altos de gel C-S-H de baja densidad porque entonces se obtienen productos quebradizos. Para mejorar la tenacidad a la fractura, se han probado aditivos funcionales específicos de carácter mineral, y los mejores resultaron ser la vermiculita y la wollastonita. Las fibras de celulosa se utilizan en todas las formulaciones como fibras de refuerzo y como un componente para evitar la propagación del agrietamiento durante los ensayos de resistencia térmica y velocidad de propagación del fuego.
El estudio de investigación de esta tecnología a escala de laboratorio ha demostrado que se pueden obtener silicatos de calcio hidratados para un rango de densidades que varían desde 280 Kg/m^3 hasta 700 Kg/m^3, utilizando cantidades óptimas de gel C-S-H sintetizado en condiciones específicas. Y se pueden obtener productos de buena calidad con menor relación agua/sólido (y por lo tanto menor dependencia energética) que en el caso de las tecnologías existentes.

En la segunda parte de esta tesis, se ha investigado más en detalle la producción de silicatos de calcio con un rango de densidad de 300 a 600 Kg/m^3 empleando la tecnología basada en la reacción hidrotermal con autoclave vertical agitado, con el objetivo de desarrollar una mejor comprensión de la reacción y mejorar la calidad del producto. En este tipo de autoclaves verticales con sistema de agitación, se sintetizan partículas de xonotlita. Las partículas de xonotlita cristalizan tras reaccionar el sistema formado por cal, sílice y agua en agitación y dentro de un ciclo en el que la suspensión acuosa se somete durante varias horas a 200-220°C de temperatura y a una presión de vapor de unos 17 bar. A continuación, la suspensión acuosa de partículas de xonotlita formadas en la autoclave se mezcla con una serie de aditivos como bentonita, fibras de celulosa, fibras de vidrio, un compuesto endotérmico (ettringita) y cemento portland. Esta mezcla acuosa se filtra y prensa simultáneamente para evacuar la máxima cantidad de agua, obteniendo placas. Finalmente, las placas se curan y se secan. Previamente a la reacción hidrotermal, en un paso inicial que se denomina apagado de la cal, el CaO se convierte en $Ca(OH)_2$ con un tamaño de cristal y una distribución de partícula específicos, los cuales son controlados por las condiciones de reacción (relación agua/sólido, temperatura) y por medio del uso de aditivos (yeso) que permiten la cristalización de $Ca(OH)_2$. El tamaño y la distribución de los cristales de $Ca(OH)_2$ influyen en la velocidad de solubilización. La solubilización de la cal conduce a un aumento del pH y esta condición alcalina, junto con el aumento de la temperatura en el reactor, favorece la solubilización del cuarzo. De este modo, se forman productos de reacción intermedios alrededor de los granos de cuarzo en disolución. El estudio realizado sobre el efecto del tamaño de partícula del cuarzo y el uso de otras fuentes de sílice, así como mezclas de sílice cristalina y amorfa, muestra que los mecanismos de reacción dependen principalmente de las reactividades relativas de la cal y la sílice: para partículas finas de cuarzo la reacción transcurre a través del gel C-S-H como fase intermediaria, mientras que para partículas grandes de cuarzo la reacción pasa por α-C_2SH como fase intermediaria. Las reacciones a través de la fase α-C_2SH transcurren de forma lenta y de forma incompleta, por lo que debe evitarse. Hay principalmente dos grupos o familias de gel C-S-H. El primer grupo, C-S-H (I) tiene una relación Ca/Si inferior a 1,5 y una estructura similar a la tobermorita. C-S-H (I) contiene principalmente dímeros y largas cadenas de silicatos. El segundo grupo, C-S-H (II) contiene cadenas de silicatos más cortas que el C-S-H (I) y tiene un menor grado de polimerización. Esta es la fase C-S-H más rica en Ca, por lo tanto, con una relación Ca/Si

superior a 1 y recristaliza más fácilmente en xonotlita que el C-S-H (I). La composición del gel C-S-H inicial depende en gran medida de la proporción de iones Ca^{2+} y SiO_4^{-4} en la solución alrededor de los granos de cuarzo o sílice de humo. Cuando se utiliza sílice amorfa, se forma C-S-H (I) como fase inicial, mientras que, en mezclas de cuarzo y sílice amorfa, generalmente se forma C-S-H (II). La estructura del gel C-S-H determina la posterior recristalización y morfología de tobermorita/xonotlita en el rango de temperatura de 120-200°C. La estructura de la tobermorita y xonotlita, así como el contenido de estas fases cristalinas son esenciales para las propiedades del producto final. Cuando se usan sílices amorfas o cuarzo fino, se forman finas agujas de xonotlita, éstas normalmente incluyen muchos poros pequeños y dan a lugar a productos finales con buenas propiedades mecánicas y térmicas.
Se han investigado los diferentes mecanismos de reacción entre distintas fuentes de sílice utilizando diferentes técnicas analíticas clásicas para caracterizar los productos intermedios como es el caso de XRD, SEM, FTIR y otras técnicas más avanzadas como NMR en estado sólido, TEM y análisis de la función de distribución de pares mediante el uso de XRD con luz sincrotrón. Esto permitió explicar parcialmente los mecanismos de reacción, no obstante, todavía quedan más incógnitas por resolver siendo necesaria una investigación futura. En cuanto a la cinética de las reacciones vía gel C-S-H, se ha determinado que sigue la ecuación de Avrami, en donde se ha obtenido un coeficiente n cercano a 1. Esto indica que al menos en algunas etapas de la reacción, la velocidad de solubilización del cuarzo parece ser el parámetro clave que controla el proceso.
Otro de los objetivos de esta segunda parte de la tesis, ha sido la búsqueda de aditivos con propiedades endotérmicas que pudieran sustituir a la ettringita como agente endotérmico de referencia. La ettringita presenta problemas en el proceso de secado (60ºC) de las placas compuestas por silicatos de calcio, ya que tiende a descomponerse parcialmente a partir de ~50ºC. Se han probado varios compuestos inorgánicos de carácter endotérmico en la matriz del producto y se ha evaluado su respuesta a altas temperaturas. También se ha realizado una modelización tomando como factores clave la temperatura de descomposición y entalpías de cada uno de estos compuestos para estimar de forma aproximada cuáles serían los picos ideales o teóricos de temperatura de descomposición, para un efecto óptimo endotérmico en toda la sección de la placa de silicato de calcio. Y con ello, se han propuesto otras alternativas para la protección al fuego y aislamiento térmico en diferentes aplicaciones (160ºC - temperatura de descomposición de endotermo para emplear en tabiques o compartimentos, 380ºC - temperatura de descomposición de endotermo para proteger estructuras de hormigón y 500ºC - temperatura de descomposición de endotermo en el caso de protección de estructuras metálicas de acero).

La tercera parte de este estudio de investigación consiste en la producción de silicatos de calcio 'libres de cuarzo' empleando la tecnología de doble tratamiento hidrotérmico a escala de laboratorio, "double autoclaving". Se ha buscado una alternativa al producto de referencia que no contenga cuarzo residual en su matriz. En esta tecnología, inicialmente se sintetizan las partículas primarias de xonotlita utilizando el proceso de reacción hidrotermal en autoclave con sistema de agitación. Después, a la suspensión acuosa formado por partículas de xonotlita se le añaden aditivos tales como fibras de celulosa, fibras de vidrio, cargas minerales, así como un conglomerante hidráulico, cemento Portland o una mezcla de cemento Portland, hidróxido de calcio y sílice. Luego esta mezcla se prensa y se obtienen placas, que a posteriori se curan a una temperatura de unos 40ºC, condición en la que el cemento OPC se hidrata y forma la fase gel aglomerante de C-S-H. En la etapa final de este proceso, las placas se someten a un tratamiento hidrotérmico en autoclave horizontal, en donde el gel C-S-H se convierte en tobermorita,

y el cuarzo reacciona con la portlandita formada durante la hidratación del OPC formando también tobermorita.
En este proceso, Promat actualmente utiliza cuarzo como fuente de sílice y wollastonita, como carga mineral (contiene cuarzo como impureza) para controlar la estabilidad térmica del producto. El cuarzo residual es una sustancia que puede tener efectos nocivos sobre la salud. Durante el corte y mecanizado de placas de silicato de calcio se pueden generar fracciones respirables de cuarzo. Por tanto, el objetivo aquí ha sido obtener silicatos de calcio libres de contenido en cuarzo, utilizando, por un lado, sílice amorfa para reemplazar el cuarzo, y por otro, xonotlita especial sintetizada y otras cargas minerales para reemplazar la wollastonita. De esta forma se ha optimizado ha diseñado una matriz que sea capaz de resistir a altas temperaturas y no sufra contracción dimensional térmica.
Los productos desarrollados mediante el proceso de doble tratamiento hidrotermal han sido desarrollados tras aplicar variaciones en la formulación estándar, y han dado lugar a propiedades mecánicas y térmicas similares a los productos existentes que contienen cuarzo residual. Estos nuevos productos presentan contenidos en cuarzo residual por debajo del 0,1% en peso.

RESUM

Els silicats de calci hidratats són materials que van començar a estudiar-se des de l'any 1920, principalment per ser emprats com a elements d'aïllament a altes temperatures al sector construcció i en altres sectors industrials. El grup Etex va començar amb la producció i comercialització de silicats de calci per a aplicacions d'aïllament tèrmic i protecció passiva contra incendis a l'empresa Promat (Alemanya) el 1958. A finals dels anys 70, aquesta companyia va introduir una nova tecnologia en el desenvolupament de aquests productes. Aquesta nova tecnologia va consistir en el desenvolupament d'una sèrie de fases minerals basades en silicats de calci hidratats sintètics més estables, la xonotlita i la tobermorita mitjançant l'ús de reaccions hidrotermals amb sistema d'agitació. Aquest procés s'anomena en anglès "stirred reactor autoclave", i és una tecnologia que consisteix en fer servir una autoclau vertical amb un sistema d'agitació controlada. Amb aquesta tecnologia s'obté una matriu mineral, i és possible el control del creixement de cristalls de xonotlita i tobermorita. Això permet la formació de diferents textures optimitzades per a diferents aplicacions a altes temperatures.

En el procés de producció implantant a Promat (Tisselt, Bèlgica), la xonotlita i la tobermorita s'obtenen en fer reaccionar una barreja d'hidròxid de calci i sílice cristal·lina en medi aquós amb una relació CaO/SiO_2 propera a 1, i en condicions hidrotermals, a una temperatura de 200°C i a una pressió de vapor de 17 bar. D'aquesta manera, en aquestes condicions es formen aquestes fases cristal·lines (xonotlita i tobermorita); partícules específiques de baixa densitat que s'utilitzen com a components principals de diversos productes i noves aplicacions que s'han desenvolupat en les darreres dècades al centre d'Investigació i Tecnologia de Promat, pertanyent al Grup Etex. Aquest procés dóna lloc a l'obtenció de productes d'alta qualitat, encara que cal una millor comprensió per poder optimitzar i controlar encara més aquest tipus de materials, i així reduir costos energètics a la tecnologia utilitzada.

En aquest projecte de tesi doctorat, es pretén assolir tres objectius principals:

1. Desenvolupar una nova tecnologia per a l'obtenció de silicats de calci hidratats, mitjançant la síntesi inicial de gel C-S-H per controlar la densitat del producte final. Aquest és un procés que el fan servir alguns competidors de Promat i que anomenem en aquesta tesi com a tecnologia 'Gel Tank'. També es pretén dur a terme un estudi profund dels paràmetres clau que influeixen en el procés. A més, es pretén investigar la viabilitat de produir silicats de calci hidratats amb diferents densitats i comparar-ne les propietats amb els obtinguts mitjançant tecnologies existents. Amb l'ús d'aquesta nova tecnologia, la idea és utilitzar menor quantitat d'aigua que en els processos convencionals, i reduir la despesa energètica i minimitzar l'impacte mediambiental.
2. Ampliar el coneixement de la tecnologia basada en tractament hidrotermal mitjançant agitació i investigar la possibilitat de millorar el caràcter endotèrmic dels materials obtinguts mitjançant aquesta tecnologia.
3. Desenvolupar una nova generació de productes lliures de contingut en quars residual (< 0,1% en pes) mitjançant l'ús de l'anomenada tecnologia doble autoclaving.

La primera part d'aquesta tesi es centra en la investigació experimental de la síntesi de silicats de calci hidratats de baixa i mitjana densitat utilitzant la tecnologia Gel Tank, una tecnologia completament nova per a Etex. Aquest procés es compon de 4 etapes: formació d'una suspensió a base de gel C-S-H mitjançant la reacció d'una sílice amorfa reactiva amb calç hidratada al voltant de 90 °C (etapa de gelificació), barreja de la suspensió de gel C-S-H amb components addicionals (fibres de reforç i minerals funcionals), premsat de la barreja per obtenir plaques i, finalment, tractament hidrotermal d'aquestes plaques per convertir la fase gel C-S-H en fases més estables, com ara xonotlita i tobermorita.
El gel C-S-H format a l'etapa inicial (gelificació), té una densitat baixa i permet assolir pressions específiques requerides durant el premsat per obtenir plaques amb suficient resistència mecànica inicial per resistir al posterior tractament hidrotèrmic en què el gel C-S-H es transforma en tobermorita i /o xonotlita. La quantitat requerida de gel C-S-H depèn de la densitat final desitjada del producte a obtenir i va disminuint conforme es requereixen densitats més grans. Per a productes de 300 kg/m3 de densitat, s'utilitza com a font de silici, sílice amorfa, en aquest cas sílice de fum. Mentre que per a productes de 600-700 Kg/m3, s'empra una combinació de sílice amorfa i cristal·lina (quars) en la formulació inicial, sent només el 25% del total del contingut de sílice, sílice de fum.
La quantitat de gel C-S-H es controla principalment variant la proporció inicial de sílice amorfa i cristal·lina. Però també s'ha estudiat la influència de diferents paràmetres (temps de gelificació, temperatura de gelificació, condicions d'agitació) a la síntesi del gel C-S-H. A més, s'ha analitzat l'ús d'additius específics i s'han determinat les propietats finals dels productes obtinguts corresponents. La caracterització del gel C-S-H, inclou la determinació de les fases mineralògiques mitjançant difracció de raigs X mitjançant anàlisi Rietveld; mesura de la distribució de partícula per difracció làser; mesura de l'àrea específica superficial i porositat mitjançant els mètodes BET i BJH; anàlisi morfològic mitjançant SEM i determinació d'espècies químiques mitjançant espectroscòpia FTIR. Els gels C-S-H sintetitzats mitjançant la tecnologia Gel Tank, tenen estructures mesoporoses amb porus de 2-50 nm.
Es van provar també diferents graus de sílice de fum en la formulació, i es van caracteritzar mitjançant diverses tècniques d'anàlisi, com ara el XRF, XRD i anàlisi de difracció làser per determinar el tamany de partícula. Aquests anàlisis van determinar que la sílice de fum ha de ser d'alta puresa i ha de contenir un baix contingut de Fe_2O_3 per evitar un impacte negatiu a l'estabilitat tèrmica del producte final i un baix contingut de Al_2O_3 per maximitzar la formació de xonotlita. És important també que la sílice de fum tingui un tamany de partícula molt xicotet, així ens assegurem una major reactivitat. La sílice de fum normalment és present en forma de partícules aglomerades que es formen per un procés de maduració d'Oswald; i és de gran importància per a un bon desenvolupament de gel C-S-H que aquests agregats es trenquin mitjançant l'aplicació d'un tractament mecànic/químic i que es formen partícules primàries de sílice de fum amb un diàmetre inferior a 10 μm. Si es compleixen les condicions de mida petita de partícula i alta puresa en la sílice de fum, ia més es manté una relació inicial C/S propera a 1, s'assegura la formació de gels C-S-H de baixa densitat. Posteriorment, en el tractament hidrotermal aquests gels es converteixen en xonotlita. Per aconseguir una bona estabilitat tèrmica i integritat del producte final, calen alts continguts de xonotlita (típicament per sobre del 70%).
La quantitat i les propietats del gel C-S-H necessàries per al producte final de densitat donada també són importants per obtenir unes bones propietats mecàniques, prestant especial atenció a la tenacitat a la fractura. Per tant, és requisit primordial comptar amb una quantitat mínima de gel C-S-H per tenir una mínima resistència mecànica inicial necessària per evitar l'esquerdament durant el tractament hidrotermal en autoclau de les

plaques premsades, encara que també cal evitar continguts massa alts de gel C-S-H de baixa densitat perquè aleshores s'obtenen productes trencadissos. Per millorar la tenacitat a la fractura, s'han provat additius funcionals específics de caràcter mineral, i els millors han resultar ser la vermiculita i la wollastonia. Les fibres de cel·lulosa s'utilitzen en totes les formulacions com a fibres de reforç i com un component per evitar la propagació de l'esquerdament durant els assaigs de resistència tèrmica i velocitat de propagació del foc. L'estudi d'investigació d'aquesta tecnologia a escala de laboratori ha demostrat que es poden obtenir silicats de calci hidratats per a un rang de densitats que varien des de 280 kg/m3 fins a 700 kg/m3 utilitzant quantitats òptimes de gel C-S-H sintetitzat en condicions específiques. I es poden obtenir productes de bona qualitat amb menor relació aigua/sòlid (i per tant menor dependència energètica) que en el cas de les tecnologies existents.

A la segona part d'aquesta tesi, s'ha investigat més detalladament la producció de silicats de calci amb un rang de densitat de 300 a 600 kg/m3 emprant la tecnologia basada en la reacció hidrotermal amb autoclau vertical agitat, amb l'objectiu de desenvolupar una millor comprensió de la reacció i millorar la qualitat del producte. En aquest tipus d'autoclaus verticals amb sistema d'agitació se sintetitzen partícules de xonotlita. Les partícules de xonotlita cristal·litzen després de reaccionar el sistema format per calç, sílice i aigua en agitació i dins d'un cicle en què la suspensió aquosa se sotmet durant diverses hores a 200-220°C de temperatura ia una pressió de vapor d'uns 17 bar. A continuació, la suspensió aquosa de partícules de xonotlita formades a l'autoclau es barreja amb una sèrie d'additius com bentonita, fibres de cel·lulosa, fibres de vidre, un compost endotèrmic (ettringita) i ciment pòrtland. Aquesta barreja aquosa es filtra i premsa simultàniament per evacuar la màxima quantitat daigua, obtenint plaques. Finalment, les plaques es curen i s'assequen. Prèviament a la reacció hidrotermal, en un pas inicial que s'anomena apagat de la cal, el CaO es converteix en $Ca(OH)_2$ amb un tamany de cristall i una distribució de partícula específics, els quals són controlats per les condicions de reacció (relació aigua/sòlid, temperatura) i per mitjà de l'ús d'additius (guix) que permeten la cristal·lització de $Ca(OH)_2$. El tamany dels cristalls de $Ca(OH)_2$ influeix en la velocitat de solubilització. La solubilització de la calç condueix a un augment del pH i aquesta condició alcalina, juntament amb l'augment de la temperatura al reactor, afavoreix la solubilització del quars. D'aquesta manera, es formen productes de reacció intermedis al voltant dels grans de quars en dissolució. L'estudi realitzat sobre l'efecte del tamany de partícula del quars i l'ús d'altres fonts de sílice, així com barreges de sílice cristal·lina i amorfa, mostra que els mecanismes de reacció depenen principalment de les reactivitats relatives de la calç i la sílice: per partícules fines de quars la reacció transcorre a través del gel C-S-H com a fase intermediària, mentre que per a partícules grans de quars la reacció passa per α-C_2SH com a fase intermediària. Les reaccions a través de la fase α-C_2SH transcorren de manera lenta i de forma incompleta, per la qual cosa s'ha d'evitar. Hi ha principalment dos grups o famílies de gel C-S-H. El primer grup, C-S-H(I) té una relació Ca/Si inferior a 1,5 i una estructura similar a la tobermorita. C-S-H (I) conté principalment dímers i llargues cadenes de silicats. El segon grup, C-S-H(II) conté cadenes de silicats més curtes que el C-S-H(I) i té un menor grau de polimerització. Aquesta és la fase C-S-H més rica a Ca, per tant, amb una relació Ca/Si superior a 1 i recristalitza més fàcilment en xonotlita que el C-S-H(I). La composició del gel C-S-H inicial depèn en gran mesura de la proporció d'ions Ca^{2+} i SiO_4^{-4} en la solució al voltant dels grans de quars o sílice de fum. Quan s'utilitza sílice amorfa, es forma C-S-H (I) com a fase inicial, mentre que en barreges de quars i sílice amorfa, generalment es forma C-S-H (II). L'estructura del gel C-S-H determina la posterior recristal·lització i morfologia

de tobermorita/xonotlita al rang de temperatura de 120-200°C. L'estructura de la tobermorita i xonotlita, així com el contingut d'aquestes fases cristal·lines, són essencials per a les propietats del producte final. Quan s'usen sílices amorfes o quars fi, es formen fines agulles de xonotlita, aquestes normalment inclouen molts porus petits i donen lloc a productes finals amb bones propietats mecàniques i tèrmiques.
S'han investigat els diferents mecanismes de reacció entre diferents fonts de sílice utilitzant diferents tècniques analítiques clàssiques per caracteritzar els productes intermedis com és el cas de XRD, SEM, FTIR i altres tècniques més avançades com a NMR en estat sòlid, TEM i anàlisi de la funció de distribució de parells mitjançant lús de XRD amb llum sincrotró. Això va permetre explicar parcialment els mecanismes de reacció, no obstant, encara queden més incògnites per resoldre essent necessària una investigació futura. Quant a la cinètica de les reaccions via gel C-S-H, s'ha determinat que segueix l'equació d'Avrami, on s'ha obtingut un coeficient proper a 1. Això indica que almenys en algunes etapes de la reacció, la velocitat de solubilització del quars sembla el paràmetre clau que controla el procés.
Un altre dels objectius d'aquesta segona part de la tesi ha estat la cerca d'additius amb propietats endotèrmiques que poguessin substituir l'ettringita com a agent endotèrmic de referència. L'ettringita presenta problemes en el procés d'assecatge (60ºC) de les plaques compostes per silicats de calci, ja que tendeix a descompondre's parcialment a partir de ~50ºC. S'han provat diversos compostos inorgànics de caràcter endotèrmic a la matriu del producte i se n'ha avaluat la resposta a altes temperatures. També s'ha realitzat una modelització prenent com a factors clau la temperatura de descomposició i entalpies de cadascun d'aquests compostos per estimar de forma aproximada quins serien els pics ideals o teòrics de temperatura de descomposició, per a un efecte òptim endotèrmic a tota la secció de la placa de silicat de calci. I amb això, s'han proposat altres alternatives per a la protecció al foc i aïllament tèrmic en diferents aplicacions (160ºC - temperatura de descomposició d'endoterm per emprar en envans o compartiments, 380ºC - temperatura de descomposició d'endoterm per protegir estructures de formigó i 500ºC - temperatura de descomposició d'endoterm en cas de protecció d'estructures metàl·liques d'acer).

La tercera part d'aquest estudi de recerca consisteix en la producció de silicats de calci lliures de quars emprant la tecnologia de doble tractament hidrotèrmic a escala de laboratori, “double autoclaving”. S'ha buscat una alternativa al producte de referència que no contingui quars residual a la matriu. En aquesta tecnologia, inicialment se sintetitzen les partícules primàries de xonotlita utilitzant el procés de reacció hidrotermal a l'autoclau amb sistema d'agitació. Després, a la suspensió aquosa format per partícules de xonotlita se li afegeixen additius com ara fibres de cel·lulosa, fibres de vidre, càrregues minerals, així com un conglomerant hidràulic, ciment Portland o una barreja de ciment Portland, hidròxid de calci i sílice. Després, aquesta barreja es premsa i s'obtenen plaques, que a posteriori es curen a una temperatura d'uns 40ºC, condició en què el ciment OPC s'hidrata i forma la fase gel aglomerant de C-S-H. A l'etapa final d'aquest procés, les plaques se sotmeten a un tractament hidrotèrmic en autoclau horitzontal, on el gel C-S-H es converteix en tobermorita, i el quars reacciona amb la portlandeta formada durant la hidratació de l'OPC formant també tobermorita.
En aquest procés, Promat actualment utilitza quars com a font de sílice i wollastonita, com a càrrega mineral (conté quars com a impuresa) per controlar l'estabilitat tèrmica del producte. El quars residual és una substància que pot tenir efectes nocius sobre la salut. Durant el tall i mecanitzat de plaques de silicat de calci es poden generar fraccions respirables de quars. Per tant, l'objectiu aquí ha estat obtenir silicats de calci lliures de contingut en quars, utilitzant, d'una banda, sílice amorfa per reemplaçar el quars, i de

l'altra, xonotlita especial sintetitzada i altres càrregues minerals per reemplaçar la wollastonita. D'aquesta manera s'ha optimitzat ha dissenyat una matriu que sigui capaç de resistir a temperatures altes i no pateixi contracció dimensional tèrmica.
Els productes desenvolupats mitjançant el procés de doble tractament hidrotermal han estat desenvolupats després d'aplicar variacions a la formulació estàndard, i han donat lloc a propietats mecàniques i tèrmiques similars als productes existents que contenen quars residual. Aquests nous productes presenten continguts en quars residual per baix del 0,1% en pes.

ABSTRACT

Calcium silicate hydrates have been studied for building and industrial applications since 1920. Etex group started its production and sales of calcium silicates for applications as insulation at high temperatures and passive fire protection in the company Promat (Germany) in 1958. In the late 70s, a new concept was introduced on the development of these products. It was based upon well controlled development of the most stable calcium silicate hydrate-based minerals, being xonotlite and tobermorite by using stirred hydrothermal conditions. This process is called stirred reactor/autoclave technology. The mineral engineering of the matrix by controlling the growth of xonotlite and tobermorite crystals allowed the formation of different optimized textures for different applications at high temperatures.

In the production process in Tisselt (Belgium), xonotlite and tobermorite are produced when reacting a mixture of calcium oxide and silica in an aqueous medium with a CaO / SiO_2 ratio near to 1 in hydrothermal conditions, at 200°C of temperature and 17 bar as vapour pressure. Therefore, in these conditions, these crystalline phases (xonotlite and tobermorite) as specific particles of low-density are formed which are used as the main components of several new products and applications that were developed in the latest decades at the Promat Research and Technology centre within the Etex Group. The process leads to products of high quality, though better understanding is required to further optimize and control these products and lower their energy dependence.

In this industrial PhD project, three targets were aimed at:

1. Develop a new process to make calcium silicate hydrates using C-S-H gel to control the density, a process that is used by some competitors of Promat and that is named in this thesis as 'gel tank' process. In addition, to carry out a deep understanding of all the influencing parameters, investigating the feasibility to make different densities and compare the properties of calcium silicates obtained in this way with the existing technologies. This technology is expected to use less water than conventional technologies, so reducing the energetic costs and hence to minimize the environmental impact.

2. Increase the understanding of the hydrothermal reaction process called 'stirred reactor' technology and investigate the possibility to enhance the endotherm character of the materials obtained through this technology.

3. Develop a new generation of products formed by the so-called double autoclaving technology with contents of residual quartz below 0.1wt%.

The first part of this thesis has focused on the experimental investigation of the synthesis of low and medium density hydrated calcium silicates, using the so-called gel tank technology, a technology that is new for Etex. The gel tank process is composed of 4 steps: formation of a C-S-H gel-based slurry by reacting a reactive amorphous silica with hydrated lime at around 90°C (gelling step), mixing the slurry with additional ingredients (reinforcing fibres and functional fillers), filter-pressing the slurry into plates and finally, hydrothermal treatment of these plates to convert the C-S-H gel phase into more stable phases, such as xonotlite and tobermorite.

The C-S-H gel formed in the initial gelling step has low density and allows the required specific pressures to be developed during the filter-pressing, forming in this way boards with enough green strength to survive the later hydrothermal treatment in which C-S-H gel is transformed into tobermorite/xonotlite. The required amount of C-S-H gel depends on the desired final density of the product one wants to form and decreases conforming higher densities are pursued. For 300 Kg/m^3 density products, only silica fume can be used as SiO_2 source whereas that for 600-700 Kg/m^3 products, a combination of amorphous and crystalline silica is used at the starting formulation, being only the 25% of total silica content, silica fume.

The amount of C-S-H gel is mainly controlled by varying the ratio of amorphous to crystalline silica. Different parameters of influence on the C-S-H gel and corresponding end-products have been studied, being mainly the microsilica characteristics, the reaction conditions (time, temperature, stirring conditions) and use of additives. The characterization of the C-S-H gel included mineralogical phase determination by Rietveld XRD analysis; particle size distribution by laser diffraction; specific surface area and porosity measurements by BET and BJH methods; morphology, texture and chemical analysis by EDAX SEM and FTIR spectroscopy. C-S-H gels synthesized by means of Gel Tank technology, have mesoporous structures with pores of 2-50nm.

Different grades of microsilica were tested by several techniques such as XRF, XRD and laser diffraction analysis. It was found that the silica fume must be of high purity and must contain low Fe_2O_3 contents to avoid negative impact on the thermal stability and low Al_2O_3 content to maximize the xonotlite formation. For a good reactivity of the silica fume its particle size must be very small. Silica fume normally is present as agglomerates that form by an Oswald ripening process; and it is very essential for good C-S-H development that these aggregates are broken by a mechanical/chemical treatment and that primary silica fume particles are formed with a diameter below 10 μm. When fulfilling the conditions of very low particle size and high purity and, respecting a C/S ratio near to 1, low-density C-S-H gels form. Later, in the hydrothermal treatment they convert into xonotlite. High contents of xonotlite (typically above 70%) are required for good thermal stability and integrity of the end-product.

The amount and properties of the C-S-H gel for end-product of given density are also important for the mechanical properties and fracture toughness. A minimum C-S-H gel amount is required to have the required green strength needed to avoid cracking during the autoclaving step of pressed boards, though too high contents of low-density C-S-H gel also must be avoided because then brittle products are obtained. To improve the fracture toughness, specific functional fillers were tested, and the best ones appeared to be vermiculite and wollastonite. Cellulose fibres were used in all compositions as reinforcing fibres and as crack-arresting phases during fire tests.

The study on this technology researched at laboratory scale showed that hydrated calcium silicates can be produced for densities varying from 280 Kg/m^3 to 700 Kg/m^3, using optimal amounts of a C-S-H gel made in specific conditions and good quality products could be obtained with lower water/solid ratio (and hence lower energy dependence) than with the existing technologies.

In the second part of this thesis, the production of calcium silicates with a density range from 300 to 600 Kg/m^3 using dynamic hydrothermal treatment technology in a vertical

autoclave with mechanical stirring (so called 'stirred reactor/autoclave technology') was investigated with the aim of developing a better understanding of the reaction and improve the product quality. In this kind of vertical stirred autoclaves, xonotlite particles are synthesized. The xonotlite particles crystallize by means of a reaction between lime, silica and water under stirring and within cycle in which the aqueous suspension is treated for several hours at 200-220°C of temperature and 17 bar of vapour pressure. Then, the xonotlite particles formed in the autoclave are mixed with a series of additives such as bentonite, cellulose fibres, glass fibres, an endothermic agent (ettringite) and cement. The aqueous mixture is filtered and pressed simultaneously to evacuate the maximum amount of water, obtaining boards. Finally, the boards are cured and dried. Before the hydrothermal reaction, in an initial step that is called slaking, CaO is converted into $Ca(OH)_2$ with specific crystal size and particle distribution, controlled by the reaction conditions (w/s ratio, temperature) and the use of additives to control the size of the $Ca(OH)_2$ crystals. The size and distribution of $Ca(OH)_2$ crystals influence its rate of solubilization. The solubilization of lime leads to an increase of the pH and this alkaline condition, together with the increase of temperature in the reactor, thereupon the solubilization of the quartz occurs and intermediate reaction products are formed around the dissolving quartz grains. The study on the effect of the particle size of quartz and the use of other silica sources as well as mixtures of crystalline and amorphous silica, performed in this research work, showed that the reaction pathways mainly depend on the relative reactivities of lime and silica: for fine quartz particles the reaction passes by C-S-H gel whilst for large quartz particles, the reaction goes by α-C_2SH. Reactions via α-C_2SH are slow and incomplete, then it must be avoided. There are mainly two groups of C-S-H gel. The first group, C-S-H (I) has a Ca/Si ratio lower than 1.5 and it has a similar structure to tobermorite. C-S-H (I) contains mostly dimers and long chains of silicates. The second group, C-S-H (II) contains shorter chains of silicates than C-S-H (I) and has a lower degree of polymerization. This is the more Ca-rich C-S-H phase, hence with a Ca/Si ratio greater than 1 and it does recrystallize more easily into xonotlite than C-S-H (I). The composition of the initial C-S-H gel depends strongly on the ratio of Ca and Si ions in the solution around the quartz or microsilica grains. When using amorphous silica, C-S-H (I) develops as an initial phase, while in mixtures of quartz and amorphous silica, generally C-S-H (II) is formed.

The C-S-H gel structure determines the later recrystallization and morphology of tobermorite/xonotlite at temperatures in the range 120-200°C. In addition, the structure and content of these phases are essential for the properties of the end-product. Fine xonotlite needles-like crystalized when using amorphous silicas or fine quartz, normally include lots of small pores and lead to end-products with good mechanical and thermal properties.

These reaction sequences were studied by using different analytical techniques as for example conventional and high-energy-based synchrotron XRD, SEM, TEM, FTIR and NMR spectroscopy, etc. It allowed us to partially explain the reaction mechanisms, though there remain further questions for future research. Concerning to the kinetics of the reactions via C-S-H gel seem to follow the Avrami equation with a coefficient n near to 1, indicating that at least in some stages of the reaction the solubilization of quartz seems the rate determining step.

Another goal in this section, it has been to search for additives with endothermic properties that could replace ettringite as a reference endothermic additive. Ettringite

presents problems in the drying process of the manufacturing calcium silicates as it tends to partially decompose in the drier. Several endothermic inorganic compounds have been tested in the product matrix and their response to high temperatures has been evaluated. A modelling based on the decomposition temperature and enthalpies of each of these compounds has also been carried out to roughly estimate what would be the ideal or theoretical peaks of decomposition temperature at which the endothermic effect is the ideal one to protect and isolate different fire protection applications (160ºC for partition walls or compartments, 380ºC for concrete structure and 500ºC in the case of metal steel structures).

Finally, the third part of this project consisted of the 'quartz-free' production of calcium silicates using double hydrothermal treatment technology at laboratory scale. A new quartz-free alternative to the existing products made with this technology was sought. In this technology, primary xonotlite particles are first synthesized in stirred hydrothermal reactor. To the slurry of xonotlite particles, reinforcing additives such as cellulose fibres, glass fibres, mineral fillers are added as well as a binder based upon Portland cement or a mixture of Portland cement, calcium hydroxide and silica. Boards are then formed by filtering and pressing, and these are cured at a temperature of about 40ºC, condition in which the OPC cement hydrates and forms a binding C-S-H gel phase. In a final stage, the board is submitted to a hydrothermal treatment in a horizontal autoclave and in these conditions, the C-S-H gel converts into tobermorite, and quartz react with the portlandite formed during OPC hydration forming also tobermorite.

In this process, Promat currently uses quartz as silica source and wollastonite to control the thermal stability. Hence the products contain residual quartz, a substance that can have health effects when generating breathable fractions on machining. Therefore, the target here has been to obtain quartz-free calcium silicates using special xonotlite or C-S-H gel particles instead, replacing quartz by amorphous silica and optimizing the matrix so that there was no need to use wollastonite to reduce the thermal shrinkage.

The products developed by means of double autoclaving process applying variations at the standard formulation presented similar properties as the quartz containing existing products, however showing contents of residual quartz below 0.1wt%.

GLOSSARY

Cement Chemistry Notation

Cement chemistry notation (CCN) was developed to simplify the formulas cement chemists use on daily basis. Therefore, there is a shorthand way of writing the chemical formula of oxides of calcium, silicon, various metals, hydration products of cement paste and mineral phases formed after that. In this thesis, it has been used this notation cause of the calcium silicate hydrates development is associated to cement chemistry field as ceramic materials.

The main oxides present in cement, ceramics or glass are abbreviated as it follows:

CCN	Formula	Name
C	CaO	Calcium oxide/Lime
S	SiO_2	Silicon dioxide/Silica
A	Al_2O_3	Aluminum oxide/Alumina
F	Fe_2O_3	Iron oxide/Rust
T	TiO_2	Titanium oxide/Titania/Rutile
M	MgO	Magnesium oxide/Periclase
K	K_2O	Potassium oxide
N	Na_2O	Sodium oxide
H	H_2O	Water
$\bar{C}$	CO_2	Carbon dioxide
$\bar{S}$	SO_3	Sulfur trioxide
P	P_2O_5	Phosphorus hemi-pentoxide

Hydrated products formed in hardened cement pastes or in ceramics are more complex because many of these products have nearly the same formula and some are solid solutions with overlapping formulas. The examples present in this thesis are listed below:

CCN	Formula	Name or mineral phase
CH	$Ca(OH)_2$ or $CaO{\cdot}H_2O$	Calcium hydroxide/Portlandite
C-S-H/ CSH	0.6-2.0 $CaO{\cdot}SiO$ 0.9-2.5 H_2O with variable composition within this range and often also incorporating partial substitution of Al for Si	Calcium silicate hydrate
AFt	$C_6A\bar{S}_3H_{32}$, sometimes with substitution of Fe for Al, and/or various other anions such as OH^- or CO_3^{2-} for SO_4^{2-}	Calcium trisulfoaluminate hydrate/Ettringite

Analysis and Characterization Techniques Notation

The different techniques used for this research have scientifically an abbreviation as it follows:

Abbreviation	Name
XRD	X-Ray diffraction
XRF	X-Ray fluorescence
SEM	Scanning electron microscopy
TEM	Transmission electron microscopy
NMR	Nuclear magnetic resonance
FTIR	Fourier-transformed infrared
DSC	Differential scanning calorimetry
TGA	Thermal gravimetry analysis
TMA	Thermomechanical analysis
RF	Fire rate propagation
BET	Brunauer-Emmett-Teller specific surface area analysis
BJH	Barrett-Joyner-Halenda pore size distribution analysis
LD-PSD	Laser diffraction of particle size distribution

CHAPTER 1

INTRODUCTION AND TARGETS

CHAPTER 1. Introduction and targets

1.1 Background

The demand of high-performance building materials has industrially increased over last years. In particular, thermal insulation and fire protection are important for safety, energy consumption and comfort in different scenarios. Calcium silicate-based products have been widely employed as high-performance insulators and as passive fire protection materials since a few decades. Actually, they are applied not only for the construction sector but also in a large number of industrial markets as energy, oil, gas, heavy industry, transportation, fired rated components and thermal appliances. They are used in these applications because of a set of very specific properties such as low bulk density, low thermal conductivity, high mechanical strength, and thermal stability. Some typical applications of fire protection materials include partition walls, fire doors, ventilation channels, smoke extraction ducts, protection of steel columns, protection of concrete, collars of cables, non-combustible furniture for marine, etc. Whereas that in thermal insulation systems calcium-silicate based materials are used for example as insulators in night storage heaters, kilns and engines of aircrafts.

For applications in fire protection and thermal insulation it is essential that calcium silicate hydrates are formed in hydrothermal conditions. In these conditions poorly crystalline phases are converted into crystalline phases. Xonotlite and tobermorite are the most important phases to obtain suitable properties. The most important variables controlling their formation are the chemical composition and particle size of starting raw materials, the CaO/SiO_2 initial ratio, processing, and autoclaving conditions. Several technologies exist to make calcium silicate hydrates. The most important ones are slurry reactor technology as well as autoclaving processes of boards formed by different techniques. In the slurry reactor technology, slurries of light-weight calcium silicate particles are produced by treating a mixture of lime, silica and some additives for a few hours around 200°C in a stirred autoclave reactor. After preparation, the slurries are mixed with other ingredients such as fibers, cement, clay and some other raw materials and then densified using a filter-press technology. In post-autoclaving technologies, boards are formed by a technology such as Hatschek, flow-on, filter-press or others and the so produced boards are treated under hydrothermal conditions in horizontal autoclaves. For low density boards, also casting of pastes and autoclaving can be applied.

The Promat Research and Technology Centre developed in the past a concept that was called ‘Mineral and Matrix Engineering’. The idea was to control processes of nucleation and growth of crystals in order to form specific structures optimized for different applications and assemble these into matrixes engineered for the desired physical and chemical properties. Very good products have been developed in the last decades in the Etex factory in Tisselt (Belgium), though there is a major drawback for these products as their production is energy intensive and hence the products are expensive and have poor Life Cycle Analysis characteristics.

Within this PhD a less energy consuming technology was explored, and a better understanding of existing technologies was developed to improve certain properties in order to make the products more competitive in the market.

1.2 Objectives

1.2.1. General objectives

The main purpose of this industrial PhD concerns the development of a new generation of low and medium density hydrated calcium silicate-based products using a new technology, increase the understanding of the existing technologies and propose ways to improve them. The intention was also to make a comparative study between these processes in order to determine the strengths and weaknesses.

1.2.2. Specific objectives

In the framework of this thesis, a set of three specific objectives has been established.

As one of the targets, Promat Research and Technology Centre requested to investigate a new and sustainable technological process called 'Geltank' as possible alternative to non-pressed autoclaving technology which was industrially implemented in the past. Another goal within this 'Gel tank'-process research was to check to what extent this technology could also be used to produce pressed medium-density products for use in different applications. The general purpose of 'Gel tank' technology is to use lower volumes of water than in the traditional processes and, hence reducing the energetic consumption. The different specifications for the raw materials needed to be established as well as the best processing conditions. On the other hand, it was also requested to compare pressed Gel tank products with 'Double autoclaving products' of medium density for thermal insulation and fire protection.

Another specific goal consisted in developing an increased understanding of the so-called technology 'stirred autoclave reactor'. A study was made using different silica-types and grades, and also classical and advanced analytical techniques were used to improve the understanding on the reaction mechanism for the formation of xonotlite and tobermorite and the impact of the structures formed on the properties of the end-products. The possibilities to propose improved energy consumption by use of specific endotherm additives and opacifiers for different fire protection applications were equally investigated.

The last specific objective was focused on the replacement of raw materials or additives containing quartz utilized in the Double autoclaving technology. Calcium silicate boards made through this technology typically contain up to 10% of residual quartz and the machining and cutting of these boards can generate quartz-containing dust with possible health impact for the users. The intention was to avoid the use of quartz and quartz-containing additives using alternative raw materials and re-designing the matrix in order to reach similar performance for the end-products.

CHAPTER 2

STATE OF THE ART

CHAPTER 2. State of the art.

In this section, a general review of literature concerning the most relevant calcium silicate hydrates and the ways to form them under hydrothermal conditions is described. Therefore, a general review of the most remarkable works reported so far appears below.

2.1. An overview of calcium silicate hydrates

Calcium silicate hydrates are compounds included in the $CaO\text{-}SiO_2\text{-}H_2O$ system. This system has been studied for many years and due to its high complexity at structural level there are still uncertainties to be figured out. Almost 40 crystalline hydrated calcium silicate phases are known, more than 20 kinds of the calcium silicate hydrates naturally exist, and they are hydrothermally formed as in deep-oil-well or geothermal cements. However, a large list of them have been synthesized applying hydrothermal conditions. Furthermore, there are calcium silicate hydrates prepared at room temperature or higher up to ~100ºC with structure ranging from nearly amorphous to semi-crystalline **[1, 2]**. This group of hydrated calcium silicates is usually named as C-S-H gel. The C-S-H gel is formed either by mixing CaO and SiO_2 sources in an aqueous system or by hydration of OPC-cement. C-S-H presents a very disordered structure and must be distinguished from other Calcium-silicate-phases that possess a higher degree of order. The C-S-H phases have a variable composition with different CaO/SiO2 ratios around 1-2.

The fact that there are many Calcium silicate phases is related to the calcium cation. The big ionic radius ratio Ca^{2+}:O^{2-} is such as that allows a high degree of coordination of calcium by oxygen and so, the formation of a variety of other species **[3]**. **Table 1** lists the crystal-structure data for the different Calcium silicate phase. From this list, this thesis is specially focused on two types of crystalline phases, 11Å tobermorite ($Ca_5Si_6O_{16}(OH)_2 \cdot 7H_2O$ and xonotlite ($Ca_6Si_6O_{17}(OH)_2$). These hydrated calcium silicates are formed by hydrothermal synthesis using a Ca/Si ratio comprised between 0.8-1. And they are particularly of great interest as components of building materials applied in thermal insulation and fire protection because of high thermal stability, meaning that they maintain their structure and properties at high temperatures which is essential for applications in fire protection and thermal insulation. Prior to the formation of tobermorite and xonotlite, along the hydrothermal reaction and more specifically at the early stages, a nearly amorphous or better to say a nanocrystalline phase occurs, the C-S-H gel. This phase is classified according to its composition, that is Ca/Si ratio, in poorly crystalline phases such as C-S-H(I) and C-S-H(II) with structures closely like 11Å tobermorite, 14Å tobermorite and jennite **[4-7]**.

Name	Formula	Ca/Si	Sy	SG	M_r cell g mol^{-1}	Z	M_r formula g mol^{-1}	V Å^3	D_c g cm^{-3}	a Å	b	c	α	β	γ
(a). Wollastonite group															
Foshagite	$Ca_4(Si_3O_9)(OH)_2$	1.33	Tc	$P\bar{1}$	845.17	2	422.59	513.0	2.736	10.32	7.36	7.04	90	106.4	90
Hillebrandite	$Ca_2(SiO_3)(OH)_2$	2.00	O	$C\,m\,c\,2_1$	1141.53	6	190.25	702.1	2.700	3.6389	16.311	11.829	90	90	90
Nekoite	$Ca_3Si_6O_{15}\cdot 7H_2O$	0.50	Tc	$P1$	654.85	1	654.85	490.3	2.217	7.588	9.793	7.339	111.77	103.5	86.53
Okenite	$[Ca_8(Si_5O_{16})(Si_6O_{15})_2(H_2O)_6]^{4-}[Ca_2(H_2O)_9\cdot 3H_2O]^{4+}$	0.56	Tc	$P\bar{1}$	1966.60	1	1966.60	1418.5	2.302	9.69	7.28	22.02	92.7	100.1	110.9
Pectolite	$Ca_2NaHSi_3O_9$	1.00[a]	Tc	$P\bar{1}$	664.821	2	332.41	382.2	2.888	7.98	7.023	7.018	90.54	95.14	102.55
Wollastonite 1A	$Ca_3Si_3O_9$	1.00	Tc	$P\bar{1}$	696.98	2	348.49	396.96	2.916	7.9258	7.3202	7.0653	90.055	95.217	103.43
Xonotlite[b]	$Ca_6Si_6O_{17}(OH)_2$	1.00	M	$P\,1\,2/a\,1$	1427.99	2	713.99	879.3	2.700	17.032	7.363	7.012	90	90.36	90
(b). Tobermorite group															
Clinotobermorite[c]	$Ca_5Si_6O_{17}\cdot 5H_2O$	0.83	M	$C\,1\,c\,1$	2923.93	4	730.98	1859.64	2.611	11.276	7.343	22.642	90	97.28	90
Clinotobermorite[d]	$Ca_5Si_6O_{17}\cdot 5H_2O$	0.83	Tc	$C\,1$	1461.97	2	730.98	929.8	2.611	11.274	7.344	11.468	99.18	97.19	90.03
'Clinotobermorite 9 Å'[c]	$Ca_5Si_6O_{16}(OH)_2$	0.83	M	$C\,12/c\,1$	2635.68	4	658.92	1528.03	2.864	11.161	7.303	18.771	90	92.91	90
'Clinotobermorite 9 Å'[d]	$Ca_5Si_6O_{16}(OH)_2$	0.83	Tc	$C\bar{1}$	1317.84	2	658.92	763.9	2.865	11.156	7.303	9.566	101.08	92.83	89.98
Oyelite	$Ca_{10}B_2Si_8O_{29}\cdot 12.5H_2O$	1.25	O	n.d.	2672.52	2	1336.26	1668.77	2.659	11.25	7.25	20.46	90	90	90
9 Å tobermorite (riversideite)[c]	$Ca_5Si_6O_{16}(OH)_2$	0.83	O	$F\,d\,2\,d$	5271.37	8	658.92	3055.25	2.865	11.16	7.32	37.40	90	90	90
9 Å tobermorite (riversideite)[d]	$Ca_5Si_6O_{16}(OH)_2$	0.83	M	$P\,1\,1\,2_1/a$	1317.84	2	658.92	764.78	2.861	6.7	7.32	18.70	90	90	123.5
Anomalous 11 Å tobermorite[c]	$Ca_4Si_6O_{15}(OH)_2\cdot 5H_2O$	0.67	O	$F\,2\,d\,d$	5543.35	8	692.92	3741.65	2.460	11.265	7.386	44.970	90	90	90
Anomalous 11 Å tobermorite[d]	$Ca_4Si_6O_{15}(OH)_2\cdot 5H_2O$	0.67	M	$B\,1\,1\,m$	1385.84	2	692.92	935.4	2.460	6.735	7.385	22.487	90	90	123.25
Normal 11 Å tobermorite[d]	$Ca_{4.5}Si_6O_{16}(OH)\cdot 5H_2O$	0.75	M	$B\,1\,1\,m$	1423.88	2	711.94	941.68	2.460	6.732	7.369	22.680	90	90	123.18

Table 1 (continued)

Name	Formula	Ca/Si	Sy	SG	M_r cell g mol^{-1}	Z	M_r formula g mol^{-1}	V Å^3	D_c g cm^{-3}	a Å	b	c	α	β	γ
14Å tobermorite (plombierite)[c]	$Ca_5Si_6O_{16}(OH)_2 \cdot 7H_2O$	0.83	O	*F 2 d d*	6280.23	8	785.03	4578.56	2.278	11.2	7.3	56.0	90	90	90
14Å tobermorite (plombierite)[d]	$Ca_5Si_6O_{16}(OH)_2 \cdot 7H_2O$	0.83	M	*B 1 1 b*	1570.06	2	785.03	1170.4	2.228	6.735	7.425	27.987	90	90	123.25
(c). Jennite group															
Jennite	$Ca_9Si_6O_{18}(OH)_6 \cdot 8H_2O$	1.50	Tc	$P\bar{1}$	1063.44	1	1063.44	759.5	2.325	10.576	7.265	10.931	101.30	96.98	109.65
Metajennite	$Ca_9Si_6O_{18}(OH)_6 \cdot 8H_2O$	1.50	M	*I 1 2/m 1*	955.30	1	955.30	631.1	2.513	9.944	3.638	17.72	90	100.09	90
(d). Gyrolite Group															
Fedorite	$(Na,K)_2(Ca,Na)_7(Si,Al)_{16}O_{38}(F,OH)_2 \cdot 3.5H_2O$[f]	0.56[e]	Tc	$P\bar{1}$	1448.66	1	1448.66	961.24	2.503	9.645	9.6498	12.617	102.43	96.247	119.89
Gyrolite	$NaCa_{16}Si_{23}AlO_{60}(OH)_8 \cdot 14H_2O$	0.71[e]	Tc	$P\bar{1}$	2685.47	1	2685.47	1824.1	2.445	9.74	9.74	22.40	95.7	91.5	120
K-phase	$Ca_7Si_{16}O_{38}(OH)_2$	0.44	Tc	$P\bar{1}$	1371.91	1	1371.91	944.39	2.412	9.70	9.70	12.25	101.9	96.5	120
Reyerite	$Na_2Ca_{14}Si_{22}Al_2O_{58}(OH)_8 \cdot 6H_2O$	0.67[e]	Tg	$P\bar{3}$	2451.07	1	2451.07	1574.6	2.585	9.765	9.765	19.067	90	90	120
Truscottite	$Ca_{14}Si_{24}O_{58}(OH)_8 \cdot 2H_2O$	0.58	Tg	$P\bar{3}$	2335.20	1	2335.20	1545.5	2.509	9.735	9.735	18.83	90	90	120
Z-phase	$Ca_9Si_{16}O_{40}(OH)_2 \cdot 14H_2O$	0.56	Tc	$P\bar{1}$	1736.27	1	1736.27	1238.3	2.328	9.70	9.70	15.24	90.94	93.19	120
(e). γ-C_2S group															
Calcium chondrodite[g]	$Ca_5[SiO_4]_2(OH)_2$	2.50	M	*P 1 1 2$_1$/b*	837.16	2	418.58	492.1	2.825	8.9207	11.4481	5.0759	90	90	108.32
Kilchoanite	$Ca_6(SiO_4)(Si_3O_{10})$	1.50	O	*I 2 c m*	2307.21	4	576.80	1275.9	3.003	11.42	5.09	21.95	90	90	90

Table 1 (continued)

Name	Formula	Ca/Si	Sy	SG	M_r cell g mol^{-1}	Z	M_r formula g mol^{-1}	V Å^3	D_c g cm^{-3}	a Å	b	c	α	β	γ
(f). Other calcium silicate phases															
Afwillite	$Ca_3(SiO_3OH)_2{\cdot}2H_2O$	1.50	M	*C* 1 *c* 1	1369.82	4	342.46	859.6	2.646	16.278	5.6321	13.236	90	134.90	90
α-C_2SH	$Ca_2(HSiO_4)(OH)$	2.00	O	*P* $2_1/b$ $2_1/c$ $2_1/a$	1522.07	8	190.26	928.8	2.721	9.487	9.179	10.666	90	90	90
Cuspidine[h]	$Ca_4(F_{1.5}(OH)_{0.5})Si_2O_7$	2.00	M	*P* 1 $2_1/c$ 1	1461.96	4	365.49	814.2	2.982	7.518	10.521	10.906	90	70.7	90
Dellaite	$Ca_6(Si_2O_7)(SiO_4)(OH)_2$	2.00	Tc	$P\bar{1}$	1069.49	2	534.74	598.8	2.966	6.825	6.931	12.907	90.68	97.57	98.18
Jaffeite	$Ca_6[Si_2O_7](OH)_6$	3.00	Tg	*P* 3	1021.38	2	510.69	654.0	2.593	10.035	10.035	7.499	90	90	120
Killalaite	$Ca_{6.4}(H_{0.6}Si_2O_7)_2(OH)_2$	1.60	M	*P* 1 $2_1/m$ 1	1258.49	2	629.24	710.2	2.943	6.807	15.459	6.811	90	97.76	90
Poldervaartite[i]	$Ca(Ca_{0.67}Mn_{0.33})(HSiO_4)(OH)$	2.00[j]	O	*P* $2_1/b$ $2_1/c$ $2_1/a$	1561.69	8	195.21	904.8	2.866	9.398	9.139	10.535	90	90	90
Rosenhahnite	$Ca_3Si_3O_8(OH)_2$	1.00	Tc	$P\bar{1}$	733.02	2	366.51	420.2	2.897	6.955	9.484	6.812	108.64	94.84	95.89
Suolunite	$CaSiO_{2.5}(OH)_{0.5}H_2O$	1.00	O	*F d* 2 *d*	2146.87	16	134.18	1317.1	2.707	19.776	5.99	11.119	90	90	90
Tilleyite	$Ca_5Si_2O_7(CO_3)_2$	2.50	M	*P* 1 2/*a* 1	1954.35	4	488.59	1131.8	2.867	15.108	10.241	7.579	90	105.17	90

Table 1 (continued)

Name	Formula	Ca/Si	Sy	SG	M_T cell g mol^{-1}	Z	M_T formula g mol^{-1}	V Å^3	D_c g cm^{-3}	a Å	b	c	α	β	γ
(g). Other high temperature cement phases															
Bicchulite	$Ca_2(Al_2SiO_6)(OH)_2$	0.67[k]	C	$I\bar{4}3m$	1168.86	4	292.22	688.9	2.818	8.8318	8.8318	8.8318	90	90	90
Fukalite	$Ca_4(Si_2O_6)(CO_3)(OH)_2$	2.00	O	$P2_12_12_1$	1626.02	4	406.50	966.2	2.794	3.786	10.916	23.379	90	90	90
Katoite Hydrogarnet[l]	$Ca_{1.46}AlSi_{0.55}O_6H_{3.78}$	0.94[k]	C	$I4_1/a\bar{3}2/d$	3211.72	16	200.73	1847.3	2.887	12.27	12.27	12.27	90	90	90
Rusturmite	$Ca_{10}(Si_2O_7)_2(SiO_4)Cl_2(OH)_2$	2.00	M	$C12/c1$	3736.56	4	934.14	2124.1	2.921	7.620	18.550	15.510	90	104.33	90
Scawtite[m]	$Ca_7(Si_6O_{18})(CO_3)\cdot 2H_2O$	1.17	M	$C1m1$	1666.21	2	833.11	1003.2	2.758	11.0394	15.1935	6.6344	90	115.645	90
Strätlingite	$Ca_2Al(AlSi)_{2.22}O_2(OH)_{12}\cdot 2.25H_2O$	0.62[k]	Tg	$R\bar{3}2/m$	1334.65	3	444.88	1079.6	2.053	5.745	5.745	37.77	90	90	120

Table 1. Crystal-structure data for calcium silicate hydrates, calcium aluminosilicate hydrates and other related phases **[2]**. The crystal system (S_y) is indicated by the following: C = cubic; M = monoclinic; O = orthorhombic; T_g = trigonal; T_c = triclinic. SG = full international space group. M_T = molecular weight of the cell unit in g/mol. Z = chemical formula units per cell. M_T = molecular weight of the chemical formula in g/mol. V is the unit cell volume. D_c = calculated density in g/cm^3. The lattice or cell parameters as the lengths (Å) of the cell edges are represented by a, b and c; and as the angles between the cell edges are indicated by α, β and γ. [a](Na + Ca)/Si; [b]Ma2bc polytype; [c]MDO_1 polytype; [d]MDO_2 polytype; [e](Na + K + Ca)/(Al + Si); [f]Actual composition: $(Na_{1.29}K_{0.79})(Ca_{4.48}Na_{2.52})Si_{16}O_{38}F_2\cdot 3.47H_2O$; [g]Synthetic phase similar to the reinhardbraunsite $Ca_5[SiO_4]_2(OH,F)_2$; [h]Cuspidine: cell parameters given in the paper transformed by the following matrix (00-1/010/100); [i]Isostructural α-C_2SH; [j](Ca + Mn)/Si; [k]Ca/(Si + Al); [l]Composition is variable; [m]Scawtite: cell parameter, a, given in the paper as 10.0394 is a mistake and has been corrected to 11.0394 Å.

2.2. Calcium silicate hydrate (C-S-H) gels

In terms of structure, the calcium silicate hydrate gels have been widely studied and a consistent number of proposed structure models are proof of this. These C-S-H phases form when a mixture of lime/portlandite and silica or an alkali silicate and a Ca salt are reacted in aqueous solution in a temperature range between room temperature and ≈100ºC. Over 100ºC C-S-H gels becomes thermodynamically unstable and convert into other C-S-H phases stable at that temperature. Also, calcium silicate hydrate (C-S-H) gels are known as the most important hydration product of cement-based materials. It is the main binding phase in all Portland cement. The hydration of the clinker phases such as alite, C_3S and belite, β-C_2S, leads to the formation of C-S-H gel and $Ca(OH)_2$. This C-S-H present in hardened pastes of C_3S/ C_2S or neat Portland cements generally has a mean Ca/Si ratio of about 1.75, with a range of values within a given paste from around 1.2 to 2.1 **[5]**. Higher values of Ca/Si in the literature could be explained by mixtures of C-S-H with portlandite, $Ca(OH)_2$ **[1]**. Unlike the highly crystalline hydrated calcium silicate phases, some people associate the C-S-H gel term as a nearly amorphous or even amorphous material. It has been reported by some authors that this C-S-H phase presents short-range order but also long-range disorder in its structure. Namely, when this phase precipitates clusters of nanoscale colloidal particles with an associated pore system are formed. So, there is a certain tendency to relate this material to a more amorphous than crystalline character. But is C-S-H gel necessary a very disordered material? Taylor defined a gel as "dispersions in which attractive interactions between the elements of the dispersed phase are so strong that the whole system develops a rigid network structure and, under small stresses, behaves elastically" **[7]**. C-S-H gel formed by hydration of lime-silica system or tricalcium/dicalcium silicate paste completely fits this definition. Thus, it may be considered as gel-like, although it is not necessarily amorphous. C-S-H gel crystallized since one always obtain a diffraction pattern when the sample is composed of C-S-H and other mineralogical phases either from $CaO\text{-}SiO_2$ mixture or from C_3S or C_2S. This diffraction pattern shows broad reflection peaks. The reason for this broadening of X-ray diffraction peaks is generally owing to different causes: the small size of the coherent domains, the presence of microdefects or both in the C-S-H-based material. C-S-H particles are very small, with a thickness of a few nanometres. These C-S-H nanoparticles are practically single nanocrystals which do not necessarily present defects as Nonat reported **[4]**. So, to define properly the nature of C-S-H gel, last studies should be considered since they give a better approach to the C-S-H gel structure. Then, one might refer to this phase as 'nanocrystalline' or 'semi-crystalline' depending on how advanced the hydration reaction of C-S-H gel is and under what conditions. Nevertheless, the structure of C-S-H gel has not been resolved exactly to date despite many attempts of intensive research over a century. **Figure 1** illustrates schematically the short Si-O chains and type of structure for a nanocrystalline C-S-H gel. According to its structural complexity, these phases often prove to be difficult to characterized by classical mineralogical methods. So, they are hardly identified by traditional (Bragg) x-ray diffraction or scanning electron microscopic techniques. Only can be obtained broad XRD peaks as mentioned above as well as non-high-resolution images showing the corresponding morphology that confirm the presence of them.

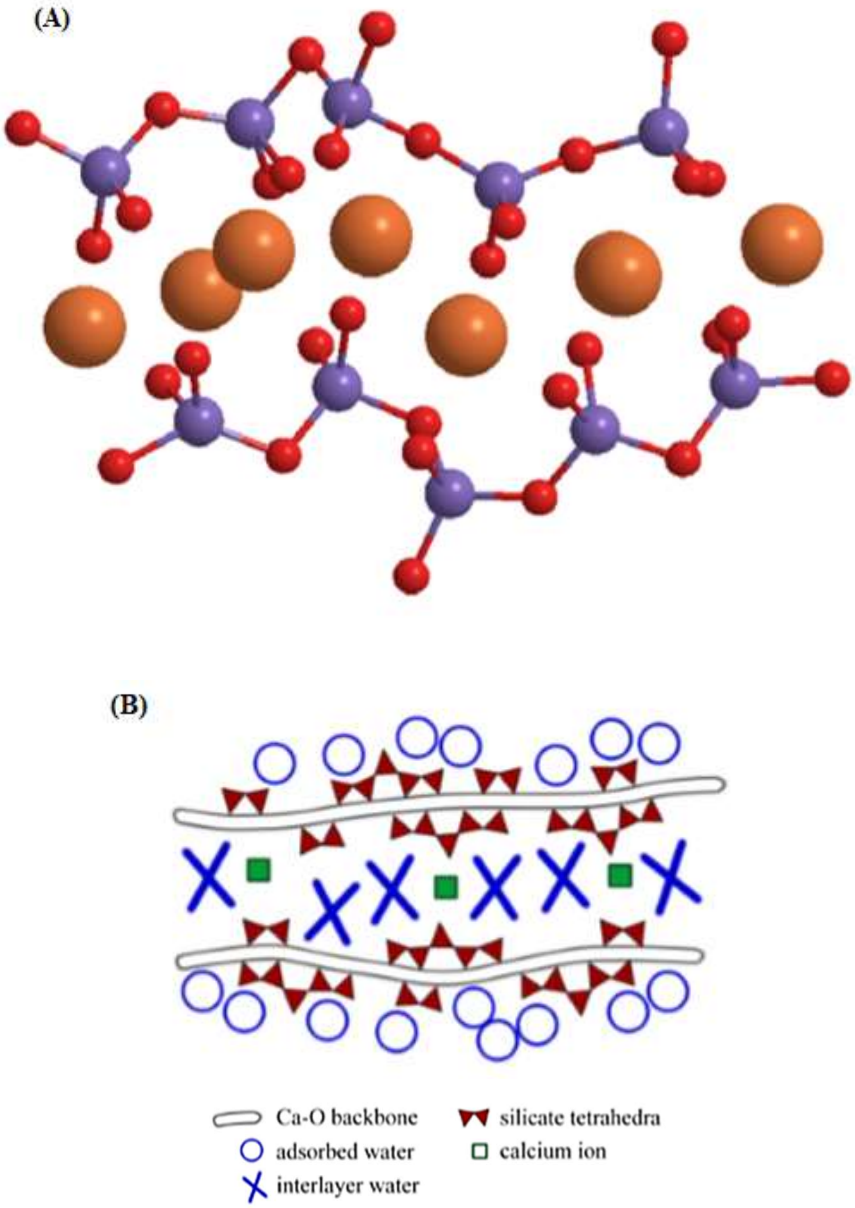

Figure 1. Schematic representation of the C-S-H gel. (A) Atomically distribution of molecules conforming CSH gel structure: medium purple spheres – silicon atoms, small red spheres – oxygen atoms and big light brown spheres – calcium atoms. (B) C-S-H gel nanostructure **[4]**.

Although to go further, high-resolution transmission electron microscopy is much more accurate for analysing the composition in terms of C/S ratio and morphology of the nanostructured CSH gel. Due to the low degree of crystallinity of C-S-H gel, spectroscopic techniques such as Micro-Raman, Fourier Transform Infrared (FT-IR), X-ray photoelectron spectroscopy (XPS) and Nuclear Magnetic Resonance have been used

as suitable methods to characterize the structure of these compounds. But most recently, small angle scattering techniques are being employed to probe the structure of C-S-H gel pastes. Specially, small angle neutron scattering (SANS) and small angle X-ray scattering (SAXS) techniques are tremendously useful in this field of colloid science because of the lengths scales they probe (on the order of 1 nm to 1 μm). Moreover, other non-traditional approach based on high-energy X-ray diffraction and atomic pair distribution function data analysis may be used instead of the traditional X-ray diffraction. This method becomes a potential tool to study the structure of materials where atoms are ordered only at short distances (i.e. less than a nanometer) as the case of C-S-H gel.

As it is mentioned in previous lines, up to date many models have been developed to describe the observed silicate nanostructure of C-S-H gels. Experimentally, Richardson observed that the silicate chains present in the C-S-H gel structure are formed of both dimeric silicate and polymeric units. Polymeric species are chains having lengths of 2, 5, 8 … (3n-1) tetrahedra, where n is an integer number for individual structure units. However, not all those models can explain this experimental observation about the distribution of 3n-1 $[SiO]_4^{-4}$ anions **[2]**. Regardless of this, the most accepted structure for C-S-H, which is in greater agreement and unanimity by the scientific community, relates C-S-H gel with the crystalline calcium silicate hydrates 1.4 nm tobermorite and jennite. It explains better the experimental observations reported by Richardson in 2004 and 2008. He considered that C-S-H has a broad similarity with these crystalline phases **[2, 6]**. Richardson described the most important models for the nanostructure of C-S-H in hardened cements. **Table 2** summarizes all this models and it includes information about the year of publication; the authors of each model; the main crystalline phase from which the model is derived; the nature of the silicate anions; if given, the main formulation or structure-composition relationship; and some comments, including a brief note of links with other models. It is clear from the table that these models can be grouped into two categories: *one where the silicate anion is entirely monomeric*, *and the other where they are derived from the type of linear silicate chain that is present in 1.4 nm tobermorite (and several other minerals), as for example the dreierkette-based models*. Besides, the models are categorized upon the type of structure used to describe the C-S-H gel. In this respect, the so-called tobermorite/jennite (T/J) model considers the C-S-H as an assembly of tobermorite regions followed by jennite domains. The tobermorite-calcium hydroxide (T/CH) models account solid solutions of tobermorite layers sandwiching calcium hydroxide to obtain a higher C/S ratio.

The models involving monomeric silicate anions were proposed by Bernal et al. (1952 and 1954), Shpynova et al. (1967) and Grudemo et al. (1984). Firstly, Bernal considered that the most part of the silica in the hydration cement products is in the form of two hydrated calcium silicates, which are called $C_2SH(II)$ and CSH(I). Then, he hypothesized that both these phases included the monomeric silicate anion $[SiO_2(OH)_2]^{2-}$, and proposed the general formula given as equation 1 in **Table 2 [8]**. Later, Shpynova et al. **[8]** and Grudemo et al. **[9]** also contributed with their proposal models based on monomeric silicate anions. Meaning that these models do not consider the (3n-1) distribution of silicate anions. Shpynova and Grudemo's models were derived from the structure of portlandite, $Ca(OH)_2$, and they were used to explain anomalous XRD peak intensities observed for $Ca(OH)_2$ in hardened cements.

Year(s)	Author(s)	Based on structure of:	Silicate anion structure	Formulation or structure-composition equation		Comments
1952	Bernal et al.	Tobermorite	Infinite			Infinite-chain models not consistent with experimentally observed distribution of silicate anions; i.e. $3n-1$ where n is integer for individual structural units.
1954	Bernal		Monomer	$Ca[SiO_2(OH)_2][Ca(OH)_2]_x[H_2O]_y$	(1)	Monomeric models not consistent with experimentally observed distribution of silicate anions; i.e. $3n-1$ where n is integer for individual structural units.
				x would be 1 for $C_2SH(II)$ and between 0 and 0.5 for CSH(I)		
1956	Taylor and Howison	Tobermorite	$3n-1$			Ca/Si ratio raised above 0.83 by the removal of some 'bridging' tetrahedra and replacement by interlayer Ca^{2+} ions
1960,1962	Kurczyk and Schwiete	Tobermorite	Infinite	$Ca[Ca_4Si_6O_{16}(OH)_2][Ca(OH)_2]_{5-7}\ mH_2O$	(2)	Ca^{2+} and OH^- ions in an interlayer region, represented in their formula as $Ca(OH)_2$ groups, together with water molecules. Formula is consistent with Kantro et al.'s [1962] model in which layers of tobermorite are sandwiched between layers of calcium hydroxide.
1967	Shpynova et al.	$Ca(OH)_2$	Monomer	$Ca_3[SiO_4](OH)_2\ 2H_2O$	(3)	As Bernal (1954) above.
1980–1987	Stade and co-workers	Tobermorite	Dimer and polysilicate	$Ca_{4+y}(OH)_z\left[\left(H_{1-\frac{z}{2}}Si_2O_7\right)\right]_2\ mH_2O$	(4)	Extension of Kurczyk and Schwiete's model by allowing silicate chains that are not infinite, and in particular dimeric. Limits on y simply correspond to the compositions studied.
1984	Grudemo et al.	$Ca(OH)_2$	Monomer			As Bernal (1954) above.
1986	Taylor	1.4 nm tobermorite and jennite	($3n$-1)			Structural elements based on 1.4 nm tobermorite and jennite (i.e. so-called T/J model). Fixed degree of protonation of the silicate chains.
1987	Glasser et al.	Tobermorite	Dimer	$Ca_nH_{6-2z}Si_2O_7\ zCa(OH)_2\ mH_2O$	(5)	Derived from Stade and co-workers dimeric model, Formula (4) above (but z does not have the same definition as in Formula (4)).
1992, 1993	Richardson and Groves	Tobermorite, jennite, $Ca(OH)_2$	($3n$-1)	$Ca_XH_{(6n-2Z)}\left(Si_{1-a}R_a^{[4]}\right)_{(3n-1)}O_{(9n-2)}\cdot I_{\frac{2}{3}(3n-1)}^{n+}\ zCa(OH)_2\ mH_2O$	(6)	Includes both T/J and T/CH formulations; Formula (6) (with no substitution) is the polysilicate equivalent of Formula (5) (Glasser).
				$\left\{Ca_{2n}H_w(Si_{1-a}R_a^{[4]})_{(3n-1)}O_{9n-2}\right\}I_{\frac{2}{3}(3n-1)}^{n+}\cdot(OH)_{w+n(y-2)}\cdot Ca_{\frac{z}{2}}\ mH_2O$	(7)	Variable degree of protonation of silicate chains.
				$Ca/Si=\frac{n(4+y)}{2(1-a)(3n-1)}\quad Ca/Si=\frac{n(4+y)+a(3n-1)}{2(1-a)(3n-1)}$	(8)*and*(9)	Incorporation of substituent ions, most importantly substitution of Si^{4+} by Al^{3+}. Possibility that T-, J- and CH-based structural elements co-exist.

Table 2 (continued)

Year(s)	Author(s)	Based on structure of:	Silicate anion structure	Formulation or structure-composition equation		Comments
1993	Taylor	Tobermorite and jennite	$3n-1$	$Ca_4[(Si_{6-4}\square_4O_{18-2A})H_{2y}Ca_{2-y}]_4(OH)_{8(1-q)}\,mH_2O$	(10)	Formulation of 1986 model in response to Richardson and Groves' model, but extended to incorporate some of their modifications (variable protonation and substituents); as a consequence it is equivalent to Richardson and Groves' T/J formulation.
				$C/S=\frac{r}{(1-\frac{p}{2})}\quad QRT=\frac{2}{(\frac{1}{m}-1)}$	(11)and(12)	
1996	Cong and Kirkpatrick	Tobermorite	$3n-1$			'Defect tobermorite' model; Eqs. (11) and (12) are equivalent to equations in Richardson and Groves' 1992 model; see section 4.4.2 in Richardson (2004).
1997–1999	Grutzeck	Tobermorite, sorosilicate	Long-chain, dimer	$Ca_4(OH)_2[SiO_{3.x}]_2\cdot mH_2O$		Long-chain T-based phase with low Ca/Si and a dimeric sorosilicate-based phase with high Ca/Si.
1998	Nonat and Lecoq	Tobermorite	$3n-1$			Two hypotheses: 1st equivalent to T units with $w/s=0$ and $y=2$ in Richardson and Groves' model (Formula (7) above); 2nd involves Ca^{2+} and OH^- ions in an interlayer region, in which respect it is similar to Kurczyk and Schwiete and Stade and co-workers.
2004	Chen, Thomas, Taylor, Jennings	Tobermorite and jennite	$3n-1$	Chen et al. presented formulae for mean chain lengths of 2, 3, 4, 5 and ∞		Formulae equivalent to T units with $w/s=0$ and $y=2$ in Richardson and Groves' model (Formula (7) above).
2004	Nonat	Tobermorite; jennite.	$3n-1$			Update of 1998 model; mentions jennite-based structure.

Table 3. Summary of models for the nanostructure of C-S-H in hardened pastes of cement **[2]**.

On the other hand, it is also found in the Table 2 the second group of models for C-S-H which is based on Dreierkette chains. Initially, the first dreierkette-based model for the C-S-H gel structure was proposed by Bernal et al. in 1952. They performed X-ray studies on hydrated C_3S pastes and diluted suspensions of C-S-H. According to them, they concluded that the C-S-H phases formed from both cases were similar. So, Bernal et al. called these calcium silicate hydrates as C-S-H(I) and C-S-H(II). C-S-H(I) had a layer structure with the layers elongated in one direction that resulted in a fibrous structure and showed similarities to tobermorite. Additionally, C-S-H(I) had a low Ca/Si ratio whilst C-S-H(II) a higher Ca/Si ratio. The tobermorite structure – that was first described by Megaw and Kelsey **[10] –** is described in more detail in Section 1.5.3. However, it is important to note here that it contains linear silicate chains of the 'dreierkette' form in which the silicate tetrahedra are co-ordinated to Ca^{2+} ions by linking in such a way as to repeat a kinked pattern after every three tetrahedra. Two of these three tetrahedra are sharing O-O edges with the central Ca-O part of the layer, these are linked together and are often referred as to as 'paired' tetrahedra (P). The third tetrahedron shares an oxygen atom at the pyramidal apex of a Ca polyhedron and connects the two paired tetrahedra. It is termed 'bridging' tetrahedra (see **Figure 2**). Taylor and Howison suggested in 1956 that the Ca/Si ratio might be raised above 0.83 – the value for Megaw and Kelsey's tobermorite – by the removal of some bridging tetrahedra and replacement by interlayer Ca^{2+} ions. This mechanism suggesting the raise of the Ca/Si ratio is a central feature of most dreierkette-based models **[11]**.

Kurczyk and Schwiete made studies on both C_3S and β-C_2S pastes. The studies involved measurements of transmission electron microscopy (TEM) with selected are electron diffraction (SAED), thermal analysis, XRD and infrared spectroscopy. They calculated the Ca/Si ratios from XRD and thermal analysis, obtaining a range between 1.80 and 1.92. Based on their results, Kurczyk and Schwiete proposed a hypothetical structure formula for the C-S-H that formed in both systems C_3S and β-C_2S, which they referred to as a 'tobermorite-like phase **[12, 13]** and fits with the same structural elements as determined by Megaw and Kelsey **[10]** to be present in tobermorite (i.e. single chains of dreierketten conformation).

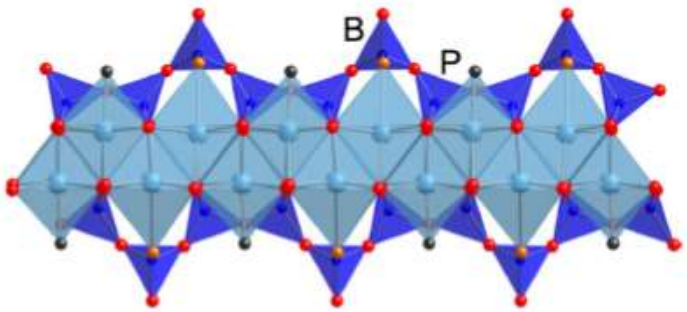

Figure 2. Schematic diagram showing dreierkette chains present in tobermorite (which in theory are of infinite length). The chains have a kinked pattern where some silicate tetrahedra share O-O edges with the central Ca-O layer (called 'paired' tetrahedra (P)), and others that do not (called 'bridging' tetrahedra (B)) **[14].**

The tobermorite-like layers included Si-OH groups and, since they were the same as in crystalline tobermorite, were presumable considered to be of infinite silicate chain lengths. To explain the Ca/Si ratios observed, they postulated that the structure has excess of Ca^{2+} and OH^- ions in an interlayer region together with water molecules. Their formula, modified with the inclusion of the interlayer water, is given as Formula (2) in **Table 2**. This formula keeps high similarity with the Kantros et al.'s model that they suggested in 1962. It was proposed a model at around the same period in which the layers of tobermorite are sandwiched between layers calcium hydroxide **[14]**.

In 1980, Stade and Wieker predicted that poorly crystalline and amorphous C-S-H phases present in cement paste are built up from CaO_x polyhedra sandwiched between two silicate layers **[15]**. Again, like Kurczyk and Schwiete, they assumed that these three-layer sequences are separated by an intermediate into which H_2O, Ca^{2+} and OH^-, and other ions may be incorporated to satisfy the observed composition. This allows for their experimental observation that the silicate chains in their C-S-H were not infinite and in certain circumstances entirely dimeric. They expressed their model in two forms: one purely dimeric, and the other incorporating both dimer and polysilicate chains. The model is illustrated schematically in **Figure 3**, which is based on figures in Stade.

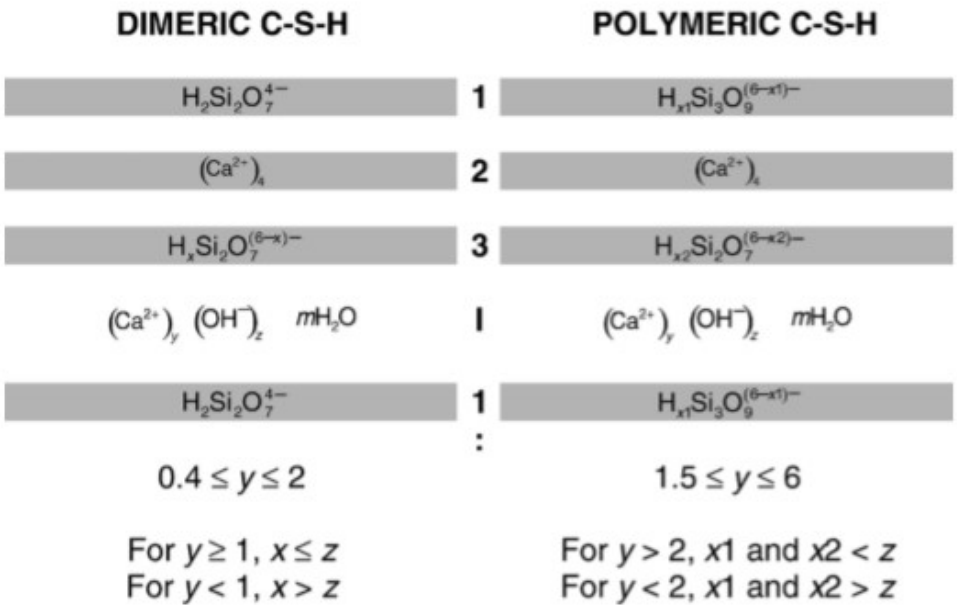

Figure 3. Schematic representation of Stade and Wieker's model illustrating the four-layer sequence (labelled as layers 1, 2, 3 and an intermediate layer, I) **[15]**.

The limits on *y* simply correspond to the compositions studied. The formula for purely dimeric C-S-H, as given by Stade and Wieker is given as Formula 4 in **Table 2**. These authors and later, Grutzeck in 1989, by means of ^{29}Si NMR spectra, described the transition between the two phases of C-S-H gel, tobermorite-type structure with long chains to a jennite-type structure containing shorter chains and dimeric silicate groups with a Ca/Si ratio of 1.0.

Regarding to Taylor's refined model in 1986, he developed it from his previous discussion published 30 years earlier with Howison **[11]**. His model envisages that C-S-H with a high Ca/Si ratio (C-S-H(II)) is composed of structural units derived from defective jennite and C-S-H with a lesser extent (C-S-H(I)) is composed of structural units derived from defective 1.4 nm tobermorite **[16]**. The silicate chains present in jennite – which are theoretically infinite long chains – are similar those in tobermorite, i.e., both are of the 'dreierkette' form. Nevertheless, whilst in tobermorite the main layer consists of a central Ca-O part sandwiched between parallel silicate chains, in jennite structure half the oxygen atoms of the central component are part of -OH groups. The Ca/Si ratio of C-S-H(I) varies from 0.67 to 1.5 by omission of a part of the bridging tetrahedra or variations in the contents of interlayer Ca and protons attached to Si-O units. C-S-H(II) has Ca/Si ratios within a range of 1.5-2.2. Taylor described some years later a transition phase between both C-S-H gels which occurs at around a Ca/Si ratio of 1.5 **[7]**. This transition phase was also observed by Klur et al. **[17]**. To support this Taylor's discussion, the structural units derived from either jennite or 1.4 nm tobermorite are identified using 'J' or 'T' as labels **[18]**. Consequently, J2 and T2 correspond to dimeric structural units that result from omission of all bridging tetrahedra from jennite and tobermorite respectively, and J∞ and T∞ represent infinite chain lengths and so correspond to the crystalline phases themselves. The removal of numbers of bridging tetrahedra intermediate between none (infinite length chains) and all (dimers) results in a sequence of finite silicate chains containing 2, 5, 8…3n-1 tetrahedra (where n = 1, 2, 3…), which is consistent with the silicate anion structure observed in hardened C_3S and OPC pastes **[5, 6]**. Taylor assumed that each bridging tetrahedron carries only one H atom, and that when one of these tetrahedra is missing only one of the broken ends of the chain is terminated by H atom. Hence, the net charge remains unchanged and the omission of a tetrahedron requires no change in the amount of interlayer Ca. He stated this, *'...there is no direct evidence for this assumption, but it is crystal-chemically reasonable and leads to a number of results that agree with experimental data'*. Taylor's model can thereby be considered a special case of Richardson and Groves' T/J formulation (i.e. formula 7 in the **Table 2**), since it allows greater flexibility in the degree of protonation of the silicate chains. At the present time, this model by Taylor (T/J model) is the most accepted one for its truth in morphological terms, whereas it is incompatible with two basic characteristics of real C-S-H: the Ca/Si ratio and C-S-H density **[19]**.

Glasser et al. proposed a compositional model for C-S-H gel derived from the dimeric model suggested by Stade and Wiecker. Whilst their thermodynamic treatment was strictly only applicable to precipitated gels with Ca/Si ratio between 1.0 and 1.4, they considered that the compositional model itself could be applied equally well to fresh C-S-H produced as a product of cement hydration. Glasse et al. referred to Stade and Wiecker's formula (i.e. formula 4 in **Table 2**) though affirmed that it was *'...difficult to write balanced equations based on this presentation for formation and dissolution equilibria of C-S-H'*. They represented their model by the formula 5 in **Table 5** and it is important to note that x and z do not have the same definitions as those in Stade and Wiecker's formula.
Richardson and Groves developed a generalized model including formulations that could be interpreted from either the tobermorite-jennite (T/J) or tobermorite-'solid solution' $Ca(OH)_2$ (T/CH) viewpoints; indeed, it is possible that structural elements based on tobermorite, jennite (or jaffeite) and CH can all occur within the same system **[18]**. The model includes maximum flexibility in the possible degree of protonation of the silicate chains, and it accounts for the substitution of Al^{3+} for Si^{4+} ions only at bridging sites **[20]**,

which is important for C-S-H present in cements containing fly ash, metakaolin or ground granulated blast-furnace slag, but which is not included in other models. The two formulations are given in **Table 2** (formulae (6) and (7); Eqs. (8) and (9) are the composition-structure relationships where charge compensation of the substitution of Al^{3+} for Si^{4+} ions is entirely by alkali cations or Ca^{2+} ions, respectively. The close relationship between Richardson and Groves's formulation and the models due to Taylor **[16]**, Cong and Kirkpatrick **[21, 22]**, Nonat and Lecoq **[23]** and Chen et al. **[1]** has been demonstrated by Richardson **[6]**. Glasser et al.'s **[24]** and Stade's **[15]** models are closely related. The special case of formula (6) for dimer (n = 1) is the same as that given by Glasser et al. **[24]**, formula (5) (i.e. formula (6) is essentially the polysilicate version of Glasser's compositional model for dimeric C-S-H) and Richardson and Groves' alternative formulation, formula (7), reduces to Stade's dimeric model (n = 1) if the number of silanol groups, w, is set equal to (1 + x/2). Like Taylor's model, Stade and Wieker's is less flexible than Richardson and Groves's in terms of the possible variation in the level of protonation of the silicate chains. Glasser's and Stade's models do not consider for the 3n-1 sequence of silicate chain lengths. This so-called T/CH model or layer-structure model of Richardson and Groves has been widely accepted, but Cong and Kirkpatrick **[21]** as well as Fujii and Kondo argue that the occurrence of jennite-type C-S-H (II) is extremely difficult to synthesize and subsequently characterize and this is why they proposed a 'defect tobermorite-like' model for C-S-H, which exists as a solid solution between tobermorite and $Ca(OH)_2$ **[25]**.

The idea of another two-phase C-S-H model that Grutzeck proposed consists of intergrowths of sorosilicate-like and tobermorite-like C-S-H, which describes the observed data better than the existing C-S-H models **[26]**. Sorosilicate is not a silicate layer structure; it is comprised of columns of dimers $(Si_2O_7)^{6-}$ ions surrounded by chains of octahedrally coordinated CaO which hold the structure together. Also, the sorosilicates normally contain rather large cavities in 2D that form channels in 3D that can host water molecules, Ca^{2+}, OH^- and possibly other ions as well.

Nonat and Lecoq initially proposed in 1998 a model based on equilibrium data obtained from both CaO-SiO_2 mixtures and fully hydrated C_3S samples in solution in which the lime concentration is maintained constant **[23]**. The model is also based on a tobermorite-like structure and applicable to a whole range of Ca/Si (0.66 to 2). However, this model does not assume a disordered structure and the layers would not contain jennite-like regions. To reach high Ca/Si values the model assumes that most of the interlayer crystallographic sites of the tobermorite model are occupied by calcium ions balanced by OH^- in interlayer positions **[2]**. Klur et al. achieved clear evidence of a transition phase at Ca/Si ratio of 1.5 and propose three types of C-S-H gel: C-S-H (α) for a C/S < 1, C-S-H (β) for 1< C/S < 1.5 and C-S-H (γ) for C/S > 1.5 **[17]**. More recently, in 2004, Nonat proposed a nanostructural model for C-S-H preceding the original one. As stated by this model, the main layer of C-S-H consists of a silicate dimeric unit charge balanced by two calcium ions and the two free extremities bear two protons, $Ca_2H_2Si_2O_7$. Two successive dimeric units may be bridged by a silicate tetrahedron and $Ca(OH)_2$ units may be accommodated in place of missing bridging tetrahedra **[4]**.

In the same year as Nonat, Kalliopi gathered in his work the latter models of cement gel structure that describe the nanostructure of C-S-H gel and its porosity. These models were proposed by Powers and Brownyard **[27]**, Feldman and Sereda **[28]**, Wittmann **[29]** and Jennings and Tennis **[30]**. The first two are based on a layered structure for the C-S-H

gel, while another are based on a colloidal model as shown in **Figure 4**. These models are not mentioned in **Table 2** but owing to their important contributions they must be mentioned in this Thesis. So, they are described as it follows.

Powers and Brownyard in their pioneering work, were the first to systematically investigate the reaction of cement and water and the corresponding formation of cement paste **[27]**. In the late 1940s, they suggested a model for the cement paste, in which unreacted water and cement, the reaction product as well as the porosity (gel and capillary) were distinguished. These authors differentiated three phases in the cement paste to wit capillary water (unreacted water), unreacted cement and cement gel. The cement gel consists of solid hydrated cement and water-filled gel pores; this water is referred to as gel or absorbed water. The gel water is visualised as being within the influence of absorbing forces, whereas the capillary water is considered as "free water". Like Taylor **[16]**, the term "hydration product" is used instead of "gel" to avoid confusion regarding "gel" and "gel water". Thus, here, the hydration product consists of hydrated cement and gel space, whereby the latter may be filled with gel water (see **Figure 4a)**.

The model of Feldman and Sereda (1970) is much more complex than the Powers and Brownyard's model. The presence and role of interlayer water in physical phenomena is significant **[28]**. This feature makes it quite distinct from the P-B model (Powers and Brownyard). They proposed that the sheets composing the C-S-H gel do not have an ordered layered structure creating an interlayer space with different shapes and sizes (between 0.5 and 2.5 nm), and these layers may come together by means of Van der Waals forces. Water can be adsorbed in the solid surface or being like interlayer water associated with the C-S-H structure. Additionally, Feldman and Sereda suggest the irreversibility of loss water during the adsorption and desorption processes. Evidence for the layered nature of hydrated Portland cement is provided through several types of experiments: length and mass change scanning isotherms, mechanical property isotherms; helium inflow methods; similarities with the behaviour of C-S-H (I) on the removal of water; dynamic mechanical analysis (DMA) of C-S-H (I) and cement paste following removal of water; relaxation experiments of C-S-H (I) and cement paste on removal of water. The types of water (physically adsorbed and interlayer hydrate water) and the nature of the disordered layer structure are illustrated in **Figure 4b**. Also, in a much more detailed is observed (see **Figure 4c)** this proposed C-S-H gel structure where the possible bonding arrangements between and along sheets and the polymerization of silicate chains are present.

In Wittmann's 'Munich model', presented in the late 1970s, the hydrated Portland cement is described as a "xerogel", namely a gel from which the dispersion medium is absent, together with the crystalline constituents **[29]**. The model is based on concepts of colloidal science, and it describes the C-S-H gel as a three-dimensional network of amorphous colloidal particles., the xerogel. These colloidal particles are held together by chemical bonds as well as Van der Waals bonds. The xerogel is considered to consist of separate particles, for which no particular internal structure is assumed (**Figure 4d**).

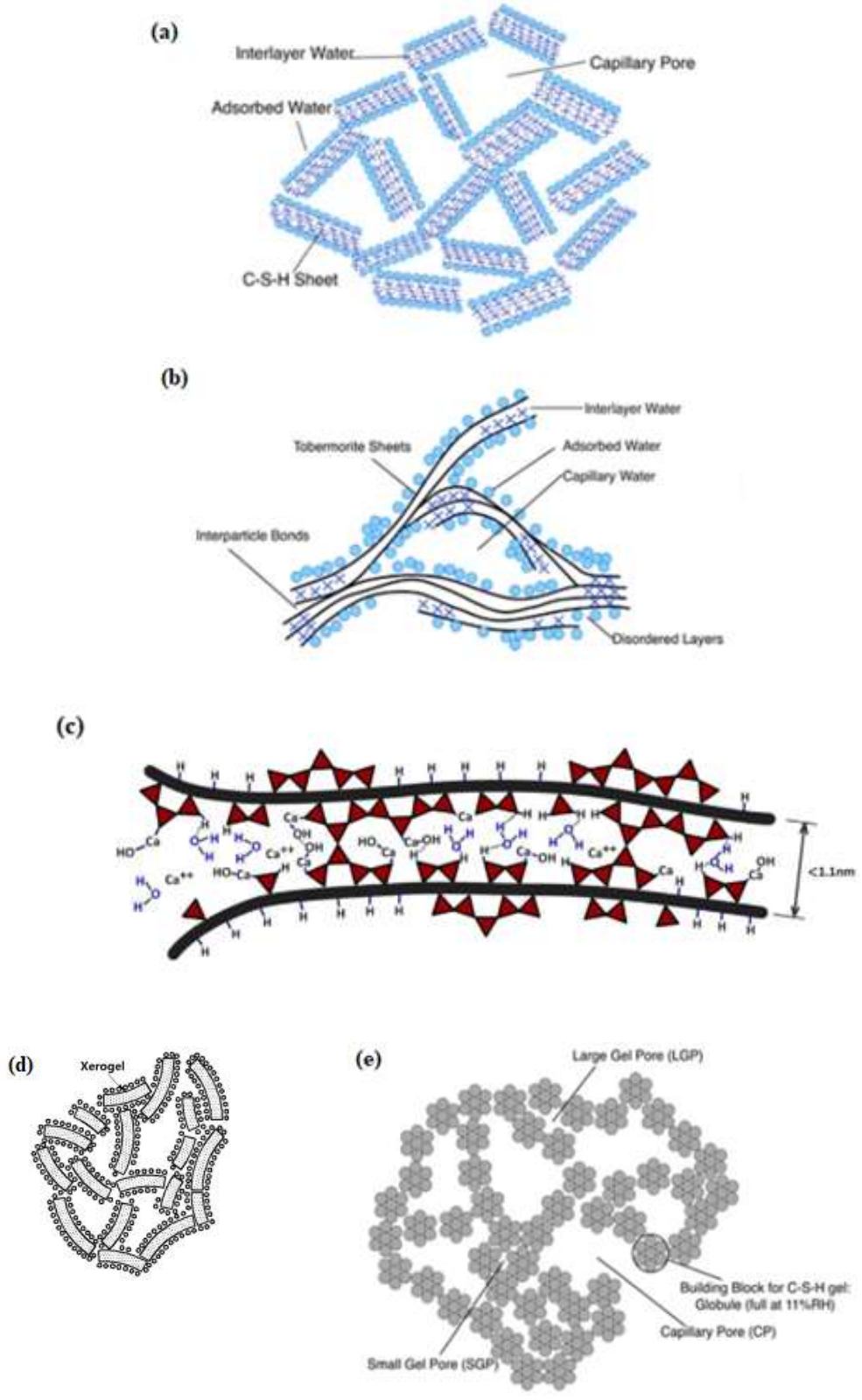

Figure 4. Schematic representation of C-S-H models. **(a)** Powers and Brownyard model; **(b)** and **(c)** Feldman and Sereda model; **(d)** Wittmann model; **(e)** Jennings and Tennis model **[27, 28]**.

It is necessary to emphasize the role of water molecules adsorbed on, or lying between, these particles. Below 50% of relative humidity the particles were in contact, but at higher humidity, intervening water molecules were considered to exert a disjoining pressure, which to some extent kept them apart. This model was used primarily in the development of a theory of dimensional changes.

As the last of these models, Jennings and Tennis presented a model in 1994 and 2000, based on nitrogen adsorption observations for simplified representation of cement paste's microstructure within the size range of about 1-100 nm **[31]**. This model, which is illustrated in **Figure 4e,** is constituted of basic building blocks that are spherical units forming clusters together to make globules with a radius of 2.5 nm or less. The Jennings-Tennis model suggests that the basic building blocks that form into globules have two possible packing arrangements: high density and low density. The interglobular spaces correlate to gel porosity and the intralobular spaces correlate to interlayer porosity that can be reversibly re-entered by nitrogen. As the water-cement ratio increases, the C-S-H particles become accessible to nitrogen. Each type of C-S-H contains a specific amount of total gel porosity: none of the pores in high density C-S-H is accessible to nitrogen, while only some of the pores in low density C-S-H are accessible to nitrogen. The surface area of the high-density type is not detected by several techniques, and this is the main cause of so many different values in the literature.

Morphologically the C-S-H gel acquires with a naked eye an amorphous structure. Apparently, it is not easy to distinguish the morphology between C-S-H gels prepared in different conditions. However, there are slightly different features although it generally presents in form of clusters, aggregates of nanoparticles as a foil- and flake-like microstructure. The chemical composition (Ca/Si ratio), the raw materials and methodology used for the synthesis of C-S-H gel determines its morphology. Recently, Tajuelo Rodríguez et al. reported that the lime concentration in solution is a more relevant force driving to morphological changes of the C-S-H phase, comparing to the kinetics of the lime-silica hydration or C_3S/C_2S hydration **[32]**. They found that samples with low calcium oxide concentrations ([CaO] < 22 mmol L^{-1}) in solution and Ca/Si ratios of 1.33, 1.4 and 1.45 showed a *foil-like* morphology examined by transmission electron microscopy. Samples with [CaO] = 22 mmol L^{-1} and Ca/Si ≈1.58 presented a combination of *foil- and fibrillar-like* morphology. And samples with higher lime concentration solution ([CaO] > 22 mmol L^{-1}) and Ca/Si ratios of 1.61 and 1.63 approximately exhibited a microstructure composed of *fibres*. These variations in morphology are also related to the silicate anion structure. The **Figure 5** corresponds to SEM and TEM images that are showing the characteristic morphology of C-S-H gel phases.

In the case of cement hydration, when C_3S or C_2S are mixed with water two types of hydration products are originated. The 'inner' products (Ip) which are located within the original boundaries of the clinker particles, and the 'outer' products (Op) which lie outside the grain boundaries **[33]**. The Ip of C-S-H has a compact and homogeneous morphology consisting of small globular particles with 4-6 nm of diameter. It presents a porosity with a pore size lower than 10 nm. Whilst the Op of C-S-H present in hardened OPC pastes or C_3S possess a fibrillar and directional morphology which is a function of space constraint (see **Figure 6**). When large pores are formed, the C-S-H fibres form with a high length to width aspect ratio which is referred to as coarser C-S-H fibres. When smaller pores are present, a directional aspect is retained but it forms in a more space-efficient manner (finer fibres).

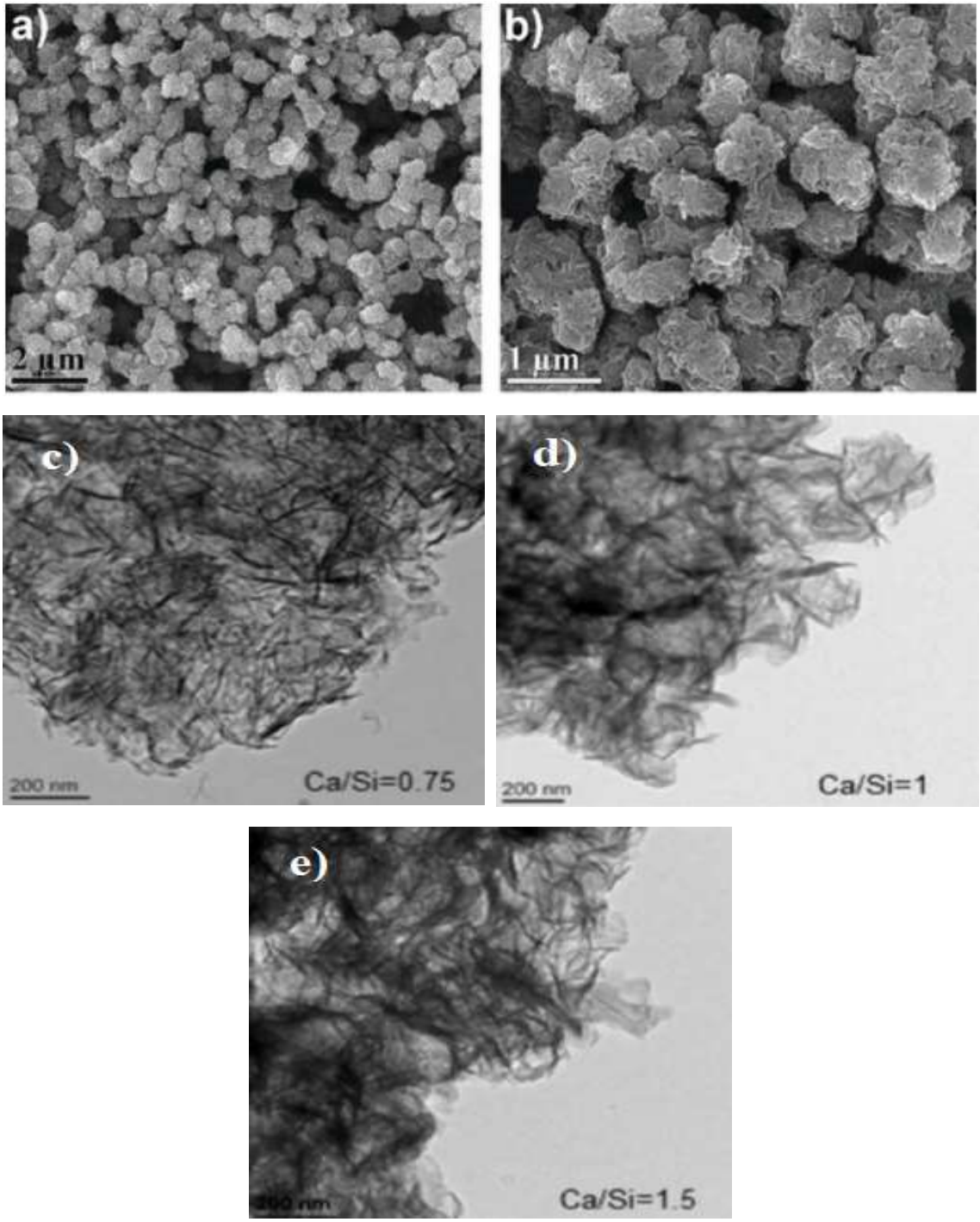

Figure 5. SEM micrographs of C-S-H gel (a) and b)). TEM micrographs of C-S-H gel prepared with different Ca/Si ratios **[33]**.

The space between the fibres belong to Op C-S-H forms a three-dimensional interconnected pore network commonly known as the capillary porosity. This Op found in a hardened C_3S paste presents coarser fibres about 100nm wide. This appears to consist of many long thin particles aligned along their length. But the outer product of C-S-H gel present in neat Portland cement typically has a finer morphology **[6, 7]**.

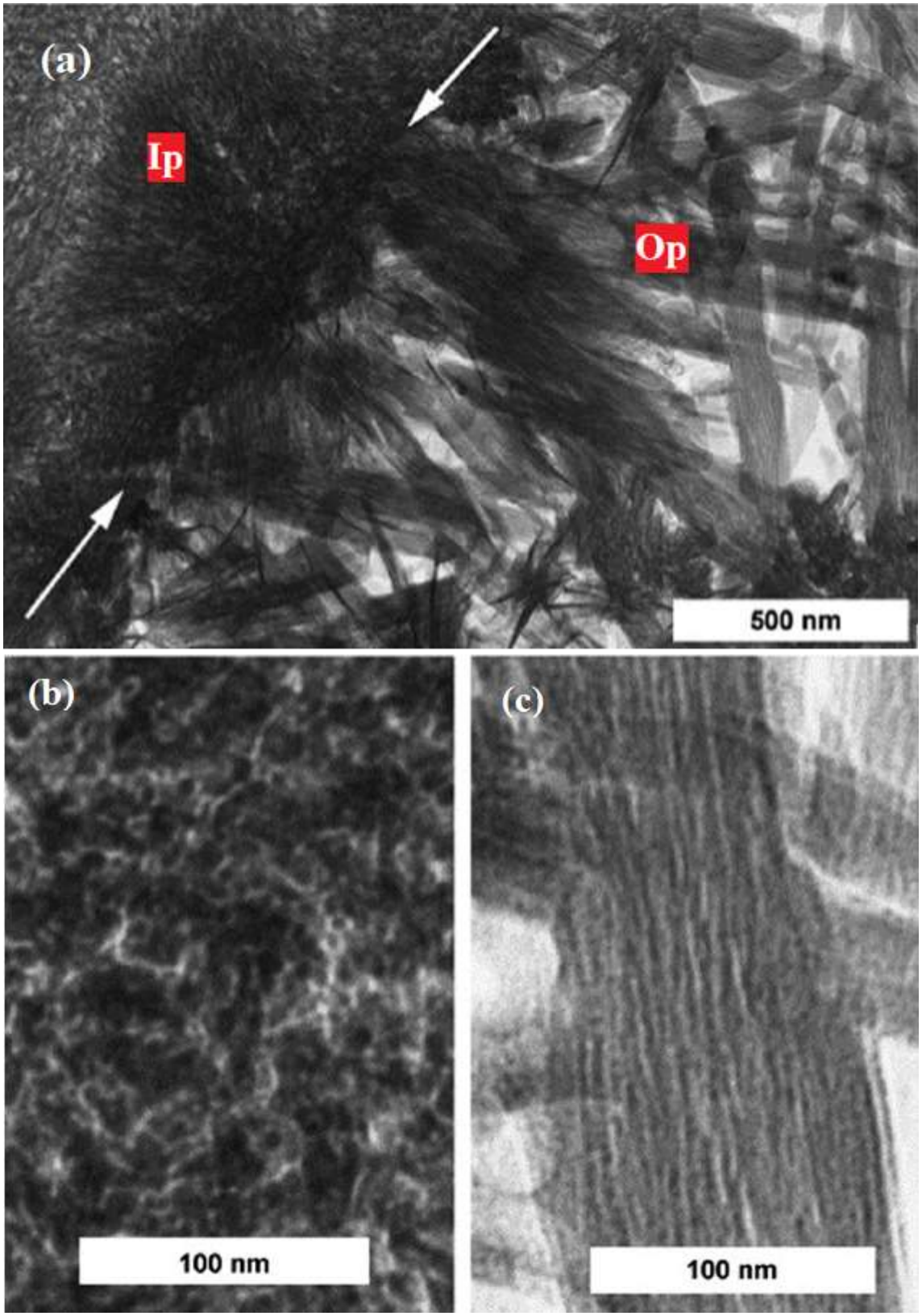

Figure 6. (a) TEM micrograph showing the Inner and Outer products of C-S-H present in hardened C_3S paste. White arrows indicate the Ip-Op boundary. (b) An enlargement of the globular Ip C-S-H region. (c) An enlargement of the fibrillar Op C-S-H region **[6, 7]**.

2.3. Tobermorite

Tobermorite is one of the crystalline calcium silicate hydrate phases synthesized in this work, thus it is necessary to describe and review this natural and synthetic mineral. Tobermorite is a rare, naturally occurring crystalline C-S-H phase that was firstly described by Heddle in 1880 and it was found around Tobermory, an island of Mull in the Hebrides Archipelago (Scotland) and from a quarry near Dunvegan in the Isle of Skye. This silicate mineral with chemical formula, $Ca_5Si_6O_2(OH)_{16}\cdot 4H_2O$ or $Ca_5Si_6O_2(O,OH)_{18}\cdot 5H_2O$, crystallizes in the orthorhombic system. It appears as a pale pinkish white rock and its crystal habit can be like minute laths, fibrous bundles, rosettes, or sheaves, among others. Tobermorite was afterwards found in several other localities such as Maqarin (Jordan) and Crestmore Heights, Riverside County, California (USA) and it was observed that only crystallizes in nature under hyper-alkaline hydrothermal conditions, generally in cavities of basic rocks or at the contact of the limestone and dolerite (one type of basaltic rock) or granodiorites (like granite) **[34, 35]**. This natural C-S-H phase crystallizes in the form of fibres or platelets/foils with three different degrees of hydration **[36-38]**. Depending on the tobermorite's degree of hydration, the basal spacing between two CaO consecutive layers varies from 14Å to 11Å or 9Å. These changes in the basal distance give the so-called 14 Å tobermorite, 11Å tobermorite or 9Å tobermorite. Then, these crystalline phases are differentiated by their layer spacing between the silicate chains of the structure. The differences in basal spacing are due to variations in the connection and orientation of the silicate chains to one another and in the occupancy of the intermediate layers. All tobermorite types have Ca-O layer with seven-coordinated calcium as the central atom **[39]**. Furthermore, they have the Si-O tetrahedron chains lying between the Ca-O layers which are connected in the form of "dreierkette". The three polymorphs of tobermorite will be explained later.

Over the years, tobermorite has been of interest by many scientists working in different disciplines as geology, mineralogy and chemistry of building materials. The fact this mineral presents a structure close and related to that of the C-S-H gel opens a big discussion. Moreover, the difficulty of obtaining large and pure crystals is also another reason why its structure has been a matter of debate for many years. Since the late 1930s, the first attempts by Flint et al. for synthesizing this metastable crystalline calcium silicate hydrate phase started a chain of scientific studies which are still ongoing. Numerous publications and contributions have been made and the research around this hydrated calcium silicate has increased. Owing to its crystal structure complexity, different structural models were developed for the various types of tobermorite, particularly in the 1980s and 1990s. More recently, Bonaccorsi et al. reported on their studies the real structure of 14 Å tobermorite and 11Å tobermorite **[40]**. What is clear and in agreement is that calcium oxide forms layers perpendicular to the c-axis and flanked on both sides by chains of silicate tetrahedra **[35, 41]**. As tobermorite shows good mechanical properties can be used for different industrial applications, the most common one in construction for aerated autoclaved concrete as well as for cement composites (used as seeding additive). Besides, it can be employed as stabilization agent for the capture of contaminants, for example in cation exchange and hazardous waste-water treatment **[42-44]**.

The 14Å tobermorite, also called *plombierite*, is the most hydrated phase of the tobermorite's group with the chemical formula $Ca_5Si_6O_{16}(OH)_2\cdot 7H_2O$. In fact, the name plombierite was firstly used in 1858 to describe a gelatinous natural material, probably

belonging to the "calcium silicate hydrate (I)" group **[45]**. Owing to the chemical similarity between this nearly amorphous material and the crystalline phase described by McConnell **[45]**, the name plombierite was later also used to define the most hydrated member of the tobermorite group, and this name has been traditionally retained in the mineralogical community and widely used in mineralogical compilations. However, most researchers in cement chemistry currently apply the name "plombierite" to poorly crystalline or amorphous calcium silicate hydrates, which can vary in Ca/Si ratio from the value for tobermorite 14Å (i.e. 0.83) to as high as about 1.5. Bonaccorsi et al. developed the crystal structure of 14Å tobermorite (plombierite) which was solved by means of the application of the order-disorder (OD) theory and was refined through synchrotron radiation diffraction data **[40]**. Two polytypes were detected within one very small crystal from Crestmore, together with possibly disordered sequences of layers, giving diffuse streaks along c axis. The structure of tobermorite 14Å is built up of complex layers, formed by sheets of sevenfold coordinated calcium cations, flanked on both sides by silicate (wollastonite-like) chains with dreierketten distribution as shown in **Figure 7**. The space between two complex layers contains additional calcium cations and H_2O molecules. Only one of the two polytypes could be refined. It has a monoclinic unit cell with space group symmetry B11b and cell parameters a = 6.735(2) Å, b = 7.425(2) Å, c = 27.987(5) Å, γ = 123.25(1)º. In this polymorph the silicate chains that belong to adjacent layers are not condensed to form double layers as for example it happens in 11Å tobermorite, the layers are moved apart and locate in between some H_2O molecules. The single chains are shifted b/2 regarding to each other (b is the lattice parameter of the unit cell) **[40]**.

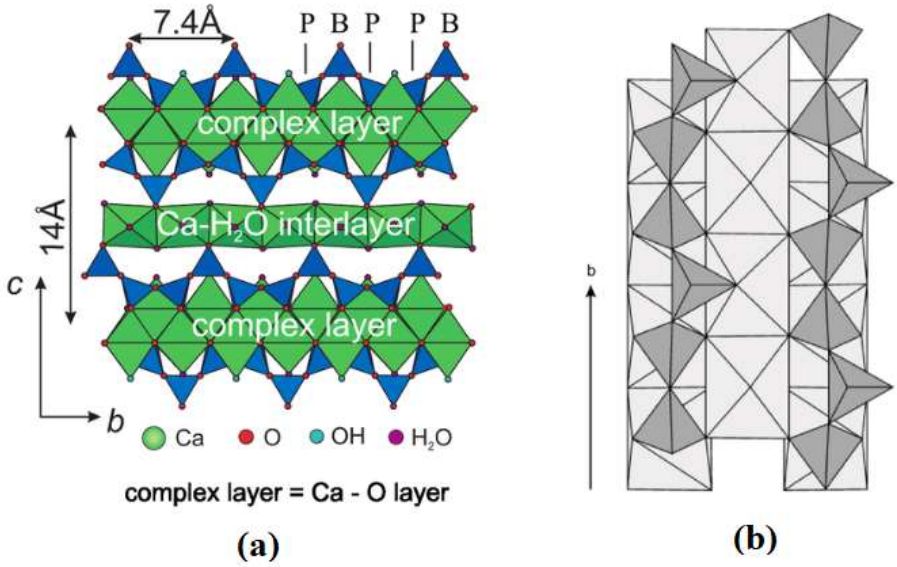

Figure 7. Structure of 14Å tobermorite. (a) The structure as seen along [100], with two "complex layers" (Ca-O layers) separated 14Å apart. (b) Connection of silicate chains (dark gray) to the layer of calcium polyhedral (light gray), as seen along [001] **[40]**.

For the 14Å tobermorite, the C/S ratio of its structure is 0.83 based on the chemical formula. An approximation of this value was determined by Maeshima et al. for samples of naturally occurring 14Å tobermorite using EDX measurements. They calculated an average value of 0.85 considering a C/S ratio between 0.80 and 0.91 **[46]**. In the same work, Maeshima et al. also performed ^{29}Si NMR studies which mainly showed Q^2 signals for theoretically infinite extended silicate chains. This is consistent with the schematic representation of tobermorite 14Å structure in **Figure 7**. Because there are no links between the individual silicate chains, so the presence of Q^3 signals is not expected. Small Q^1 peaks were also observed which were assigned either to contamination by another mineralogical specie or to the end groups of the silicate chains of the 14Å structure. This type of tobermorite dehydrates and transforms into 11Å tobermorite after a heat treatment at 80-100ºC. At this range of temperature, the water molecules from the intermediate layer are removed. The Ca^{2+} ions are coordinated again due to the lack of coordination points with the oxygen from the Si-O tetrahedra, which leads to a reduction in the space between layers **[39, 47]**. In contrast to naturally occurring and synthetically produced 11Å tobermorite, the crystalline phase obtained by heating 14 Å tobermorite has not a double silicate layer, but like the starting material, a simple silicate chain structure **[34, 39, 47]**. This chain structure is shifted in the plane along the chains by b/2 to each other. This could be confirmed based on the Q^2 signals present in ^{29}Si NMR studies of the dehydrated samples, with an almost complete absence of Q^3 signals **[48]**. Tobermorite phases with a layer spacing of 11Å can be distinguished as their crystal structure in three different classes: clinotobermorite, normal 11Å tobermorite and anomalous 11Å tobermorite. Owing to the existence of these polymorphs, the structure of 11Å tobermorite is slightly complex than the one of the 9Å. Moreover, an exact formulation for these phases is still under study and many authors describe the structure of this compound with different compositions. Although all those 11Å tobermorites have in common the dreierkette in their structure, which consists of a Ca-O layer with condensed silicate-chains as the basic building block, they differ in the way the silicate chains are linked to form double chains and in the assignment of the intermediate layers of the double chains. For the clinotobermorite, with the chemical formula, $Ca_5Si_6O_{17}\cdot 5H_2O$, and Ca/Si ratio of 0.83, the crystal structure of this mineral was finally determined in 2000 by Merlino et al. **[47]**. Clinotobermorite has Ca^{2+} ions coordinated in the intermediate layers of the double silicate chains. Due to the structural similarity of the double silicate chain structure to zeolites, the Ca^{2+} ions are often referred to as "zeolitic" cations, which are bound in the structure in a highly complex manner through water molecules and oxygen atoms of the polyhedral **[39]**. The crystal structure of clinotobermorite is seen in **Figure 8**. It can be observed the way that the double silicate chains of clinotobermorite are linked. On the other hand, as in clinotobermorite the normal 11Å tobermorite and anomalous 11Å tobermorite also present the silicate chains of the individual layers condensed into double chains with the difference that in normal 11Å tobermorite the zeolitic calcium occupation is just partial which is reflected in the different Ca/Si for each polytype (see **Figure10**). Another difference is in the space group symmetry that in the clinotobermorite is C12/m1 with two possible unit cell configurations, monoclinic and triclinic, whilst the space group symmetry of the normal 11Å tobermorite is C2/mm with a monoclinic unit cell. Besides, these two different species suffer a different thermal decomposition in terms of structure, since while the normal 11Å tobermorite transforms into 9Å tobermorite upon heating at 300ºC, the anomalous one remains stable (despite the loss of water molecules) [36, 49, 50]. It has been hardly to elucidate the structure of 11Å tobermorite because of the poorly crystalline or microcrystalline character with high structural disorder. McConell was the first one in 1954 who studied the crystallography of this mineral using

a sample from Northern Ireland which they described as normal tobermorite. It was described as orthorhombic with a space group symmetry C222 and the preference growing direction is along the c axis which indicates that this mineral is built up of perfect structural blocks perpendicular to c with structural defects between them **[45]**. Two years later, a similar study by Megan and Kelsey was published. They used a specimen from the same origin which was based on a "pseudo-orthorhombic" structure, with layers parallel to (001) built up by a central sheet of CaO. This sheet contains in both sides' silicate chains with dreierketten arrangement whereas those layers are stacked in a way the ridges of each layer are precisely facing those of adjacent layers. The remaining calcium ion and the water molecules are placed in the cavities between the ridges and some hydrogen atoms are attached to the silicate chains **[10]**.

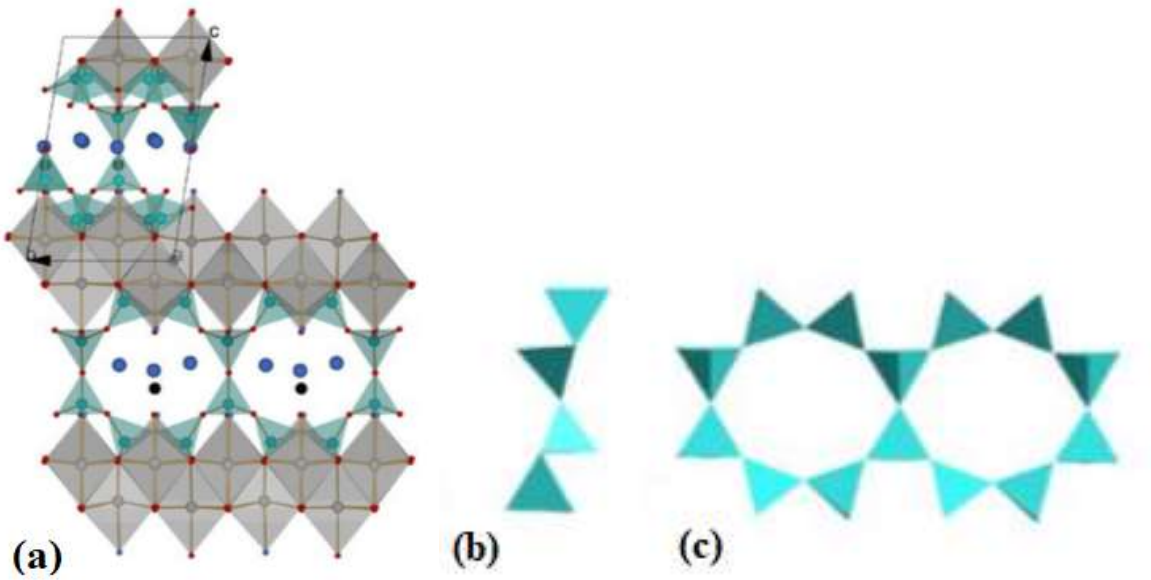

Figure 8. (a) Crystal structure of clinotobermorite (triclinic, space group symmetry C1, cell parameters a = 11.273 (1) Å, b = 7.350 (2) Å, c = 11.498 (2) Å, α = 99.17 (1) º, β = 97.19 (1)º, γ = 89.97 (2)º, polytype MDO_2). Grey octahedra: Ca polyhedron; black spheres: Ca in the intermediate layer; turquoise tetrahedra: Si tetrahedron; red spheres: oxygen atoms; dark blue spheres: oxygen from H_2O. (b) and (c) Type of linkage of the silicate double chains of clinotobermorite displaying 2/m symmetry **[10]**.

Hamid characterized a sample from Germany in 1981 without specifying the polymorph, that is, normal or anomalous. He classified the crystal structure in the space group symmetry Imm2. And it was described as a continuous sheet of seven-coordinated calcium polyhedral with dreierketten silicon chains in both sides. These sheets occupy two alternative positions displaced by b/2. Hamid proposed two reasons of the disorder

in the structure: the bridging tetrahedral might take two different mirror orientations perpendicular to the axis; besides, the calcium cations in the cavities between the layers present only half occupancy which would be correlated with the orientation of the bridging tetrahedral. Finally, after all the previous structures were proposed, and there was not a solid concordance in the stated models, Merlino et al. performed a broad study to unravel the structure of 11Å tobermorite. These researchers studied via X-ray diffraction specimens of 'anomalous' 11Å tobermorite from Wessels mine in South Africa and 'normal' 11 Å tobermorite from Bašcenov, Urals, Russia which had outstanding well-developed crystals. The crystal structure proposed by Merlino et al. was not much different than the structures developed in older studies, but the accuracy of their experimental measurements allowed to achieve what they call the "real" structure. Merlino and co-workers define the tobermorite as infinite layers of sevenfold-coordinated calcium polyhedral parallel to the direction (001). Therefore here, the feature that differs this conformation from the other tobermorite is at the apical sites of the pyramidal parts of the calcium polyhedral where OH^- anions and H_2O molecules regularly alternate along the b axis if in the other ones they are oxygen atoms instead of hydroxyls.

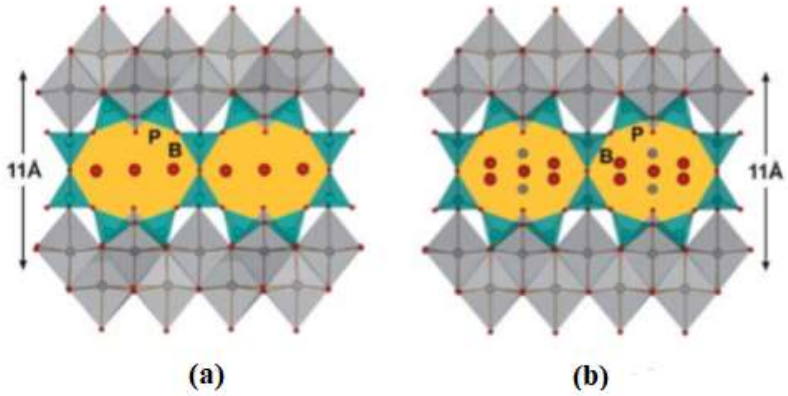

Figure 9. Scheme of the 11Å tobermorite. (a) Crystal structure of the monoclinic polytype of the anomalous 11Å tobermorite (orthorhombic, space group symmetry F2dd, a = 11.265(2) Å, b = 7.386(1) Å, c = 44.970(9) Å, polytype MDO_1) and (b) crystal structure of the monoclinic polytype of the normal 11Å tobermorite (monoclinic, space group symmetry B11m, a = 6.732(2) Å, b = 7.369(1) Å, c = 22.680(4) Å, γ = 123.18 (1)º, polytype MDO_2) . Turquoise: Si/Si-O tetrahedra, grey: Ca/Ca-O polyhedra, red: O atoms; B: bridged Si-O tetrahedra, P: paired Si-O tetrahedra **[10]**.

Merlino et al. agree with the basic structure of silicate chains in dreierketten statement along the b direction link together to two successive calcium polyhedral layers. The symmetry of the structure might be classifying as 2 mm. Besides, some wide channels were described along the b direction where three H_2O molecules are hosted and sometimes also calcium ions. Thereby, Merlino et al. developed the chemical formula, as follows: $Ca_{4+x}Si_6O_{15+2x}(OH)_{2-2x}\cdot 5H_2O$, where x varies from 0 to 1 **[51]**.

When comparing crystal structure of both tobermorites, anomalous 11Å and normal 11Å, Mitsuda et al. claimed that: for the anomalous tobermorite the silicon chains are attached to different calcium layers linked together via Si-O-Si bonds giving place to a firm structure **[50]**. However, Merlino et al. supported the idea that such links exist in both cases, and the difference is uniquely owing to the presence of zeolitic calcium ions tightly bonded to three water molecules in the normal variety which are missed in the dehydration process **[34, 50]**. During the dehydration step, there is a chain condensation that gives 9Å tobermorite. The presence of those zeolitic Ca^{2+} ions might also be associated to a small change in stoichiometry that, according to Merlino et al., varies from $Ca_{4.5}Si_6O_{16}OH\cdot 5H_2O$ for normal tobermorite to $Ca_4Si_6O_{15}(OH)_2\cdot 5H_2O$ for anomalous tobermorite **[34]**. Albeit the mechanism of the transformation along the dehydration process is still unclear. **Figure 9** shows a schematic representation of the crystal structure of the two different polytypes, anomalous 11Å tobermorite and normal 11Å tobermorite.

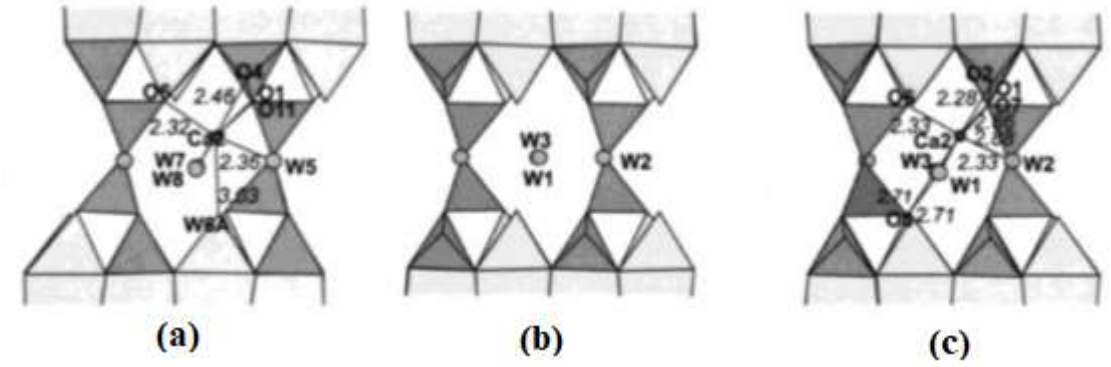

Figure 10. Schematic drawing of the structural cavities, as seen along [010] in (a) anomalous tobermorite 11Å, (b) normal tobermorite 11Å and (c) clinotobermorite **[39, 47]**.

As already explained above, the 9Å tobermorite is obtained by heating treatment of normal 11Å tobermorite at 300ºC. Then, the products of the dehydration process are 9Å clinotobermorite with the resulting chemical formula, $Ca_5Si_3O_8(OH)_2$ and 9Å tobermorite, riversideite, with the formula, $Ca_5Si_6O_{16}(OH)_2$, respectively. On the one hand, the structure of 9Å clinotobermorite has been fully elucidated. On the other hand, the structural subtleties (bond lengths and exact positions of the Ca^{2+} ions in the intermediate layers) of 9Å tobermorite, riversideite, have not yet been known **[39, 47]**. **Figure 11** illustrates schematically the 9Å tobermorite, riversideite that of Merlino et al. determined **[51]**. Comparing the crystal structures of normal 11Å tobermorite and its dehydration product, Merlino et al. describe the mechanism of structural change when heated **[39]**. Accordingly, the double chains of the normal 11Å tobermorite structure decondensed by reaction with H_2O in a first step as follows:

$$[Si_6O_{17}]^{10-} + H_2O \longrightarrow 2[Si_3O_8(OH)]^{5-}$$

The formula above corresponds to a double chain of the "dreierkette" structure (six Si tetrahedra). The two individual silicate chains condense after the loss of water, offset by b/2. Then, with this topotactic reaction the structure of the Ca-O polyhedral layers together with the individual silicate chains is formed. Again, the typical structure of tobermorite repeated in all the previously named conformations is also observed in the 9Å tobermorite **[47, 51]**. It is shown in **Figure 11**; where the calcium layers are parallel to [001] but in this case, they are closer to each other and connected through single chains of silicates with dreierketten accordance. Four of the five water molecules that are in the 11Å tobermorite disappear and the remaining one is in the form of Si-OH. The zeolitic channels are now narrower after the dehydration, and they only host Ca^{2+} in positions slightly displaced with occupancy factor of 0.5.

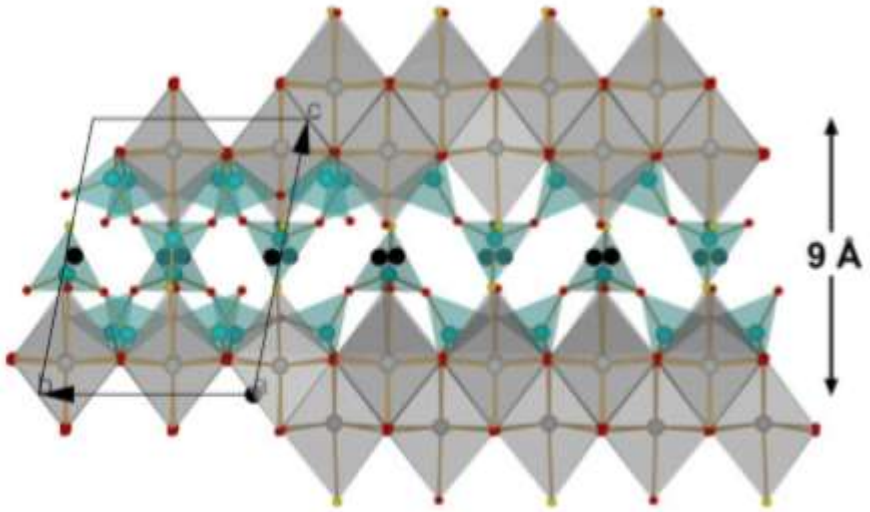

Figure 11. Crystal structure of 9Å tobermorite, riversideite (triclinic, space group symmetry C1, a = 11.156(5) Å, b = 7.303(4) Å, c = 9.566(5) Å, α = 101.08(4)º, β = 92.83(5)º, γ = 89.98(4)º, polytype MDO_2). Grey: Ca/Ca-O polyhedron, black: Ca atoms in the intermediate layer (occupancy factor 0.5), turquoise: Si/Si-O tetrahedron, red: O atoms, yellow: O atoms from OH **[47, 51]**.

Tobermorite can be partially substituted in its structure by some metallic elements, specially by Al which is called as "Al-substituted" tobermorite and, on fewer occasions, by Fe, Mg, Na, etc. This replacement has been widely demonstrated in natural formations where it is more common to find the Al-substituted one rather than the pure one **[52]**. Historically, aluminium substituted tobermorite is known to be a key ingredient in the longevity of ancient undersea Roman concrete. The volcanic ash that Romans used for construction of construction of sea walls contained phillipsite, and that an interaction with sea water caused the crystalline structures in the mortar to expand and strengthen, making

that material substantially more durable than modern concrete when exposed to sea water **[53-55]**. Nevertheless, X-substituted tobermorite has also been synthesized by some scientists. They have discussed in the published literature the degree of substitution and structural changes when Al is incorporated. It is reported that aluminium provides tobermorite some stability during the transformation into xonotlite under specific hydrothermal conditions **[35, 56-59]**. The way how the Al is incorporated into tobermorite lattice has been discussed by many authors. In some silicates with a layer structure, the Al^{3+} can assume tetrahedral coordination where it would enter as a substitution of the Si^{4+} or assume a higher coordination and substitute the Ca^{2+} ions **[60]**. However, in the case of tobermorite, it has been reported by Diamond et al. that the aluminium occupies the position of the silicon in the structure **[61]**. This was determined using their measurements of X-ray fluorescence spectroscopy. Kalousek proposed different possibilities for the incorporation of Al^{3+} into the crystal structure according to the principles of isomorphous substitution **[60]**. The first possibility is the substitution of $Al^{3+} + H^{+}$ for one Si^{4+}, the second one is the substitution of $2Al^{3+}$ for $Si^{4+} + Ca^{2+}$, and the last one consists of the substitution of $4Al^{3+}$ for $3Si^{4+}$. The latter would imply special geometrical arrangements, and this is not the case. Therefore, the first one is the most probable though the second possibility might also happen sporadically. Many authors have also discussed the position that Al^{3+} cation takes in the silicate chain of tobermorite structure. Generally, most of them agree that the substitution of Al for Si does not take place in terminating positions of the silicate chains; rather in bridging and branching sites since they are the preferable ones **[62]**. This is reflected on **Figure 12**, where all the possible positions that the Al and Si ions can occupy are schematically illustrated as Wang et al. reported **[63]**. It is plenty of publications that have concluded the advantage of adding Al for the stabilization of tobermorite, and many of them remark that the optimum Al/(Si+Al) molar ratio is 0.15 **[35, 58, 59]**. For higher ratios than 0.15, some authors have reported the formation of hydrogarnet as a secondary product **[60, 64]**. As mentioned before, aluminium is not the only ion that can access into the structure of tobermorite. Diamond et al. studied the effects of iron and magnesium, and Barnes et al. the effect of sodium **[64, 65]**. In case of sodium ion effect, this is quite relevant because of "ion-exchange" properties that it may provide to tobermorite **[66]**. Sodium would occupy in the structure of tobermorite the position of H^{+} in the interlayer space and the Al-Na-tobermorite might have this formula, $Ca_5Na_{0.7\pm0.2}Al_{0.8\pm0.15}Si_{5.2\pm0.2}O_{16}(OH)_2{\cdot}4H_2O$ **[64]**. On the other side, the calcium present in the zeolitic space of Al-Na-tobermorite is very hydrated; this effect is the reason why the tobermorite acquires the ion- exchanging properties. So, for example the Cs^{+} has more affinity for the Na^{+} instead of Ca^{2+} **[66]**. With respect to other alkalis such as K^{+} and Rb^{+}, they can also be part of the structure although the affinity is lower **[67]**.

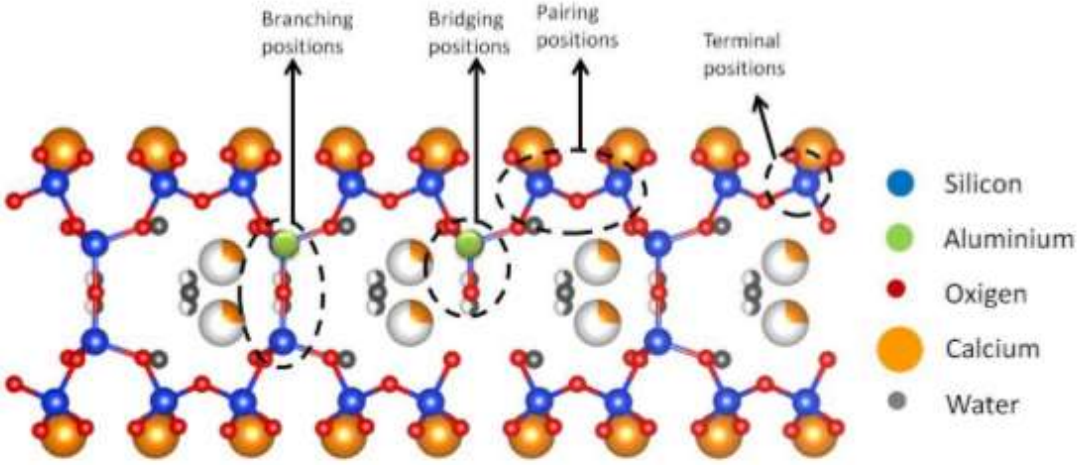

Figure 12. Representation of the Si and Al atoms positioning in the tobermorite structure according to Wang et al. **[72]**. The spheres with one part in white represent the portion of the atom that belongs to another unit cell.

In the case of selective Cs^{+} exchange on such tobermorite, this may be useful in decontaminating circulation water in nuclear reactors and radioactive waste solutions **[66]**. Some ions of heavy metals as for example Pb^{2+} and Cd^{2+} might be exchanged, and so captured in the tobermorite structure **[68]**. The Al-Na-substituted tobermorite is well-known due to its partial or total exchange capacity of structural Ca^{2+} for divalent ions such as Co^{2+}, Ni^{2+}, Cd^{2+} and Zn^{2+} **[67, 69]**. Moreover, X-substituted tobermorite can be also applied to purify waters which are polluted with heavy metals and phosphates **[70]**. On this one, the Ca^{2+} exchange promotes the formation of hydroxyapatite ($Ca_5(PO_4)_3(OH)$) layer over the tobermorite which would retain the phosphates and clean the water **[42]**.

Regarding to the morphology of tobermorite crystals, a tobermorite crystal growing in natural conditions is highly crystalline and forms fibres or plates **[36, 37]** as it has been explained at the beginning of this section. However, when tobermorite is synthesized may vary in morphology from platy to lath-like and fibrous, even lamellar for X-substituted tobermorite as seen in **Figure 13**. Synthesis of pure tobermorite in its crystalline form is a challenge, and the amount and final morphology of the synthetic tobermorite particles depends on the starting materials, temperature, C/S ratio, pH, reaction time and the synthesis process. The different tobermorite polymorphs exhibit variation in morphology where tobermorite 14Å and normal tobermorite 11Å form relatively large pseudohexagonal platy crystals slightly elongated parallel to *b* axis in contrast to anomalous tobermorite 11Å **[34, 40]** which tends to form lath-like morphology **[50, 71]**.

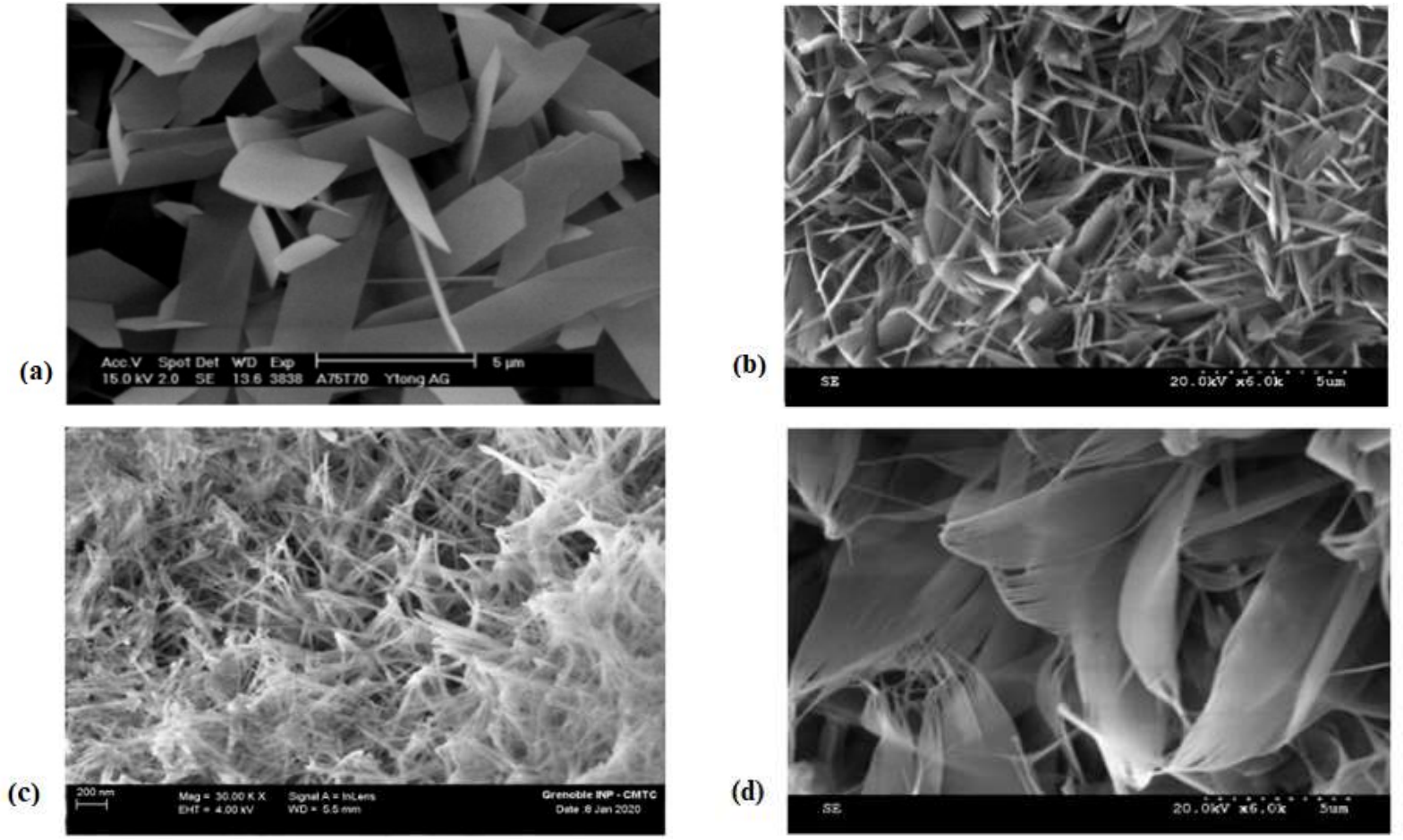

Figure 13. SEM micrographs of tobermorite samples. (a) Tobermorite with platy crystallites, (b) Tobermorite exhibiting lath-like crystallites, (c) Tobermorite with acicular needles shape, fibrous morphology and (d) AlS-tobermorite showing leafy and lamellar-shape **[36, 37]**.

2.4. Xonotlite

Xonotlite is another crystalline calcium silicate hydrate phase that is synthesized hydrothermally in this research, and it is the most fundamental one in the calcium silicates-based materials produced in this thesis because of their thermal stability and mechanical properties. It was firstly discovered by Rammelsberg in 1866 and named for its natural occurrence in Tetela de Xonotla, Puebla, Mexico. Besides, xonotlite was later found in other locations such as Crestmote (USA), Franklin (USA), Scwat Hill (Ireland) and Wessels mine (South Africa). It is a mineral that can adopt different colour such as grey, light grey, lemon white or pink or even can be colourless. This considered rare mineral only occurs in nature under hyper-alkaline hydrothermal conditions **[35]**. Xonotlite is found as a product of Ca-metasomatosis in metamorphic deposits within limestones, as veins in serpentinites and in metavolcanics rocks **[72]**. Normally, xonotlite appears together with other minerals of the same family, inosilicates, as for example wollastonite, tobermorite and rosenhahnite. The chemical composition of most natural xonotlite samples does not differ substantially from the ideal formula, with traces of Fe, K, Mn and Na occasionally being incorporated **[37]**. Qian et al. showed that significant Mg substitution may occur, thus giving the formula $Ca_{3.58}Mg_{2.41}Si_{6.04}O_{17}(OH)_2$ **[73]**. For a synthetic xonotlite, the chemical formula is $Ca_6Si_6O_{17}(OH)_2$, or C_6S_6H in cement chemistry notation. It crystallizes in the monoclinic – prismatic crystal system with typically an acicular crystal form or habit.

Mamedov and Belov **[74]** were the first whom proposed a structure model for xonotlite which was later confirmed by Eberhard et al. **[75]**. The structure of xonotlite consists of Ca-O polyhedral layers and double silicate chains $[Si_6O_{17}]$, they are called "dreier-doppelketten" **[76]**. Two of the calcium atoms are in sevenfold coordination surrounded by 6 oxygens in form of a trigonal prims and one additional oxygen on one prism plane, the third calcium atom is in octahedral coordination (see **Figure 14**). CaO_6-octahedra and CaO_7 polyhedra in sevenfold coordination are both edge-sharing to form infinite chains in the b-direction. These structural elements were confirmed by extended X-ray absorption fine structure (EXAFS) investigations of Ca by Lequeux et al. **[77]**. The different chains are linked together by sharing edges and build up layers parallel to (001). Between these layers the $[Si_6O_{17}]$-dreier-doppelketten are located. Each of these double chains are based on two wollastonite-like dreiereinfachketten with two paired tetrahedra and one bridging tetrahedron as show in **Figure 14**. These structural units were also confirmed by ^{29}Si NMR measurements carried out by Cong et al. and Noma et al. on synthetic samples **[78, 79]**. In comparison to Cong et al. **[78]**, Noma et al. **[79]** observed a splitting of Q^2 sites which was attributed to different Si-O bond lengths and Si-O-Si angles of the paired tetrahedra and additional Q^1 sites which were interpreted in terms of disorder and may be due to the synthesis pathway. In xonotlite the bridging tetrahedra are connected to the Ca-polyhedral layers. Owing to the same length of $[Si_6O_{17}]$-dreier-doppelketten and two Ca-polyhedra there exist two different ways of attachment of the double chains to the polyhedral layers and hence various polytypes are possible **[80]**. The OH group is located at the free apex of a CaO_6-octahedron where no bridging tetrahedra are attached **[81]**. Either every CaO_6-octahedra carries one OH group, or CaO_6-octahedra containing two OH groups are alternating with non-hydroxylated one depending on the polytype developed. Noma et al. measured a ^1H NMR signal of 1.86 ppm in synthetic xonotlite **[79]**. This proton was attributed as a component of a silanol group. According to the xonotlite structure silanol groups should not exist and their occurrence was not confirmed by other NMR studies **[78, 82]**. In addition, Noma et al.

detected a broad shoulder at 5.26 ppm assigned to interlayer water **[79]**, which was not verified by NMR-, IR- and TGA/DSC-studies **[78, 83, 84]**.

As mentioned above, xonotlite structure can suffer from some changes when some of the elements in the structure are replaced by others with similar characteristics. The Si^{4+} can be substituted by Al^{3+} up to 5% **[85]**. The Ca^{2+} can be almost completely substituted by Co^{2+}, or Ni^{2+} **[86]** and partially by Mg^{2+} **[87]**. Regarding the Mg^{2+} substitution, there has been further work investigating the incorporation of magnesium into xonotlite, and hydrothermally synthesized xonotlite and magnesium-substituted xonotlite monoliths have been shown to possess considerable compressive strengths and dimensional stabilities **[88]**.

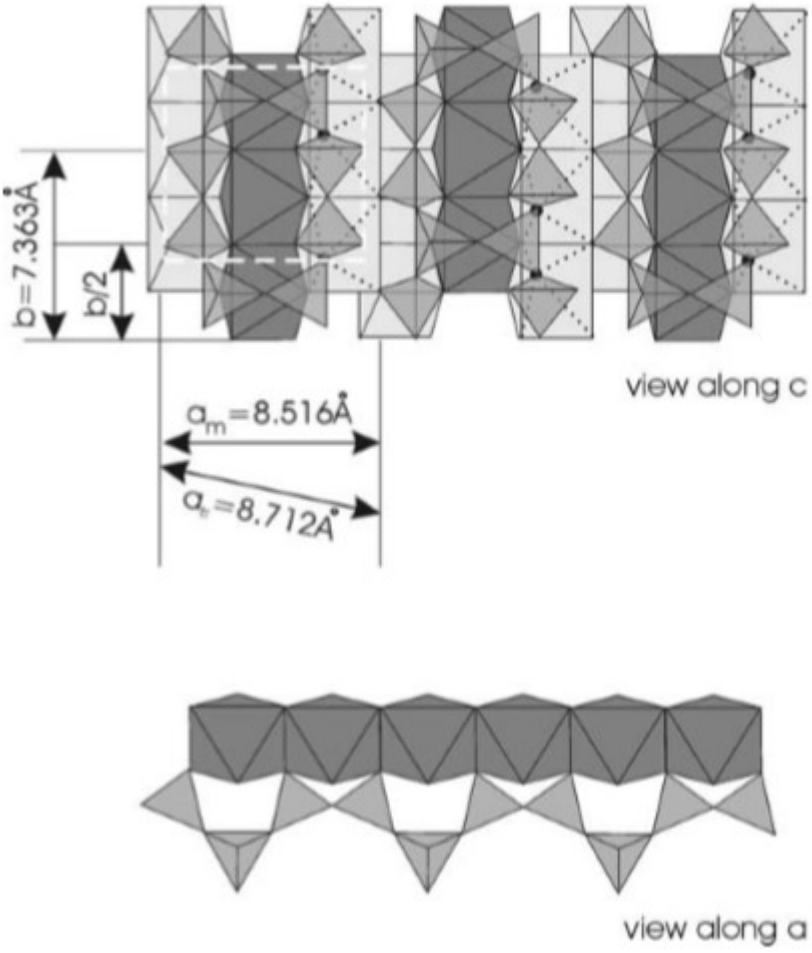

Figure 14. Structure of xonotlite; Ca-polyhedra: dark grey in octahedral coordination and light grey in sevenfold coordination; Si_6O_{17} tetrahedral-double chains in middle grey: protoxonotlite-cell with white dashed outlines; notice the two different possibilities (light and middle grey) of connecting a SiO_4-tetrahedral chain to the Ca-polyhedra **[76]**.

Leaning on the crystal structure model of Mamedov and Belov **[74]** and the confirmation of Eberhart et al. **[75]** six different polytypes (four ordered and two one-dimensional disordered) for xonotlite were suggested. These polytypes can be observed as different stacking in [100]- and [001]-direction of a protoxonotlite-cell introduced by Kudoh and Takeuchi **[81]**. In [100]-direction a continuous shift of +b/4 or -b/4 or an alternating shift of +b/4 and -b/4 is possible. In [001]-direction the protoxonotlite-cells are either in juxtaposed positions or shifted by b/2. The combination of these different stacking models leads to four ordered polytypes M2a2bc, M2a2b2c, Ma2bc and Ma2b2c as shown in **Figure 15**.

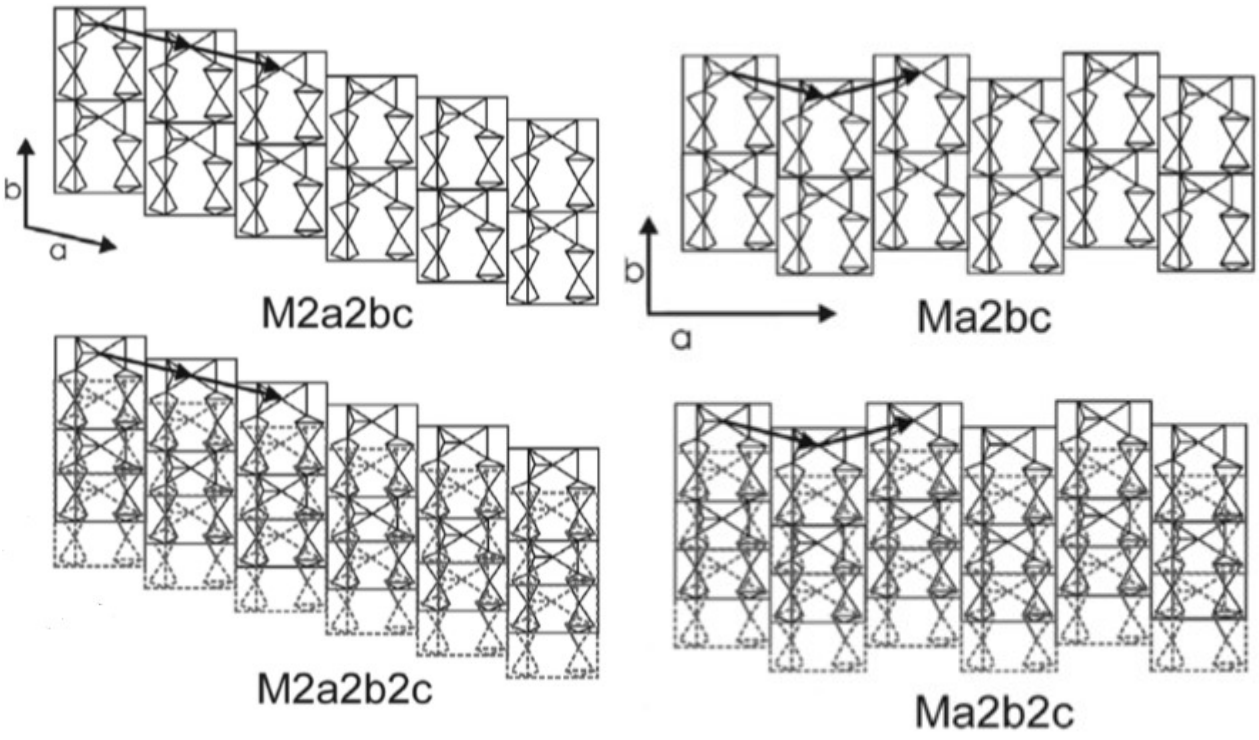

Figure 15. Representation of the four ordered polytypes of xonotlite. The OD polytypes are shown as different stacking of the protoxonotlite-cell (dark outlines) after Hejny and Armbruster **[72]**; cells with displacement in c-direction are drawn with dashed outlines.

In these 4 ordered polytypes, M is meaning the monoclinic symmetry group of the protoxonotlite-cell and the three lower case letters (a, b and c) along with the numerical values in front, if necessary, are indicating the periodicity of the three directions in space according to the modified Gard-notation **[80]**. The different cell parameters were determined by Henjy and Armbruster **[72]** and are listed in **Table 3**. For M2a2bc and M2a2b2c twinning is possible if one species displays intergrowth of domains with continuous shift of +b/4 in a-direction and continuous shift of -b/4. Streaks parallel to a*

observed in single crystal patterns by Gard **[80]** were assigned to the two-known disordered polytypes P∞21 and A∞22 (it corresponds to Mad2bc and Mad2b2c in modified Gard-notation). Hejny and Armbruster **[72]** extended the group of possible polytypes by Ma2bcd and M2a2bcd, which have one-dimensional disorder in c-direction as indicated by streaks observed parallel to c* **[72]**. Short spikes recorded perpendicular to the c* streaks have been interpreted in terms of two-dimensional disorder; they are termed with the corresponding symbol Mad2bcd **[72]**.

	a [A]	b [A]	c [A]	α [º]	β [º]	γ [º]	Space group
protoxonotlite cell	8.516	7.363	7.012	90.00	90.37	90.00	
M2a2bc	8.712	7.363	7.012	89.99	90.36	102.18	P1
M2a2b2c	8.712	7.363	14.023	89.99	90.36	102.18	A1
Ma2bc	17.032	7.363	7.012	90.00	90.36	90.00	P2/a
Ma2b2c	17.032	7.363	14.023	90.00	90.36	90.00	A2/a

Table 4. Lattice parameters and space symmetry group of the ordered polytypes after Hejny and Armbruster **[72]**.

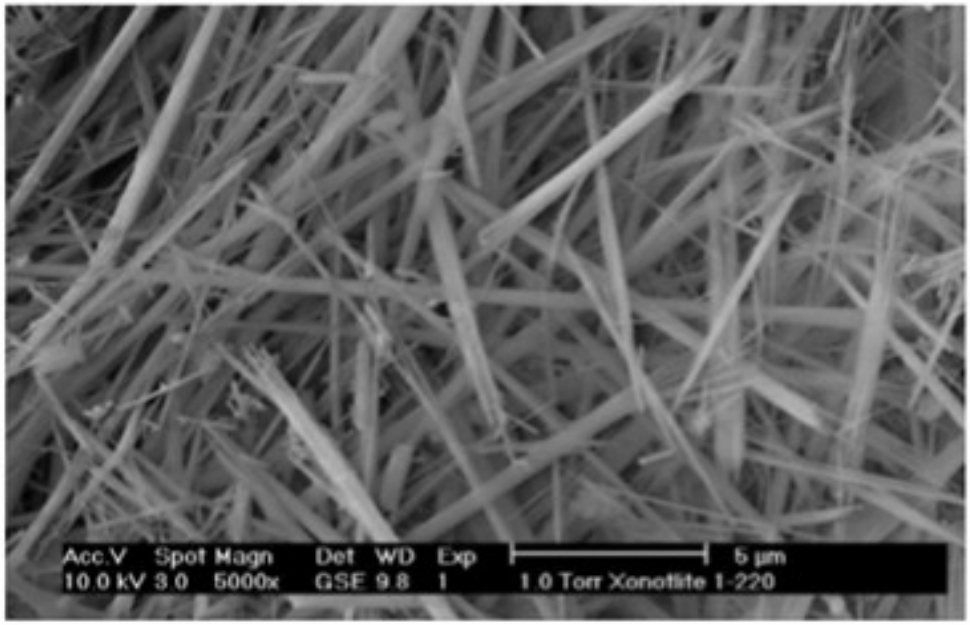

Figure 16. SEM image of needle-like xonotlite crystals.

The morphology of xonotlite crystals can vary depending on different factors, especially the raw materials and additives, the temperature and time of hydrothermal curing used for the synthesis of this C-S-H phase. Regardless of this, the most commonly morphology observed both in natural occurring xonotlite and synthetic xonotlite is based on needle-like crystals. **Figure 16** shows a scanning electron microscopy image corresponding to a sample of pure xonotlite, where long fibrous needles can be seen. During the hydrothermal reaction of lime and silica to form xonotlite in stirred conditions, spherical (or quasi-spherical) particles grouping inside those needles-shape crystals are developed (see **Figure 17a**).

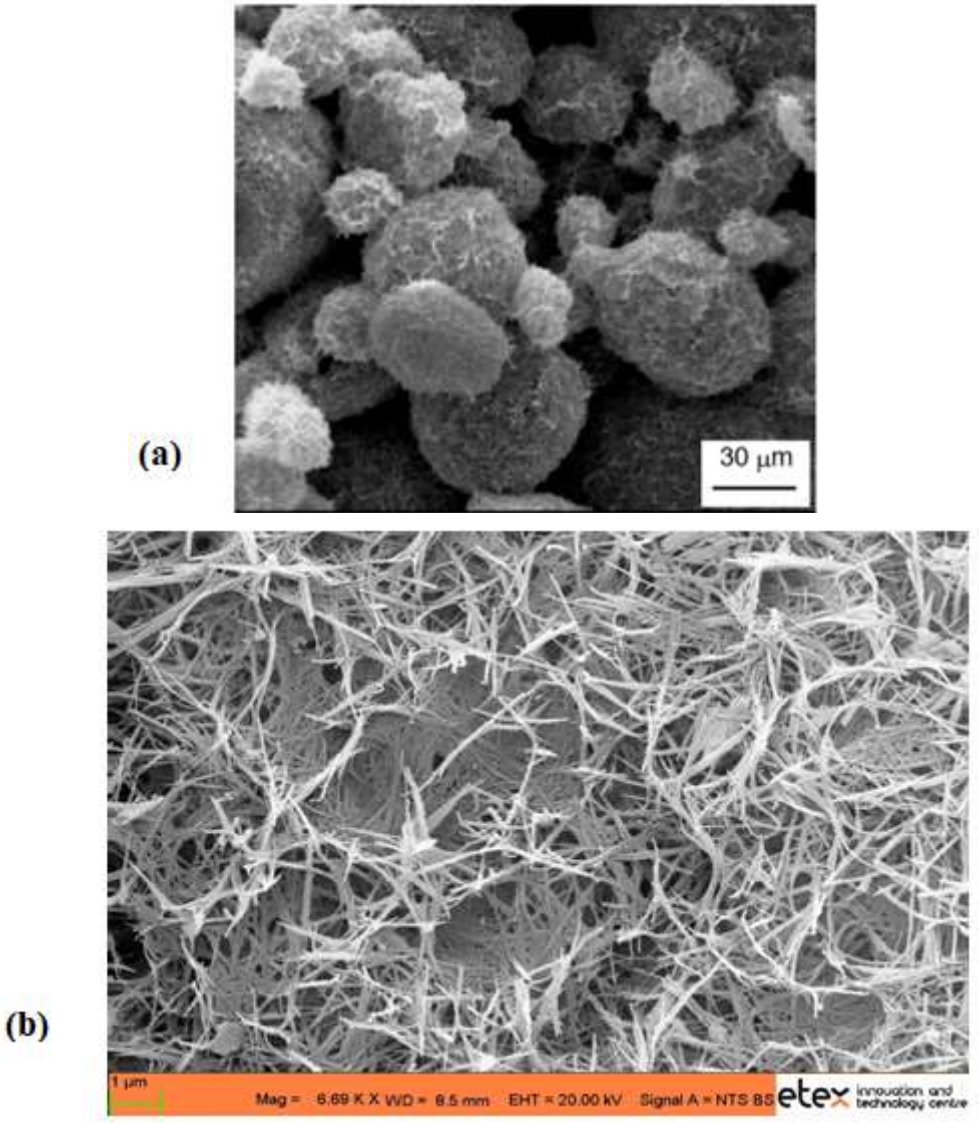

Figure 17. Typical morphology of xonotlite crystals synthesized hydrothermally. (a) SEM image of a sample composed of spherical xonotlite particles prepared via dynamic hydrothermal reaction; (b) SEM image of a sample composed of xonotlite whisker particles forming a fibrous matrix and prepared via static hydrothermal reaction.

Whereas if it is chosen the static hydrothermal reaction, that is, without any agitation, the xonotlites particles produced are a kind of whiskers, forming a fibrous network as it is shown in **Figure17b**.

The interest on the synthesis of xonotlite using hydrothermal conditions on industrial level started in the middle of the 20th century. The Japanese were the pioneers in developing a dynamic hydrothermal technology, also called 'stirred autoclave' which allows to control the size and morphology of the xonotlite crystals. Therefore, companies involved in calcium silicates production started to use this type of methodology at their industrial plants for use in passive fire protection and insulating materials due to several specific properties (low thermal conductivity, good mechanical properties, excellent thermal stability). Furthermore, many other applications also employ xonotlite as for example: friction extender in brake pads of automobiles **[89]**, pigment in paper and dye industry, thixotropic agent in composites, drip suppressant in composites **[72]**, filler material to improve flexural strength of cement matrices **[43, 90]**, filler in organic polymers in moulded materials. And it is very used in compositions of well cement for oil deposits as well as in nuclear waste deposits to capture and immobilize radioactive elements. More surprisingly is the possibility of using xonotlite nanofibers as a precursor for the formation of wollastonite nanofibers for biological and orthopaedic applications **[91]**. Recently, research has proved the feasibility of the xonotlite nanofibers use directly for those same orthopaedic applications simplifying and reducing the cost of the synthesis process **[92]**.

2.5. Hydrothermal synthesis of calcium silicate hydrates

The term *hydrothermal* is purely of geological origin. It was firstly used by the British geologist, Sir Roderick Murchinson (1792 – 1871) to describe the action of water at elevated temperature and pressure in bringing about changes in the Earth's crust and leading to the formation of various rocks and minerals **[93]**. Geologists performed the earliest work on the hydrothermal technique in the nineteenth century to understand the genesis of rocks and minerals by simulating the natural conditions existing under the Earth's crust. However, materials scientists popularized this technique, particularly during 1940's. Today, the hydrothermal technique is being applied widely by various specialist from different disciplines of science including organic chemistry, geochemistry, inorganic chemistry, biochemistry, mineralogy, biotechnology, food and nutrition, environmental safety, nanotechnology and nanobiotechnology.

The concept of hydrothermal synthesis is usually referred to any heterogeneous reaction in the presence of water under-high-pressure-high-temperature (HPHT) conditions to dissolve and recrystallize materials that are relatively insoluble under ordinary conditions **[93]**. When considering a hydrothermal reaction, it is necessary to fix a lower limit of pressure and temperature conditions. Then, as hydrothermal temperature is it one that is above the room temperature and as hydrothermal pressure is that one greater than 1 atm. This method of synthesis of crystalline materials depends strongly on the solubility of the minerals in heated water under high pressure. The crystal growth under hydrothermal conditions is carried out in an apparatus consisting of a metallic (stainless steel, iron, nickel…) pressure vessel, popularly known as an *autoclave*, which is filled by the aqueous solution containing the reactive agents. There are some advantages of the hydrothermal reactions over other types of crystal growth reaction. For example, they include the ability

to develop crystalline phases which are not stable at the melting point. Besides, materials with a high vapour pressure near their melting points can be grown by the hydrothermal reactions. Also, the fact that this process uses water as solvent means a sustainable and green chemical method. Water is non-toxic, non-flammable and non-carcinogenic, so it is already an enormous advantage in comparison with most of the organic solvents employed for many syntheses. Under hydrothermal conditions the viscosity is lower; thereupon this favours the ion diffusion in the media and so, the reactivity **[94, 95]**. The method is particularly suitable for the growth of large-quality crystals while maintaining control over their composition. By contrast, disadvantages of the method include the need of expensive autoclaves and the high maintenance costs.

The synthesis of calcium silicate hydrates by hydrothermal techniques has been employed for many years as a successful method to obtain amounts of large crystals of CSH phases with controlled properties and apply them industrially in a big number of sectors. The reaction is usually based on $CaO\text{-}SiO_2\text{-}H_2O$ system where the solid materials are silica and lime **[96, 97]**. In this aqueous system, the water plays a very important role since in hydrothermal synthesis acts as a medium which can depress the temperature of solids and liquids, lower down its viscosity as mentioned above, break the crystal lattice of the substance and further improve the solubilization **[93]**. Thus, the product formed during the hydrothermal treatment shows an increased grain size. Owing to the presence of water, the transport of ions becomes much easier. Therefore, seeding, nucleation and crystal growth are accelerated. Generally, the formation of the final product is related by one or several relevant factors such as solubility of the reactants, transporting rate of ions, formation of complex substance, nucleation rate and growth of crystals. In this case, the crystallinity and morphology of the products formed via hydrothermal reactions are directly dependent on the hydrothermal synthesis conditions, that is, Ca/Si molar ratio, isothermal temperature, time of reaction, and water to solid ratio **[97, 98]**. The synthesis of the C-S-H phases that compose the $CaO\text{-}SiO_2\text{-}H_2O$ system is quite complex because of the high difficulty to obtain a pure single-phase compound with high crystallinity. Most of the studies are focused on the stability between the following species: tobermorite, jennite, xonotlite, Z-phase, gyrolite, and truscottite **[35, 39, 99, 100]**. Taylor summarized the formation of calcium silicate hydrates under various conditions such as temperature and C/S ratio as seen in **Figure 18a**. He proposed a phase diagram where those crystalline CSH phases along with semi-crystalline CSH phases as CSH (I) and CSH (II) are distributed according to the temperature (y axis) and Ca/Si ratio (x axis) of the hydrothermal reaction. Later, this diagram was modified by Meller **[101]** including more C-S-H phases (see **Figure 18b**).

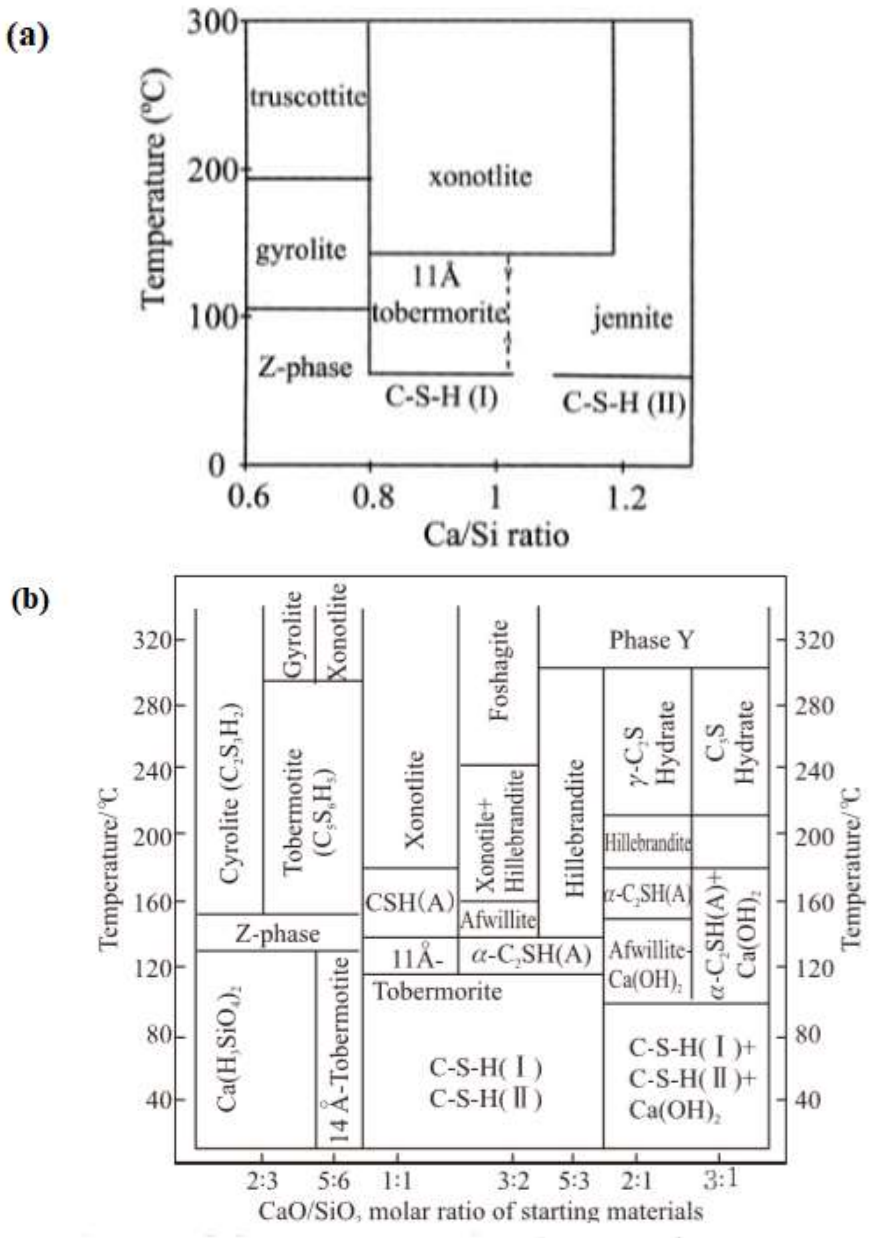

Figure 18. (a) CaO-SiO_2-H_2O phase diagram from Ca/Si of 0.6 to 1.3 and range of temperature from 0ºC to 300ºC. (b) CaO-SiO_2-H_2O phase diagram from Ca/Si < 0.67 to Ca/Si > 3 and range of temperature from T < 40ºC and T > 320ºC.

Nonetheless, these diagrams developed by Taylor and Meller are not very accurate since they do not consider other factors on the hydrothermal treatment as for example time. In a more recent study made by Hong et al., they proposed a phase diagram based on experimental results obtained from hydrothermal reactions at different Ca/Si ratios from 0.85 to 2 as it is shown in **Figure 19a [102]**. Differently from these authors, Harker drew another kind of C-S-H phases diagram based on temperature and pressure conditions to which these phases are stable (see **Figure 19b**).

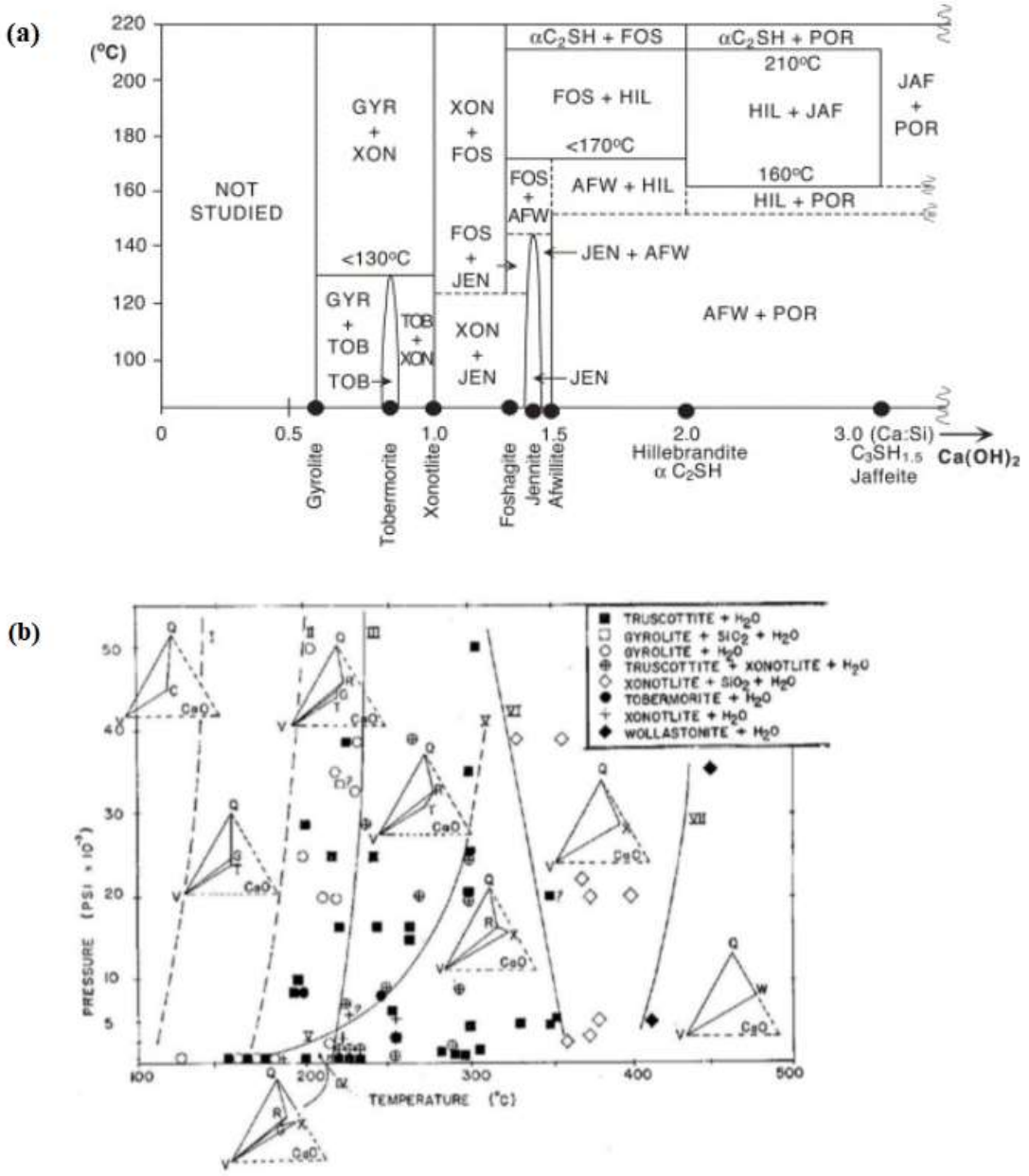

Figure 19. (a) Phase diagram obtained from several hydrothermal experiments, the dashed lines indicate uncertainties; (b) Phase boundaries of the CaO-SiO_2-H_2O system components as function of temperature and pressure. Q = quartz, C = CSH(I) T = tobermorite, G = gyrolite, R =truscottite, X = xonotlite, W = wollastonite, and V = H_2O.

If it is observed all these diagrams, poorly ordered C-S-H phases are usually formed at a relatively low temperature (<120ºC). They are metastable thermodynamic phases (dash in C-S-H indicates the non-stoichiometry of the substance). Otherwise, more crystallized phases, such as 11Å tobermorite, xonotlite and gyrolite, are normally stable at relatively higher temperature, over 150ºC. For this work, we are interested in the transition that starts from very disordered C-S-H phases (C-S-H(II), C-S-H(I)) and ends to xonotlite

taking as initial Ca/Si ratio 1. Depending on the starting raw materials used in our hydrothermal syntheses, tobermorite as intermediate product can be found or not.

Many authors have discussed the hydrothermal conditions at which the tobermorite converts into xonotlite, what is really challenging. Although there are so many parameters should be considered to identify this transformation properly, that the literature has not arrived at any clear conclusion so far **[103, 104]**. The lowest temperature at which xonotlite is formed has been reported to be 160ºC with a starting Ca/Si ratio of 1 **[105].** But a well-crystallized synthetic tobermorite shows signs of changing to xonotlite at 185ºC. Then, Harker et al. with this information considered that the xonotlite/tobermorite boundary region is at 170ºC ± 20ºC [120]. Buckner et al. reported that the thermal stability between tobermorite and xonotlite also depends on the Ca/Si **[104]**; they stated that tobermorite is more stable at a C/S ratio of 0.8 rather than 1. Moreover, they also explained in their work the effect of high pressure in the tobermorite-xonotlite equilibria **[104]**. This can be observed in Figure 20a, at high pressures (up to 207 MPa) the phase change occurs at 280ºC. Nevertheless, the time as kinetic variable is not represented in these experiments (not all the experiments lasted the same), and it is key point to understand the equilibrium. Anyway, in this work performed by Buckner et al., it is proved that at higher pressures and temperatures the phase tobermorite becomes more stable thermodynamically. Similar hydrothermal studies were made by Speakman concluding that tobermorite is formed in a very narrow range of temperature; below 100ºC only amorphous C-S-H is formed, and above 140ºC xonotlite starts to be formed **[106]**. Hence, he lays in this temperature the equilibrium boundary between tobermorite and xonotlite. However, he confirms that tobermorite becomes stable up to 285ºC in experiments done at high pressures (up to 275MPa) as seen in **Figure 20b**. Shaw et al. studied the effect of the structural Si substitution for Al in the tobermorite structure with the aim of stabilizing this phase **[35]**. **Figure 21** represents this effect. These authors proposed a mechanism for the formation of tobermorite because of a thorough kinetic study based on in-situ synchrotron spectroscopy in the temperature range comprised between 235ºC and 310ºC. Initially, a disorder C-S-H gel is formed at room temperature, after that CaO layers become ordered, and an increasing periodicity in the (001) direction is developed until tobermorite crystallizes **[35]**. In this process as mentioned in previous lines, temperature plays a fundamental role to avoid xonotlite formation, since at higher temperatures, the system becomes unstable. Black et al. reported that the 11Å tobermorite has lower polymerization comparing with xonotlite as in the structure occurs a combination of single “dreienfachketten” silicate chains with the typical double chains [125]. So, they propose that the stability of the double chains in tobermorite is not as high as in xonotlite, and so leading to instability at high temperatures.

Despite the various scientific contributions that have been made in this field, due to the complexity of $CaO\text{-}SiO_2\text{-}H_2O$ system, and the tobermorite-xonotlite boundary, as a high number of variables can affect it, this reminds still unclear, and it is very hard to extract conclusion about the hydrothermal conditions where those C-S-H phases are stable.

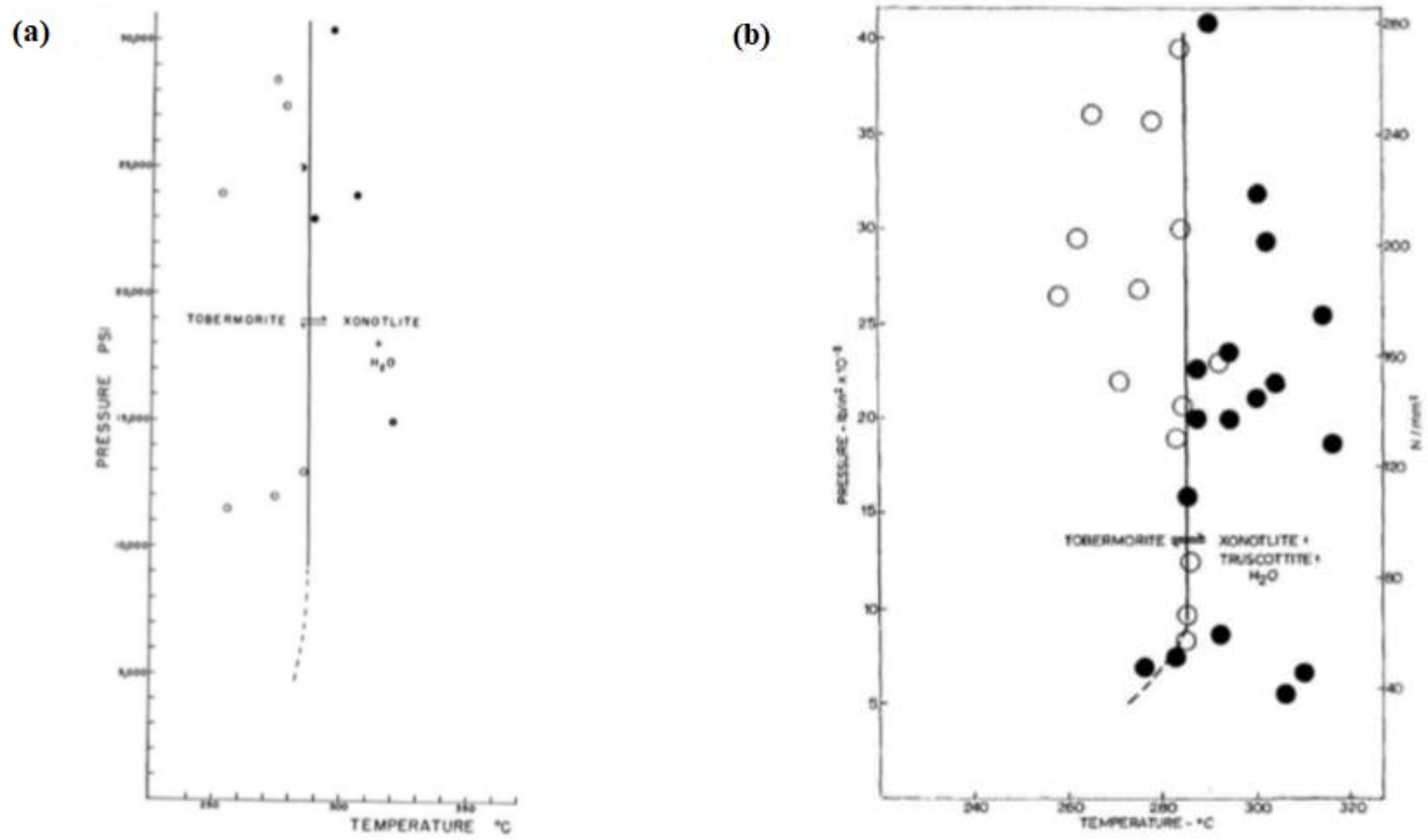

Figure 20. Tobermorite-xonotlite phase boundary at high pressures. (a) Experiments made by Buckner et al. **[104]**; (b) Experiments made by Speakman **[106]**.

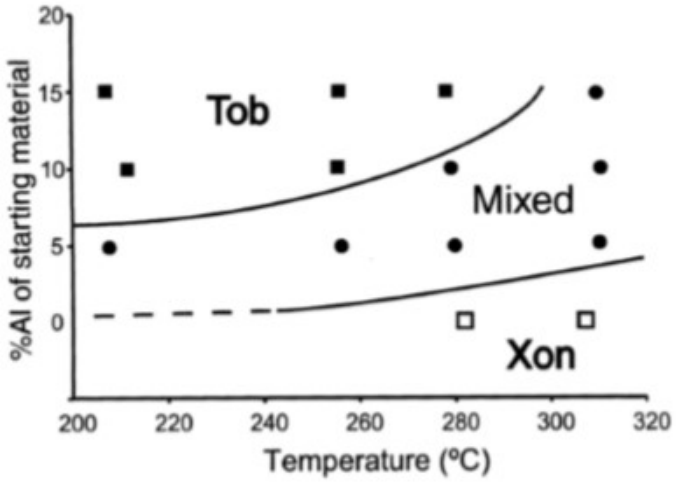

Figure 21. Phase diagram of tobermorite-xonotlite system, introducing a % of Al as a variable.

Regarding to the hydrothermal synthesis of tobermorite, there is only literature about 11Å tobermorite, since it is not possible to find anything related to the synthesis of 14Å tobermorite neither about the synthesis of 9Å tobermorite which is obtained via dehydration thermal from 11Å tobermorite but not hydrothermally produced. For the tobermorite synthesis the hydrothermal conditions are more controversial comparing with the xonotlite synthesis, because xonotlite's stability is higher and it is much easier to obtain it in a wide range of temperature. Over the last decades, different ways to synthesize tobermorite 11Å tobermorite have been proposed and most of them attempt to obtain highly crystalline 11Å tobermorite, understand the tobermorite-xonotlite phase boundary and study the effect of the Si substituted in the silicate chains structure for Al.

A lot of researchers have studied the effect of different parameters such as time, C/S ratio, temperature, pH, precursors, and partial substitution of Al for Si on the kinetic hydrothermal reaction. Normally most of the studies employed as precursors CaO and SiO_2 (crystalline or amorphous), but some works have exhaustively investigated the effect of some different precursors on the synthesis of 11Å tobermorite as for example EDTA, borosilicate, sucrose, Ca-formate, calcsilicate alkoxide gel, $Ca(NO_3)_2$ and Na_2SiO_3 **[35, 107-109]**. Besides, it has also been explored this synthesis using other precursors from industry waste products, such as oil shale ash, cement kiln dust, soda-lime-silica container glass and paper recycling residues **[69, 110]**. It is reported in literature that to synthesize pure tobermorite, the reaction times vary from some hours to months, using a temperature hardly ever above 200ºC.

Flint et al. was the first one in 1938 that reported the synthesis of 11Å tobermorite. He performed three syntheses using lime and silica with an initial Ca/Si ratio of 0.8 at three different temperatures, 150ºC, 225ºC and 250ºC and obtained 11Å tobermorite after 42, 14 and 7 days, respectively **[111].** In his work, Flint demonstrated that higher temperature and shorter reaction times could give to the same product.

Approximately twenty years later, Kalousek et al. carried out a huge study about 11Å tobermorite formation **[60]**. He targeted to understand the stable conditions for the formation of the pure product. For it, as a first variable, he modified the Ca/(Si + Al) ratio. Kalousek and his co-workers concluded that with low quantities of Al, they could obtain 11Å tobermorite. But with higher amounts, the most part of the product was 11Å tobermorite although also was formed a small percentage of katoite. Moreover, they also proved that the Al stabilizes the formation of 11Å tobermorite, with a maximum limit of 12%, since above that limit secondary phases are formed. Mitsuda worked in the same topic as Kalousek, but he introduced a new variable, the silica source **[58]**. After his experiments, the conclusions were such that he reconfirmed that the addition of the aluminium in low amounts stabilizes the tobermorite formation. Also, the formation of this phase is more favourable when the Ca/(Si + Al) ratio is 0.8 rather than 1. And the use of higher temperatures leads to a faster crystallization of tobermorite. With respect to the silica sources that he used, aluminosilica gel gave better results, but this was not completely clear. Sato et al. also studied the effect of silica source in the tobermorite formation, and between all the precursors used, quartz was the one that gave higher crystalline tobermorite **[112]**.

El-Hemaly et al. worked in a broad study focused on the formation of anomalous and normal tobermorite **[56]**. They employed a large combination of precursors to investigate different syntheses in the CaO-SiO_2-H_2O system, using as silicon precursors quartz with different particle size, colloidal silica, silica by-product and cristobalite. Moreover, they also did research on the effect of alumina and alkalis addition in the tobermorite formation. Despite all their effort could not arrive to conclude clearly about which are the conditions that determine the formation of 11Å anomalous tobermorite and 11Å normal tobermorite.

As it was explained in the previous section of this thesis, it is possible to find different morphologies of tobermorite crystals, but usually it appears as platelets or as fibres. Most of the hydrothermal syntheses performed in literature obtain more frequently platy-like morphology, but some modifications in the synthesis pathway may give fibrous-like morphology as well. There are some works where it has been used organic additives, alkali compounds or waste products from metallurgy or construction industry to the formation of tobermorite modifying its final morphology **[69, 107-110, 112]**.

On the other hand, the hydrothermal synthesis of xonotlite has also been extensively studied by so many people, but unfortunately there are remaining uncertainties to be solved since the mechanism of xonotlite formation is difficult and suffers changes depending on a lot of parameters as mentioned above. Again, the first scientist who worked on the hydrothermal reaction of xonotlite was Flint and his co-workers. They used silica gel and lime as precursors and different C/S ratios, temperatures, pressures, and timings **[111]**. Xonotlite was synthesized from three different Ca/Si ratios, 0.8, 1 and 1.5. For the first two C/S ratios, it was possible to obtain pure xonotlite using a temperature range between 175 and 390ºC. And only when the C/S ratio of 1.5 was used, an unknown secondary phase was obtained. This work was the unique that reports the use of supercritical water conditions to form xonotlite.

It is mentioned above that Speakman also studied the stability of the tobermorite-xonotlite boundary, in his research he carried out a broad number of reactions at different Ca/Si ratios, temperatures and pressures. Finally, he could demonstrate the stability of xonotlite at high pressures within a wide range of temperatures **[106]**.

As the literature reports so far, the most common precursors for the hydrothermal synthesis of xonotlite are silica, whether crystalline or amorphous, and lime **[22, 78, 100, 106, 111]**. Some other works reported the use of another kind of precursors such as $Na_2SiO_3 \cdot 9H_2O$ as silicon source and $Ca(NO_3)_2 \cdot 4H_2O$ or carbide slag as calcium source **[113, 114]**.

2.6. Technologies based on hydrothermal synthesis

Among the most common and well-known technologies that use hydrothermal conditions as well as other additional processing steps to produce calcium silicate products at industrial scale, these are the following: *stirred autoclave reactor*, prereaction-autoclaving (geltank called in this PhD), *casting*, *double autoclaving*, *Hatschek* and *Magnani*. Depending on the final application, the calcium silicate products can be manufactured in a wide bulk density range from around 150 Kg/m3 to 1.500 Kg/m3. To achieve the desired density is required to employ a specific technology since throughout these processes it is possible to control this parameter. **Figure 22** represents an outline by flow chart with different technological routes (A/B/C/D/E) for calcium silicate boards production.

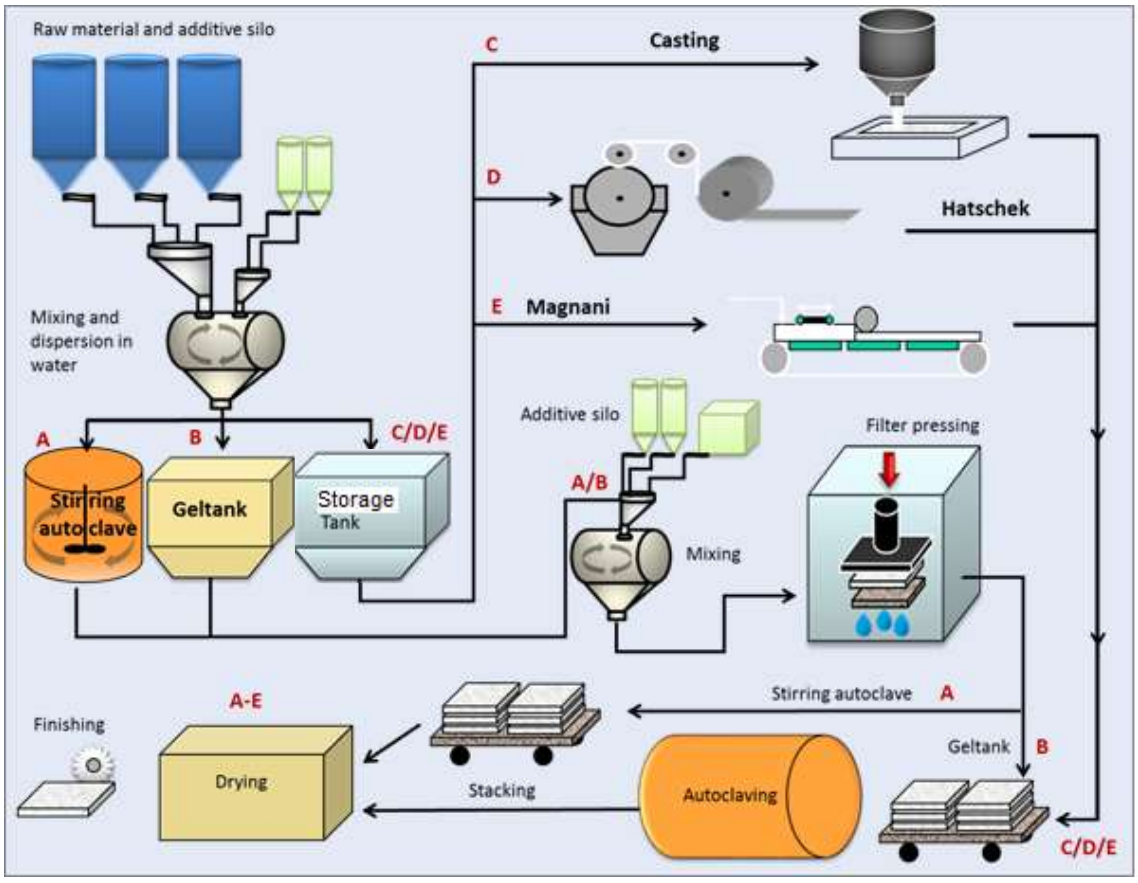

Figure 22. Flow diagram of calcium silicate boards process production.

One of the conventional technologies mentioned above to produce calcium silicate boards with low and medium bulk densities (150-550 Kg/m^3) that has been largely used since last decades until today is the stirred autoclave reactor. This method consists of dynamic hydrothermal synthesis of calcium silicate hydrates, especially in the formation of porous spherical xonotlite particles. This process has the great advantage of possible control of the shape and size of xonotlite crystals formed during the reaction. An aqueous mixture of lime and silica is treated in a vertical autoclave with stirring that operates at a temperature over 200ºC and a pressure of 2 MPa approximately. Then, the hydrothermal reaction takes place inside of the autoclave and finally after a determined period, a slurry composed basically of xonotlite as the majority crystalline phase and other CSH phases is formed as more or less spherical composite particles. Stirring during hydrothermal synthesis plays an important role in the formation of those sphere-like xonotlite particles and it is a key parameter for the successful synthesis of them. **Figure 23** shows a stirred vertical autoclave for dynamic hydrothermal process. Once the xonotlite slurry is obtained, it is usually mixed with additives such as reinforcement organic fibres, clays, Portland cement, fillers, etc. which possess specific functions. This process follows with a filter pressing to form a board and later, it is cured and dried in an oven (as seen in **Figure 22**). SiO_2

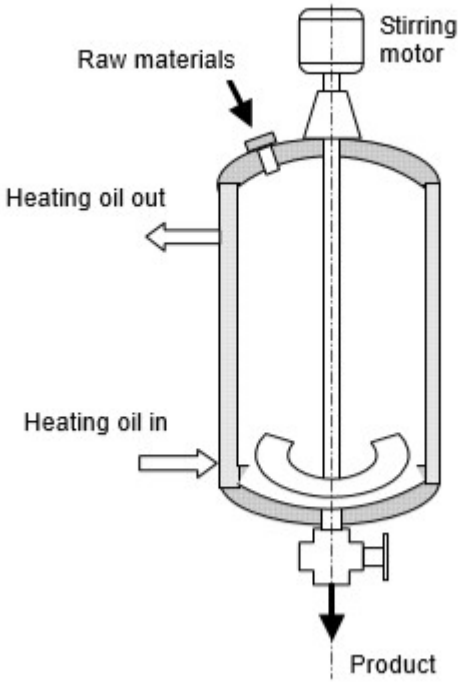

Figure 23. Vertical autoclave with agitation system for dynamic hydrothermal process.

Other technology listed above that is still under development, although it is already being used at industrial level by some manufacturers of calcium silicates outside Etex group, is the so-called 'Geltank' by us or a technology based on C-S-H gel pre-reaction and autoclaving a pressed C-S-H gel containing board. In this thesis, Geltank process is broadly studied at laboratory due to the interest of Etex. This technology offers the possibility to produce lightweight calcium silicate boards with a density ranging from 150 to 750 Kg/m^3. This method takes place in three steps: the first one is the pre-reaction of silica and quick lime in water (50-100ºC,30-60 min), forming a specific C-S-H gel; the second step is the addition of organic fibres and other additives to the gel and the filter pressing of this slurry to obtain boards; and the third step is the steam assisted curing of these boards in a horizontal or vertical autoclave. Throughout the hydrothermal treatment of the boards composed mainly of C-S-H gel, this crystallizes into xonotlite and tobermorite (if crystalline is used initially).

To produce C-S-H gel in pressure-less conditions, it is necessary to use a reactive amorphous silica in the initial composition. In this technology the consumption of water can be reduced considerably being an advantage from an economic and sustainable point of view. **Figure 24** shows an industrial horizontal autoclave for the hydrothermal curing of calcium silicate boards and other building materials such fibre cement boards.

Figure 24. Images of the exterior and interior parts of a horizontal industrial autoclave.

Casting is also a conventional technology to manufacture calcium silicates, especially for low bulk densities. This method leads to the formation of large pores in the calcium silicate blocks or boards due to air inclusion during the casting process. The process is divided in the following three stages. The first one consists of the mixing of starting raw materials (silica sources, lime source, glass fibers, cellulose fibers and clay. The slurry is then poured into a mold and finally, it is cured in an autoclave. In the first step, a small amount of a very reactive type of amorphous silica (pyrogenic silica) is used to form a minimum amount of C-S-H gel that is required to make the mixture more viscous and avoid sedimentation. Besides, other particular aspect in this technology to consider is the use of glass fibers. They are consumed during the hydrothermal curing, thereupon these fibers act as channels through which water vapor and air flow get away. However, there is a big number of large pores formed that are trapped inside the matrix of these calcium silicate products. This results in a higher thermal conductivity and less good mechanical properties. Casting is a very simple technology with the advantages of a low investment cost and the chance to make boards or blocks with a wide range of thickness.

Double autoclaving is a sophisticated technology that combines stirring autoclave (route A, **Figure 22**) and a second autoclaving (final stage of route B, **Figure 22**). This technology was developed in order to manufacture calcium silicate-based products with densities ranging from 450 up to 800 Kg/m^3 and with specific mechanical properties. The process is a mixture of dynamic and static hydrothermal treatment consisting of the following steps: first, spherical xonotlite particles are synthesized by stirred autoclave reactor; thus, the slurry obtained that is composed mainly of xonotlite particles is mixed with sand, Portland cement, organic fibers and additives. Then, the aqueous mixture is filter-pressed obtaining a green board which is cured at low temperature in a kiln to form boards with a certain green strength. Later, this board is hydrothermally treated in a horizontal autoclave. What is different from the rest of technologies described so far, is that there is a second hydrothermal reaction where nanocrystalline C-S-H phases are converted into tobermorite crystals and these bind the xonotlite particles forming a compact matrix. In this way, a product with high mechanical properties is obtained and the products formed have high elastic modulus and better interlaminar strength than boards formed via the stirred reactor technology.

On the other hand, there are also other technologies to manufacture calcium silicate-based products such as Hatschek and Magnani processes as indicated in **Figure 22**. These technologies use specific machinery for processing the lime-silica aqueous slurry mixed with fibers, fillers or other additives and transforming it into thin layers that are then rolled upon on a cylinder until the desired thickness is obtained that are later cured and possibly also hydrothermally treated.

The Hatschek machine was first developed by Ludwig Hatschek, an Austrian engineer that pre-formed asbestos-cement products in the 1890's using this technology for the first time **[115]**. This machine consists of a wet transfer roller (see **Figure 25**) that is still used in the same basic form nowadays although the new Hatschek machines are much more productive than the early models. An aqueous slurry of calcium hydroxide, silica, cellulose fibers, and other additives, about 5-10% solids by weight, is supplied to a holding tank which contains a number of rotating screen cylinders. These cylinders pick up the solid matter draining through a continuously rotating porous roller, depositing a layer of wet solids on the surface, which are then picked up by a continuous loop of permeable mat called a 'felt'. This felt with the layer of green fiber reinforced lime-silica mixture

attached, passes over a vacuum dewatering machined, where most of the remaining water is sucked out, consolidating the wet solids into a dense but flexible green-sheet product. Several layers are assembled until a given board thickness is reached. It is then cut to size and further shaped if required (e.g., into corrugated forms), before curing (air-cured products) or curing and autoclaving **[116, 117]**.

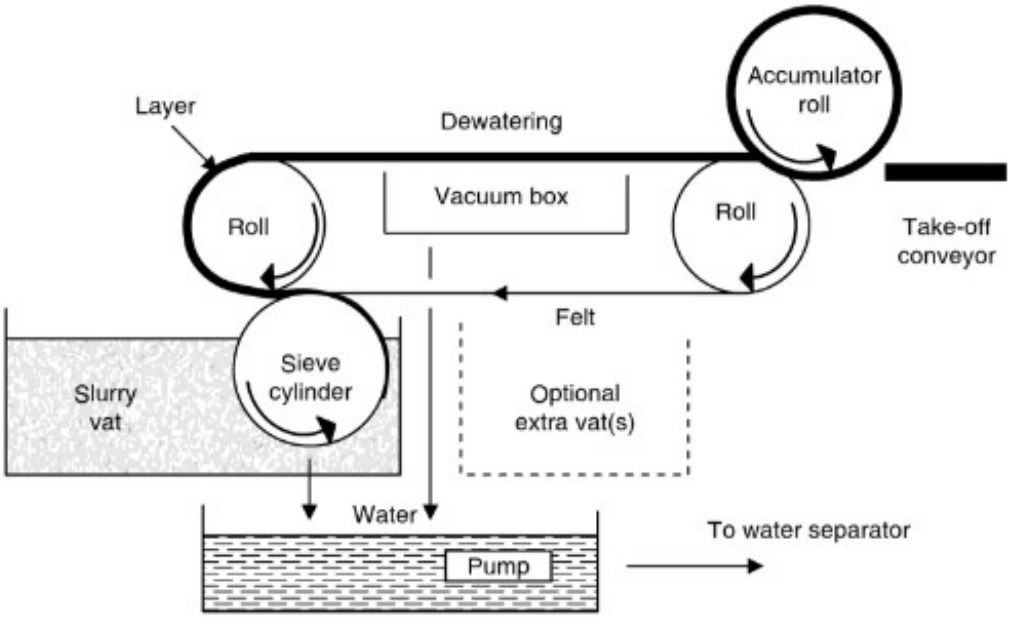

Figure 25. Scheme of the Hatschek process.

The Magnani is also used to prepare boards of calcium silicate panels. About 50% solids of the thick slurry materials of this process can flow equivalently and directly onto a felt conveyor (it distributes homogeneously the slurry) which goes through numerous vacuum boxes to dewater the formulation. Then, the board is compressed by a shaped roller **[118]**. After that, it is cut to a desired size, and later cured hydrothermally (see **Figure 22**).

CHAPTER 3

EXPERIMENTAL

CHAPTER 3. Experimental

3.1. Materials

For the hydrothermal synthesis of hydrated calcium silicates, lime, silica and water were the key raw materials. Different types of synthetic silica and lime were used for the preparation of Ca-silicates, depending on the specific technology. In addition, several additives with specific functionality were selected and integrated in the final products.

3.1.1. Materials for Geltank technology

'Geltank' technology was applied to manufacture low and medium density calcium silicate boards ranging from ca. 250 to 500 Kg/m^3 at laboratory scale. To prepare these boards the components of the formulation were *quicklime*, *quartz*, silica fume and *cellulose fibres along with deionized water*. Whereas in some specific trials, several mineral fillers such as wollastonite, exfoliated vermiculite and expanded perlite were added to the slurry formed before the hydrothermal treatment. The detailed list of materials used in Geltank technology is given in **Table 4.**

The 2 main ingredients for the synthesis of C-S-H-gel are lime and amorphous silica. As lime, a reactive lime was used that was in an initial step converted into calcium hydroxide $Ca(OH)_2$. As amorphous SiO_2, eight commercial grades of silica fume were purchased from different suppliers to study different relevant parameters during this experimental methodology. On the other hand, as crystalline SiO_2 source, an industrial type of quartz with small particle size was also used at the starting formulation. Although this raw material did not practically react during the C-S-H gel formation due to its low solubility at lower temperature, it contributed later as seeding agent and reactant, during the hydrothermal conversion of C-S-H into xonotlite or xonotlite/tobermorite. In the second step of Geltank methodology, the filter pressing of C-S-H gel admixture, cellulose fibres were added to the viscous slurry before moulding. They were used as reinforcement component to enhance the flexural strength of the calcium silicate matrix slabs. Moreover, a few functional fillers were chosen in some experimental batches. Three different types of mineral additives were evaluated to influence the mechanical and thermal properties of the end-products, being wollastonite, exfoliated vermiculite and expanded perlite.

Material	Trade name	Supplier	Description
Lime	Fassa quicklime	UNICALCE S.P.A.	Very reactive (quicklime) calcium oxide - CaO
Silica fume	Elkem Microsilia® 940-U	Elkem Silicon Materials	Undensified dry amorphous silica - (SiO_2). Grey powder.
Silica fume	Microwhite®	Elkem Silicon Materials	High purity dry amorphous silica - (SiO_2). White powder
Silica fume	Elkem Microsilia® 971-U	Elkem Silicon Materials	Undensified dry amorphous silica - (SiO_2). Grey powder
Silica fume	Emsac® 500	Elkem Silicon Materials	Aqueous suspension of amorphous silica - (SiO_2).
Silica fume	Elkem Microsilica® slurry	Elkem Silicon Materials	Aqueous suspension of amorphous silica fume - (SiO_2).
Silica fume	Mikrosilika Trade Light	Mikrosilika Trade Natalia Kurcz	Dry amorphous silica - (SiO_2). Light grey powder.
Silica fume	Mikrosilika Trade Dark	Mikrosilika Trade Natalia Kurcz	Dry amorphous silica - (SiO_2). Dark grey powder.
Silica fume	Microsilia Light Grey	CETA Sp.J.	Dry amorphous silica - (SiO_2). Light grey powder.
Quartz	Silverbond® M500	Sibelco	Crystalline silica - (SiO_2). White powder.
Cellulose fibres	K25®	Oji Fibre Solutions	Unbleached wood pulp
Wollastonite	CASIFLUX® F75	Sibelco	Acicular wollastonite, naturally occurring calcium silicate – ($CaSiO_3$)
Vermiculite	Vermiculite Superfine	Dupré Minerals Ltd.	Exfoliated vermiculite. Magnesium aluminium iron silicate - $(Mg,Fe^{2+},Fe^{3+})_3[(Al,Si)_4O_{10}](OH)_2 \cdot 4H_2O$
Perlite	DICALITE® Cryo 4 Expanded Perlite	Dicalite Europe	Amorphous volcanic silicate with a high-water content.

Table 5. Raw materials and additives selected in Geltank technology.

3.1.2 Materials used in Stirred Autoclave Reactor technology

To produce the calcium silicate boards by means of *Stirred Autoclave Reactor technology*, firstly xonotlite slurry is synthesized. Afterwards, this slurry is mixed with a set of different functional additives and the consequent blend is processed for making calcium silicate slabs. Two existing Promat products were chosen to modify their properties and improve them by means of new formulations. These products were PROMATECT-L500 and PROMATECT-LS.

Material	Trade name	Supplier	Description
Gypsum	Rookgasontzwaveling(s)gips	VLIEGASUNIE	Dihydrate calcium sulfate - $CaSO_4 \cdot 2H_2O$
Lime	Lime Q 0/63µ los	L'Hoist	Calcium oxide - CaO
Calcium hydroxide	Calcium hydroxide-ACS reagent	Sigma-Aldrich	Calcium hydroxide – $Ca(OH)_2$
Quartz	Silverbond® M300	Sibelco	Crystalline silica – SiO_2. White powder.
Quartz	Silverbond® M400	Sibelco	Crystalline silica – SiO_2. White powder.
Quartz	Silverbond® M500	Sibelco	Crystalline silica – SiO_2. White powder.
Quartz	Silverbond® M8	Sibelco	Crystalline silica – SiO_2. White powder.
Silica fume	Elkem Microsilia® 940-U	Elkem Silicon Materials	Undensified dry amorphous silica. Grey powder.
Silica fume	Elkem Microsilia® slurry	Elkem Silicon Materials	Aqueous suspension of amorphous silica fume.

Table 6. Raw materials selected in Stirred reactor autoclave technology to produce xonotlite slurry.

On one side, the raw materials used for the xonotlite slurry preparation are shown in **Table 5**. They were gypsum, lime, sand and silica fume and water. Gypsum ($Ca_2SO_4 \cdot 2H_2O$) was used as inorganic chemical retardant to control the calcium hydroxide crystals growing during slaking of lime that occurs before the hydrothermal reaction inside the autoclave. The lime quality used for the stirred reactor technology is a lime with lower reactivity comparing with the quicklime used in Geltank technology. This is reflected by the higher T60-values (time to reach 60°C in specific conditions: 1.5-4' while the T60 for the Gel tank technology has t60 values below 1.5'). The siliceous materials used as precursors were several commercial grades of sand with different particle size and two types of commercial silica fume in powder and aqueous suspension. Different kinds of silica were tested was to develop a better understanding of the reaction mechanism and to investigate the effects on the xonotlite reaction and on the final properties of calcium silicate boards. On the other side, a list of different additives with specific functionality that compose PPRMATECT-L500 and PROMATECT-LS boards is presented in Table 6. Some specific new additives were tested to improve the performance of the PROMATECT-products.

Special bentonites are used in the recipe of PROMATECT L-500 as well as in PROMATECT-LS. This clay improves the mechanical properties of these two products at room temperature and it increases the resistance at high temperature when a calcium silicate board is exposed to fire. Again, organic fibres were included as in Geltank products. They play a very important role in the fracture toughness of the end-product. Depending on the type of product made, different commercial fibres were used: two kinds of cellulose fibres (bleached and unbleached wood kraft pulp) and one kind of glass fibres The used E-CR glass fibres are boron-free alumina-lime silicate with less than 1% w/w alkali oxides, and high chemical and high acid resistance. As hydraulic binder included in the aqueous admixture, two kinds of industrial cement were considered for every product. Ordinary Portland Cement CEM-I was used to make PROMATECT L-500 samples. On the other hand, an alumina cement is used for the PROMATECT LS preparation. It contains approximately 40% of alumina and is mainly composed of calcium aluminate phases. In case of PROMATECT-L500, OPC is used to bind bentonite clay into larger particles and enhance the filtering properties of the mixture. However, the alumina cement in addition to playing the same role as Portland cement, is also used to have additional binder formation during the curing stage of calcium silicate boards after pressing. This cement is partially hydrated, then partially forms ettringite in situ acting as additional binder. The main function of ettringite in PROMATECT-LS is to reduce the transfer heat in the product applied in passive fire protection applications that concern mostly ventilation and smoke extraction ducts. Several synthetic minerals with potential fire-retardant benefits, that is, with endothermic capacity, were selected to be used in the formulation of this product. They are calcite, gypsum, hydrotalcite, aluminium hydroxide, zeolite, magnesium hydroxide, silica gel and nesquehonite (see **Table 6**). PROMATECT-LS was already formulated in the past including ettringite as an endotherm agent with low thermal conductivity (k) and high heat absorption capacity. But in this research work, we wanted to find alternatives to replace ettringite as this additive makes the drying of the boards more difficult. In case of PROMATECT-L500 the incorporation of rutile as opacifier in the mixture was tested for decreasing the radiation part of the heat transfer, mainly for higher temperature applications such as protection of steel structures. It must be remarked that for the experimental followed at the geochemistry laboratory of ISTerre, calcium hydroxide was used at the initial recipe replacing the lime as calcium silica source in the hydrothermal reaction of xonotlite. By this reason, this raw material is also included in the list given by **Table 5**.

Material	Trade name	Supplier	Description
Bentonite	Colclay D90	Ankerpoort NV	Aluminium phyllosilicate clay
Cellulose fibres	K25®	Oji Fibre Solutions	Unbleached wood kraft pulp
Cellulose fibres	Botnia Nordic Pine KMI	Metsä Fibre Oy	Bleached softwood kraft pulp
Glass fibres	WS 6050-16W /wet chopped strand	Binani 3B	E-CR glass fibres. Boron-free alumina-lime silicate
Cement	CBR Cement CEM-I	Heidelberg Cement Group	Ordinary Portland cement
Cement	CIMENT FONDU® LAFARGE	Lafarge Calcium Aluminates Inc	Alumina cement
Ettringite	Non-commercial / Produced by Promat International	Promat International	Hydrous calcium aluminium sulfate mineral - $Ca_6Al_2(SO_4)_3(OH)_{12}\cdot 26H_2O$
Calcite	Calcium carbonate	AppliChem GmbH	Calcium carbonate – $CaCO_3$. White powder.
Gypsum	Rookgasontzwaveling(s)gips	VLIEGASUNIE	Dihydrate calcium sulfate.
Hydrotalcite	Synthetic hydrotalcite	Sigma-Aldrich	Magnesium aluminium hydroxycarbonate – $CH_{16}Al_2Mg_6O_{19}\cdot 4H_2O$

Aluminium hydroxide	Aluminium hydroxide SH150	Sigma-Aldrich	$Al(OH)_3$ – white powder with finer particle size
Aluminium hydroxide	Aluminium hydroxide SH300	Sigma-Aldrich	Al(OH)3 – white powder with coarser particle size
Zeolite	Zeolite Y	ZEOCHEM	Crystalline alumina-silicate (zeolite). High Al_2O_3/SiO_2 ratio, white powder.
Magnesium hydroxide	Magnesium hydroxide Ph. Eur.	VWR	Magnesium hydroxide - $Mg(OH)_2$. White powder.
Silica gel	Silica gel with indicator (orange gel)	Sigma-Aldrich Company Ltd.	Amorphous and porous form of silicon dioxide. Soft orange transparent coarse granulates.
Silica gel	Davisil grade 633	Sigma-Aldrich Company Ltd.	Amorphous and porous form of silicon dioxide. Soft orange transparent coarse granulates.
Nesquehonite	Non-commercial / Supplied by ISTerre	ISTerre – University of Grenoble Alpes	Magnesium carbonate trihydrate – $MgCO_3 \cdot 3H_2O$. White solid powder.
Rutile	Titanium (IV) oxide	Sigma-Aldrich Company Ltd.	Titanium dioxide – TiO_2. White solid powder.

Table 7. Additives selected in Stirred reactor autoclave technology to produce Promatect-L500 and Promatect-LS.

3.1.3 Materials used in Double Autoclaving technology

A special combination of raw materials, intermediate products and additives were used to produce a quartz-free version of PROMATECT-MLT boards. All the materials selected for the experiments performed are collected in **Table 7**.

Material	Trade name	Supplier	Description
Cement	CBR Cement CEM-I	Heidelberg Cement Group	Ordinary Portland cement
Quartz	Silverbond® M400	Sibelco	Crystalline silica – SiO_2. White powder.
Quartz	Silverbond® M500	Sibelco	Crystalline silica – SiO_2. White powder.
Silica fume	Elkem Microsilia® 940-U	Elkem Silicon Materials	Undensified dry amorphous silica. Grey powder.
Silica fume	Elkem Microsilia® slurry	Elkem Silicon Materials	Aqueous suspension of amorphous silica fume.
Lime	Lime Q 0/63µ los	L'Hoist	Calcium oxide - CaO
Lime	Cal 85	Carmeuse	Calcium oxide - CaO
Wollastonite	Kemolit	Wolkem Industries Ltd	Calcium silicate – ($CaSiO_3$)
Vermiculite	Vermiculite Micron	Dupré Minerals Ltd.	Exfoliated vermiculite Magnesium aluminium iron silicate - $(Mg,Fe^{2+},Fe^{3+})_3[(Al,Si)_4O_{10}](OH)_2 \cdot 4H_2O$
Cellulose fibres	Botnia Nordic Pine $_{KMI}$	Metsä Fibre Oy	Bleached softwood kraft pulp
Glass fibres	WS 6050-16W /wet chopped strand	Binani 3B	E-CR glass fibres. Boron-free alumina-lime silicate
Aluminium hydroxide	ALOLT 01	MAGYAR ALUMÍNIUM	Aluminium hydroxide - $Al(OH)_3$. White powder with finer particle size.

Table 8. Additives selected in Double autoclaving technology to produce Promatect-MLT.

In the different MLT-formulations, spherical xonotlite particles were used to control the density of the end-product. Several types of xonotlite slurry were used for the different formulations proposed here. The standard one (see raw materials in previous section) and other xonotlite slurries prepared from similar recipe as the reference but adding small quantities of alkaline activators to favour the silica solubilisation to avoid residual quartz. Another common ingredient was OPC-cement. OPC works as a glue in the blend, linking

the spherical xonotlite particles during the curing process that is applied before the autoclaving process. Using the OPC-binding in the curing step, allows the MLT product to have enough green strength to avoid crack formation during the autoclaving process. Different sources of silica such as quartz and silica fume were tested. These grades of silica react with the $Ca(OH)_2$ formed when the OPC cement is hydrated, forming a C-S-H that converts into tobermorite during the hydrothermal process that leads to the end-product. In few trials, some grades of calcium oxide were used instead of OPC as Ca-source. In a couple of experiments, aluminium hydroxide was used as additive that chemically favours the tobermorite crystallization. The standard formulation includes wollastonite as mineral filler to enhance the thermal stability of the boards. Furthermore, cellulose fibres were included as mechanical reinforcement elements to the MLT boards. A commercial type of super fine exfoliated vermiculite was added to the admixture in a couple of experiments as mineral additive with the purpose of increasing the fracture toughness of the product. Finally, to complete the list of ingredients used in the range of formulations to make MLT boards, C-S-H gel synthesized by our own, was incorporated to the mix in several experiments for replacing partially the xonotlite slurry. This intermediate product was obtained through Geltank methodology as already explained in the text, but in this case using only Elkem Microsilica® 940-U as silica source, Fassa quicklime and the desired amount of demineralized water.

3.2 Methods

Low and medium density calcium silicate boards were made at laboratory scale applying *geltank*, *stirred autoclave reactor combined with filter pressing* and *double autoclaving technologies*. So, different experimental procedures were followed to prepare the corresponding samples. They are described in the next lines.

3.2.1. Geltank technology

Observing the **Figure 22** shown in Chapter 1, route B schematically represents the different stages of Geltank process. Summarizing, the process starts with the mixing of raw materials and formation of C-S-H gel, secondly the addition of additives (normally cellulose as reinforcement material only, and if needed mineral fillers, binding materials, organic compounds, etc.), followed by a filter pressing moulding to get shaped samples such as rectangular boards and finally, the hydrothermal curing of those boards in a horizontal autoclave. Here, the full procedure including all the steps is described. For this kind of technology reproduced at laboratory scale, our experimental roadmap is presented in **Figure 26**.

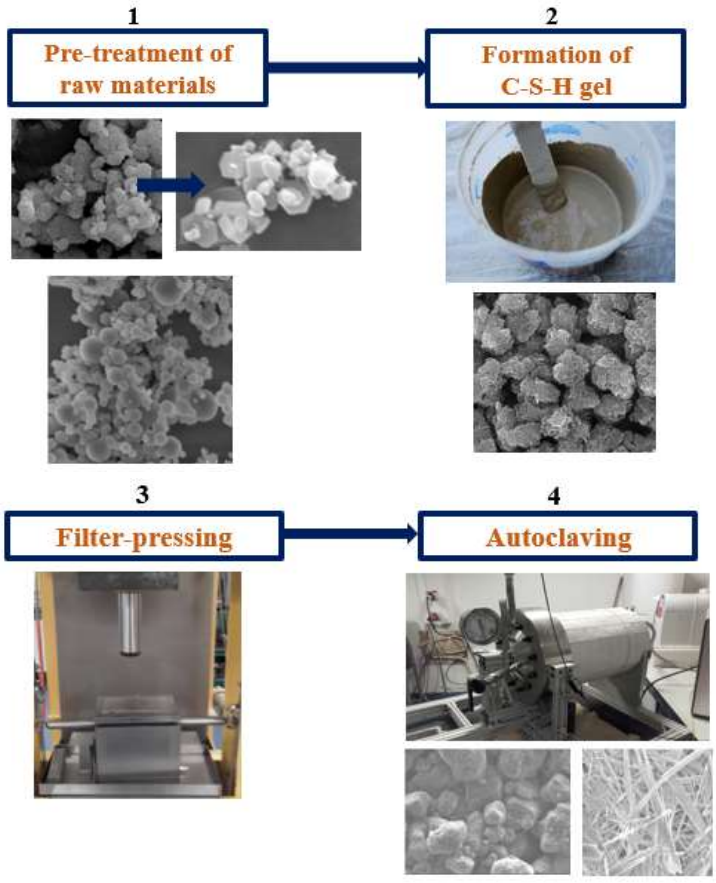

Figure 26. Scheme of the Geltank procedure at the laboratory.

In the first stage, the starting raw materials such as silica fume and lime are pre-treated before the mixing in a vessel reactor. The silica fume is subjected to mechanical high shearing in demineralized water solution because of its high degree of agglomeration. The target is to break up those agglomerated spherical particles, reduce the particle size, and consequently increasing the solubilization rate of this microsilica. A mechanical high shear mixer IKA T25 ULTRA TURRAX® was used as seen in **Figure 27**. After the corresponding dispersion time a silica slurry is obtained (see **Figure 27**) and ready to be used immediately.

Figure 27. Dispersion of silica fume in water by high shear mixing tool.

Parallel to the microsilica dispersion step, slaking of lime is done separately in three short steps with intermittent agitation to guarantee the proper hydration of calcium oxide and the growth of portlandite crystals as calcium source for the C-S-H gel pre-reaction. An alkaline milk-like slurry is obtained with a pH around 11-12 (see **Figure 28**).

Figure 28. Slaking of lime in demineralized water by stirring in a non-continuous way.

In the second stage, both calcium hydroxide-water slurry and microsilica-water dispersion are mixed in a water jacket glass vessel shown in **Figure 29**. An extra amount of demineralized water is also added into the vessel if desired to raise up the targeted w/s ratio, 7 for Geltank technology. In case that quartz as well as other additives such as mineral fillers are required, they are also added into the glass vessel. Meanwhile the water of the vessel's jacket is heated up to 90ºC (setting temperature) by a coupled electric heating water chamber and the aqueous mixture is heated by heat transfer and stirred at 500 rpm using a metallic agitator (see **Figure 29**). Once, the setting temperature is reached, being the slurry at approximately 80-82ºC, we leave the reaction stirring for 1 hour, but this time at lower speed (350 rpm) and keeping the temperature constant at 90ºC. During this time, the gelling occurs. A grey C-S-H gel-like with certain viscosity is formed. When gelling time is over, the heating and agitation are switched off. Then, the hot gel is transferred from the reactor to a big plastic bucket and cellulose fibers are added to be mixed and well dispersed in the gel using a metallic stirrer. In this way, the admixture is available for the next stage. SiO_2

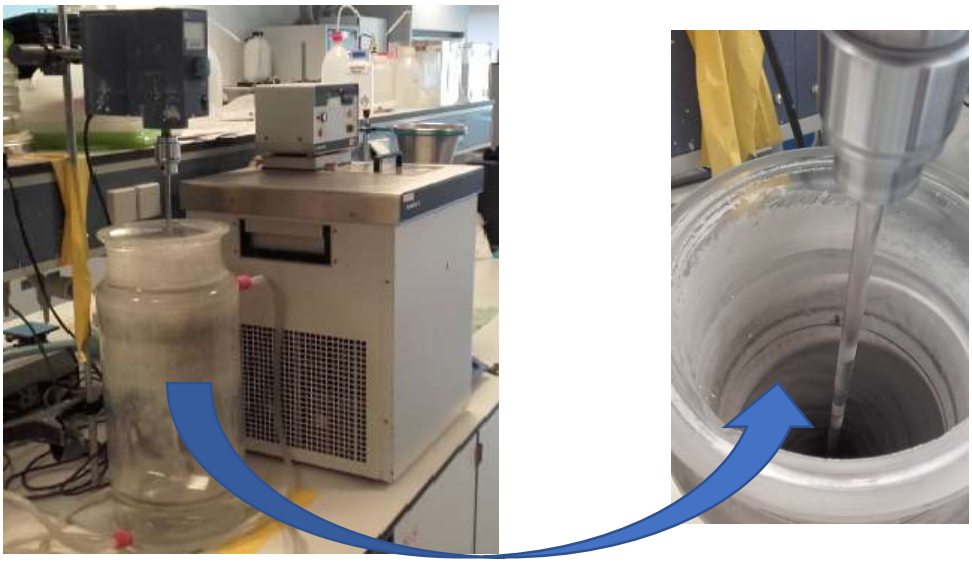

Figure 29. Water jacket reactor coupled with electric heating water chamber and a mechanical stirrer actioned by an electrical engine.

The third stage of Geltank procedure is based on filter pressing. So, the mixture of gel and fibers (plus mineral charges if applied) is poured into a metallic filter-type mold. Then, it is pressed using a ENERPAC hydraulic oil-press as shown in **Figure 30**. When pressing the slurry, a big quantity of water is evacuated through the filtering system of the mold. To avoid the loss of slurry through the inner holes of the mold, a metallic mesh along with a filter-paper is placed so that it does not the solid passing, only the water. A minimum pressing time is required as the board needs a minimum green strength to avoid cracking formation during autoclaving, keeping its integrity. When pressing time is finished, the board is demolded manually.

Figure 30. (Left) ENERPAC Hydraulic yellow press, (right) metallic mold with inner filtration holes.

The aspect of the so-called 'green boards', that is, the boards before hydrothermal curing, is observed in **Figure 31**. This grey colored platelet measures 150 x 75 x 20 mm and it still contains a high degree of moisture. For every batch of slurry prepared, three boards are normally pressed to have enough samples to calculate an average of properties after characterization.

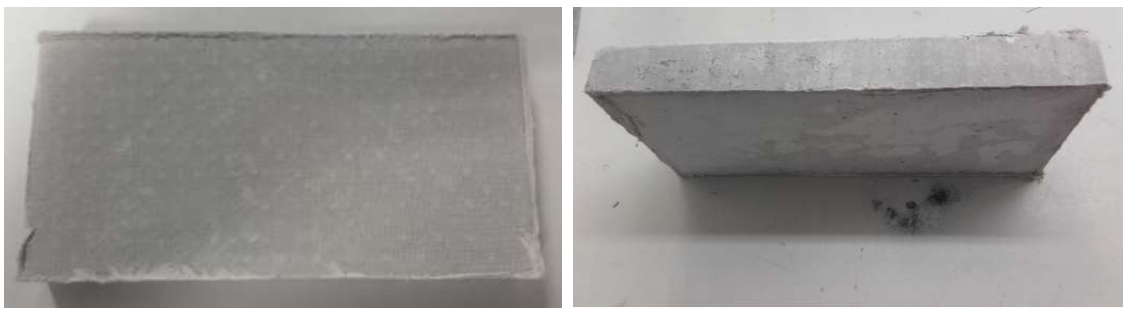

Figure 31. Calcium silicate board after filter pressing. (Left) Top view and (right) side-view.

According to **Figure 22**, the next and final stage of Gel tank process is the hardening of the green boards using a horizontal autoclave. Before the hydrothermal curing starts, the autoclave is preheated up to 80-90ºC. When this range of temperature is reached, the autoclave is opened, and the boards (three mostly) are placed inside this horizontal autoclave. They are stacked one on top of the other and separated by ceramic supports. As the autoclave is cylindrical, a metallic grill is put at the bottom holding the pile of plates (see **Figure 32**). The horizontal autoclave is tightly closed, to ensure properly the hydrothermal curing. This equipment was a tailored-made reactor by Parr Instrument Company. It is monitored by a Parr 4848M Reactor Controller and it is assisted by a Cellkraft water steam generator E-6000. The **Figure 33** shows a few pictures of the different components.

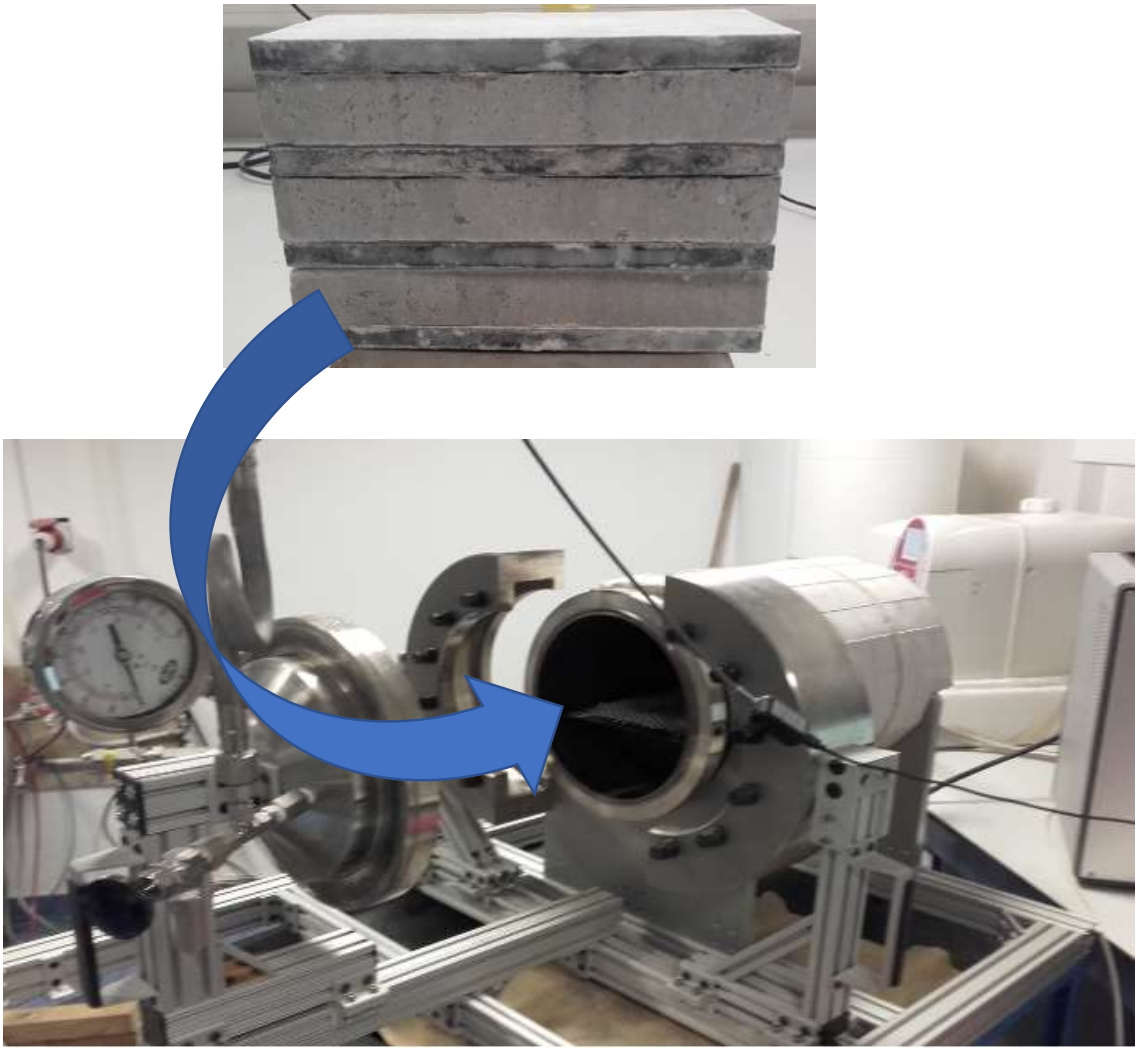

Figure 32. (Top picture) Stacked green calcium silicate boards; (bottom picture) opened horizontal autoclave.

The established autoclaving cycle for Geltank technology is divided in three steps. Initially, the heating ramp starting from 80-90ºC up to 180ºC which takes 7 hours. At 180ºC, the vapor pressure reached inside the autoclave is 12 bar. After, the dwell time step takes place for 7 hours keeping the temperature. Finally, the cooling ramp for 5 hours ends the hydrothermal treatment of the boards. For safety reasons, the autoclave shall not be opened until the temperature inside is not lower than 100ºC. When the autoclave is cool enough, it is opened carefully. The boards are taken out and dried at 105ºC until constant weight.

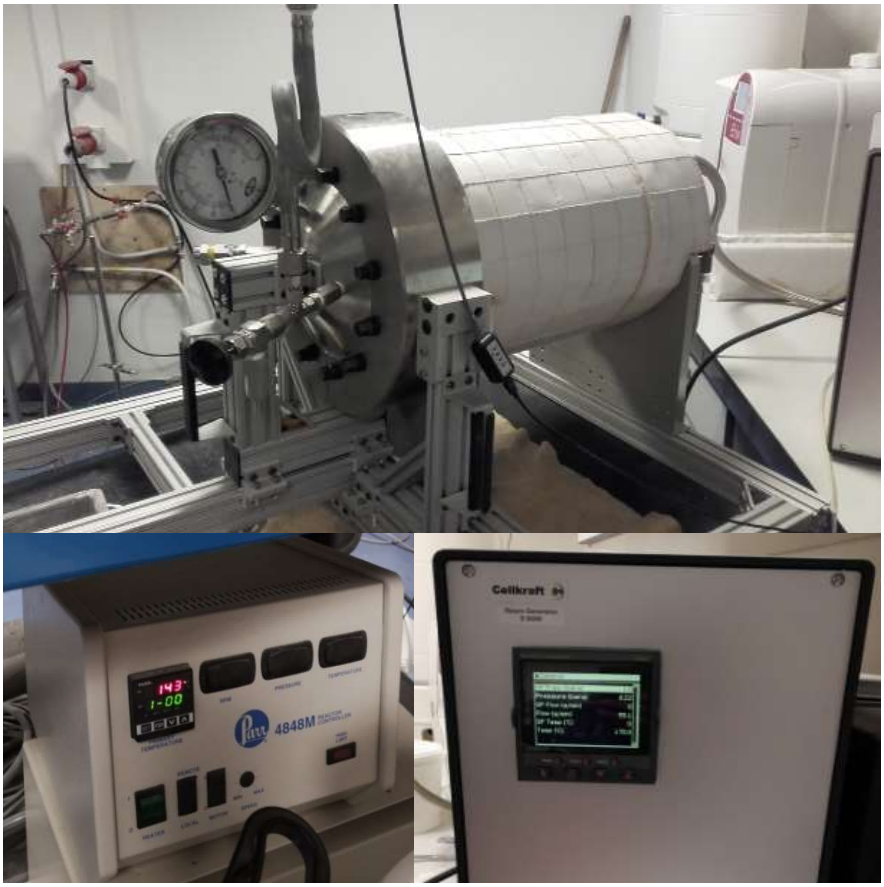

Figure 33. (Top picture) Horizontal autoclave assisted by steam; (left bottom picture) Reactor controller Parr 4848M; (right bottom picture) Steam generator Cellkraft E-6000.

3.2.2. Stirred autoclave reactor-filter pressing technology

Stirred autoclave reactor in combination with filter pressing is a mixed technology that is divided in several parts as represented by **Figure 22.** The pathway A (see **Figure 22**) starts first by pre-mixing of raw materials and after that by the formation of xonotlite slurry. Whilst the second part consists of mixing additives with xonotlite slurry, filter pressing this mixture to produce plates and finally, it ends by curing these boards. A short scheme about the experimental route is shown below in **Figure 34.**

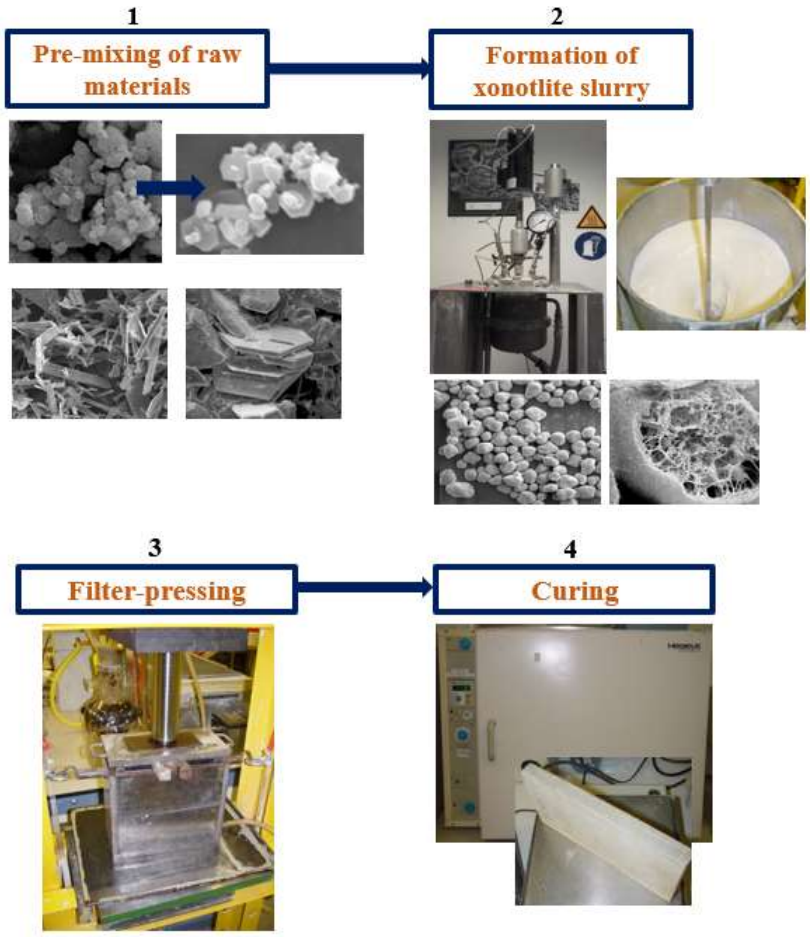

Figure 34. Scheme of the Stirred autoclave reactor-filter pressing procedure at the laboratory.

In the step number one of this experimental process, gypsum, lime, quartz and/or microsilica (in powder, or in aqueous suspension mechanically o chemically treated) as raw materials for xonotlite slurry formation are pre-mixed with demineralized water.

Figure 35 shows two images of these materials as well as the mixing bowl and the laboratory tools used. Here, the slaking of lime occurs, and it is chemically controlled by the presence of a small amount of gypsum. Thereby, calcium hydroxide is produced as calcium source in the aqueous solution to the synthesis of xonotlite spherical particles. On the other hand, depending on the initial recipe developed either one type of silica or another is added to this mixture. During the pre-mixing stage the quartz does not react, not even if silica fume is used because of the low temperature and atmospheric pressure conditions and short pre-mixing time. The reference formulation was designed to use quartz M400 as crystalline silica source for the hydrothermal reaction with calcium hydroxide. But other types of quartz, silica fume and even a combination of quartz and the silica fume were also included for new formulations.

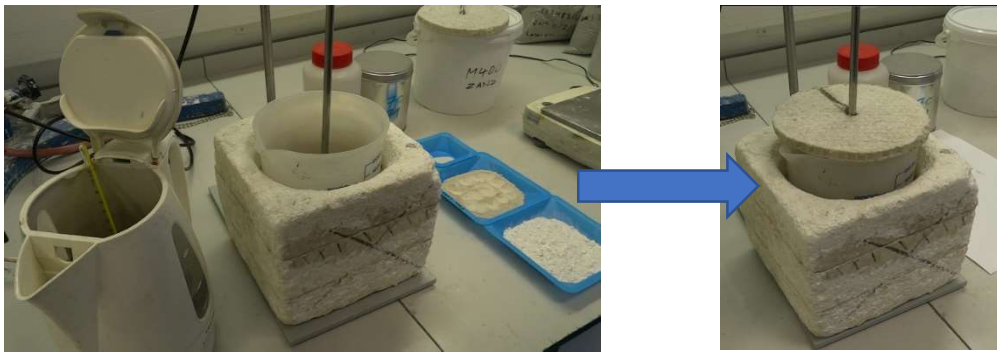

Figure 35. Pre-mixing of raw materials in a plastic bowl partially insulated by hand-made cork accessories.

In the step 2, prior to the hydrothermal dynamic reaction, the vertical stirred autoclave is preheated up to 80-90ºC. Once this range of temperature is reached, the autoclave is opened, the water-solid blend already pre-mixed is poured inside and extra amount of demineralized water is also added into the autoclave in order to guarantee the desired w/s ratio (10 for this technology) before the hydrothermal reaction starts. The autoclave is tightly closed, to ensure mainly the hydrothermal synthesis of xonotlite crystals as well as other crystalline C-S-H phases and to guarantee the safety. This vertical steel autoclave 3000 cm^3 capacity equipped with a metallic stirrer was tailored-made by HEL Ltd. A HUBER Unistat temperature control system is coupled to the autoclave for heating purposes. Unlike the horizontal reactor, the heat transfer fluid used in the vertical autoclave is oil in the mantle around the autoclave. Moreover, this stirred reactor is computer assisted by a specific-software developed by HEL Ltd. The setting of all the processing parameters is done by this IT tool. **Figure 36** shows a picture of the vertical autoclave accessories. Regarding to the autoclaving cycle, this is divided in three time-based steps. Firstly, the heating ramp starting from 80-90ºC up to 200ºC (17 bar or vapor pressure) which takes 2 hours. Then, the cycle follows with the dwell time which can vary from 1 to 4 hours (depending on the type of slurry studied). During this time, the temperature is kept constant. As third step, the cooling ramp for 2 hours. For safety

reasons, the autoclave cannot be opened until the temperature inside is not lower than 80ºC. When the autoclave is cool enough, the slurry is collected at the bottom of the reactor.

Figure 36. Vertical stirring autoclave reactor system at PRTC laboratory.

The third stage consists of filter pressing of a mixture depending on the product to be made (PROMATECT-L500 or PROMATECT-LS). The xonotlite slurry is well mixed by stirring together with extra water and the rest of additives (see **Table 6**) except cement in a first step. Whereas that in a second step, the cement is added to the mixture and well dispersed. The slurry is then poured into the metallic filter-type mold as observed in **Figure 37a** in order to be pressed using a ENERPAC hydraulic oil-press (see **Figure 30**). Once pressing time is over, the molded plate is removed manually from the mold (see **Figure37b)**. The PROMATECT-L500 and PROMATECT-LS-boards have the same dimensions as the Gel tank boards, being 150 x 75 x 20 mm. In the same way as Gel tank methodology, a set of three boards is normally pressed. The fourth stage for this methodology corresponds to the curing of plates at low temperature for a minimum number of hours. As cement is added, it is hydrated forming a binder in the matrix of these calcium silicate plates. For an optimal curing/hardening the plates are covered by a plastic bag and they are placed inside an oven at 50ºC for 12 hours. Last, when curing

stage is finished, the samples are dried until constant weight. The product PROMATECT-L500, is dried at 105ºC whilst the product PROMATECT-LS, as the samples contain endothermic compounds (ettringite in reference recipe, magnesium hydroxide, gypsum, etc.), they are dried at 60ºC in order to avoid decomposition of the endotherm additives.

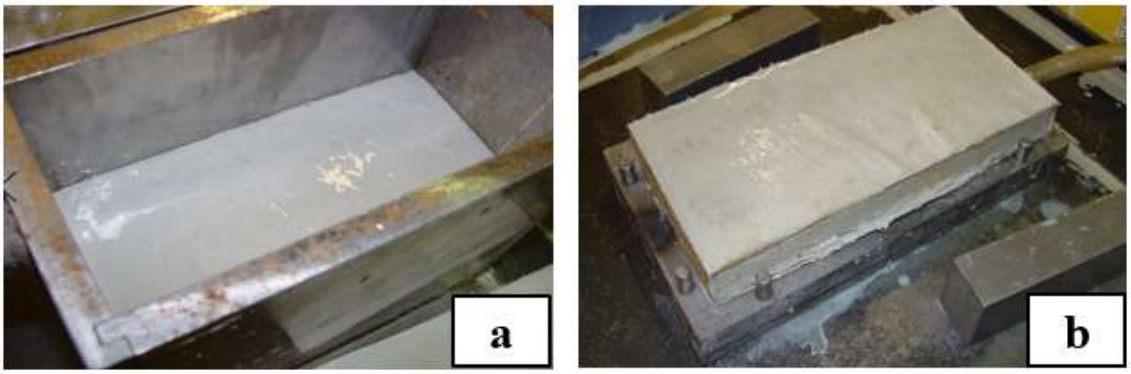

Figure 37. (a) Slurry mixture of Promatect-L500/Promatect-LS before filter pressing; (b) Promatect-L500/Promatect-LS plate after filter pressing.

Additionally, another set of experiments was carried out at the geochemistry group laboratories of the Institute of Earth Sciences, University Grenoble-Alpes (France) throughout a research collaboration. In order to do a further investigation on the formation on of early C-S-H stages and crystallization of xonotlite when using quartz or silica fume, a laboratory methodology of Professor Montes-Hernández (researcher of geochemistry group, ISTerre) was followed. The procedure is divided in three experimental steps which are pre-heating, removal of reactive gasses (CO_2 and O_2) and hydrothermal reaction of xonotlite slurry. The key raw materials used for the hydrothermal synthesis of xonotlite were calcium hydroxide, silica fume or quartz (depending on the reaction to be studied) and deionized water. To perform the reactions, an electrical heat jacketed stirred autoclave was utilized. Moreover, an argon gas supply unit was coupled to the autoclave, this gas was also employed to keep an inert atmosphere avoiding the maximum carbonation as possible. **Figure 38** shows in detail the hydrothermal reaction system assembled.

In the pre-heating stage, first an amount of demineralized water is added to the stirred autoclave. Then, the autoclave is closed, the heating is switched on and the stirrer is turned on at low speed. The setting temperature was 60ºC. At this temperature, the solubility (molar fraction) of CO_2 and O_2 is nearly 0, thereby it is easy to remove them later.

To minimize the carbonation phenomenon of portlandite ($Ca(OH)_2$) throughout the reaction, argon is injected to the autoclave (keeping the gas evacuation vale completely closed) until a certain safe pressure is reached. After closing properly all the valves that

connect the pressurized argon bottle and stirred autoclave system, the water-gas mixture is stirred for 24 hours at 60ºC.

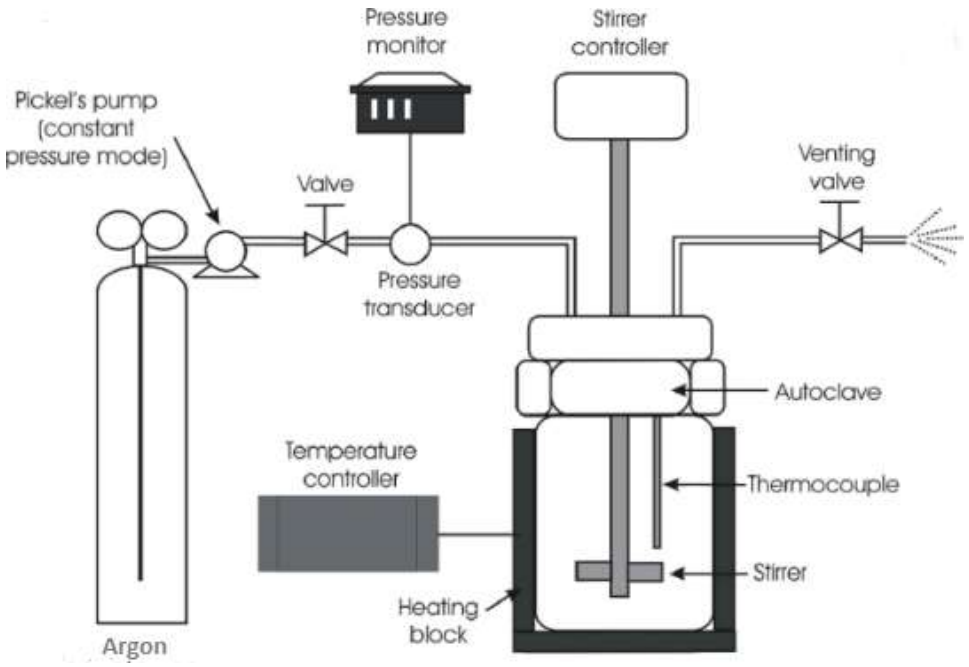

Figure 38. Scheme of the hydrothermal reaction system.

The next stage of this procedure is the removal of CO_2 and O_2 dissolved in the water and partially reminding in the autoclave's atmosphere. To purge these gases, again argon is injected. But this time, the gas evacuation vale of the autoclave is opened, allowing the flow of argon through the system. The argon stream carries the gases dissolved in the water and so, removing them from the reactor.

Finally, the raw materials (calcium hydroxide and silica) are added to the water (w/s ratio to 10) and mixed manually few seconds to avoid initial sedimentation). The reactor is well closed again, the stirring speed is fixed at 400 rpm and the autoclaving cycle is started. The cycle and operational conditions applied to the synthesis of xonotlite that were optimized in previous rehearsals are the following: heating ramp – 35 min / dwell time – (1/2/3/4 hours) / cooling ramp – 1h 30 min at 200ºC and 17 bar. To run the hydrothermal reactions, the apparatus utilized as mentioned above was an electrical heat jacketed stirred autoclave supplied by the company Parr Instruments company. It is a 4523 Bench Top Reactor, with a volume capacity of 1000 ml, made by titanium and equipped with an electric rotor that drives a mechanical agitation system of two set of propellers (some placed in a higher position and other lower). The reactor is also equipped with a heating and stirring speed controller Parr 4848M (see **Figure 39**).

When hydrothermal reaction is over, the slurry is recovered. Depending on the analytical technique applied to characterize this product, the slurry is treated in one way or another. As liquid suspension, some aliquots are taken, and they are cooled down at room temperature in plastic test tubes hermetically closed. Whilst a powder is desired, the slurry is left to be sedimented 24 hours in a glass beaker at room temperature. After that, the supernatant is separated from the sedimented solid, and the latter is dried at 80ºC for 1 day. The dried solid is manually crushed getting a fine powder to be characterized.

Figure 39. Stirring autoclave reactor system at ISTerre laboratory.

3.2.3. Double autoclaving technology

The experimental methodology applied to prepare PROMATECT-MLT plates via Double or Post autoclaving combines different stages of the previous methods detailed above. The stages are formation of xonotlite slurry by stirred autoclave, filter pressing of a cementitious-based mixture, curing of the pressed boards formed and autoclaving of these boards. **Figure 38** gives an overview of the methodology with its main stages.

Figure 40. Scheme of the Stirred autoclave reactor-filter pressing procedure at the laboratory.

For the Double autoclaving process different xonotlite types were used: standard xonotlite slurry, xonotlite with added KOH in the formulation to improve the quartz-dissolution and xonotlite with a reduced amount of gypsum in the slaking process to make lighter xonotlite particles. Concerning the autoclaving cycle for these xonotlite slurries hydrothermally formed, it is 2 hours -ramp time/4 hours – dwell time/2hours – cooling time at 17 bar. The next step is the mixing of xonotlite slurry with the additives according

to the established formulation for every batch of samples (see the list of materials/additives in **Tab. 7**). After this intermediate step, the filter pressing of the cementitious admixture is performed. The following is the curing the moulded boards at the same conditions as for PROMATECT-L500 and PROMATECT-LS samples (50ºC in a plastic bag for 12 hours). After the curing, the boards are hydrothermally treated using the same horizontal autoclave as in Geltank procedure. Although the autoclaving cycle is modified for PROMATECT-MLT boards, being 4 hours -ramp time/9 hours – dwell time/4 hours – cooling time at 12 bar (180ºC). Finally, the autoclaved boards are dried at 105ºC for 24 hours.

3.3. Characterization techniques

To determine the chemical, physical and mechanical properties of calcium silicate-based materials produced by the experimental methods in this investigation, a series of basic and advanced laboratory techniques as well as standardized mechanical and thermal tests were used. There is a large list of analytical techniques for the analysis of building materials, especially cementitious materials. Among the most important techniques stand out x-ray diffraction, thermal analysis, microscopy (optical, SEM, TEM), particle size distribution, surface area measurement, spectroscopy techniques (Infra-Red, NMR...), Mercury Intrusion Porosimetry, etc. But also, it is necessary to characterize these materials in terms of processability, thermal and mechanical performance as they are addressed to resist high temperature conditions. Therefore, the use of specific testing (flexural strength test, fire resistance, shrinkage) to characterize the materials from a mechanical and thermal point of view will allow us to know better the material and understand its strengths and weaknesses. This part of the document is focused on the techniques and equipments of measurement that were used to obtain the most relevant parameters about the quality of calcium silicates.

3.3.1. X-Ray Diffraction

X-ray diffraction (XRD) is one of the most widely used technique for the identification of unknown crystalline materials (minerals, inorganic compounds, etc). in cement chemistry. It is a rapid analytical tool primarily utilized to determine the crystalline phases of a material. Besides, this technique can provide information on unit cell dimensions and preferred orientation of certain planes. Crystals of a molecule or a compound are regular arrays of atoms, and x-rays can be considered waves of electromagnetic radiation. Atoms scatter x-ray waves, primarily through the electrons of the atoms. Thereupon, an x-ray striking an electron produces secondary spherical waves emanating from the electron. This phenomenon is **known** as elastic scattering, and the electron is called as scatterer **[119, 120]**. A regular array of scatterers gives a regular array of spherical waves. Although these waves cancel one another out in most directions through destructive interference, they add constructively in a few specific directions, determined by Bragg's law:

$$2d\sin\theta = n\lambda$$

Here d is the spacing between diffracting planes, θ is the incident angles, n is any integer, and λ is the wavelength of the beam (see **Figure 41**). These specific directions appear as spots on the diffraction pattern called *reflections*. Accordingly, x-ray diffraction results

from an electromagnetic wave (the x-ray) impinging on a regular array of scatterers (the repeating arrangement of atoms within the crystals). X-rays are used to provide the diffraction pattern due to their wavelength λ is typically the same order of magnitude (1-100 Å) as the spacing d between planes in the crystal. In principle, any wave impinging on a regular array of scatterers produces diffraction. To produce significant diffraction, the spacing between the scatterers and the wavelength of the impinging wave should be similar in size.

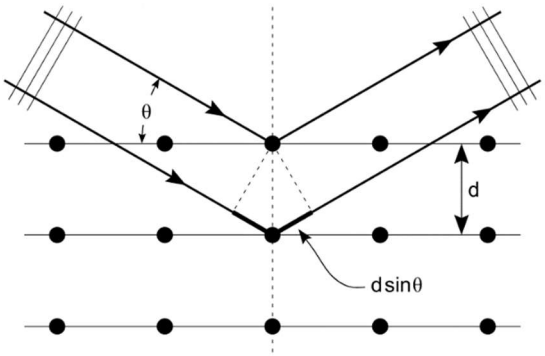

Figure 41. Bragg diffraction from a cubic crystal lattice. Plane waves incident on a crystal lattice at angle $\boldsymbol{\theta}$ are partially reflected by successive parallel crystal planes of spacing $\boldsymbol{d}$. The superposed reflected waves interfere constructively as long as the Bragg condition $\boldsymbol{2dsin\theta = n\lambda}$ is satisfied **[119, 120]**.

Quantitative phase analysis of x-ray powder diffraction data using Rietveld Refinement Quantitative Analysis is a powerful method for determining the quantities of crystalline and amorphous components in multiphase mixtures. Rietveld's method relies on the simple relationship:

$$W_p = S_p(ZMV)_p / \sum_{i=1}^{n} S_i(ZMV)_i$$

where W is the relative weight fraction of phase p in a mixture of n phases, and S, Z, M, and V are, respectively, the Rietveld scale factor, the number of formula units per cell, the mass of the formula unit (in atomic mass units) and the unit cell volume (in Å3) **[121]**.

In this investigation, two x-ray diffractometers were used to identify the crystalline phases of the samples prepared. They were both same equipments, although using different accessories. The measuring conditions slightly differ from one to another (see **Tab. 8**). One diffractometer at PRTC (Tisselt, Belgium) was a Bruker D8 Advance equipped with a LYNXEYE XE-T Si solid state detector and an automatic sampler. DIFFRAC EVA software provided by a specific library for inorganic compounds was employed to analyse the spectra obtained. When this apparatus was used the analyses were carried out for powder samples. Whereas that at ISTerre (Univ. of Grenoble-Alpes, France), the XRD

pattern were recorded with a Bruker D8 Advance equipped with a SolXE Si solid state detector from Baltic Scientific Instruments and an automatic sampler. Here, the samples were measured in wet conditions.

Location	PRTC - Tisselt	ISTerre -Grenoble
Diffractometer	Bruker D8 Advance	Bruker Axs D8
Goniometer	Vertical θ-θ. Equipped with rotating sample holder, capillary, controlled environment chamber	Vertical θ-θ. Equipped with rotating sample holder, capillary, controlled environment chamber
Radiation	$CuK_{\alpha 1}$, λ = 1.5406 Å	$CuK_{\alpha 1}$, λ = 1.5406 Å
Generator power	40kV/40mA	40kV/40mA
Range (deg)	From 4 to 50	From 5 to 90
Step Size (deg)	0.020	0.026
Step Time (sec)	4	3
Divergence Slit (mm)	0.6	0.6
Reception slit (mm)	0.2	0.2
Soller Slit (deg)	2.5	2.5
Detector Energy, Window	8.05 keV, <350 eV	8.05 keV, <350 eV

Table 9. Measurement specifications of the x-ray diffractometers

Furthermore, a quantitative x-ray diffraction analysis by Rietveld Refinement method was done using a non-linear least squares approach to refine a theoretical line which matches with the experimental one. It was performed with the Bruker Infractal[ass] TOPAS 4.2 software using Rutile (TiO_2) as an internal standard. A known amount of a standard needs to be added so that the software program can calculate the wt% of the present phases. At the PRTC, this is done by adding 0.1 g of rutile to 0.9 g of sample. Then, it is grinded and mixed before it is shaped into a circular holder. The sample needs to be flat and have a clean surface as the x-rays hit this surface and the emitted diffraction pattern will be influenced by the roughness and quality surface. Calculations based on the diffraction pattern were executed by the Bruker Infractal[ass] TOPAS 4.2 software to reveal the percentage of crystalline phases and residual amorphous content.

3.3.2. X-Ray Fluorescence

X-ray fluorescence (XRF) allows to identify and quantify all the elements contained in sample. It consists of the emission of characteristic “secondary” or “fluorescent” x-rays from a material that has been excited by being bombarded with high-energy x-rays or γ-

rays **[122]**. This technique is frequently used for elemental analysis and chemical analysis of building materials.

The measuring procedure follows three sequential steps. Firstly, the loss of ignition (LOI) is determined on a milled sample and the dried ignition sample is formed. For this, the empty mass of a crucible that has been heated in a muffle furnace at 1000ºC for 4 hours needs to be calculated (m_a). Then, approximately 3g of sample are added to the crucible and it is placed in an oven at 105ºC for 4 hours. After cooling, the mass of the sample and the crucible is noted (m_c). The crucible and the sample are heated again by last up to 1000ºC for 2 hours, this is weighed after cooling down (m_d). The LOI is calculated based on the following formula:

$$\textbf{LOI}\ (\%) = \frac{(m_c - m_d)}{(m_c - m_a)} * 100\%$$

Secondly, the fused beads are formed in a Phoenix VFD S single stage gas powered fusion machine from XRF Scientific. This is a fusion machine based on natural gas heating. To make the beads, 0.8992 g of dried ignition sample is added to the platinum cup of the fusion machine. To this sample, 9.012g of 66wt%/34wt% lithium tetraborate/lithium metaborate flux is added. This flux has 0.2% lithium bromide added as a release agent. The components are mixed in the crucible and placed into the fusion machine where they are melted at 1100-1200ºC. Once the bead is formed and cooled, which takes almost 30 minutes, it is transferred to the S8 tiger XRF were the surface is exposed to x-rays. Based on the LOI and the weight of the sample as well as the flux, the chemical composition is figured out using a SPECTRA^{plup} V3 software.

3.3.3. Laser Diffraction

Laser diffraction spectroscopy is a simple technique that uses diffraction patterns generated by a laser beam which passed through any sample ranging from nanometres to millimetres in size to measure geometrical dimensions of a particle. This process does not depend on volumetric flow rate, that is, the number of particles that passes through a surface over time **[123]**.

Laser diffraction analysis is based on the Fraunhofer diffraction theory, stating that the intensity of light scattered by a particle is directly proportional to the particle size. The angle of the laser beam and particle size have an inversely proportional relationship, where the laser beam angle increases as particle size decreases and vice versa. **Figure42** illustrates the working principle of lase diffraction to determine the particle size.

Laser diffraction analysis is accomplished via a red He-Ne laser, a commonly used gas laser for physics experiments that is made up of a laser tube, a high-voltage power supply, and structural packaging . Alternatively, blue laser diodes or LEDs of shorter wavelength may be used. Angling of the light energy produced by the laser is detected by having a beam of light go through a suspension and then onto a sensor. A lens is placed between the object being analysed and the detector's focal point, causing only the surrounding laser diffraction to appear. The sizes that the laser can analyse depend on the lens' focal length, the distance from the lens to its point of focus. As the focal length increases, the area the laser can detect increases as well, displaying a proportional relationship. A computer can

then be used to detect the object's particle size from the light energy produced and its layout, which the computer derives from the data collected on the particle frequencies and wavelengths . To calculate the particle size (d_v) by means of assuming Mie scattering, the correlation between the measured intensity and the angle of scattering is applied.

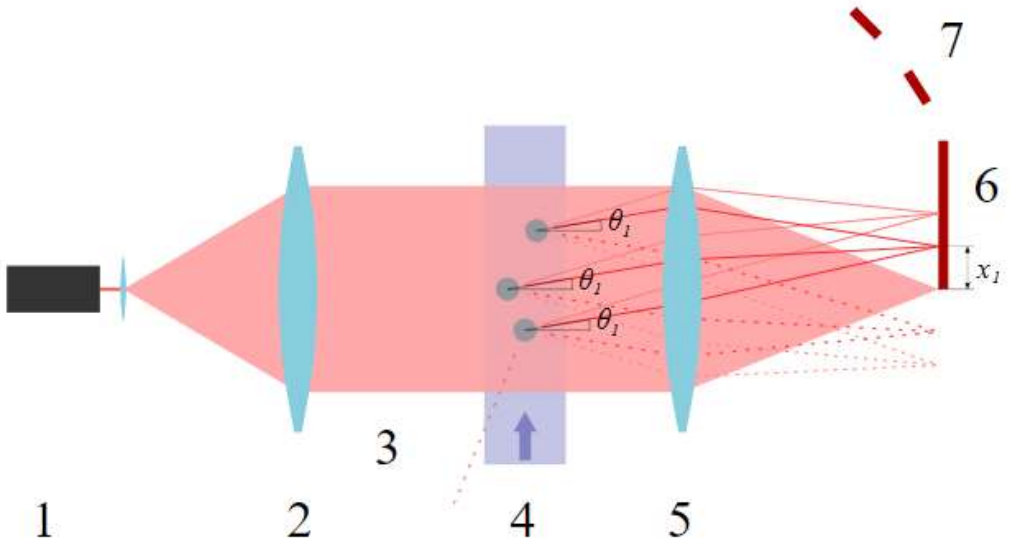

Figure 42. Working principle of laser diffraction analyser. Particles moving through the spread parallel laser beam.

To measure the particle size distribution of the samples (raw materials, intermediate and final products) two equipments were used. A Sysmex Malvern Mastersizer 2000 from the analytical laboratory of PRTC and a Sysmex Mastersizer 3000 from the analytical laboratory of Eternit Innovation Centre (RedCo). Both Mastersizer 2000 and 3000 can measure the particle size distribution of materials ranging from 0.02µm up to 2000µm. The dispersion of the product can be done in two different ways: via dry method using air as dispersant, or via wet method using water as dispersant. In this investigation, the wet method was chosen owing to its better accuracy. The dry method does not fall in the right specifications giving a high deviation in the coefficient of variation (% COV) comparing with the wet method. Reasons for this might be a too high pressure during the measurement, or segregation of the sample during the vibrations of the tray (one of the accessories of the apparatus to introduce the sample). For the wet method, the sample is added to water and the software performs the calculations. The results are shown in a volume-weight diagram. In this diagram three important percentiles are calculated. They are the 10, 50 and 90 percentiles. Generally, the d_{50} value is used as representation of the particle size. For the success of this research, the particle size of the raw materials was determined.

3.3.4. Nitrogen Adsorption-Desorption. BET and BJH.

One of the most common techniques of determining pore size, total pore volume, surface area and bulk and absolute densities in porous solids is nitrogen adsorption-desorption. Within Nitrogen adsorption-desorption technique, two methods were applied: Brunauer-Emmett-Teller (BET) Surface Area Analysis and Barrett-Joyner-Halenda (BJH) Pore Size and Volume Analysis. BET analysis provides precise specific surface area evaluation of materials by nitrogen multilayer adsorption measured as a function of relative pressure using a fully automated analyser **[124]**. The technique encompasses external area and pore area evaluations to determine the total specific surface area in m^2/g, yielding important information in studying the effects of surface porosity and particle size in many applications. On the other hand, BJH analysis can also be employed to determine pore area and specific pore volume using adsorption and desorption techniques. This technique characterizes pore size distribution. It uses the modified Kelvin equation to relate the amount of adsorbate removed from the pores of the material, as the relative pressure (P/P_0) is decreased from a high to low value, to the size of the pores **[125]**.

Two BET/BJH surface and pore size analyzers were used to characterize the calcium silicate-based materials. A Nova 2000e Quantachrome from PRTC laboratory and an ASAP 2020 Plus model Micromeritics from mineralogy and geochemistry mixed analytical laboratory at the ISTerre. A small amount of sample (around 0.5g) is tested and added to a long glass tube. Then, this tube is placed in the analyzer. Note that the first step is done by applying heat and vacuum only. The N_2 used in this process is at boiling point (196ºC), which is under its critical temperature.

This means that it will condense at the surface, assumingly in a monolayer. The correlation between the amount of gas that is adsorbed, and the surface area is given by the BET theory. The desorption step takes place at the end of this process. By looking at how much adsorbate can be removed from the pores when the pressure is increased, the pore size distribution can be calculated. This is performed by the BJH correlations made by Barrett, Joyner and Halenda based on the Kelvin theory **[125]**.

3.3.5. Mercury Intrusion Porosimetry.

Mercury intrusion porosimetry (MIP) is a technique commonly utilized for the evaluation of porosity, pore size distribution, and pore volume (among others) in a wide variety of materials, such cement-based materials. The instrument, known as a porosimeter, employs a pressurized chamber to force mercury to intrude into the voids in a porous substrate. As pressure is applied, mercury fills the larger pores first. As pressure increases, the filling proceeds to smaller and smaller pores. Both the inter-particle pores (between the individual particles) and the intra-particle pores (within the particle itself) can be characterized using this technique.

The Washburn Equation relates the applied pressure to pore diameter using physical properties of the non-wetting liquid (mercury in this case) **[126]**. The physical properties include the contact angle between the mercury and the material, as well as surface tension. Instruments utilized at PTL allow for pressures ranging from approximately 1 psi up to 60,000 psi which correlates to measurement of pores from about 250 µm to 0.003 µm (3

nm). The contact angle of the mercury on the material under test is an important consideration for optimal results. It can either be measured or default values can be entered during the analysis. On the other side, the volume of mercury intruded into the sample is monitored by a capacitance change in a metal clad capillary analytical cell called a penetrometer. The sample is held in a section of the penetrometer cell, which is available in a variety of volumes to accommodate powder or intact solid pieces. Sample size is limited to dimensions of approximately 2.5 cm long by 1.5 cm wide.

The mercury intrusion porosimetry measurements were carried out externally at the Laboratory for Scientific Particle Analysis (LabSPA) of 3P Instruments company. A 3P densi 100 single station automatic gas pycnometer was used for determination of pore size distribution and pore volume of Promatect-L500 samples prepared using different xonotlite slurries which were synthesized by a variety of silica sources.

3.3.6. Scanning Electron Microscopy

Scanning electron microscopy (SEM) is a technique frequently used to investigate the structure of materials. The electron microscope produces images of a sample by scanning the surface with a focused beam of electrons. The electrons interact with atoms in the sample, producing various signals that contain information about the surface topography and composition of the sample. The electron beam is scanned in a raster scan pattern, and the position of the beam is combined with the intensity of the detected signal to produce an image. In the most common SEM mode, secondary electrons emitted by atoms excited by the electron beam are detected using a secondary electron detector (Everhart-Thornley detector). The number of secondary electrons that can be detected, and thus the signal intensity, depends, among other things, on specimen topography. Some SEMs can achieve resolutions better than 1 nanometre.

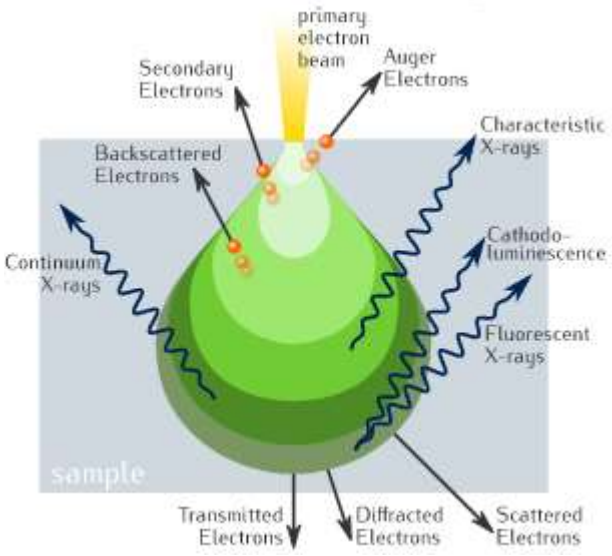

Figure 43. Electron-matter interaction volume and types of signals generated.

Specimens are observed in high vacuum in a conventional SEM, or in low vacuum or wet conditions in a variable pressure or environmental SEM, and at a wide range of cryogenic or elevated temperatures with specialized instruments **[127]**.

Concerning to the various types of signals produced, they include secondary electrons (SE), reflected or back-scattered electrons (BSE), characteristic X-rays and light (cathodoluminescence) (CL), absorbed current (specimen current) and transmitted electrons as shown in **Figure 43**.

Secondary electrons have very low energies on the order of 50 eV, which limits their mean free path in solid matter. Consequently, SEs can only escape from the top few nanometres of the surface of a sample. The signal from secondary electrons tends to be highly localized at the point of impact of the primary electron beam, making it possible to collect images of the sample surface with a resolution of below 1 nm. Back-scattered electrons (BSE) are beam electrons that are reflected from the sample by elastic scattering. Since they have much higher energy than SEs, they emerge from deeper locations within the specimen and, consequently, the resolution of BSE images is less than SE images. However, BSE are often used in analytical SEM, along with the spectra made from the characteristic X-rays, because the intensity of the BSE signal is strongly related to the atomic number (Z) of the specimen and hence, BSE images can provide information about the distribution of different elements in the sample. Characteristic X-rays are emitted when the electron beam removes an inner shell electron from the sample, causing a higher-energy electron to fill the shell and release energy. The energy or wavelength of these characteristic X-rays can be measured by Energy-dispersive X-ray spectroscopy or Wavelength-dispersive X-ray spectroscopy and used to identify and measure the abundance of elements in the sample and map their distribution. Due to the very narrow electron beam, SEM micrographs have a large depth of field yielding a characteristic three-dimensional appearance useful for understanding the surface structure of a sample.

To explore the fracture surface of hydrated calcium silicates, five different electron microscopes were used in various laboratories from Belgium, Spain and France. The SEM microscope utilized at PRTC (Tisselt, Belgium) was a FEI Inspect S50 equipped with a Bruker Quantax 50 EDX probe/XFlash 1000 detector with an energy resolution of 125eV. Whilst a FESEM Zeiss Sigma fitted with a Bruker Quantax 200 EDX Probe/XFlash 4010 detector with 127eV at the analytical laboratory of RedCo (Kappelle-op-den-Bos, Belgium) was also used. Besides, some images were captured using a FESEM equipment of the Electron Microscopy Service from Polytechnic University of Valencia (UPV, Spain). It was a coupled Zeiss Ultra 55 - EDX Point Probe Plus (Oxford Instruments). During the research work at the ISTerre, on one side a Tescan Vega3 SEM fitted with a EDX Probe SiriusSD (Rayspec) was used to characterize some powder samples for a primarily morphological analysis. And on the other side, a FESEM was employed to explore deeply the fracture surface of certain samples. The apparatus was a Zeiss Ultra 55 fitted with a EDX Bruker AXS SSD detector from the Technological Platform of Materials Characterization of the Engineering and Management Institute (INP), as part of

the Consortium of technological common resources (CMTC) at the University Grenoble-Alpes (UGA).

3.3.7. Transmission Electron Microscopy

Transmission electron microscopy (TEM) is a microscopy technique in which a beam of electrons is transmitted through a specimen to form an image **[127]**. The TEM microscope uses the physical and atomic phenomena produced when a sufficiently accelerated electron beam collides with a suitably prepared thin sample. When the electrons collide with a sample, depending on its thickness and the type of atoms in the sample, some of them disperse selectively, i.e., there is a gradation between the electrons that pass through it directly and those that are fully diverted. They are all driven and modulated by lenses that form a final image on a CCD that can be magnified thousands of times with a definition that is unattainable for any other instrument. The information obtained is an image with different intensities of grey corresponding to the level of dispersion of the incident electrons. The TEM image described offers information on the sample structure, whether amorphous or crystalline. Furthermore, if the sample is crystalline -in other words, there is a periodic plane structure- various families of these planes may meet the Bragg condition and coherently diffract the incident electron wave. The result is a diffraction diagram, which is an image of different points ordered with respect to a central point (non-deviated transmitted electrons); this offers information on the orientation and structure of the crystal/crystals present.

This technique was especially suitable for a morphological nanocharacterization from a structural and analytical point of view. The equipment for HR-TEM analysis was a high resolution JEOL-TEM 2100F with 200Kv acceleration voltage and a field-emission electron gun (FEG) and equipped with an EDX-Max 80 detector (Oxford Instruments) from the Electron Microscopy Service from Polytechnic University of Valencia (UPV, Spain).

3.3.8. Optical Microscopy

Optical microscopy was used too as a complementary technique for a basic and primary view analysis of xonotlite spherical particles and their roundness, as well as to determine their density, area and diameter. For this study, a Leica DMLB optical microscope was handled with an objective lens of 10x0.25. To calculate the parameters mentioned here, a software program called Image Pro Premium was used.

3.3.9. Fourier Transform-Infra red Spectroscopy

Fourier-transform infrared spectroscopy (FTIR) is an analytical technique used in some cases to obtain information about the structure of materials. This technique measures the absorption of infrared radiation by the sample material versus wavelength. The infrared absorption bands identify molecular components and structures. When a material is

irradiated with infrared radiation, absorbed IR radiation usually excites molecules into a higher vibrational state. The wavelength of light absorbed by a particular molecule is a function of the energy difference between the at-rest and excited vibrational states. The wavelengths that are absorbed by the sample are characteristic of its molecular structure **[128, 129]**.

The FTIR spectrometer uses an interferometer to modulate the wavelength from a broadband infrared source. A detector measures the intensity of transmitted or reflected light as a function of its wavelength. The signal obtained from the detector is an interferogram, which must be analysed with a computer using Fourier transforms to obtain a single-beam infrared spectrum. The FTIR spectra are usually presented as plots of intensity versus wavenumber (in cm^{-1}). Wavenumber is the reciprocal of the wavelength. The intensity can be plotted as the percentage of light transmittance or absorbance at each wavenumber. To identify the material being analysed, the unknown IR absorption spectrum is compared with standard spectra in computer databases or with a spectrum obtained from a known material. Moreover, Quantitative concentration of a compound can be determined from the area under the curve in characteristic regions of the IR spectrum. Concentration calibration is obtained by establishing a standard curve from spectra for known concentrations.

As complementary technique to investigate the chemical bonding of calcium silicates, two FTIR spectrophotometers were used in different locations. One Bruker Vertex 70 fitted with ATR and DRIFT modes at the RedCo's analytical laboratory (Kappelle-op-den-Bos, Belgium) and one Thermo Scientific Nicolet iS50 with ATR mode at the mineralogy-geochemistry analytical laboratory of ISTerre (Grenoble, France).

3.3.10. Inductively Coupled Plasma Atomic Emission Spectroscopy

Inductively coupled plasma atomic emission spectroscopy (ICP-AES) is an analytical technique used for the quantification of chemical elements. It is a type of emission spectroscopy that uses the inductively coupled plasma to produce excited atoms and ions that emit electromagnetic radiation at wavelengths characteristic of a particular element. The plasma is a high temperature source of ionised source gas (often argon). The plasma is sustained and maintained by inductive coupling from cooled electrical coils at megahertz frequencies. The source temperature is in the range from 6000 to 10,000 K. The intensity of the emissions from various wavelengths of light are proportional to the concentrations of the elements within the sample **[130]**.

For the determination ex situ of [Ca] and [Si] in solution of certain samples taken from the hydrothermal reactions, an ICP-AES Varian 720ES was utilized at the geochemistry laboratory of ISTerre (Grenoble, France).

3.3.11. Nuclear Magnetic Resonance Spectroscopy. High Resolution ^{29}Si Solid-State NMR.

Solid-state NMR (ssNMR) spectroscopy is a special type of nuclear magnetic resonance (NMR) spectroscopy, characterized by the presence of anisotropic (directionally dependent) interactions. Compared to the more common solution NMR spectroscopy, ssNMR usually requires additional hardware for high-power radio-frequency irradiation and magic-angle spinning. The resonance frequency of a nuclear spin depends on the strength of the magnetic field at the nucleus, which can be modified by the electron cloud or the proximity of another spin. In general, these local fields are orientation dependent. In media with no or little mobility (e.g.crystalline powders, glasses, large membrane vesicles, molecular aggregates), anisotropic local fields or interactions have substantial influence on the behaviour of nuclear spins. In contrast, in a classical liquid-state NMR experiment, Brownian motion averages anisotropic interactions to zero and they are therefore not reflected in the NMR spectrum **[131]**.

This work of investigation presents complex chemical nature of C-S-H based materials which often involve disordered phases in terms of crystallography, and which continue to evolve as a function of time as long as they are exposed to hydrothermal conditions. The understanding of their atomic structure is highly complex. High resolution ^{29}Si solid-state nuclear magnetic resonance can resolve key atomic structural details within these cementitious-like materials and has emerged as a crucial tool in characterising cement structure and properties.

The most investigated nucleus in cement chemistry is silicon. A relatively high natural abundance of ^{29}Si (4.67%) as well as its principal structural role in the calcium silicate hydrates makes it favourable for such studies. Silicate tetrahedra are present in hydrated cement systems in various degrees of polymerization. In NMR, polymerization that results in more electron shielding makes the chemical shifts more negative and ranges from –60 to 120 ppm **[132]**. The polymerization of a silicate tetrahedron (Q) is expressed by Q_n, where n is the number bridging oxygens per tetrahedron. If the oxygen is shared with other silicate tetrahedra, the possible Q_n sites (n=0 to 4) are usually observed at the following ranges shown in the **Figure 44**:

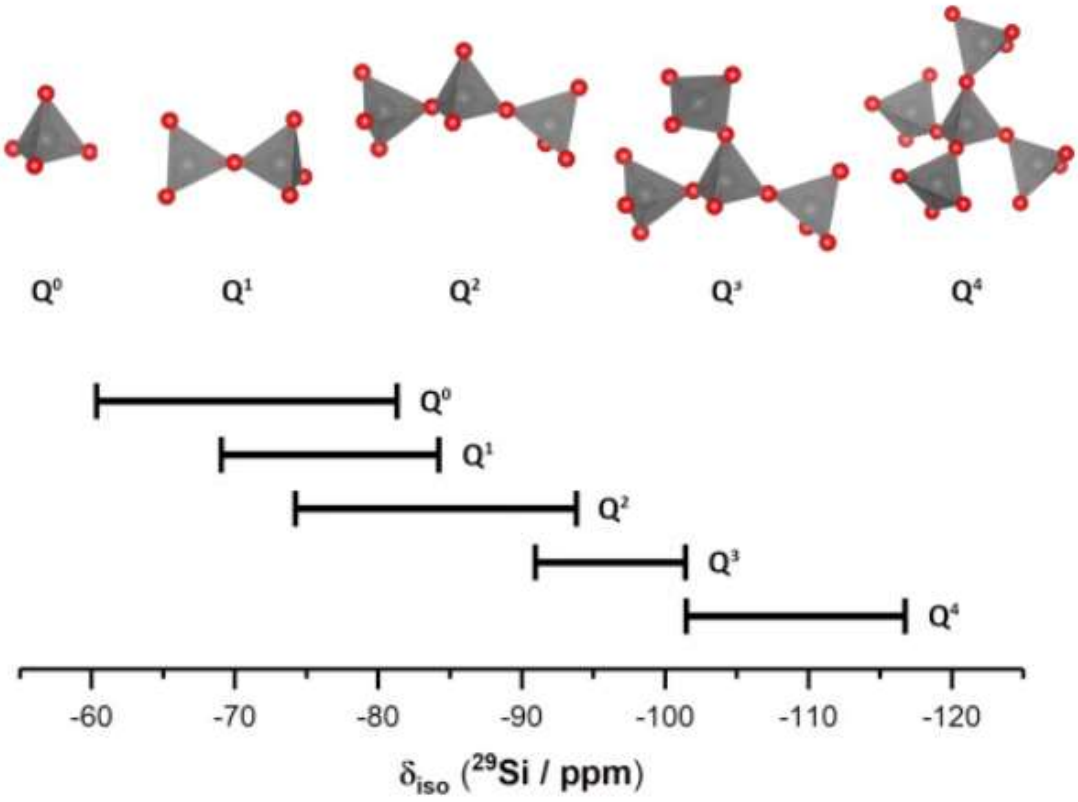

Figure 44. Ranges of ^{29}Si chemical shifts of Q_n units in solid silicates. The well-separated ranges are hatched.

A few measurements using High Power Decoupling (HPDEC) and Cross Polarization Magic-Angle Spinning (CPMAS) ^{29}Si solid-state nuclear magnetic resonance were run externally by the NMR/X-Ray Platform for Convergence Research of the Centre for Surface Chemistry and Catalysis, in the Department of Microbial and Molecular Systems at KU Leuven. ^{29}Si NMR spectra were acquired with a Bruker Advance III 500 MHz spectrometer, equipped with a 4 mm H/X/Y probe and a 7 mm H/X/Y probe, operating at a ^{29}Si frequency of 99.5 MHz. The samples were filled in a ZrO_2 rotor (4/7 mm) and spun at 10 kHz (4 mm) or 2.5 kHz (7 mm), and the rotor periods (tr) are 100 μs and 400 μs, respectively. Furthermore, additional NMR measurements were carried out by the Magnetic Resonance Unit from University of Alicante (UA, Spain). A Bruker Advance DRX500 500 MHz spectrometer provided with CPMAS Probe was utilized.

3.3.12. Simultaneous Thermal Analysis. DSC-TMA

Simultaneous thermal analysis (STA) generally refers to the simultaneous application of thermogravimetry (TGA) and differential scanning calorimetry (DSC) to one and the

same sample in a single instrument. The test conditions are perfectly identical for the thermogravimetric analysis and differential scanning calorimetry signals (same atmosphere, gas flow rate, vapor pressure of the sample, heating rate, thermal contact to the sample crucible and sensor, radiation effect, etc.). Thermal analysis is a branch of materials science where the properties of materials are studied as they change with temperature **[133]**.

Thermogravimetric analysis or thermal gravimetric analysis (TGA) is a method of thermal analysis in which the mass of a sample is measured over time as the temperature changes. This measurement provides information about physical phenomena, such as phase transitions, absorption, adsorption and desorption; as well as chemical phenomena including chemisorption, thermal decomposition, and solid-gas reactions (e.g., oxidation or reduction) .

Differential scanning calorimetry (DSC) is a thermo-analytical technique in which the difference in the amount of heat required to increase the temperature of a sample and a reference (a metallic crucible) is measured as a function of temperature. Both the sample and the reference are maintained at nearly the same temperature throughout the experiment. Generally, the temperature program for a DSC analysis is designed such that the sample holder temperature increases linearly as a function of time. The reference sample should have a well-defined heat capacity over the range of temperatures to be scanned.

For the DSC-TGA measurements, three different equipments were employed. A Netzsch STA 449C (PRTC analytical laboratory/Tisselt, Belgium) and a Mettler-Toledo DSC-TGA 1 UMX5 (RedCO analytical laboratory/Kappelle-op-den-Bos, Belgium). Also, a Mettler Toledo TGA-DSC3+ (Geochemistry-mineralogy analytical laboratory, ISTerre/Grenoble, France). Before to run the machine, a powder sample must be completely dried. After drying, first the crucible is tared and then, a small amount of powder is placed in this crucible to be weighed. A heating ramp [RT-max. Temp.] is set with a maximum temperature ranging from 1100 to 1200ºC depending on the equipment and the corresponding heat flow (10 ºC/min).

3.3.13. 3-Point Flexural Test

The three-point bending flexural test provides values for the modulus of elasticity in bending E_f, flexural stress σ_f, flexural strain ϵ_f and the flexural stress–strain response of the material. This test is performed on a universal testing machine (tensile testing machine or tensile tester) with a three-point or four-point bend fixture. The main advantage of a three-point flexural test is the ease of the specimen preparation and testing. However, this method has also some disadvantages: the results of the testing method are sensitive to specimen, loading geometry and strain rate.

To determine the flexural strength of the calcium silicate boards, they were firstly sawn lengthwise in two equal parts. The half board is placed in a Retro line test control 2 made by Zwick Roell, with a span of 120 mm. This testing equipment will then lower the middle rod by 2 mm/min. The accompanying software, which is Test Expert 2, will plot a graph showing the stress in function of the strain, based on the force measurements. The measurement ends once the sample is broken.

3.3.14. Thermal Shrinkage

The shrinkage is the reduction of the dimensions of a sample during heating until a given temperature.

The measurements were done on samples of 50x35x20 mm. They were placed in different ovens (Nabertherm and Carbolite) according to the temperature profile program applied. Temperatures of 950°C or 1050°C were maintained during 3 hours after which the oven was cooled down. The difference in dimensions before and after this test gives the thermal shrinkage (%).

3.3.15. Thermal Mechanical Analysis

Thermomechanical analysis is a technique in which a deformation of the sample under non-oscillating stress is monitored against time or temperature while the temperature of the sample, in a specified atmosphere, is programmed. The stress may be compression, tension, flexure or torsion.

The sample is inserted into the furnace and is touched by the probe which is connected with the length detector and the force generator. The thermocouple for temperature measurement is located near the sample. The sample temperature is changed in the furnace by applying the force onto the sample from the force generator via probe. Then, the sample deformation such as thermal expansion and softening with changing temperature is measured as the probe displacement by the length detector. Linear variable differential transformer (LVDT) is used for length detection sensor.

A NETZSCH TMA 402 F3 Hyperion apparatus was used for several measurements to characterize calcium silicate-based samples at the analytical laboratory of PRTC.

3.3.16. Thermal Conductivity by Hot Wire Method

The measurement of the thermal conductivity on calcium silicates were performed using the Hot Wire Method. The hot wire method is a standard transient dynamic technique based on the measurement of the temperature rise in a defined distance from a linear heat source (hot wire) embedded in the test material. If the heat source is assumed to have a constant and uniform output along the length of test sample, the thermal conductivity can be derived directly from the resulting change in the temperature over a known time interval. The hot wire probe method utilizes the principle of the transient hot wire method. Here the heating wire as well as the temperature sensor (thermocouple) is encapsulated in a probe that electrically insulates the hot wire and the temperature sensor from the test material **[134]**.

The ideal mathematical model of the method assumes that the hot wire is an ideal, infinite thin and long line heat source, which is in an infinite surrounding from homogeneous and isotropic material with constant initial temperature. If q is the constant quantity of heat production per unit time and per unit length of the heating wire (W.m-1), initiated at the

time t=0, the radial heat flow around the wire occurs. Then the temperature rise DT(r,t) at radial position r (see Figure 1) from the heat source conforms to the simplified formula:

$$\Delta T(r,t)=\frac{q}{4\pi k}\ln\frac{4at}{r^2C}$$

where k is the thermal conductivity ($W\cdot m^{-1}\cdot K^{-1}$), a thermal diffusivity ($m^2\cdot s^{-1}$) ($a = K/\rho C_P$, with is ρ the density (Kg/m^3) and C_P the heat capacity ($J\cdot Kg^{-1}\cdot K^{-1}$) of the test material and C = exp(γ), γ = 0,5772157 is the Euler's constant.

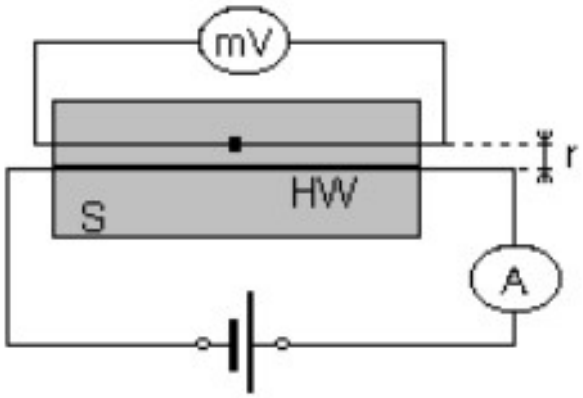

Figure 45. Schematic view of the sample.

The equation above is valid only when r^2 4at << 1 is fulfilled, i.e. for a sufficiently long time (*t*) larger than certain minimum time (t_{min}) and for a small distance r. Thus, the measurement of temperature rise ΔT(r,t) as a function of time is employed to determine the thermal conductivity *k*, calculating the slope *K* of the linear portion of temperature rise ΔT(r,t) vs. natural logarithm of the time (ln(t)) evolution from:

$$k = \frac{q}{4\pi K}$$

The hot wire temperature rise reaches usually up to 10ºC, and its time evolution has typically the form as shown in the **Figure 46**.

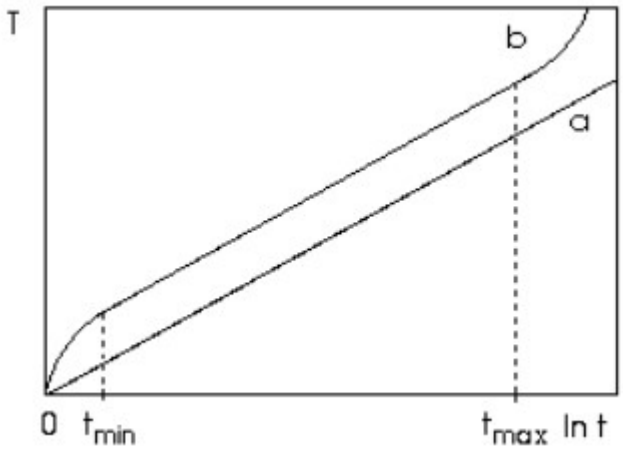

Figure 46. Typical temperature rise curve (a - ideal, b – non-ideal case).

The hot wire method according to ISO 8894 can be applied in several experimental modifications. For the performed thermal conductivity measurements of calcium silicate plates at the PRTC laboratory, the standard cross technique was utilized. In this technique, the wire cross is embedded in ground grooves between two equally sized specimens. The cross consists of a heating wire and the legs of a thermocouple, which acts as the temperature sensor. The hot spot of the thermocouple is in direct contact with the heating wire. A NETZSCH Thermal Conductivity Tester (TCT) 426 was the equipment used as seen in **Figure 47**. Concerning to the samples, two calcium silicate-based rectangular plates were required to run the measurement. Their dimensions were up to 230x110x50 mm.

Figure 47. Images of the thermal conductivity NETZSCH TCT 426 at PRTC analytical laboratory. (Top picture) General overview of the accessories; (Left and right bottom pictures) View of the thermal conductivity measurement system by hot wire standard cross method.

3.3.17. Fire Resistance Test

Fire Resistance abbreviated as RF, or also called short for Résistance au feu, is a Belgian term describing the fire resistance. This term is since 2016 replaced by the European REI classification which follows the EN 13501-1 Norm. However, for the purpose of this work the RF value will provide enough information about fire resistance. To obtain the RF value, calcium silicate board first is conditioned for a minimum of 3 days at room temperature in a climate chamber with a 90% RH. Afterwards, the board is measured and weighed, to calculate density and moisture of the board. A specially developed electrical kiln called VECSTAR Furnace is used for this test. The sample is placed in a frame (see **Figure 48**) and the kiln is at the beginning pre-heated up to 90ºC.

Figure 48. VECSTAR Furnace coupled with a wool glass-frame for the RF Test.

Once, the kiln is ready, the board is placed inside the frame to hold it during the RF test as shown in **Figure 49**. Then, the system is additionally isolated using extra glass wool chunks to close any space between the frame and the kiln. The board is positioned a few centimetres from the electrical resistances. One side (hot side) of the plate is exposed to the heat and the other (cold side) is exposed to room temperature. For the applied tests, the furnace is heated following a temperature profile as described by ISO 834-11:2014 at one side of the sample ('hot side'). A thermocouple is assembled at the so called 'cold side' to register the temperatures.

Figure 49. VECSTAR Furnace coupled with a wool glass-frame containing the calcium silicate board.

CHAPTER 4

RESULTS AND DISCUSSION

CHAPTER 4. Results and Discussion

4.1. Geltank technology

4.1.1. Basics

The first target of this PhD was to develop know-how and understanding of a method called 'gel tank' which some of the competitors of Promat apply, mainly to make low density products. This method comprises of the following steps:

1. Formation of a C-S-H gel (so called pre-reaction)
2. Adding additional ingredients (cellulose fibers, toughening additives)
3. Filter-pressing
4. Hydrothermal conversion of C-S-H into xonotlite and tobermorite.

In the first step (pre-reaction/gelling), a porous low-density C-S-H gel is formed from the starting formulation composed of amorphous silica and lime as raw materials. The C-S-H gel significantly occupies more volume than the original amount of CaO and SiO_2 which is due to the inclusion of large volumes of tiny pores in the developing C-S-H-phases. This change in volume is schematically presented in **Figure 50**.

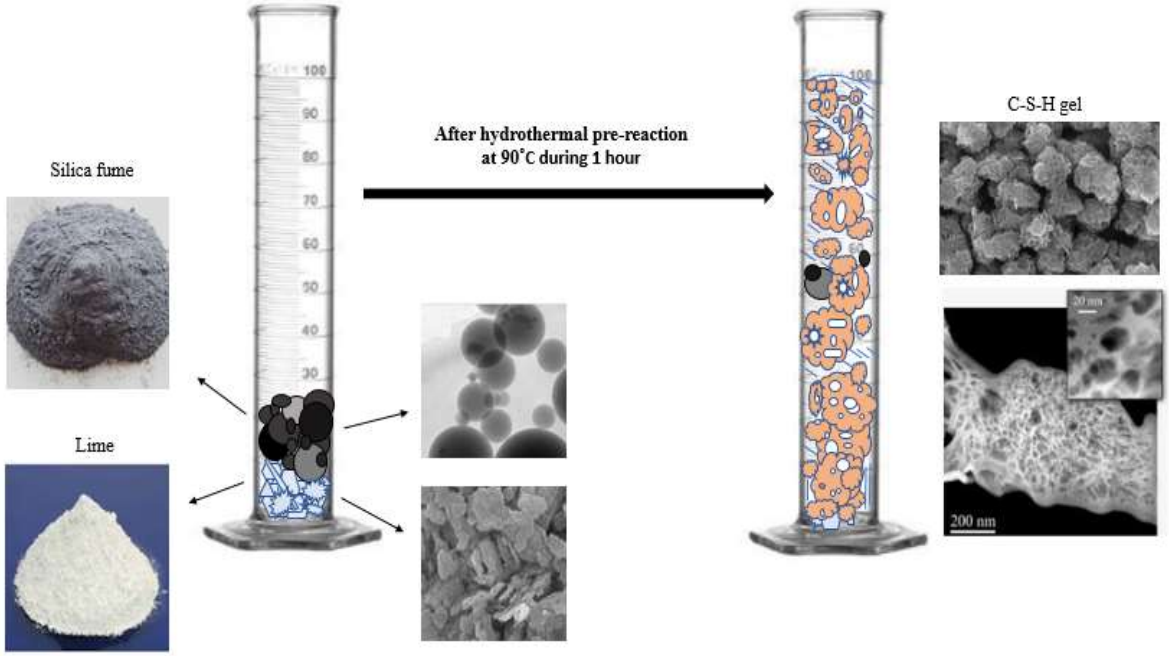

Figure 50. Schematic representation of the lime-silica mixture volume transformation through the gelling stage (C-S-H gel formation).

Suppose a volume "*x*" for a given mass "*y*" corresponding to the initial mixture of solids (lime + silica). For example, as **Table 9** shows, the volume for 10g of the starting lime-silica mix and the volume of the C-S-H gel synthesized from this mixture at 90˚C are clearly different.

Initial mixture	Total mass (g)	Total volume before gelling (ml)	Total volume after gelling (ml)
Lime/Microsilica	10	18.8	51.7

Table 10. Volumetric changes during C-S-H formation.

During the pressing stage, these C-S-H gel particles and the other ingredients are rearranged and end up in a nicely packed structure with the required strength, depending on the final desired density (see **Figure 51**). The lower the density of the final product, the more C-S-H gel will be needed for building up pressure during the filter-pressing. In this investigation, we aimed to develop densities around 450-500kg/m^3, though also the requirements for lower density were looked at.

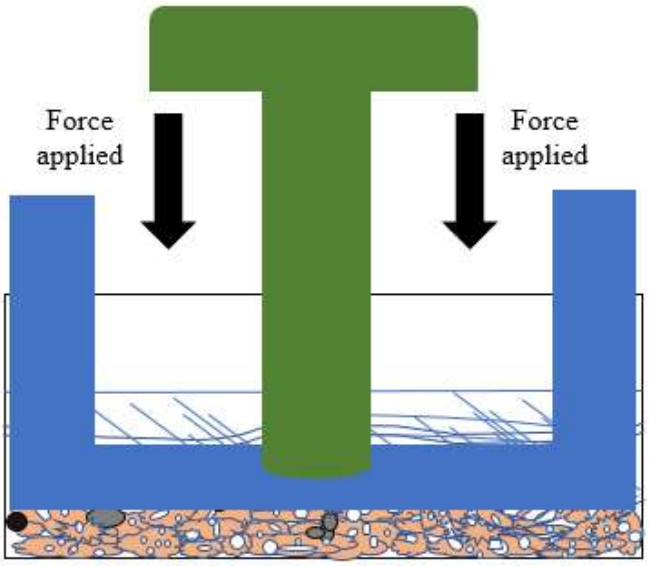

Figure 51. Schematic presentation of rearrangement of particles during the action of a press load.

4.1.2. Factors of influence on the C-S-H gel formation and properties of end products

The influence of different processing parameters as well as raw materials was examined. For the different parameters, the properties of the C-S-H gel as intermediate product and the pressed end product after hydrothermal treatment were investigated.

4.1.2.1. Influence of pre-reaction time

During the pre-reaction step, calcium hydroxide reacts with silica fume forming a low-density C-S-H gel. The characteristics of this gel are strongly related to a number of variables, among which the time, temperature, the type of silica source and the agitation. Here, the effect of pre-reaction time was studied for 2 formulations. In one case, silica fume as silica source. Whereas that in another case, a combination of 50% silica fume (SF) and 50% of quartz (Q).

When lime and silica fume are hydrated at a certain range of temperature above room temperature, the C-S-H gel starts to be formed by the following reaction:

$Ca(OH)_2 + SiO_2\ (SF) \rightarrow C_xS_yH$

with x and y depending on the processing conditions and the silica quality

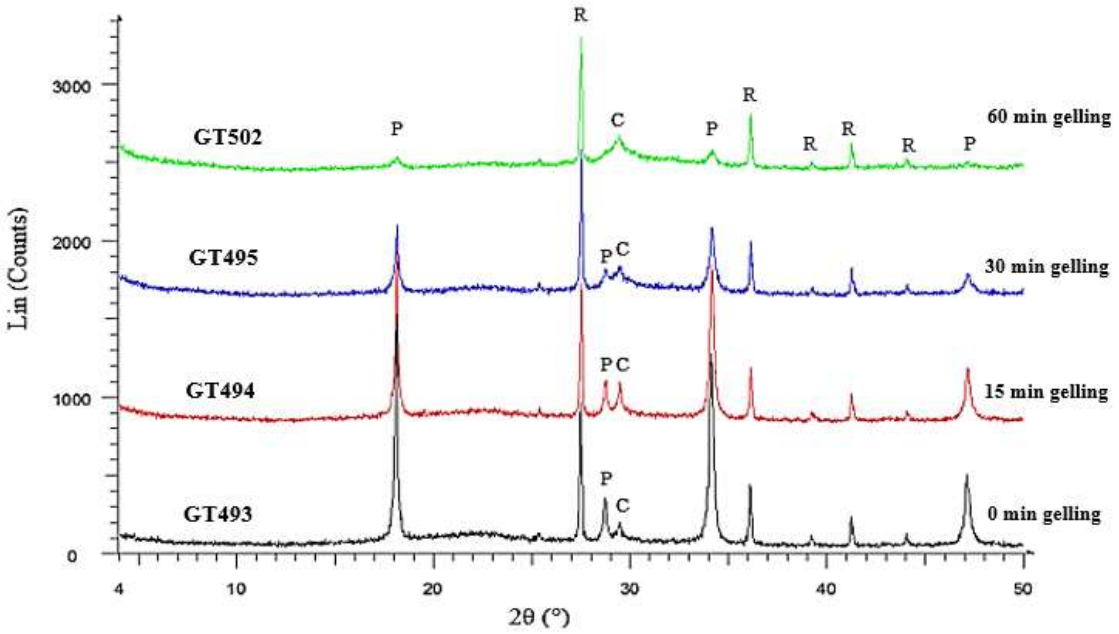

Figure 52. XRD-spectra of GT-CSH samples prepared at different pre-reaction time and from lime and amorphous silica. P: Portlandite; C: Calcite; R: Rutile (internal standard for Rietveld analysis).

During this reaction, there is a fast decrease on the initial percentage of portlandite over time and hence, a progressive increase of amorphous/nanocrystalline C-S-H gel phase as seen in the x-ray diffraction spectra given by **Figure 52**. C-S-H gel is a very disordered phase, mostly non-crystalline or nanocrystalline which gives only a broad reflection in x-ray diffraction. This broad reflection occurs at approximatively $2\theta = 29^{o}$ and starts to become visible for gelling times of at least 30 minutes. It is observed in **Figure 52** how a hump appears in the blue spectrum corresponding to GT495 and continues widening later in GT502. The changes of the contents in the different crystalline and non-crystalline phases with increase of the gelling time are given in **Table 10**. Logically, with increase of reaction time (t_r), the content of C-S-H gel increases. Parallelly, the higher the t_r, the lower the percentage of non-reacted calcium hydroxide and some $CaCO_3$ development is equally observed. In this quantitative analysis must be remarked that the total amount of amorphous content corresponds to the sum of C-S-H gel phase and residual silica fume.

Sample	t_r (min)	Portlandite (%)	Calcite (%)	Amorphous content (%)
GT493	0	34.6	3.9	61.5
GT494	15	28.6	6.8	64.6
GT495	30	15.7	7.4	76.9
GT502	60	4.6	10.2	85.2

Tab. 11. Rietveld Refinement analysis results of GT-CSH gel samples for different pre-reaction times when using only SF.

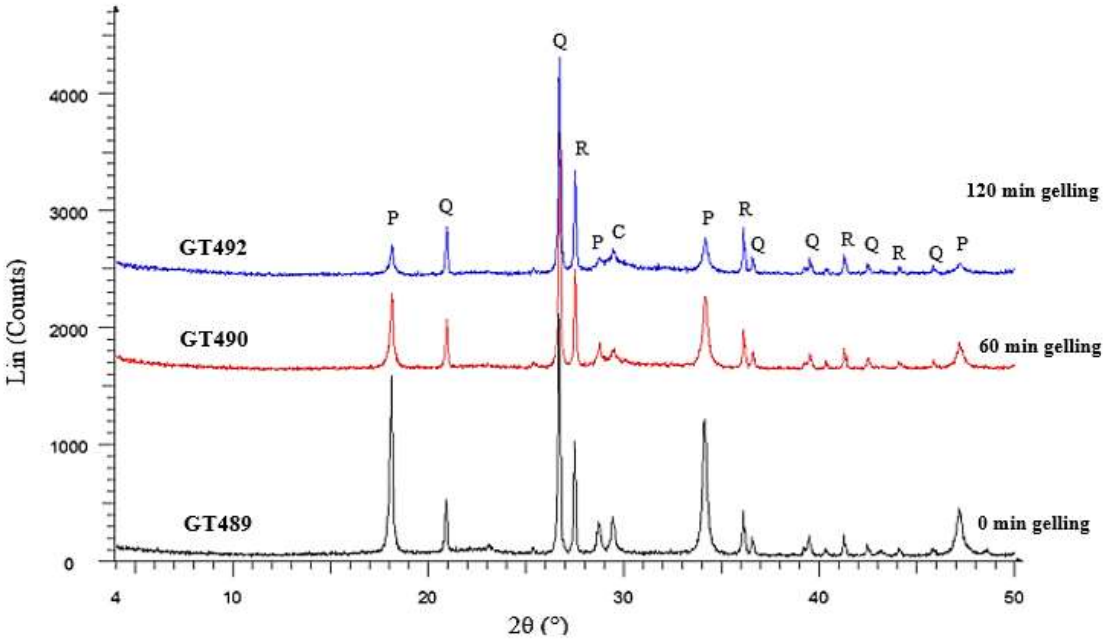

Figure 53. XRD-spectra of GT-CSH samples prepared at different pre-reaction time and from lime, silica fume and quartz. P: Portlandite; C: Calcite; R: Rutile (internal standard for Rietveld analysis).

For the case of an initial composition based on 50% silica fume and 50% quartz, the pre-reaction proceeds in the same way as explained before. But here, with the difference that quartz is not really soluble in these conditions and hence does not react. Looking at the XRD spectra of GT powder samples shown in **Figure 53**, a very similar tendency is followed comparing with previous spectra in **Figure 52**. In these trials, longer reaction time was applied because of the quartz use. As there is less reactive silica, longer time is needed to observe the growth of the C-S-H gel broad peak at $2\theta = 29^{o}$.

The quantification results of the crystalline and amorphous phases content by means of Rietveld method is given in **Table 11**. It is clearly observed that the initial concentration of quartz (25%) does not practically change after each synthesis.

Sample	t_r (min)	Portlandite (%)	Quartz (%)	Calcite (%)	Amorphous content (%)
GT489	0	33.8	21.3	7.7	37.2
GT490	60	22.6	22.3	6.4	48.7
GT492	120	9.8	21	8	61.2

Table 12. Rietveld Refinement analysis results of GT-CSH gel samples for different reaction times when using a mixture of 50% SF and 50% Q.

The consumption of portlandite is lower than in mixtures using only silica fume. Assuming that an equimolar C-S-H is formed, it would be expected at the end of the gelling step a portlandite concentration of ca. 25%. Actually, a lower amount of $Ca(OH)_2$ (around 10%) is present at the end of the gelling reaction because of building Ca-rich C-S-H phases and some carbonation effects (see **Figure 54**). The formation of Ca-richer C-S-H phases was also observed in the stirred autoclave reactor technology when working with mixtures of quartz and amorphous silica. This is due to the fact that during the gelling time quartz is not reacting, meaning that more Ca^{2+} is available for the reactive amorphous silica.

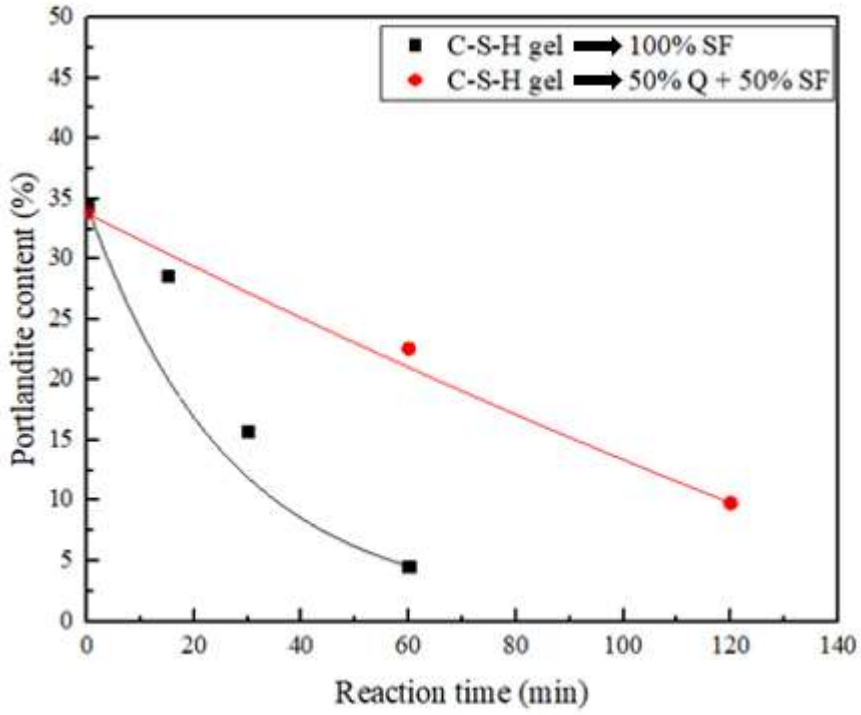

Figure 54. Evolution of residual portlandite content over pre-reaction time.

Figure 55 shows SEM micrographs of C-S-H preparations synthesized at 90ºC for 15 minutes gelling (GT494) and 60 minutes gelling (GT502). Both present a similar trend concerning the morphology. They consist of clusters, aggregates of amorphous nanoparticles as a flake- and foil-like microstructures. Looking at the two samples, the SEM image (a) apparently shows smaller aggregates of C-S-H gel. On the other hand, SEM image (b) presents bigger aggregates of C-S-H gel nanoparticles, and the BET-analysis shows that these are more porous. The Rietveld Refinement analysis results confirm quantitatively these morphological differences. C-S-H preparations after 15 minutes still contain a $Ca(OH)_2$ content > 25%, meaning that only the other 25% or a bit more of portlandite was reacted with silica to form C-S-H gel. Whilst C-S-H preparations after 60 minutes show a $Ca(OH)_2$ content < 5%, that is, practically more than 95% of calcium hydroxide was reacted with SiO_2 and so, a full conversion of $Ca(OH)_2$-SiO_2 into C-S-H gel phase was produced. Therefore, higher yields will be ensured using 60 minutes as a gelling time. On the other hand, the chemical composition of these C-S-H preparations is related with the initial mixture (silica sources and amorphous/crystalline silica ratio) and pre-reaction time applied.

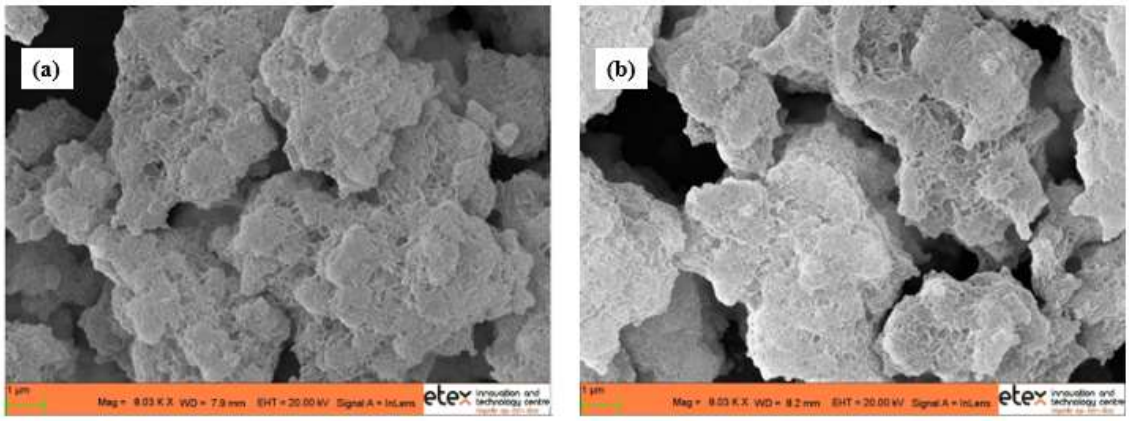

Figure 55. SEM images of C-S-H gel particles. (a) GT494: C-S-H gel after 15 minutes; (b) GT502: C-S-H gel after 60 minutes.

Energy dispersive x-ray analysis was done to determine the calcium and silicon content in these samples. The EDX spectra in **Figure 56** show a C-S-H gel with a nearly equimolar CaO/SiO_2 ratio. The particle size distribution of GT493, GT494 and GT502 samples was determined by laser diffraction analyser. At longer reaction time, the reaction proceeds further and a slight breaking down of the particles is observed as can be derived from the PSD curves shown in **Figure 57** below.

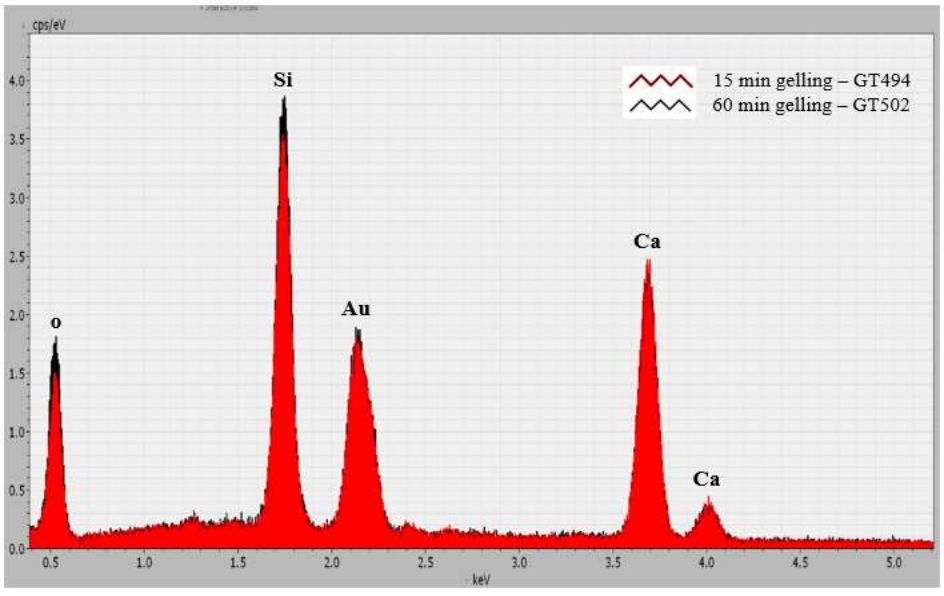

Figure 56. EDX spectra of GT494 and GT502 powder samples containing mainly C-S-H gel. (Red spectrum) GT494 sample obtained after 15 minutes gelling; (Black spectrum) GT502 sample obtained after 60 minutes gelling.

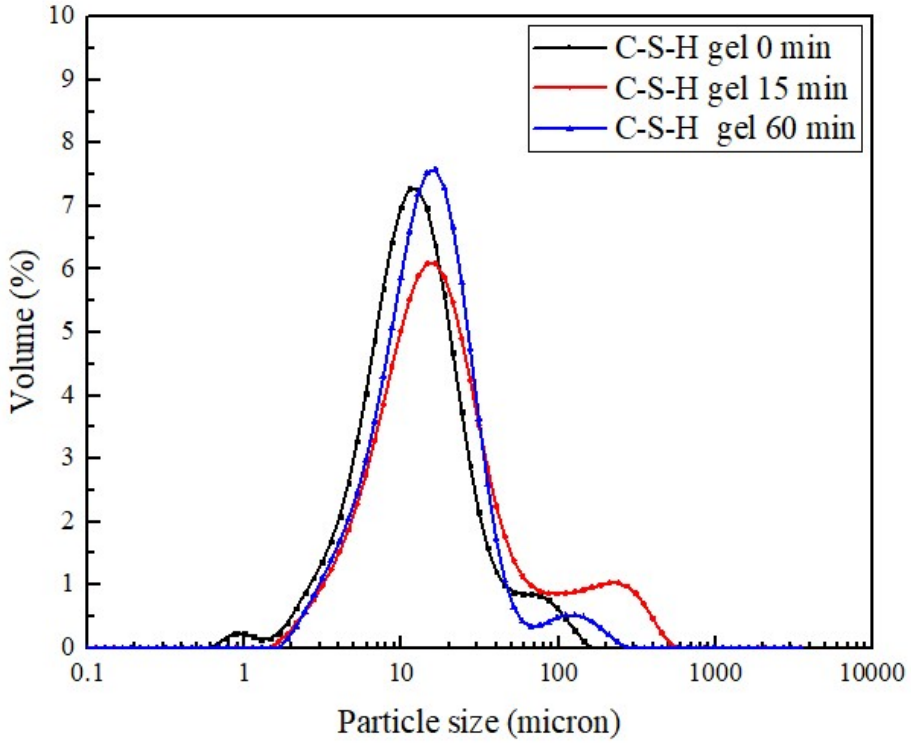

Figure 57. Particle Size Distribution (PSD) curves of C-S-H gel pastes formed at different reaction time and using lime and silica fume. (Black curve) GT493; (Red curve) GT494; (Blue curve) GT502.

The N_2 adsorption-desorption isotherms for the C-S-H gels reacted at different times are presented in **Figure 58**. The curves show type IV isotherms that are characteristic of mesoporous (2 nm < pore size < 50 nm) materials and a hysteresis loop at high relative pressure between 0.6 and 1. The size of the hysteresis loop clearly increased as the pre-reaction time was increased from 15 to 60 minutes and the shape is like type H3 according to the UPAC classification, which is typical of materials with slit- or plate-like particles. **Figure 59** shows the cumulative pore volume and the pore size distribution of the C-S-H gels. The total pore volume, and S_{BET} increased as the pre-reaction time of C-S-H gel was extended as seen in **Table 12**. Therefore, it indicates that longer pre-reaction times lead to the formation of C-S-H gels with higher porosity and the size of the pores is larger.

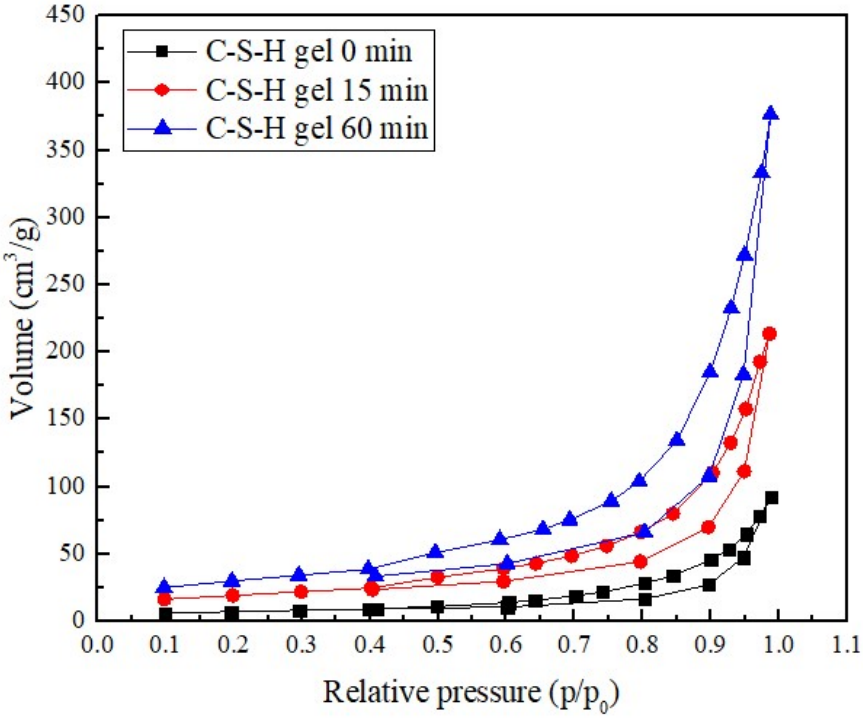

Figure 58. N_2 adsorption-desorption isotherms for C-S-H pastes pre-reacted at various times, 15 and 60 minutes.

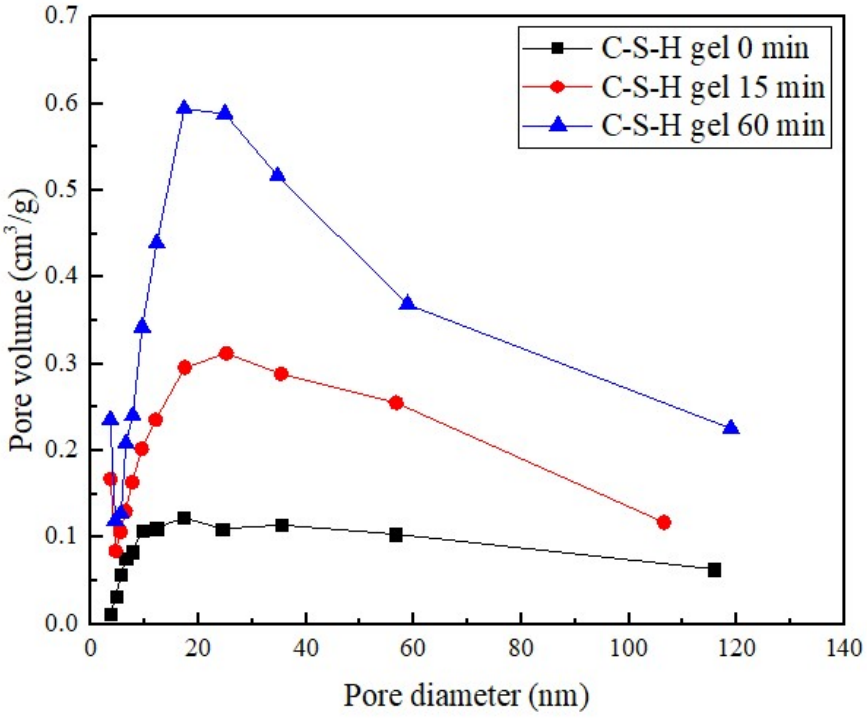

Figure 59. Cumulative pore volume and pore size distribution of gels pre-reacted at various times

Sample	t_r (min)	Total volume (cm^3/g)	Peak pore diameter (nm)	S_{BET} (m^2/g)
GT493	0	0.15	17.2	29
GT494	15	0.34	25.2	64
GT502	60	0.60	17.3	95

Table 13. S_{BET} values and pore size parameters of C-S-H gel samples.

The chemical structure, especially the bonding system of C-S-H gel was investigated using Attenuated Total Reflection-Fourier Transformed Infra-red spectroscopy (ATR-FTIR). **Figure 60** shows two FT-IR spectra corresponding to GT494 (15 min) and GT502 (60 min) samples. The Infra-Red spectra seem to be quite similar, though with some points of difference. The reason why these differences appear are mainly owing to an increasing degree of C-S-H gel formation as the reaction time is longer, some carbonatation effects and reduction of silica fume and $Ca(OH)_2$.

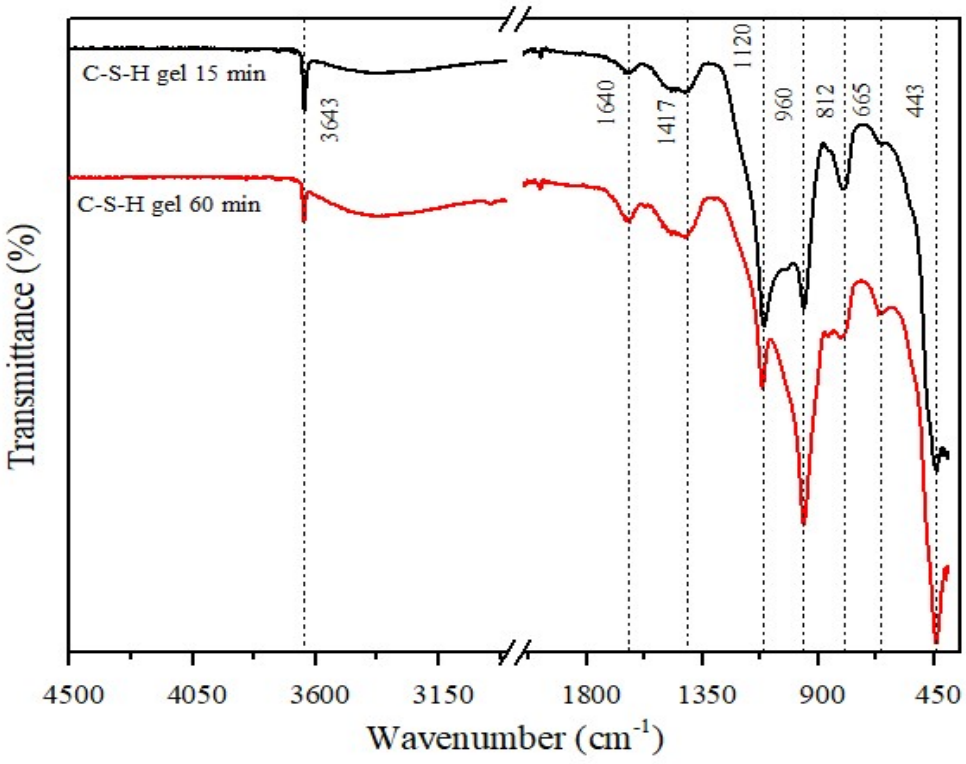

Figure 60. FT-IR spectra of C-S-H pastes prepared with amorphous silica and different gelling time. (Black spectrum) GT494; (Red spectrum) GT502.

The FTIR absorbance spectra exhibit overlapping signals at 3.643 cm^{-1} generated by Ca-O-H bond stretching vibrations associated with the presence of unreacted calcium hydroxide after the pre-reaction of C-S-H gel. As expected, the C-S-H gel synthesized after 15 minutes gave a more intense signal because of a less complete reaction of $Ca(OH)_2$ and micro-silica. Small bands observed at around 1.640 cm^{-1} are produced by H-O-H bond bending vibration and they are attributed to the absorbed water molecules in C-S-H gel. After 60 minutes of pre-reaction, this band became wider indicating a higher degree of C-S-H formation and possibly a higher degree of water bonded to the C-S-H gel structure too. The spectrum presents small wide bands found at 1.417 cm^{-1}, the result of C-O (υ_3) asymmetric stretching vibrations (CO_3^{-2}) due to carbonatation of calcium hydroxide during the pre-reaction. As long as the reaction continues the carbonatation is increased, by this reason the C-S-H gel after 60 minutes showed a broader band. Overlapping signals at 1.120 cm^{-1} were detected as result of Si-O bond asymmetric stretching vibrations related to SiO_4 group in Q^4 units. Logically, for a C-S-H gel with a shorter pre-reaction time, this peak is wider because of a higher percentage of residual amorphous silica. The presence of the band at 960 cm^{-1} is related to Si-O vibrations in Q^2 units in the C-S-H gel. Specially, after 60 minutes the signal was really strong as hydration evolved and so, confirming a higher degree of silicate chain linear polymerization.

Absorption band	Type of vibrational mode	Evolution over time
443 cm^{-1}	Si-O-Si bending vibration mode due to SiO_4 tetrahedral deformation	Increasing. Higher peak intensity
665 cm^{-1}	Si-O-Si bending vibration of paired SiO_4 tetrahedra	No variation
812 cm^{-1}	Si-O stretching vibration of Q^1 tetrahedra	Decreasing. Lower peak intensity
960 cm-1	Si-O stretching vibrations of the Q^2 tetrahedra	Increasing due to SiO_2 polymerization. Higher peak intensity
1120 cm-1	Si-O asymmetric stretching vibrations associated to SiO_4 tetrahedra in Q^4 units from silica fume	Decreasing
1.417 cm^{-1}	C-O (υ_3) asymmetric stretching vibrations (CO_3^{-2}) due to carbonatation of calcium hydroxide	Slight increasing
1.640 cm^{-1}	H-O-H bending vibration of H_2O	Slight increasing
3.643 cm^{-1}	Ca-O-H stretching mode of vibration	Decreasing

Table 14. Characteristic absorbance bands for Calcium Silicate Hydrate (C-S-H).

A band appeared at around 812 cm^{-1} on the FT-IR spectrum of GT494 sample, this was formed by the (υ_1) Si-O symmetric stretching vibrations attributed to the SiO_4 group in Q^0 units in C-S-H gel phase. Whilst on FT-IR spectrum of GT502 sample, this signal shifted slightly to a higher wavenumber (813-814 cm^{-1}), denoting the contribution of a new band associated with the formation of C-S-H gel Q^1 units. This spectrum also showed small signal at around 665 cm^{-1} corresponding to Si-O-Si bending vibrations of paired SiO_4 tetrahedra in C-S-H. The 60 minutes sample had a wider peak which indicates a greater formation of gel. Finally, the presence of a band at 443 cm^{-1} was attributed to in-plane (υ_4) bending vibrations associated with the O-Si-O bonds in the C-S-H gel. Comparing each sample, the signal was much more intense for the gel reacted after 60 minutes. This signal was generated by internal bending vibrations in the SiO_4 tetrahedra constituting the C-S-H gel silicate chains.

Another important parameter related with the C-S-H gel properties is the pressing force required to mold the C-S-H gel-based slurry obtained during pre-reaction stage. The pressing force increases over gelling time due to the formation of low-density C-S-H gel and this is of course higher when the initial content of silica fume at the starting formulation is increased (see **Figure 61**).

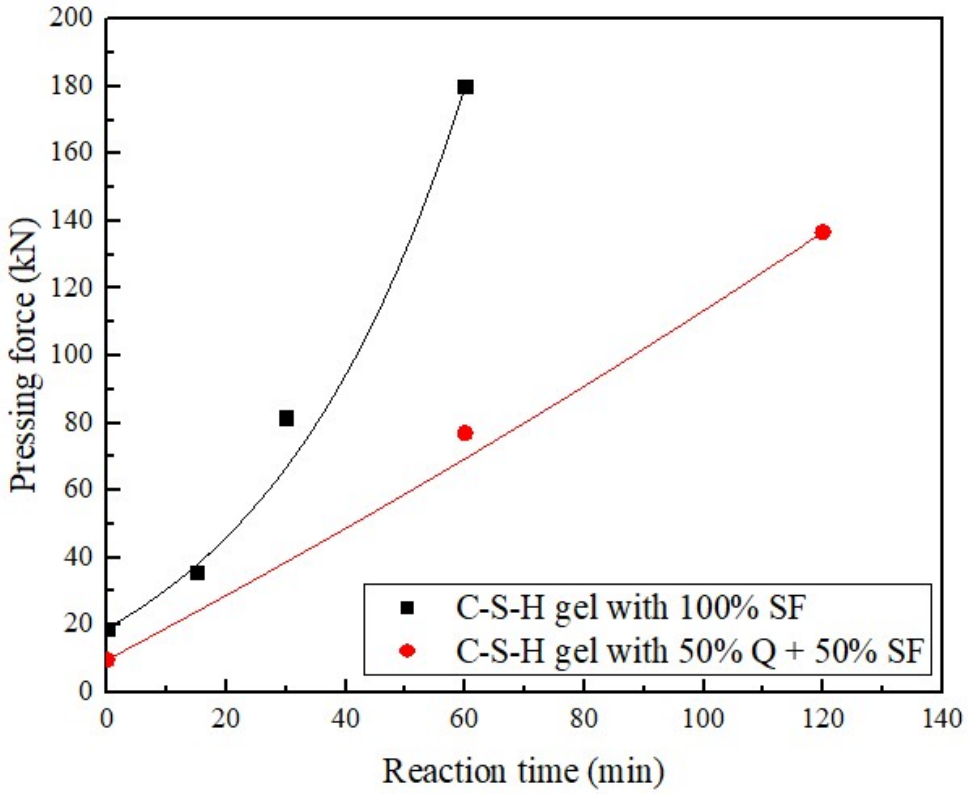

Figure 61. Pressing force vs. Reaction (gelling) time graph.

During the hydrothermal reaction cycle at the horizontal autoclave, C-S-H gel composing the molded plates, recrystallizes finally into xonotlite or into tobermorite and part of this latter into xonotlite. The reaction occurs as follows:

$$Ca(OH)_2 + SiO_2\ (SF) + H_2O \rightarrow C_xS_yH \rightarrow CSH\ (I) \rightarrow Xonotlite + Tobermorite$$

Figure 62 is showing the XRD patterns of the hydrothermally cured plates, previously prepared from slurries of C-S-H gel pre-reacted at different gelling time when using silica fume as silica source. The main crystalline phase is xonotlite. As pre-reaction time gets longer, the intensity of the xonotlite peaks increases. This is due to the increasing degree of conversion of the C-S-H that is formed during the gelling reaction. This C-S-H is nearly equimolar though with slight excess of CaO, converting mainly in xonotlite during the autoclaving step. The reaction of the remaining $Ca(OH)_2$-silica mainly in the samples with shorter gel-reaction times has a silica-richer composition and do not easily convert into xonotlite during the autoclaving process, as can derived from the lower overall contents of xonotlite in these samples with low gel-reaction time.

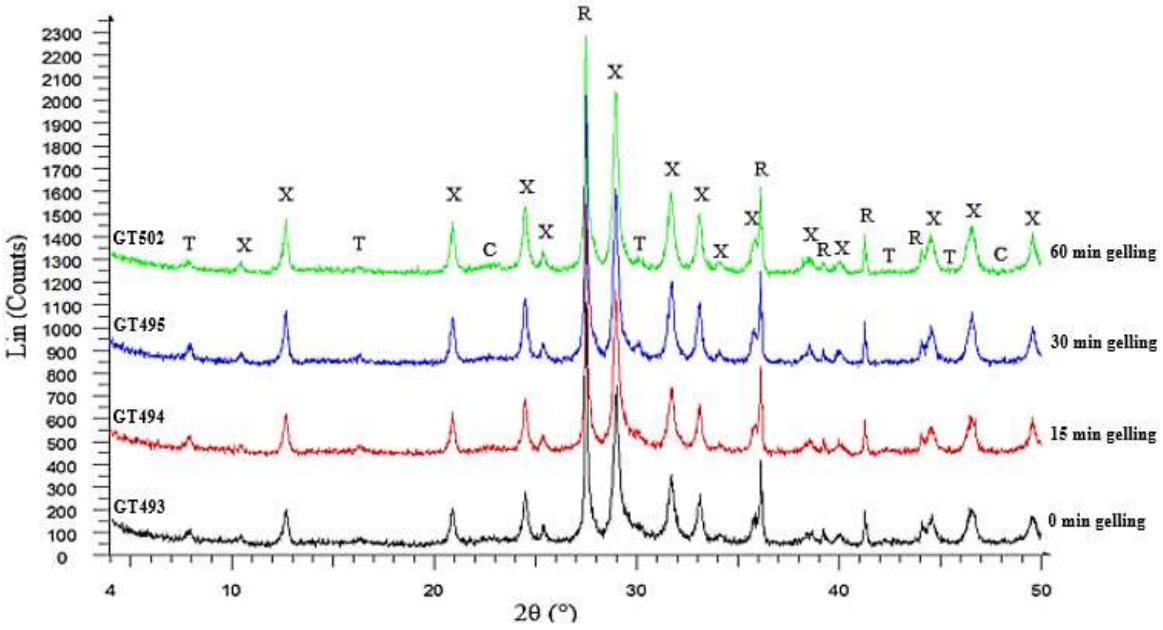

Figure 62. XRD-spectra of GT-autoclaved samples prepared prepared via different pre-reaction time when using only SF. T: Tobermorite; X: Xonotlite; C: Calcite; R: Rutile (internal standard for Rietveld analysis).

The Rietveld analysis by x-ray diffraction measurements of GT-autoclaved samples shown in **Table 14**, confirms the observations made before.

Sample	t_r (min)	Xonotlite (%)	Tobermorite (%)	Calcite (%)	Amorphous content (%)
GT493	0	56	8.7	0.7	34.6
GT494	15	57.6	12.3	4.8	25.3
GT495	30	68	10	1.4	20.6
GT502	60	79.4	6.1	1	13.5

Table 15. Rietveld Refinement analysis results of GT autoclaved boards prepared via different pre-reaction time when using only SF.

Morphological and microstructure analysis was also done in different samples. The fracture surface of the GT-autoclaved boards prepared from C-S-H gel synthesized after 0 minutes (GT493) and 30 minutes (GT495) was analyzed by scanning electron microscopy. The images showed similar morphological aspect and microstructure (see **Figure63**).

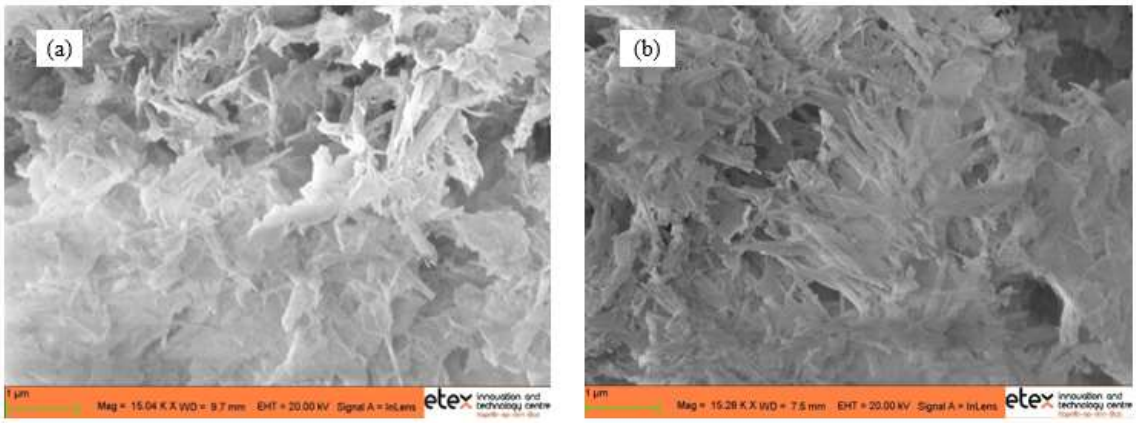

Figure 63. SEM images of fracture surface. (a) GT493 sample and (b) GT495 sample.

The GT boards prepared from mixtures of quartz (M500) and silica fume with initial C/S ratio to 1, were also characterized by x-ray diffraction. **Figure 64** shows the XRD-pattern for these samples. Xonotlite is still the predominant crystalline phase and tobermorite peaks present higher intensity comparing with the GT samples prepared with of amorphous silica.

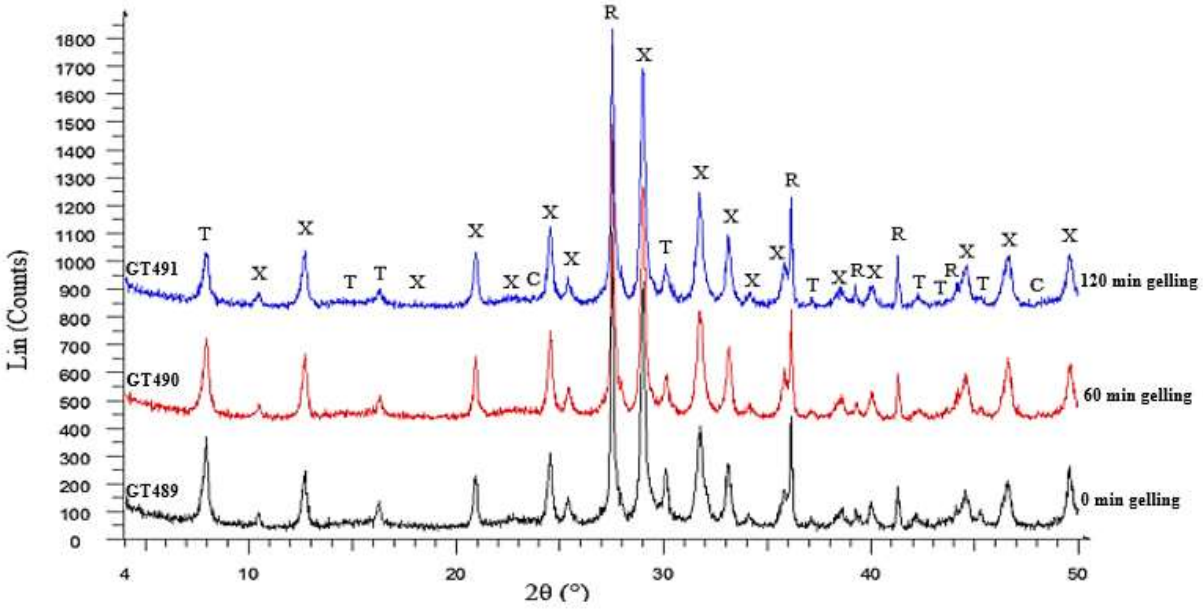

Figure 64. XRD-spectra of GT-autoclaved samples prepared via different pre-reaction time when using a mixture of SF and Q. T: Tobermorite; X: Xonotlite; C: Calcite; R: Rutile (internal standard for Rietveld analysis).

It is reported in literature that quartz as crystalline silica source, when reacting in hydrothermal conditions with calcium hydroxide precipitates forming initially C-S-H (II), which is later converted in a C-S-H with lower C/S ratio in order to be recrystallized firstly into tobermorite and the latter, into xonotlite. Thereupon, as expected higher contents of tobermorite are found as **Table 15**, which is indeed the phase that if formed when using quartz with a particle size of ca. 10 micron. Moreover, due to the formation of initial of Ca-rich gels in the gelling reaction (higher CaO/reactive SiO_2 than in the case of 100% silica fume), the remaining CaO in the C-S-H is below the required level for xonotlite formation.

Sample	t_r (min)	Xonotlite (%)	Tobermorite (%)	Quartz (%)	Calcite (%)	Amorphous content (%)
GT489	0	55.3	26.9	0.1	2.9	14.8
GT490	60	61.8	21.4	0.1	0.8	15.9
GT491	120	64.8	19	0	1.1	15.1

Table 16. Rietveld Refinement analysis results of GT-autoclaved boards prepared via different pre-reaction time when using a mixture of SF and Q.

The mechanical properties of the GT-autoclaved boards were determined using the 3-bending point test. As gelling time is increased, the amount of C-S-H gel produced is higher as demonstrated by the XRD measurements and hence, also a higher pressing force was reached during the moulding process of slurry.

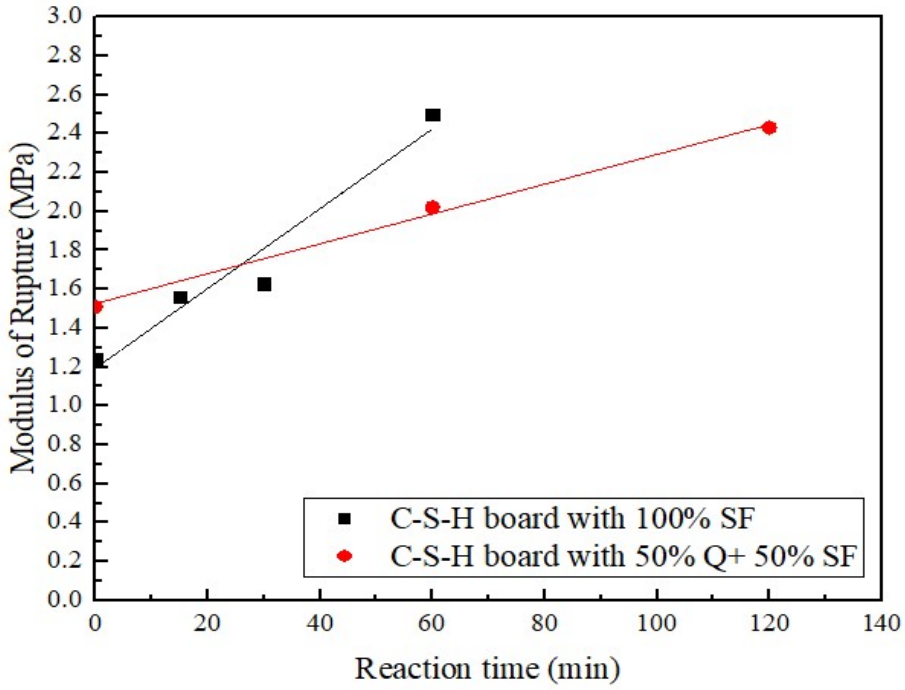

Figure 65. Bending strength dependence on the pre-reaction time and silica sources.

As a result of this, a higher degree of matter compaction occurs. This leads to higher green strength for the intermediate product and to an increase of the bending strength as well as the E-modulus of the end-product. As expected, this development of mechanical strength is much faster for GT plates made by using C-S-H gel produced with silica fume (see Figure 65).

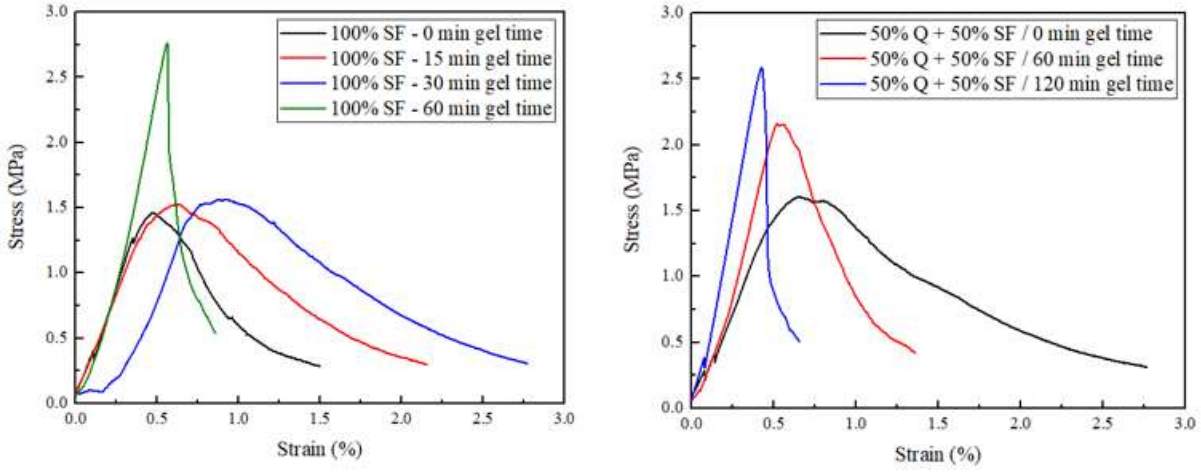

Figure 66. Stress-strain curves for GT-autoclaved boards. (Left) GT samples made by solely silica fume (SF) at the starting recipe and using different gelling time; (Right) GT samples prepared by an equitable mixture of silica fume and quartz at the starting formulation and using different gelling time.

On the other hand, the higher degree of compaction results in strong interfaces implies a decrease of the fracture toughness and the formation of a more fragile matrix. The increase of the brittleness for longer gelling time is visible in the stress-strain curves plotted in **Figure 66**. This also means that a condition of combination of high strength and high fracture energy is difficult to reach in this kind of engineered matrixes (inverse relationship between MOR and i.PL20, see **Figure67**). The differences between GT samples made with only amorphous silica (labelled as 100% SF) and a mixture of quartz and amorphous silica (labelled 50% Q +50% SF) are quite small.

To study the influence of the pre-reaction time on the thermal stability of GT boards after autoclaving, thermal shrinkage tests were performed at 950ºC and 1050ºC for 3 hours. The results obtained are given by the **Figure 68.** The green curve gives the thermal shrinkage versus pre-reaction time for GT-autoclaved samples prepared from C-S-H gel pre-reacted via silica fume. The thermal shrinkage values are very high for the GT493 and GT494 samples (> 8%) because of its high content of amorphous phase and the lower content of xonotlite in these samples.

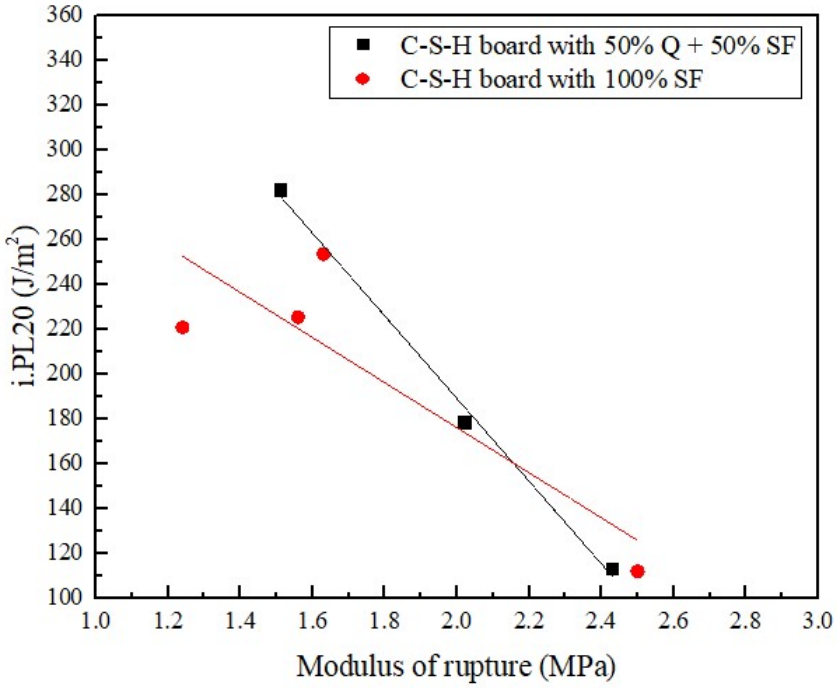

Figure 67. Bending energy (i.PL20) dependence on the bending strength for GT-autoclaved samples prepared using different initial mixtures.

Gelling time longer than 30 minutes is required to make calcium silicate-based products with the required thermal stability when using 100% amorphous silica as silica source. Samples GT495 and GT502 though present a good fire resistance performance as seen in **Figure 68.** The thermal shrinkage values of these samples are slightly higher than 2% and remain constant.

On the other hand, the red line represents the thermal shrinkage vs. pre-reaction time for GT-autoclaved samples made from C-S-H gel pre-reacted via mixtures of 50% SF/50% Q. For these samples there is no variation on thermal shrinkage regardless of the gelling time applied during the pre-reaction stage to synthesize C-S-H gel. The values of thermal shrinkage are more or less constant, being around 2.5%. Unlike the other samples prepared through silica fume as the unique silica source, these GT samples have a lower content of residual amorphous phases after the hydrothermal cycle. This is due to the crystallization of tobermorite from the quartz reaction during the autoclaving reaction and this is related to the composition of the C-S-H phase formed around the quartz grains.

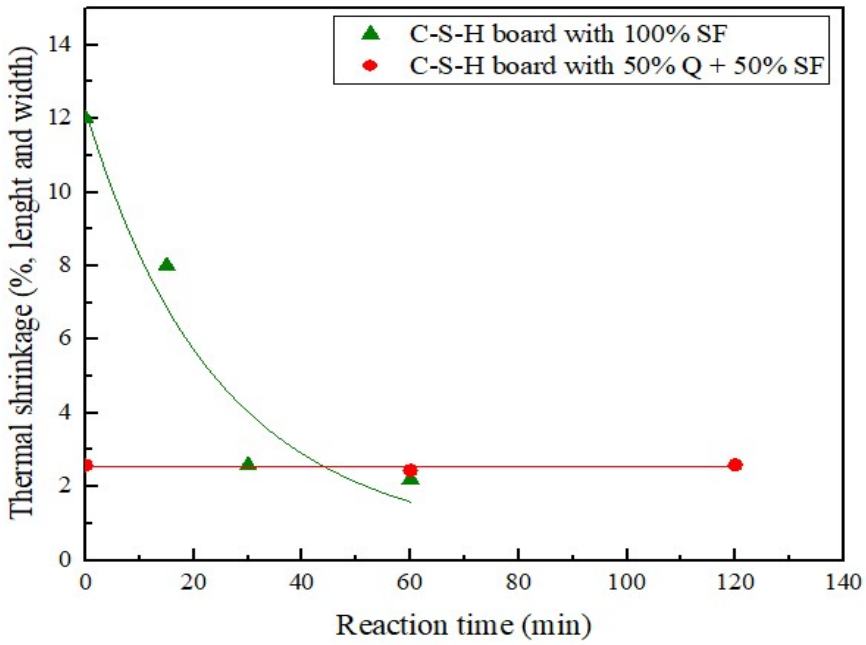

Figure 68. Thermal shrinkage dependance on pre-reaction time.

The less good thermal stability for samples made with 100% amorphous silica and short gelling times (GT493-494) is shown in **Figure 69.** Longer gelling times lead to a clearly better thermal stability and integrity (GT495-502).

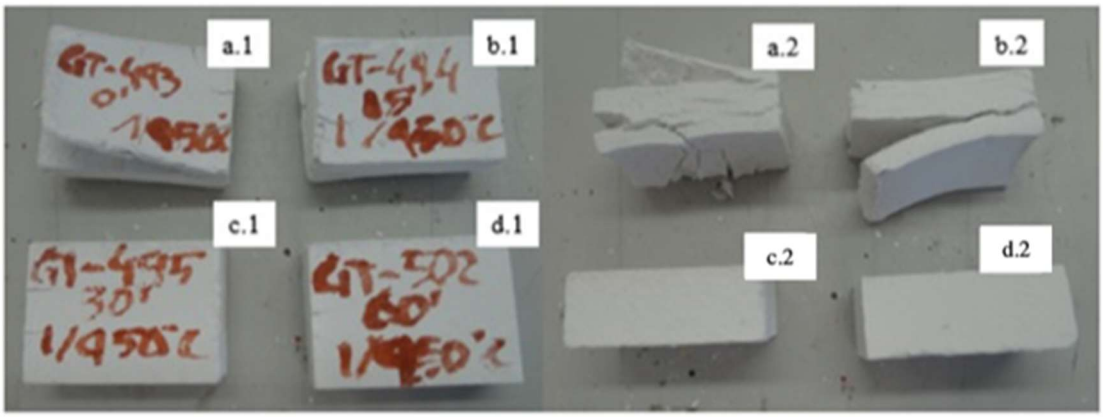

Figure 69. GT-autoclaved samples after thermal shrinkage test. (a.1/a.2) GT493; (b.1/b.2) GT494; (c.1/c.2) GT502.

The fire rate of GT samples was also a very important parameter to be determined for these kinds of materials at least for use in passive fire protection applications. By way of an example, the RF curves for GT samples with 50% SF/50% Q are shown in **Figure 70**. The fire rate values obtained were quite similar for the different samples and this is related to their similar phase composition.

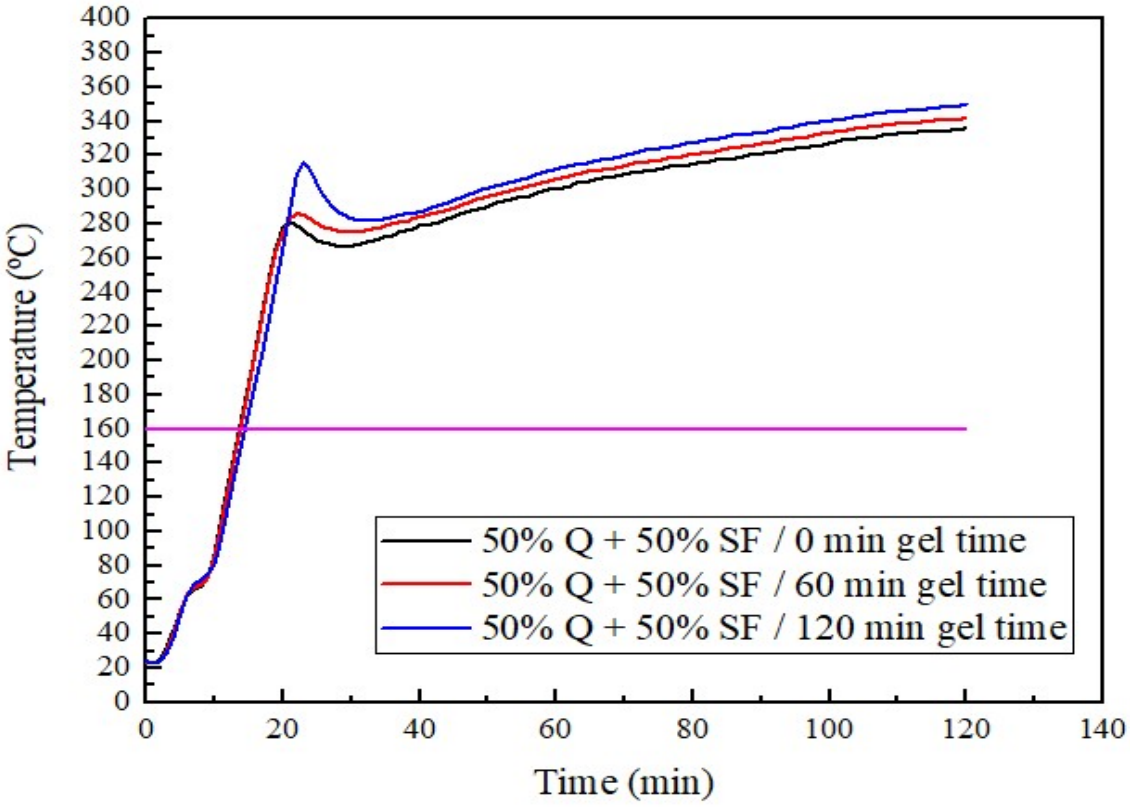

Figure 70. ISO Fire Rate curves for GT-autoclaved boards (Black) GT489; (Red) GT490; (Blue) GT491.

The condition of GT boards prepared with different C-S-H gels after firing in the electric kiln are shown in **Figure 1**. It can be observed in **Figure 71** that the integrity of the GT boards for samples with 100%SF is only good after longer gelling times while the samples prepared with a mixture of silica fume and quartz shown much less variation with the gelling time. This is in line with the thermal shrinkage.

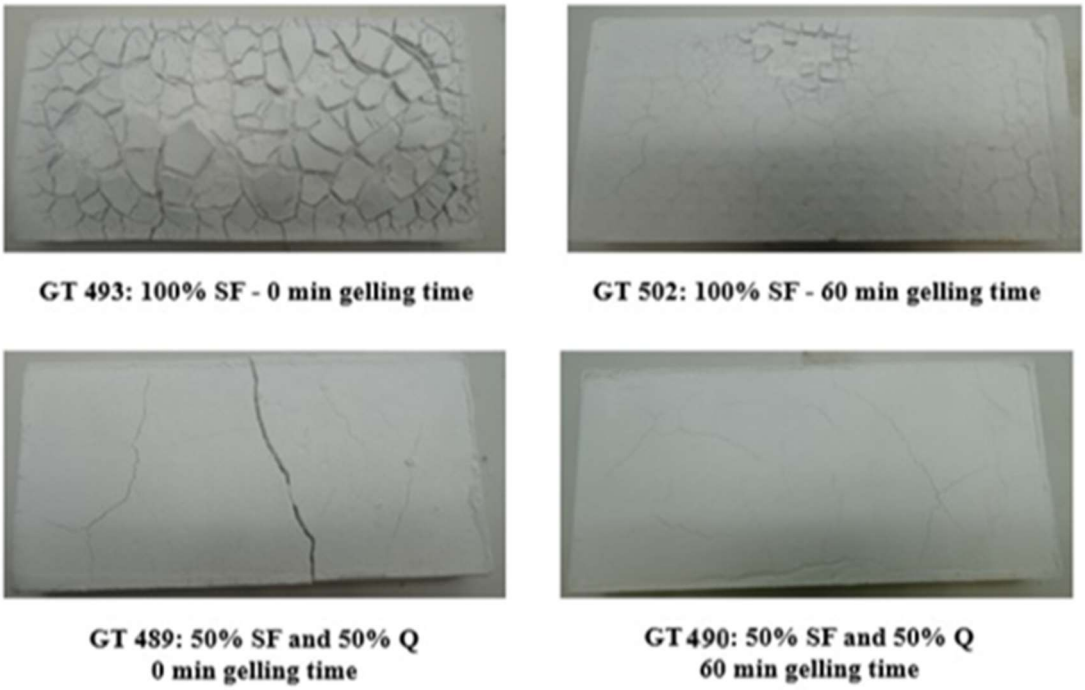

Figure 71. GT-autoclaved samples after Fire Rate ISO test.

Summarizing, it can be stated the following concerning the gelling time:

- During the pre-reaction, lime and amorphous silica react to form a low-density C-S-H gel. The longer the gelling time, the higher amount of C-S-H gel is formed and the higher the pore volume. The composition of the C-S-H-gel depends on the silica-source (silica fume only or mixture of silica fume and quartz), and this leads to different phase-compositions in the end-products.
- For mixtures using only amorphous silica, a certain gelling time is needed to obtain products with low thermal shrinkage and cracking resistance during fire tests.
- The higher the gelling time, the higher the pressure reached during the filter pressing. Thus, leading to higher values for the bending strength, though the products become more brittle.

4.1.2.2. Influence of pre-reaction temperature

The effect of the pre-reaction temperature was investigated for C-S-H-gels made with silica fume as silica source and for a gelation time of 2 hours.

Figure 72 shows the XRD patterns of the pre-reacted C-S-H gels at various temperatures, indicating on one side the reduction of reflection peaks corresponding to portlandite as pre-reaction temperature was raised up (even the full disappearance of portlandite peaks at 90ºC), and on the other side a growing evolution of the broad peak at 2θ = 28-30º related to the C-S-H gel phase formation as the temperature was increased.

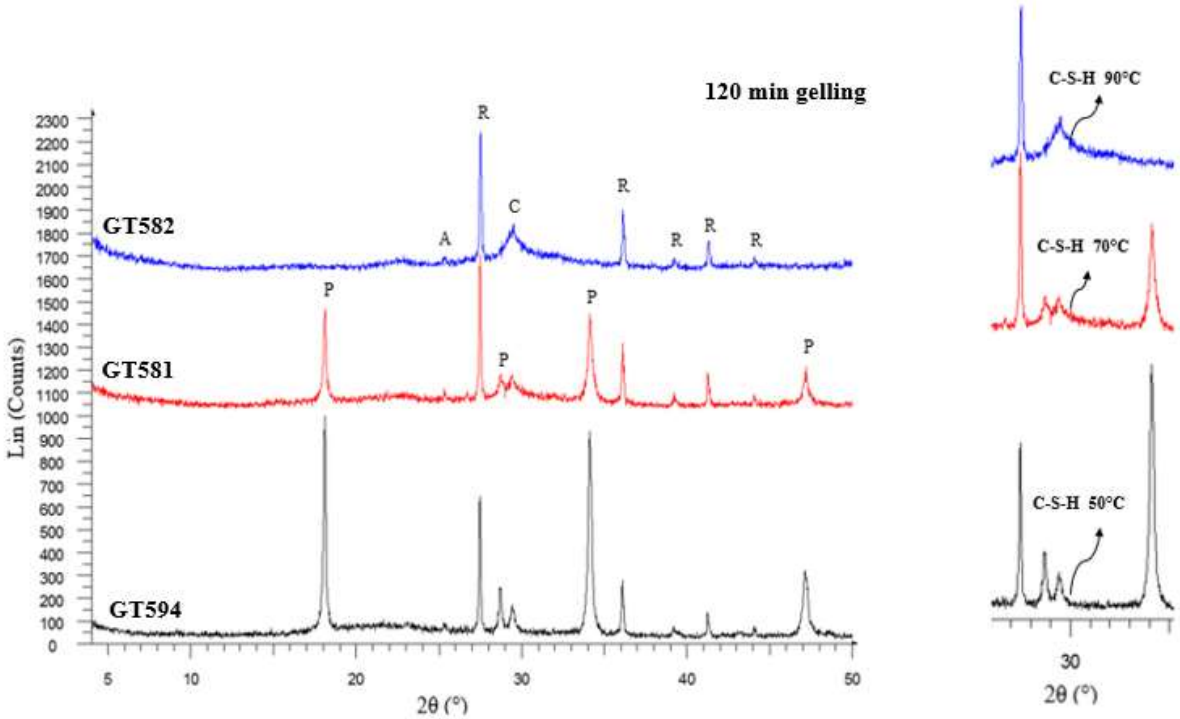

Figure 72. XRD-spectra of GT-CSH samples prepared at different pre-reaction temperature. P: Portlandite; C: Calcite; A: Anatase; R: Rutile (internal standard for Rietveld analysis).

The phase composition results of C-S-H gel preparations obtained through XRD measurements and applying the Rietveld refinement technique are given in **Table 16**. Higher temperatures accelerate the C-S-H gel phase formation as it was expected. Results on Rietveld refinement analysis indicate that still a high content of portlandite remained after the gelling stage at 50ºC for 2 hours, meaning a little quantity of amorphous C-S-H gel phase is formed and hence, a high content of unreacted silica fume. At 70ºC instead, it is appreciated a big drop on the initial portlandite content and finally, at 90ºC all the calcium hydroxide is either partially reacted or in solution.

The increase of the temperature increases the silica-solubilization, showing that this is the rate-determining step in the C-S-H-formation. With increase in temperature, the lime solubility decreases.

Sample	T_r (ºC)	Portlandite (%)	Calcite (%)	Amorphous content (%)
GT594	50	37.2	5.9	56.9
GT581	70	17.9	6.6	75.5
GT582	90	0.2	10.3	89.5

Table 17. Rietveld refinement analysis results of GT-CSH gel samples prepared at different pre-reaction temperatures.

The N_2 adsorption-desorption isotherms for the gels pre-reacted at various temperatures are presented in **Figure 37**. The three samples show type IV isotherms that are characteristic of mesoporous (2 nm < pore size < 50 nm) materials with plate-like pores. On the other hand, **Figure 74** shows the cumulative pore volume and the pore size distribution of the gels pre-reacted at 70 and 90ºC. The total pore volume, and S_{BET} increased as the pre-reaction temperature of C-S-H gel increased as seen in **Table 17**. It indicates that higher pre-reaction temperatures led the formation of more C-S-H gel including a higher quantity of pores with larger size.

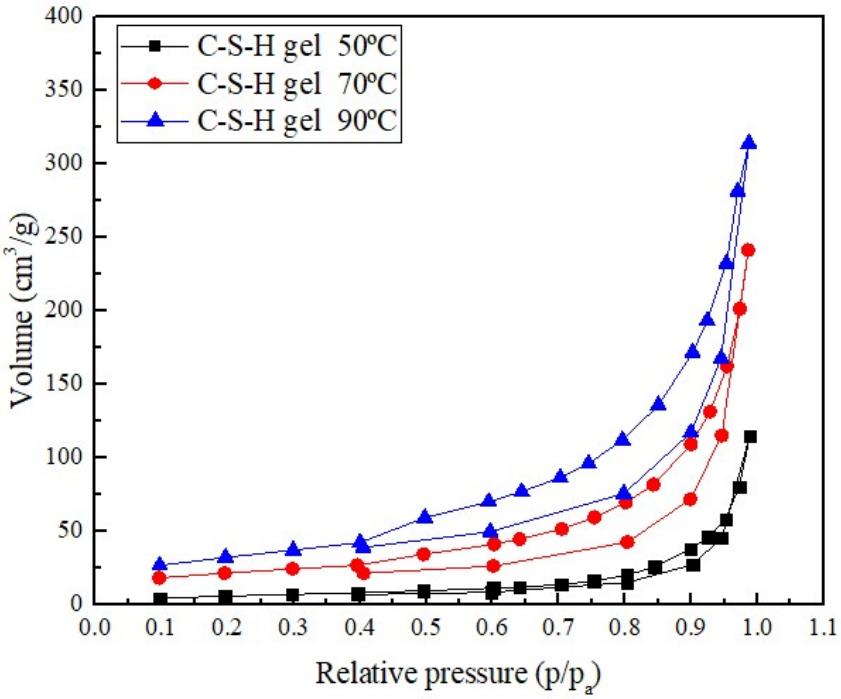

Figure 73. N_2 adsorption-desorption isotherms for gels pre-reacted at different temperature.

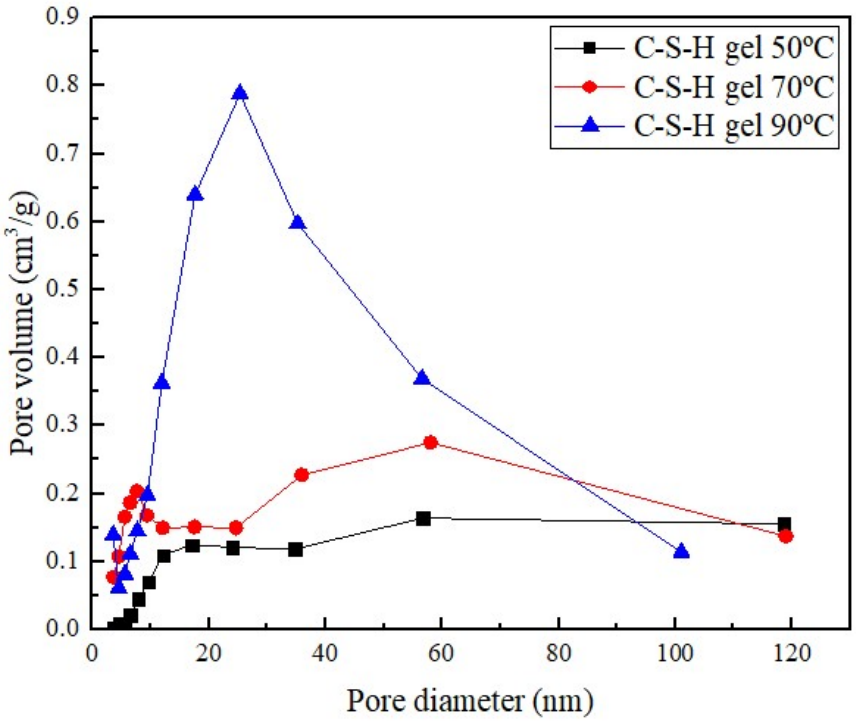

Figure 74. Cumulative pore volume and pore size distribution of gels pre-reacted at various temperature.

Sample	T_r (ºC)	Total volume (cm^3/g)	Peak pore diameter (nm)	S_{BET} (m^2/g)
GT594	50	0.18	56.7	24
GT581	70	0.29	58	45
GT582	90	0.54	25.3	80

Table 18. Specific BET surface areas and pore parameters of GT C-S-H gel preparations at different temperature.

SEM analysis confirmed that the C-S-H gel-based samples become more porous at higher pre-reaction temperatures. This might be due to differences in structure and morphology of C-S-H particles, changing from a 'flaky' structure into a more network-like structure as seen in **Figure 75**(a), (b) and (c). The increase of pre-reaction temperature gives a more open and porous structure. As the EDX analysis results, the composition of C-S-H gel preparations made at higher temperature showed lower CaO/SiO_2 ratio. It corresponds with the change on solubility of lime and silica with temperature.

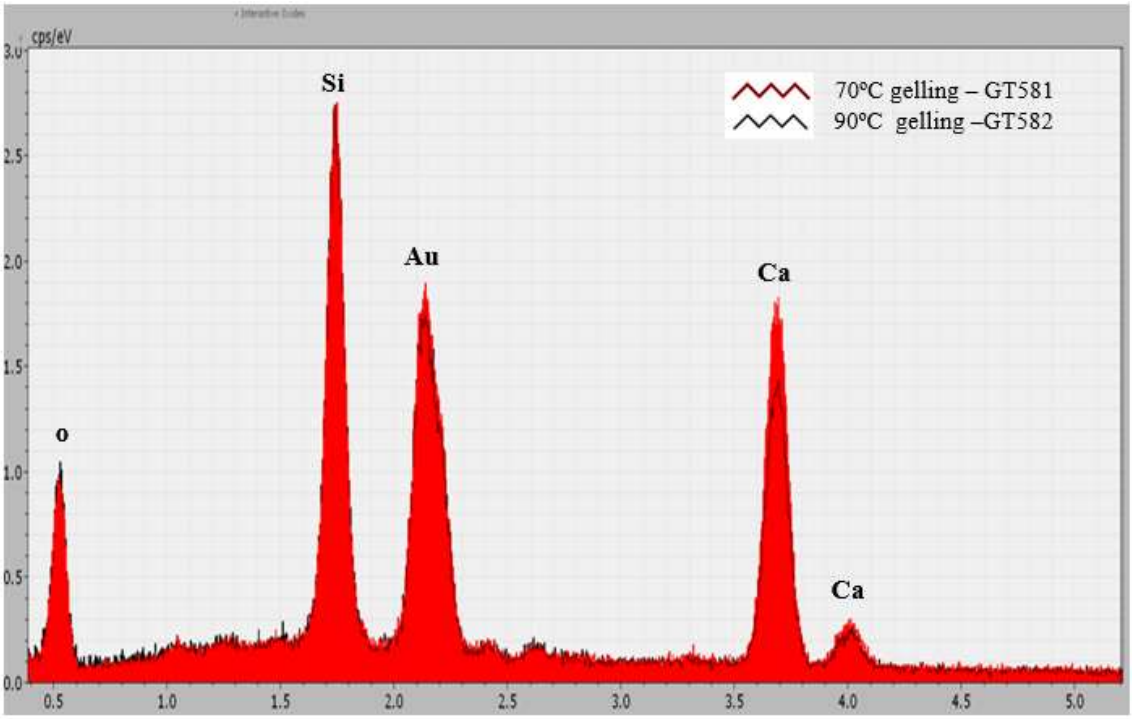

Figure 75. EDX spectra of C-S-H gel powder samples containing mainly C-S-H gel. (Red spectrum) GT581 sample obtained at 70ºC gelling; (Black spectrum) GT502 sample obtained at 90ºC gelling.

This change in composition also implies a structural change. This shows that at higher temperatures, C-S-H-gels composed of longer and more branched chains are formed instead of shorter ones in C-S-H-gel formed at lower temperatures. This higher degree of ordering and connection makes the recrystallization to xonotlite somewhat more difficult. Regarding to the distribution of chemical species in the C-S-H gel samples pe-reacted at 70ºC and 90ºC, FTIR spectra shown in **Figure 76** present similar pattern to the ones of C-S-H gels synthesized after 15 and 60 minutes of gelling time with some minor points of differences related to the longer gelling time.

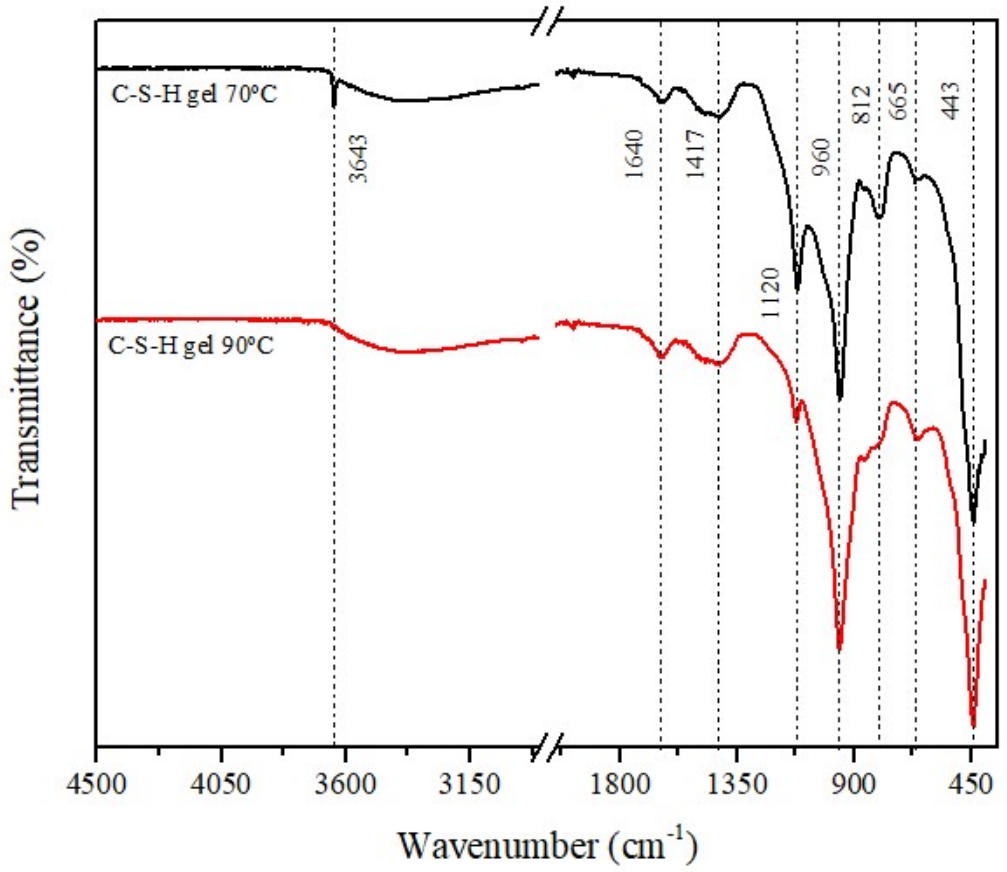

Figure 76. FT-IR spectra of C-S-H gel samples made at 70°C and 90°C. (Black spectrum) GT581; (Red spectrum) GT582.

Again, the main absorption bands detected in these samples are listed in **Table 19**. And the corresponding type of vibrational modes of these absorption bands are described too.

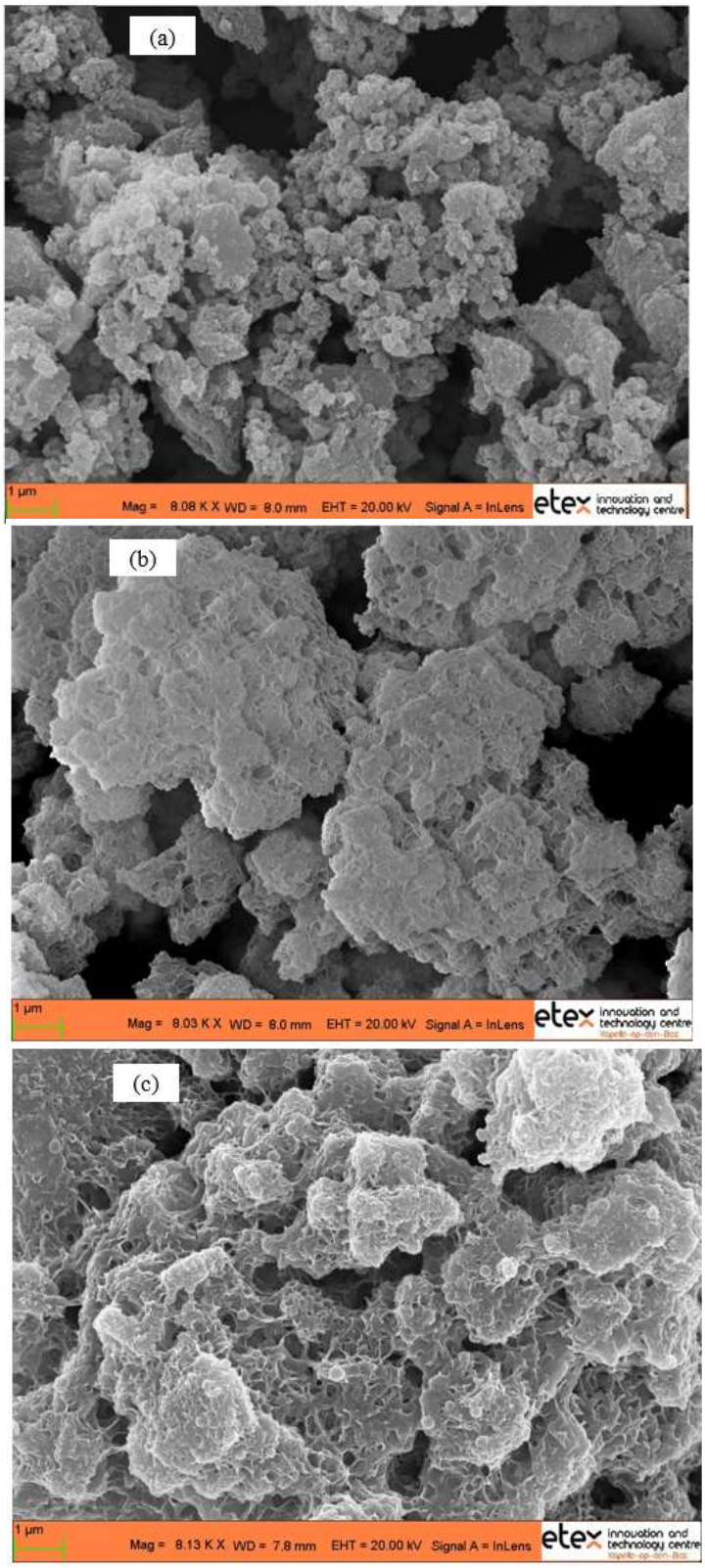

Figure 77. SEM micrography of C-S-H gel pre-reactions. (a) GT594; (b) GT581; (c) GT582.

Absorption band	Type of vibrational mode	Evolution over temperature
443 cm^{-1}	Si-O-Si bending vibration mode due to SiO_4 tetrahedral deformation	Increasing. Higher peak intensity
665 cm^{-1}	Si-O-Si bending vibration of paired SiO_4 tetrahedra	No variation
812 cm^{-1}	Si-O stretching vibration of Q^1 tetrahedra	Decreasing. Lower peak intensity
960 cm^{-1}	Si-O stretching vibrations of the Q^2 tetrahedra	Increasing due to SiO_2 polymerization. Higher peak intensity
1120 cm^{-1}	Si-O asymmetric stretching vibrations associated to SiO_4 tetrahedra in Q^4 units from silica fume	Decreasing
1.417 cm^{-1}	C-O (υ_3) asymmetric stretching vibrations (CO_3^{-2}) due to carbonatation of calcium hydroxide	Slight increasing
1.640 cm^{-1}	H-O-H bending vibration of H_2O	Slight increasing
3.643 cm^{-1}	Ca-O-H stretching mode of vibration	Decreasing

Table 19. Characteristic absorbance bands for Calcium Silicate Hydrate (C-S-H).

In addition to the C-S-H gel particles formation from 50ºC up to 90ºC, it must be pointed out the presence of some remaining and partially dissolved portlandite crystals visible in the SEM micrographs shown in **Figure 78** as well as spherical particles of unreacted silica fume also detected (see **Figure 79**).

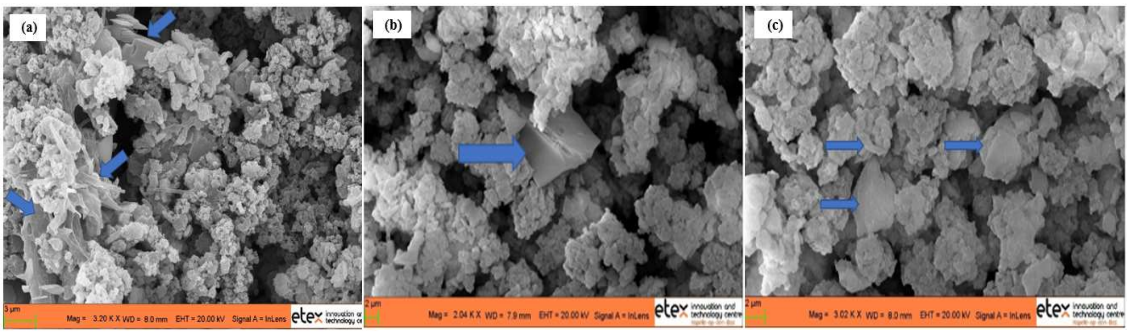

Figure 78. SEM images of C-S-H gel preparations using various gelling temperatures. Blue arrows point out portlandite unreacted or partially reacted crystals. (a) GT594; (b) and (c) GT581.

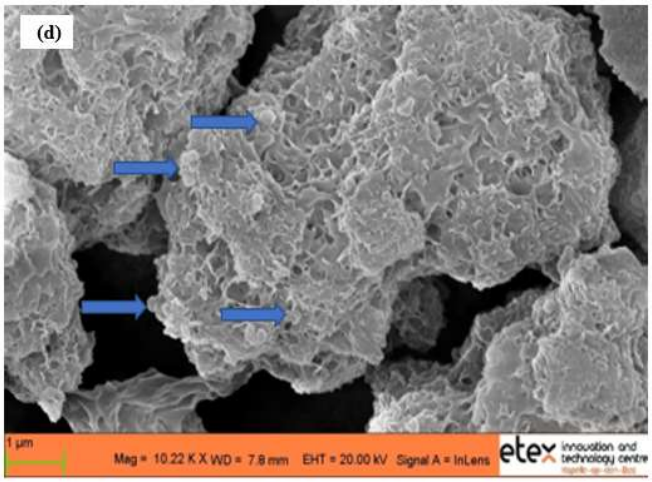

Figure 79. (d) SEM image of C-S-H gel preparation at 90ºC. Blue arrows indicate residual silica fume microspheres.

Due to the lower density of the C-S-H-gel made at higher temperature, some breakage of agglomerates occurs during the pre-reaction stage most likely owing to the mechanical shear produced by the metallic stirrer. Resulting on a slight shift of the particle size distribution as can be seen below in **Figure 80**.

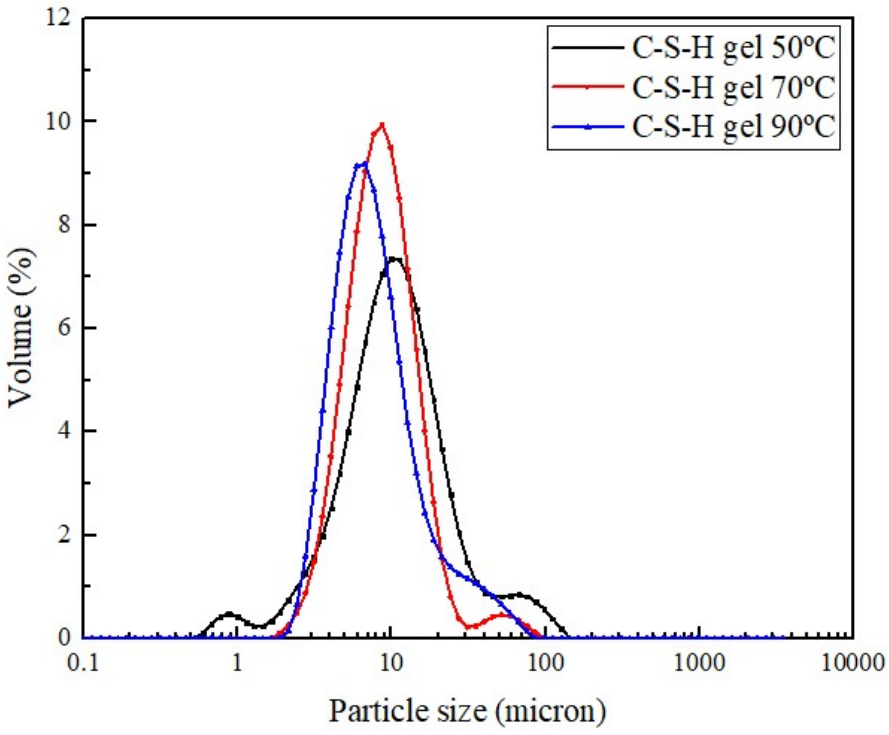

Figure 80. Particle Size Distribution curves of C-S-H gel pastes formed at different pre-reaction temperature. (Black curve) GT594; (Red curve) GT581; (Blue curve) GT582.

The phase composition for the end-products, as determined by XRD is shown in **Figure 81** and the Rietveld analysis is given in **Table 19.**

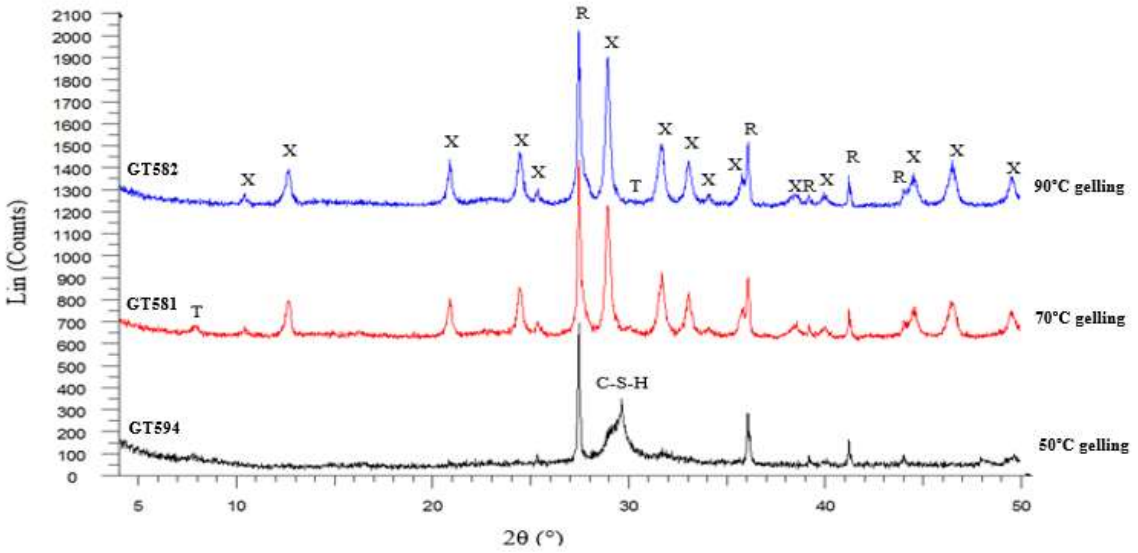

Figure 81. XRD-spectra of GT-autoclaved samples prepared via different pre-reaction temperature. (T) Tobermorite; (X) Xonotlite; (C) Calcite; R: Rutile (internal standard for Rietveld analysis).

According to the XRD spectra and the Rietveld analysis, GT594 sample shows clearly a very poor recrystallization of C-S-H gel into xonotlite and the presence of semicrystalline C-S-H phase at 2θ = 29-30º after the hydrothermal cycle. Conversely, a high degree of crystallinity is observed for GT581 and GT582. Xonotlite is the main C-S-H phase in both XRD-patterns. These differences are mainly related to C-S-H gel characteristics.

In case of a C-S-H gel pre-reacted at 50ºC, this is poorly formed (very low content) during the gelling step and its chemical structure is not favorable to be recrystallized easily into xonotlite (expected too high CaO/SiO_2, corresponding to the solubilities of $Ca(OH)_2$ and SiO_2 at low temperature). Therefore, the main C-S-H gel formation occurs later, during the autoclaving. Most likely a Si-rich C-S-H gel is synthesized which hardly recrystallizes into xonotlite. The reason for this Si-rich C-S-H gel formation is that at these hydrothermal conditions, calcium hydroxide solubility is low whilst silica fume solubility is increased.

Sample	T_r (ºC)	Xonotlite (%)	Tobermorite (%)	Calcite (%)	Amorphous content (%)
GT594	50	42.4	14.9	7	35.6
GT581	70	81.7	6.5	0.8	10.9
GT582	90	77.9	0.4	0.7	21

Table 20. Rietveld Refinement analysis results of GT-autoclaved boards prepared at different pre-reaction temperature.

However, this does not occur from a C-S-H gel is pre-reacted at higher temperature, for example 90ºC. High amounts of C-S-H-gel form during the gelling conditions and a C-S-H with C/S ratio around 1 is expected that recrystallizes into xonotlite in hydrothermal conditions. For a higher pre-reaction temperature (≥70ºC), the C-S-H gel phase formed tends to recrystallize into xonotlite in hydrothermal conditions without any problem.

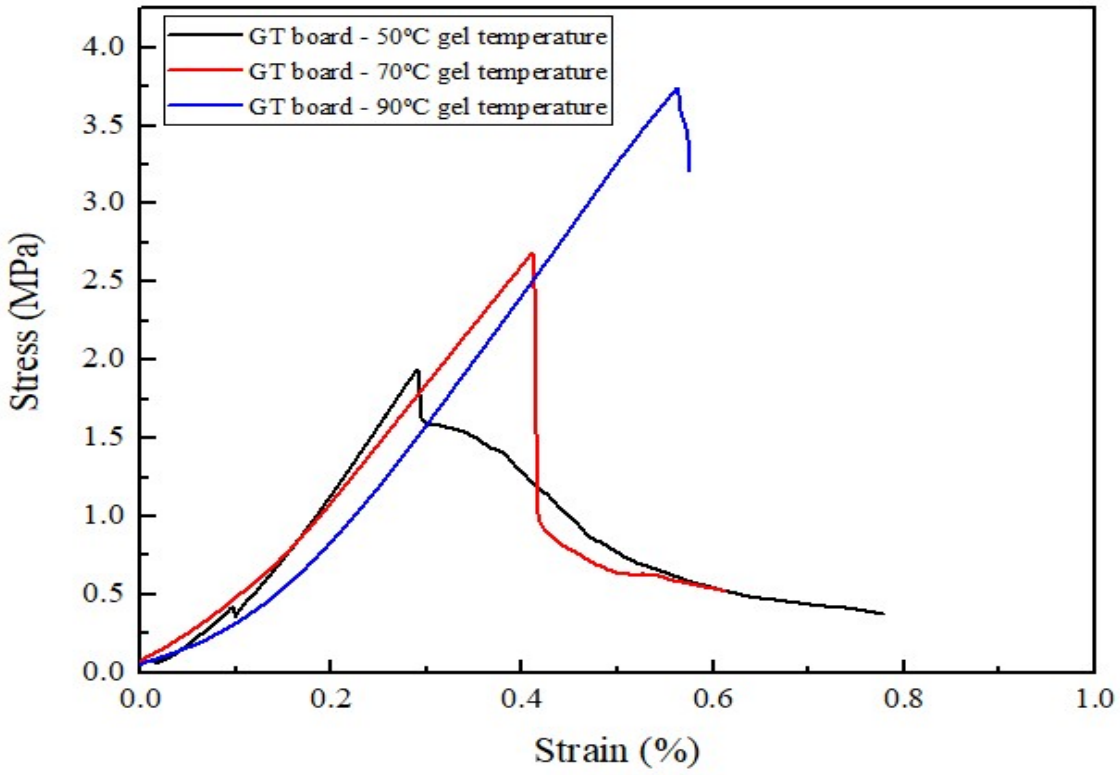

Figure 82. Stress-strain curves for GT-autoclaved boards. (Black) GT594; (Red) GT581; (Blue) 582.

.

The mechanical properties of the GT-autoclaved boards were also evaluated. As mentioned in the previous section, the pressing force used to shape the C-S-H gel does influence the calcium silicate hydrate-based slurry processing and so, the mechanical properties of the final products. It was found that this force was increased up to 180 kN when the pre-reaction time is extended to 2 hours and the pre-reaction temperature is 90ºC, because of a high increase on the low-density C-S-H particles formation.

The 3-bending point tests of GT594, GT581 and GT582 samples give stress-strain curves as shown **Figure 82** with strength values that increase with the gelling temperature and in general but with quite low fracture toughness.

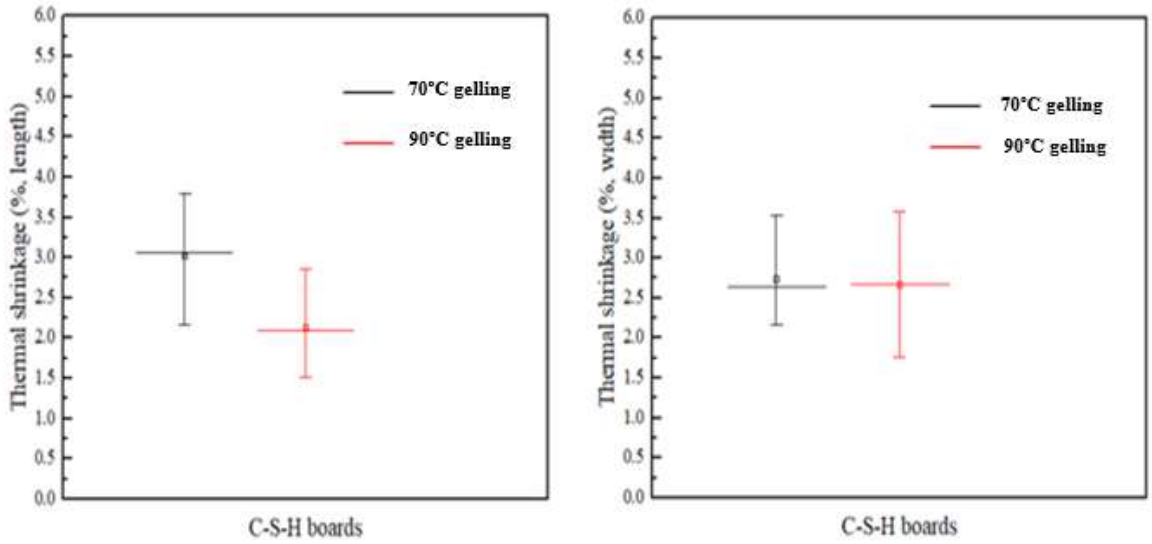

Figure 83. Whisker-plot diagrams of thermal shrinkage values for GT-autoclaved samples. (Black) GT581; (Red) GT582.

The thermal shrinkage of GT581 and GT582 boards made from C-S-H gel formed at 70 and 90ºC are quite comparable as can be seen in the whisker-plot diagrams plotted in **Figure 83**. The samples show good thermal integrity after the thermal shrinkage test. On the other hand, the sample GT594 shows high shrinkage and was completely cracked after the high temperature exposure (see **Figure 84**). This is due to the low content of xonotlite and the high amount of amorphous phase.

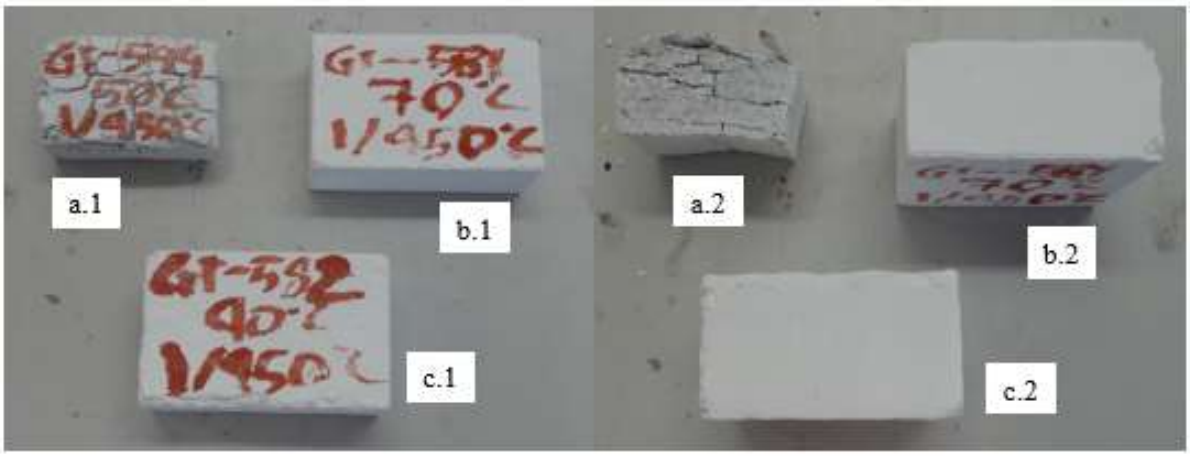

Figure 84. GT-autoclaved samples after thermal shrinkage test. (a.1/a.2) GT594; (b.1/b.2) GT581; (c.1/c.2) GT582.

To wrap up, a number of partial conclusions were deducted from the results above discussed concerning the influence of the pre-reaction temperature on the C-S-H gel formation and these are given below.

- The conclusions obtained on the study of pre-reaction temperature impact are quite similar as for the investigation of pre-reaction time influence.
- If there is an increase of pre-reaction temperature, a completer and more developed C-S-H gel formation occurs and consequently, it recrystallizes in the second step into xonotlite. The xonotlite-based boards possess acceptable thermal stability and keep their integrity at high temperature.
- Higher pre-reaction temperature favors the formation of higher quantity of low-density C-S-H gel. This results in end-products with higher mechanical strength, but low fracture toughness.

4.1.2.3. Influence of pre-reaction stirring: Dynamic gelling vs Static gelling.

Amongst the main processing parameters to obtain C-S-H products via Geltank, the agitation for the mixing of raw materials during the pre-reaction stage is an essential one to be investigated. Stirring during C-S-H gel synthesis has impact on the solubilization and diffusion rates, on the nucleation and growth of phases and the aggregation of phases. Unfortunately, no reporting of this in the literature was found. So, the effect of stirring intensity on the gelling step was examined in this work as well as the impact of non-stirring. A comparison between dynamic (via mechanical stirring) and static (without mechanical stirring) gelling conditions was also made.

In the dynamic gelling protocol used in this work, the different ingredients from the starting recipe, are mechanically stirred in an aqueous suspension using the metal stirrer seen in **Figure 85** which is driven by an electronic device. Different trials were performed applying high and low agitation velocities for the mixing of calcium hydroxide, silica fume and water in the C-S-H gel pre-reaction step.

Figure 85. Metal stirrer composed of four curved cross-shape blades used as mixing tool during pre-reaction stage.

There are a number of essential requirements for the C-S-H gel pre-reaction stage to be successful, and one of those requirements is the type of stirrer which must be such that:

- Aggregates of lime and silica and C-S-H are formed that convert into xonotlite throughout the hydrothermal cycle.
- Sedimentation of reactants is avoided.
- Segregation by centrifugal forces is avoided.
- Lump-formation is avoided.

As the standard experimental procedure explained, the stirring speed was initially high enough (500 rpm) to keep more dense phases (lime and silica) in suspension during the mixing. Later, when the C-S-H gel starts developing, the speed was reduced (350 rpm) to avoid breaking up and damage the aggregates formed containing C-S-H gel phases. However, in these tests both low and high stirring speed were used during the gelling.

The experiments were done using mixtures from amorphous silica (silica fume) as the unique silica source, and calcium hydroxide. These mixtures were stirred at different speed, 200 rpm and 800 rpm. The application of higher speed results in some decrease of the particle size of C-S-H gel aggregates. The particle size distribution curves of the GT C-S-H gel preparations, GT580 and GT579 are shown in **Figure 86**.

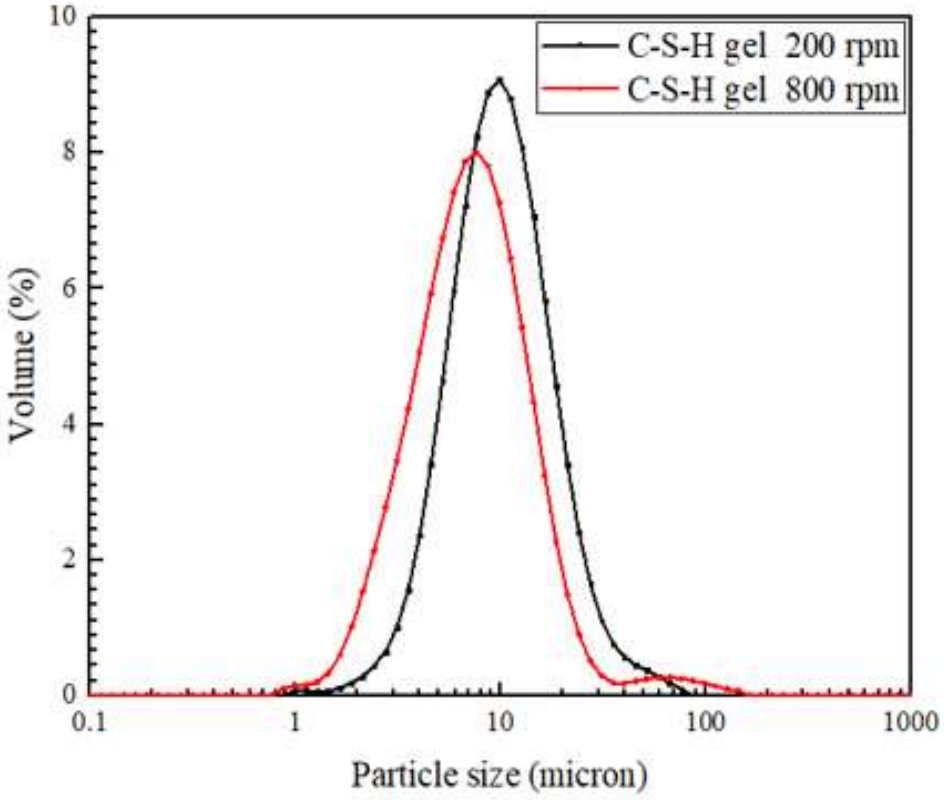

Figure 86. Particle Size Distribution (PSD) curves of C-S-H gel preparations formed at different pre-reaction stirring. (Black curve) GT580; (Red curve) GT579.

X-ray diffraction patterns of both samples show that the reduction of the initial portlandite content was somewhat larger when applying lower speed, 200 rpm (see **Figure 87**) instead of higher agitation velocity. This might be due to the fact that under higher rotation speed, aggregates of C-S-H, $Ca(OH)_2$ and silica fume are broken. Then, the reactants separate from one another. In the sample made applying low stirring speed, a higher degree of carbonation was also observed.

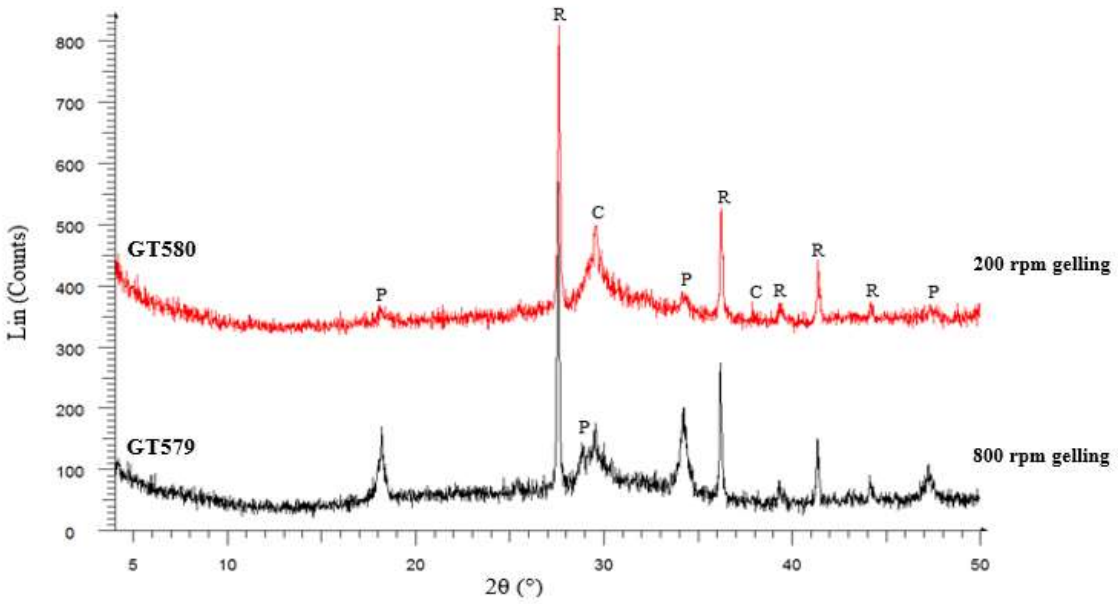

Figure 87. XRD spectra of GT-CSH samples prepared at different pre-reaction stirring. P: Portlandite; C: Calcite; R: Rutile (internal standard for Rietveld analysis).

It is clearly seen that a slight broader C-S-H gel peak appears at $2\theta = 28\text{-}30^{o}$ in GT580, whilst in XRD spectrum of GT579, that peak is a little narrower. It might be due to a more favorable incorporation of the raw materials ($Ca(OH)_2$ and SiO_2) in the C-S-H gel particles of larger dimensions synthesized at low stirring speed. Meaning that, C-S-H gel was gluing the $Ca(OH)_2$ and SiO_2 particles together. At higher agitation velocity, aggregates might be broken by shear forces and reacting phases separated. The effect of agitation is mainly reflected on the particle size of C-S-H gel and the porosity as exposed below.

Sample	v_r (rpm)	Portlandite (%)	Calcite (%)	Amorphous content (%)
GT579	800	10.2	6.9	82.9
GT580	200	3	11	86

Table 21. Rietveld refinement analysis results of GT-CSH gel samples prepared at different pre-reaction stirring (v_r).

It was found a C-S-H gel with higher porosity and somewhat larger pores in conditions of lower stirring speed. This is visible from the nitrogen adsorption-desorption isotherms and corresponding pore size distribution curves shown in **Figures 88-89**. C-S-H gel preparations (GT580-800 rpm/GT579-200 rpm) show again type IV isotherms. Meaning the same mesoporous material (2 nm < pore size < 50 nm) was obtained regardless the agitation velocity applied during the C-S-H gel pre-reaction stage.

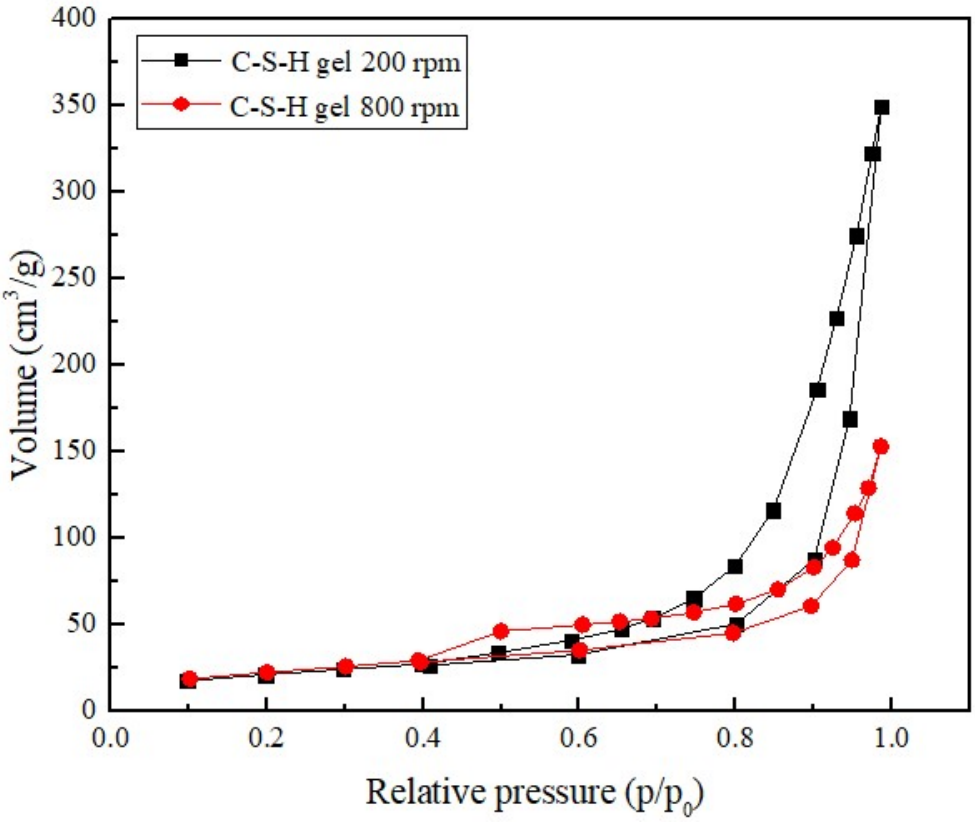

Figure 88. N_2 adsorption-desorption isotherms for gels pre-reacted at different stirring speed.

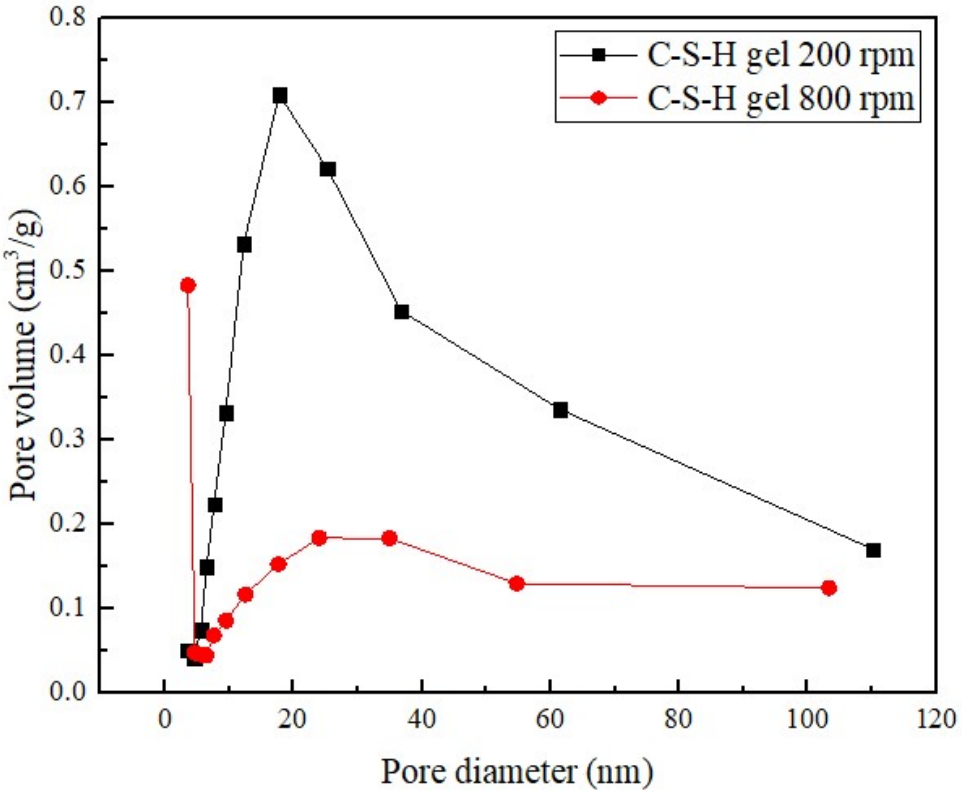

Figure 89. Cumulative pore volume and pore size distribution of gels pre-reacted at different stirring speed.

On the other hand, it can be seen in **Table 21** that the differences in S_{BET} values for samples prepared with different mixing speed are small. The use of higher speed leads to slightly higher values possibly as a result of the shift of the particle size distribution to smaller sizes.

Sample	v_r (rpm)	Total volume (cm^3/g)	Peak pore diameter (nm)	S_{BET} (m^2/g)
GT580	200	0.57	12.3	75
GT579	800	0.24	12.6	80

Table 22. Specific BET surface areas and pore parameters of GT-C-S-H samples at different stirring speed.

A SEM analysis was also carried out to have more information about the morphology, and some clear differences were observed concerning the particle size of C-S-H gel clusters formed at both low stirring speed (GT580) and high stirring speed (GT579). Applying a lower rotational velocity of 200 rpm through the C-S-H gel pre-reaction stage, larger clusters composed of nanocrystalline C-S-H gel particles, and unreacted portlandite crystals and silica fume particles are sticking together as shown in **Figure 90**. Even an enormous block formed by the union of a lot of C-S-H gel clusters was found in the GT580 sample. It indicates that a slow and less aggressive agitation of the raw materials favours the growth of C-S-H gel aggregates, while in conditions of higher rotation speed CSH-aggregates are broken and part of the porosity gets lost or less pores develop.

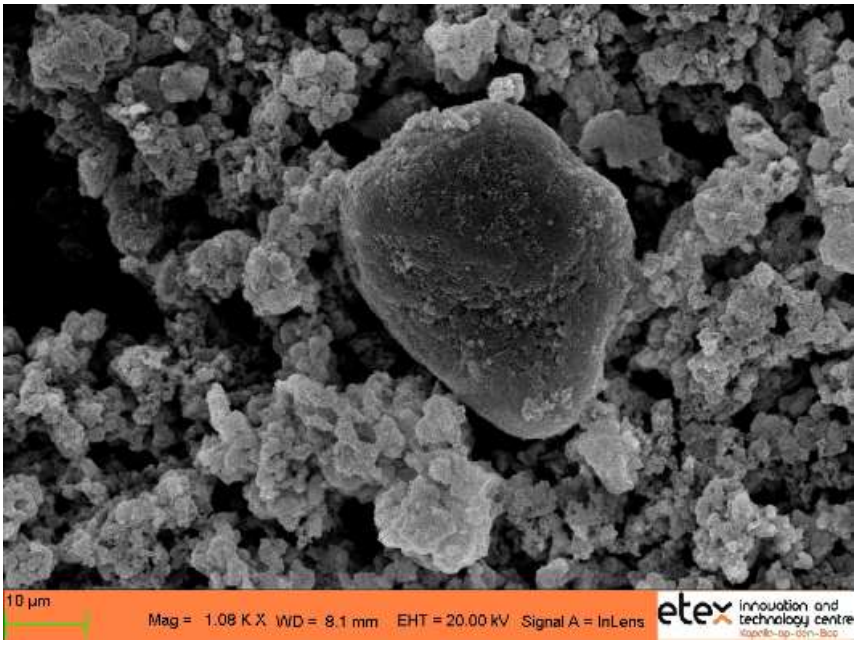

Figure 90. SEM image of GT580, as C-S-H gel preparation stirred at 200 rpm.

On the other hand, the agglomerates or clusters of C-S-H gel particles obtained at higher stirring speed (800 rpm) presented smaller diameters. A high content of these small agglomerates can be seen in **Figure 91**. The application of high stirring speed, limits the agglutination of particles, perhaps breaking them up. On the other hand, C-S-H gel particles formed when applying higher agitation velocity seem to be denser and contain a less porous microstructure. This is visible in the results of BJH analysis.

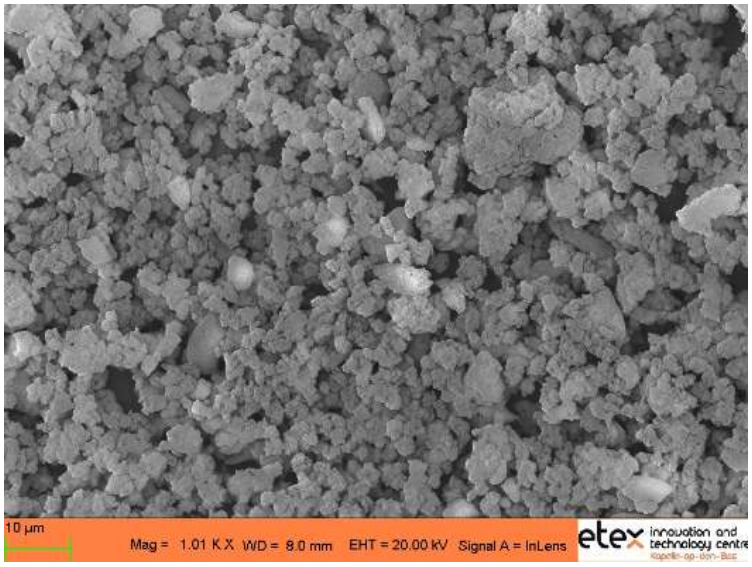

Figure 91. SEM image of GT579, as C-S-H gel preparation stirred at 800 rpm.

After autoclaving stage GT579 and GT580 samples presented similar average contents of highly crystalline phases such as xonotlite and tobermorite as **Figure 92** shows. Meaning that agitation velocity of raw materials for C-S-H gel pre-reaction has not a great impact on the re-crystallization process.

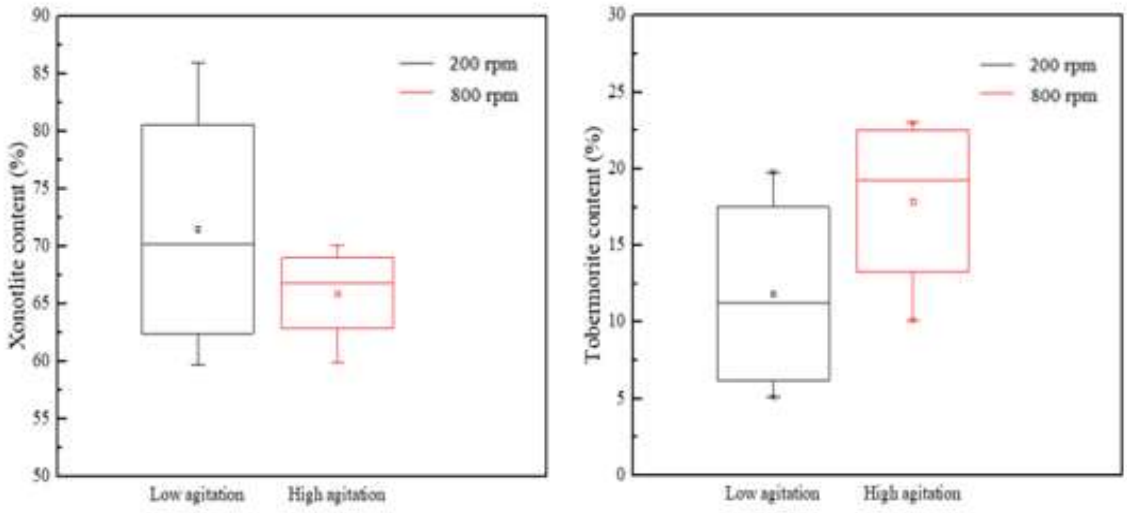

Figure 92. Whisker-plot diagrams of xonotlite and tobermorite content for GT-autoclaved samples (GT579/GT580) prepared from C-S-H gel pre-reacted at high and low agitation.

Reviewing the stress-strain curves plotted in **Figure 93**, it is observed a great change on the mechanical behaviour of GT579 and GT580 boards. The autoclaved crystalline matrix from a C-S-H gel prepared at higher stirring speed (GT579), in this case 800 rpm, shows a very high modulus of rupture (>4Mpa). Conversely, GT580 sample has a microstructure such that allows to reach acceptable flexural strength values over 2MPa though seems less fragile.

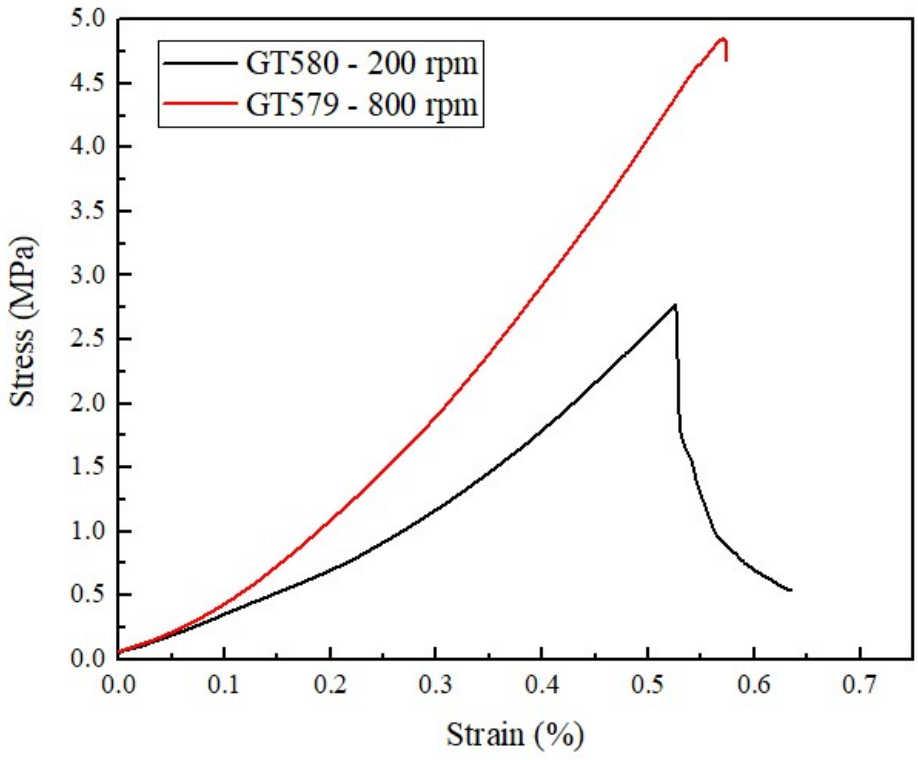

Figure 93. Stress-strain curves for GT-autoclaved boards. (Black) GT580; (Red) GT579.

That variation found on the mechanical response of these GT boards might be related with the morphology of the xonotlite crystals grown during the hydrothermal treatment. Looking at the Field-Emission Scanning Electron Microscopy micrographs shown in **Figure 94**, it is clear that the morphology of xonotlite crystals differs from GT579 to GT580. For sample GT579 made with high agitation velocity, thicker and shorter xonotlite crystals were found, whereas that in sample GT580 made with low stirring speed, longer and thinner xonotlite needles seem to be developed during the autoclaving process.

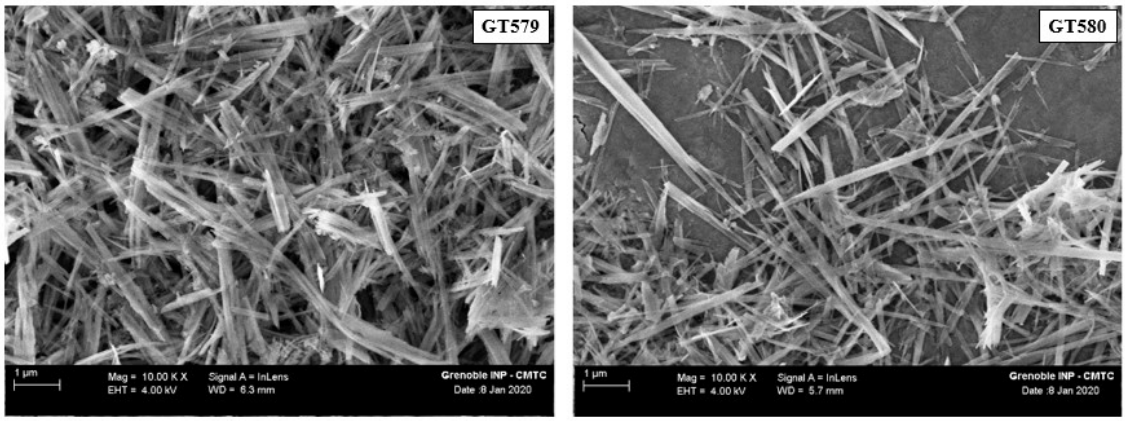

Figure 94. FESEM images of xonotlite fibres crystallized after autoclave cycle. (Left) GT579 board prepared via C-S-H gel at high stirring speed; (Right) GT580 board prepared via C-S-H gel at low stirring speed.

The thermal shrinkage variations were similar for the two GT boards made from C-S-H gel stirred at different speed (see **Figure 95**). This is because of the impact of the stirring speed on phase composition of the final products was very small and within the spread of error as seen in **Figure 92**. Thereupon, the thermal stability of GT579 and GT580 at high temperature is not affected by the agitation velocity applied during the C-S-H gel formation.

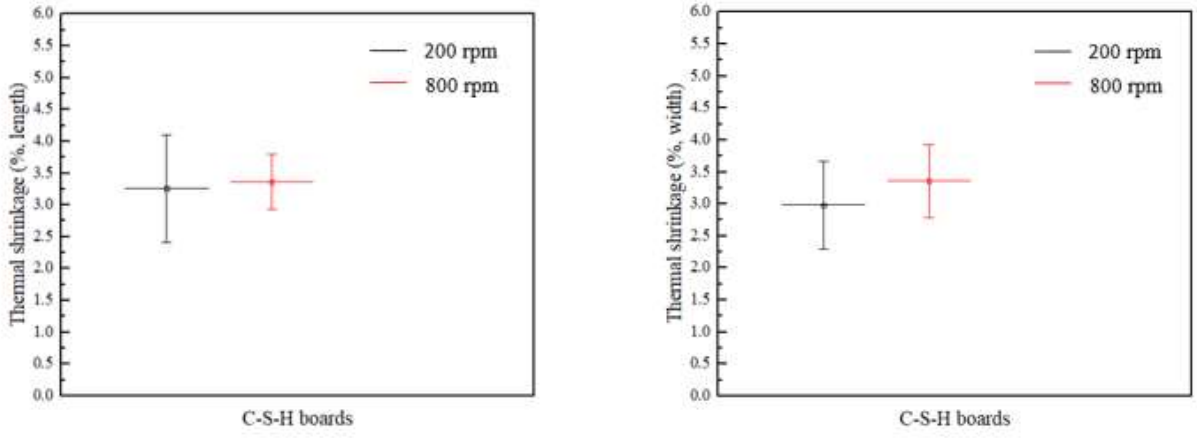

Figure 95. Whisker-plot diagrams of thermal shrinkage values for the length and width corresponding to the GT579 (800 rpm) and GT580 (200 rpm) samples.

As an extreme case of C-S-H gel pre-reaction, it was also investigated a particular gelling step in conditions where no stirring was applied. Only the raw materials were firstly mixed by stirring up to the pre-reaction temperature was reached, that is, 90ºC. After that, the slurry is poured in a plastic container. It is closed and cured for 2 days at 80ºC inside a kiln. This type of gelling process will be called '*static gelling'* whereas that the usual applied gelling step under agitation that was called dynamic gelling.

X-ray diffraction patterns of the C-S-H gel synthesized from lime and silica fume via static and dynamic gel pre-reaction are shown in **Figure 96**. For the dynamic gelling process, the full reaction of portlandite is reached in 1 hour. On the other hand, in the static gelling process 2 days were needed to react most of the portlandite. The much faster reaction in the dynamic gelling conditions is because of flow brings the different reacting species in contact with each other. In the static process, much more diffusion is required before reaction occurs. A disadvantage of the dynamic process is that in these conditions, much more carbonation occurs.

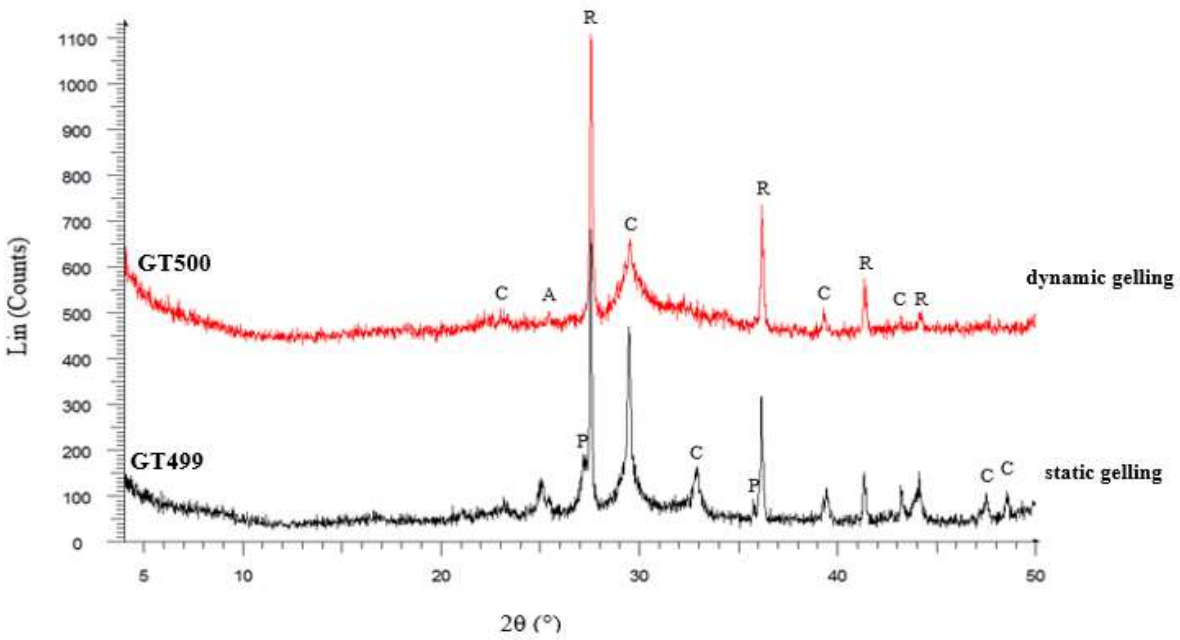

Figure 96. XRD-spectra of C-S-H gel preparations made by means of different gelling type. (Black) static gelling for 2 days; (Red) dynamic gelling for 1 hour. P: Portlandite; C: Calcite; A: Anatase; R: Rutile (internal standard for Rietveld analysis).

Figure 97 shows the cumulative pore volume and the pore size distribution of the C-S-H gel preparations obtained via static gelling and dynamic gelling. The differences in porosity are large between GT499 and GT500. Stirring of the mixture of raw materials is definitely very important to develop a highly porous C-S-H gel structure of a suitable composition and structure to recrystallize in hydrothermal conditions. This is much less the case for the static gelling process.

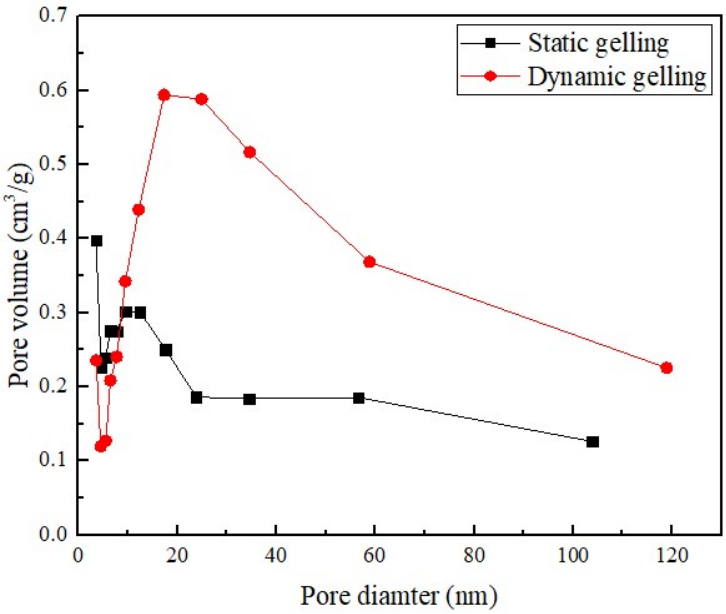

Figure 97. Cumulative pore volume and pore size distribution of C-S-H gels pre-reacted in static and dynamic gelling conditions. (Black) GT499-static gelling; (Red) GT500-dynamic gelling.

For equal crystalline phase composition in the end-product after hydrothermal treatment, obtained either for GT500 sample (prepared via dynamic gelling-stirring 1 hour) or GT499 sample (prepared via static gelling-2 days curing inside an oven), it was observed that the dynamic gelling led to better mechanical properties (see **Figure 98**) which is due to the formation of a more porous C-S-H gel.

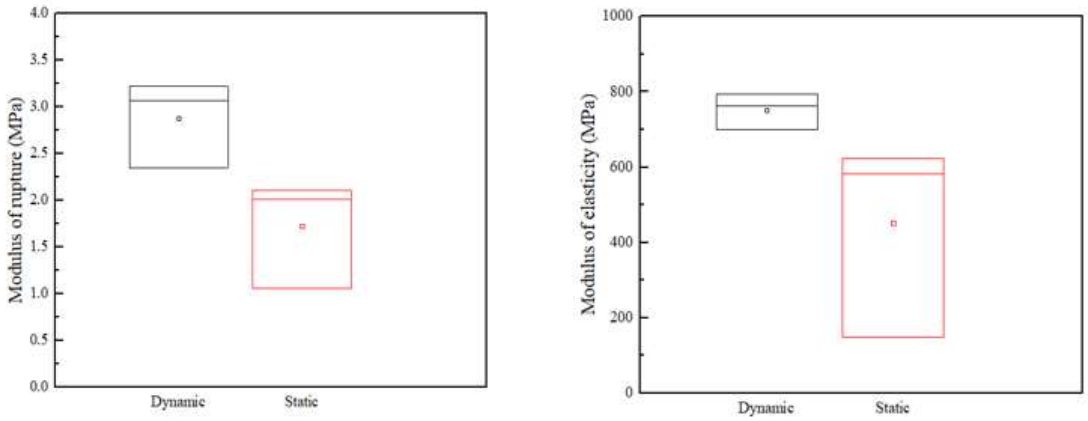

Figure 98. Bending strength and E-modulus for GT-autoclaved boards made from C-S-H gel preparations via dynamic and static gelling.

The main conclusions concerning the effects of the stirring conditions are the following:

- The dynamic gelling favors the kinetics of C-S-H pre-reaction and results in the formation of a more porous gel. For static gelling, the process is very slow and limited by longer diffusion distances for reaction to occur. Less porous materials were obtained via static gelling.

- The use of a rather low agitation velocity in the gelling step is recommended as it seems to lead to a more porous gel and an end-product that consist of longer and finer xonotlite. This morphology results in better mechanical properties.

4.1.2.4. Influence of silica fume source

Silica fume or also named microsilica was used as one of the silica sources that acts as a precursor in the chemical reaction to synthesize C-S-H gel. Amorphous silica was selected since it its more reactive than quartz and has a certain solubility at the temperature (90ºC) used for the C-S-H gel pre-reaction. Silica fume is an amorphous, highly reactive pozzolan and it possesses high specific surface area values. It is an amorphous form of SiO_2. Silica fume appears as an ultrafine powder with a colour variation from white to dark grey (depending on the Fe and C content) collected as a by-product of the manufacture of metallurgical silicon, ferro-silicon and silico-alloys. This is produced from high pure silica, normally quartz, when this is reduced by C in electric arc furnace with electrodes at temperatures above 2000ºC. The chemical reaction is shown below:

$$SiO_2\ (s) + C\ (s) \longrightarrow Si\ (s) + CO_2\ (g)$$

Then, it is formed when SiO-gas given off in the reduction of quartz, mixes with O_2 and condenses as silica-fume **[2]**. A dust-like silica fume is generated and collected in bag-filters. Silica fume particles are spherically shaped and very fine, having a mean size of 0.1–0.3 μm as shown in **Figure 99**. In some cases, individual particles can fuse together to form small agglomerates that may range from 1 to 100 μm in size (ACI-Committee-234, 2006). The specific gravity of silica fume is 2.20–2.30. The surface area of silica fume particles can range between 13,000 and 30,000 m^2/kg, measured by nitrogen absorption equipment. The fine particle size of the as-produced silica fume makes it challenging to handle, from a practical perspective. To improve the ease of handling, alternative forms of silica fume have been used to overcome this practical difficulty. Some suppliers handle silica fume as a water-based slurry, and others densify and compact the silica fume, which can markedly reduce the amount of dust associated with the fine particles. The bulk density of the as-produced silica fume ranges from 130 to 430 kg/m^3. Compacted or densified silica fume and silica fume slurry have a bulk density that can range from 200 to 600 and 1300 to 1400 kg/m^3, respectively (ACI-Committee-234, 2006). Silica fume is often used to improve cementitious based products, SCM's, by

the pozzolanic reaction and the formation of denser matrices. Silica fume is also used as silica source in the formation of Ca-silicates. It can also be pelletized, whereby the silica fume is mixed with water and some cement. The silica fume pellets can be ground with Portland cement clinker to form a blended cement.

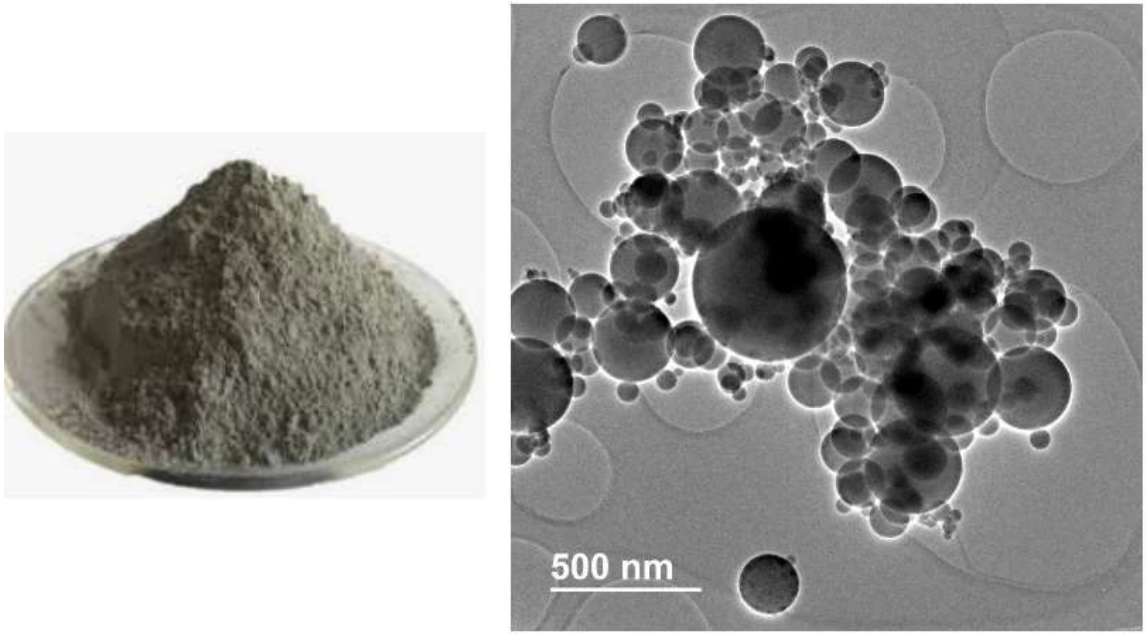

Figure 99. Images of silica fume aspect at the macroscopic and microscopic level. (Left) Silica fume as fine grey powder; (Right) High-resolution Transmission electron microscopy photograph showing individual particles of microsilica.

In this work, we found that the particle size distribution of amorphous silica plays a crucial role in the chemical reaction with $Ca(OH)_2$ for the conversion into C-S-H, as well as in the crystallization into xonotlite and/or tobermorite later on. Therefore, methods to disperse and break up agglomerates of amorphous silica were needed in order to have a sufficiently reactive silica fume **[1]**. Other factors such as impurities were found to influence the final crystallization of xonotlite and/or tobermorite. Eight commercial grades of microsilica with different qualities and provided by different suppliers were characterized and used to produce calcium silicate boards at the laboratory. The idea was to study the influence of these silica fume types on the C-S-H gel pre-reaction and the crystallization of xonotlite under hydrothermal conditions as well as the properties of the final product.

A bulk chemical analysis of each microsilica source in its powder state was determined by means of x-ray fluorescence spectroscopy. The data are given in **Table 22**. This table also included data on the loss on ignition test results and the specific surface area calculated using BET method by N_2 adsorption-desorption. As it can be observed, the purity of these microsilica grades is mostly high with a SiO_2 content over 90% and in most samples even > 95%. Concerning the impurities, it must be pointed out that the non-crystalline silicas contain mainly carbon and oxides of alkaline and earth alkaline metals which were most likely present in the original raw materials utilized for the Si-manufacturing process.

MS Type	SiO_2	Al_2O_3	Fe_2O_3	CaO	MgO	Na_2O	K_2O	P_2O_5	LOI	SSA
E1	97.4	0.4	0.1	0.2	0.6	0.3	0.9	0.1	1.4	16
TLG1	94.2	0.1	1	1.2	1.3	0.6	0.8	0.2	2.6	26.2
TLG2	95.7	0.3	0.9	0.2	1.2	0.6	0.9	0.1	3.3	27.4
CE	95.1	0.2	0.3	0.2	1.2	0.8	1.3	0	1.5	16.4
E2	97.8	0.3	0.1	0.2	0.5	0.2	0.6	0.1	0.5	17.1
EM	97.5	0.3	0.7	0.5	0.4	0.2	0.5	0.1	2.6	25.2
E3	95.6	0.9	0.5	0.4	0.8	0.4	1.2	0.1	1.7	22.1
E4	98.8	0.2	0.1	0.3	0.2	0.2	0.2	0	0.7	20.3

Table 23. Chemical composition of Microsilicas (E1-Elkem MS940U; TLG1-MS Trade Light Grey; TLG2-MS Trade Dark Grey; CE-CETA Light Grey; E2-Elkem Micro White; EM-Emsac 500; E3-Elkem Microsilica Slurry; E4-Elkem MS971U). (LOI) loss on ignition; (SSA) specific surface measured by BET.

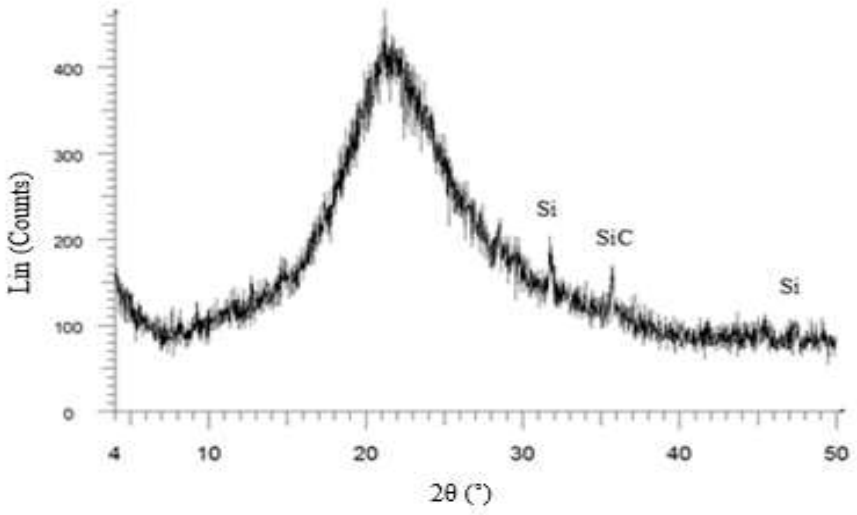

Figure 100. XRD spectrum of MS Trade Light Grey silica fume. (Si) Silicon metal; (SiC) Silicon carbide.

Loss on ignition or LOI, is the percentage of mass loss when the silica fume is heated to high temperature. LOI value gives an indication of the amount of carbon present in all these silica fume-based samples. The specific surface area of the eight silica fume sources varies according to particle size and degree of agglomeration. **Table 22** shows a significant variation between some silica fume sources meaning that there are important differences on the particle size as well as the degree of silica fume spheres agglomeration with irregular shapes and sizes.

Silica fume is mostly amorphous (broad peak around 2θ=22°), though small quantities of crystalline phases are present. The most important ones are SiC and Si. A typical example of X-ray diffraction pattern of silica fume showing its amorphous nature and some minor contents of crystalline phases is shown in **Figure 100**. Silica fume typically occurs as agglomerates, an example of which is shown in the SEM image in **Figure 101**. The sizes of the agglomerates are quite variable, though most have sizes between 10-100 μm. A more detailed image of the structure within the agglomerates is presented in **Figure 101B**, which shows them to be composed of very fine primary silica spheres of sizes of ca. 20-200nm. In **Figure 101B**, some evidence of one of the processes responsible for agglomeration can be observed, being neck formation between the SiO_2 spheres by dissolution of convex parts and deposition in concave areas. This process leads to flattening of particles and formation of necks. Other sources of agglomeration are Oswald ripening, sintering during the production process or post-treatment (as applied for the grade Elkem Micro white) and weaker bonds such as Van der Waals **[5]**.

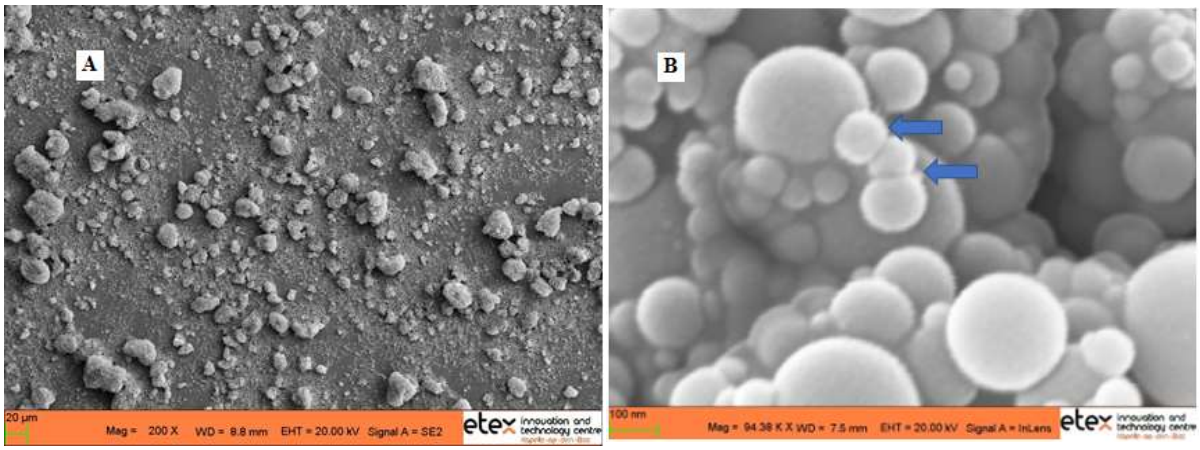

Figure 101. SEM-images of the morphology of silica fume: (A) Overview showing agglomerates; (B) Detail of particles including evidence of flattening and formation of necks between particles.

Because of these different agglomerates, the silica fume has a wide range of particle size, and these differ for the various silicas tested in this investigation. A few examples are shown in **Figure 102**. **Figure 102A** shows the particle size distribution (PSD) of silica

fume as such, that is, without particle opening/dispersion treatment and it also shows the psd after high shear mixing as treatment.

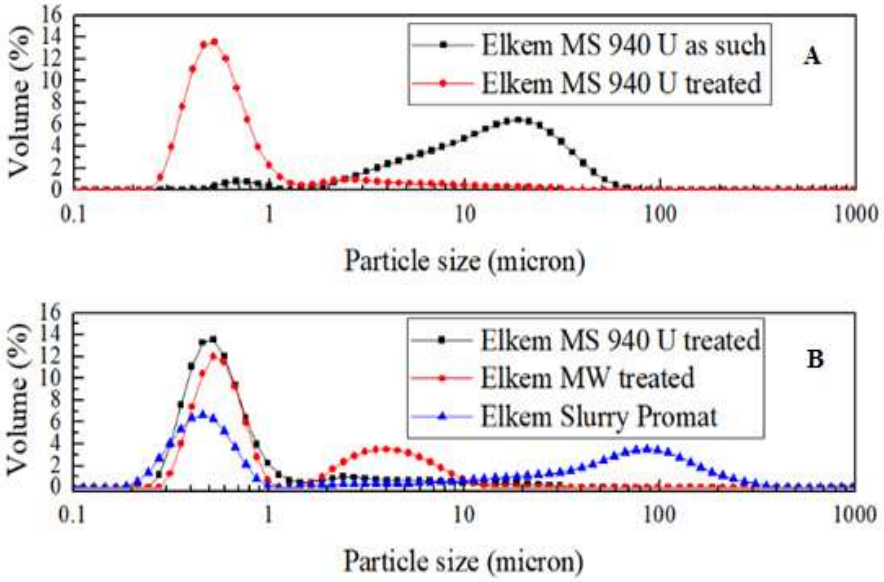

Figure 102. Particle size distribution of non-treated and treated Elkem MS 940 U by high shear mixing(A); treated Elkem MS 940 U, Elkem Micro White and Elkem Slurry Promat by high shear mixing (B).

It is observed that high shear mixing results in a very significant reduction of the agglomerates size. In some of the silica fume sources, when high shear mixing was applied, only one population of aggregates is visible (around 0.6-0.7 μm), while in others (e.g. Elkem Micro White and Elkem slurry) additional peaks representing larger agglomerates are visible (see **Figure 102B**).

The rate of solubilization for silica fume Elkem MS 940 U (with and without opening treatment) and Elkem Micro White (with opening treatment) is shown in **Figure 103** as comparative example.

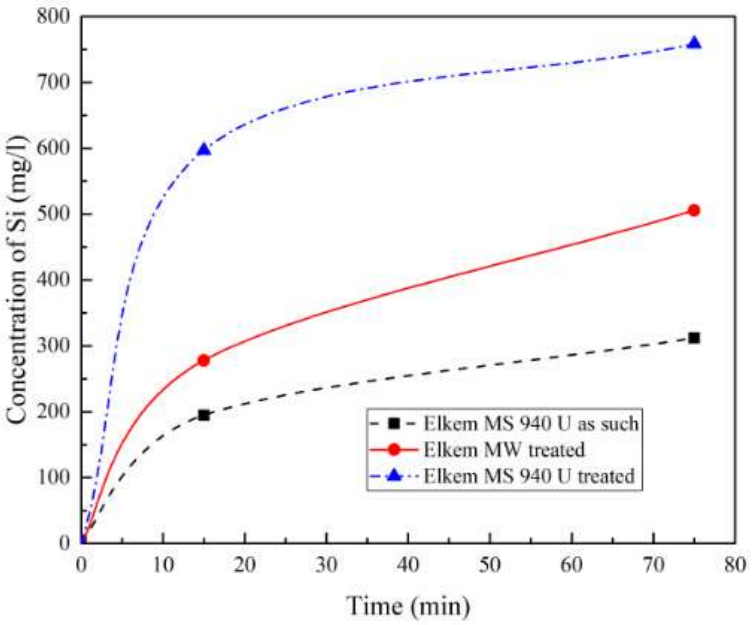

Figure 103. Solubility curves of Elkem Micro White (with treatment) and Elkem MS 940 U (with and without treatment).

From **Figure 103**, it is clear the agglomeration of the silica fume particles impacts the rate of solubilization. The differences between Elkem Micro White and Elkem MS 940 U are due to the higher degree of agglomeration of the former in which sintering during the heating treatment creates stronger aggregates that are not completely broken by mechanical mixing.

The C-S-H gel preparations made by the eight microsilica grades were characterized. In this part, only a few representative results of specific samples are presented to make a comparative analysis.

XRD-patterns of C-S-H gel formed from non-dispersed and dispersed Elkem MS 940 U as amorphous SiO_2 source are shown in **Figure 104**. In spite of the fact that it might be expected that microsilica is reactive in the applied conditions, the non-treated or non-dispersed by mechanical shearing silica fume reacts very slow. When using non-sheared silica fume, it is found that important concentrations of portlandite still remain after the gel formation step. However, when using silica fume opened by high shear mixing, most of the $Ca(OH)_2$ reacts during the C-S-H gel reaction as XRD-spectra shows in **Figure 104**.

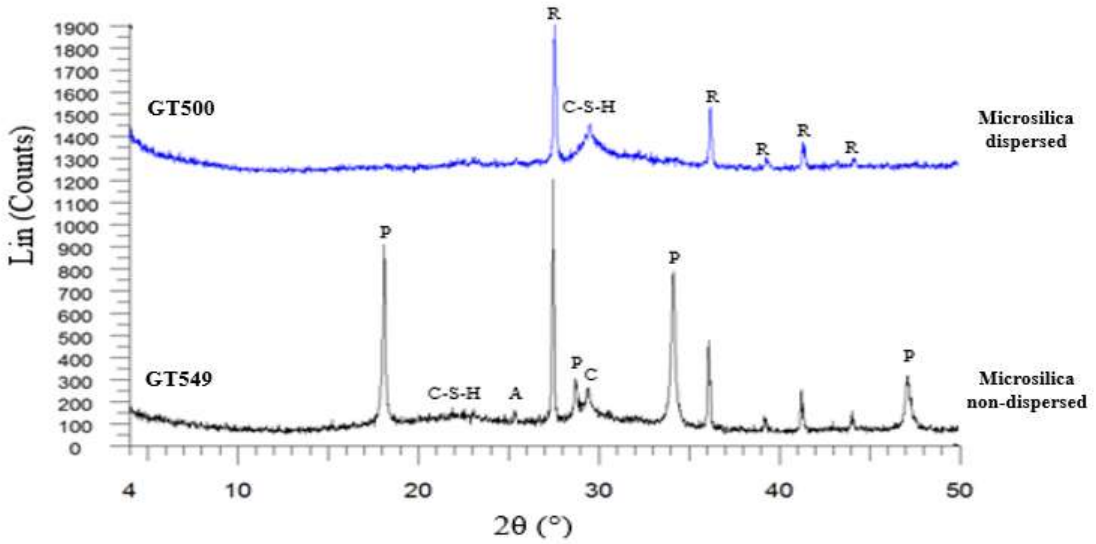

Figure 104. XRD spectra of C-S-H gel preparations. (Black) C-S-H gel with non-treated Elkem MS 940 U; (Blue) C-S-H gel with treated Elkem MS 940 U. P: Portlandite; R: Rutile as internal standard; A: Anatase; C: Calcite; C-S-H: Calcium silicate hydrate.

On the one hand, it is seen in the black spectrum two high peaks of portlandite at 2θ = 17˚C and 2θ = 34˚C and a very weak hump corresponding to early C-S-H gel stage. On the other hand, in the blue spectrum, there is no presence of unreacted calcium hydroxide and a broad peak at 2θ = 29.6˚C which corresponds to C-S-H gel phase is clearly visible. The Rietveld analysis given in **Table 23** confirms the large differences related to crystalline phases in one case and another.

Sample	Dispersion	Portlandite (%)	Calcite (%)	Amorphous content (%)
GT549	No	19	6	75
GT500	Yes	1	9	90

Table 24. Rietveld analysis of C-S-H gel preparations. (GT549) Non-treated Elkem MS 940 U and (GT500) treated Elkem MS 940 U.

The difficult reaction of silica fume was reported in previous studies and is due to the strong tendency of silica fume to agglomerate and form larger particles **[4, 6]**. Reactions with Ca^{2+} and OH^- occur mainly at the surface of these agglomerate particles, meaning that the reactive surface is limited and much smaller than the specific surface area. On the surface of the silica agglomerates, small amounts of silica will go into solution and react

with the Ca^{2+} and OH^- (coming from the lime solubilization) forming C-S-H. The composition of this C-S-H depends on the solubility of lime (determining the Ca^{2+} and OH^- concentrations) and also on the size of the silica fume agglomerates, since these will influence the rate of silica solubilization as seen in the previous section. Therefore, depending on the size of the silica fume agglomerates, C-S-H phases with different chemical composition and structure are formed and not all of them allow an easy recrystallization into xonotlite and tobermorite. The C-S-H-particles with a CaO/SiO_2-ratio between 1 and 1.5, are expected to have an easy recrystallization into xonotlite or tobermorite **[8-11]**, while compositions very rich in either SiO_2 or CaO, will transform more slowly and possibly less complete. The larger the size of the silica fume agglomerates, the higher the CaO/SiO_2 ratio of the C-S-H phases that develop on the surface. A SEM image of C-S-H gel and a few examples of the variability in C-S-H composition as determined by EDX analysis are shown in **Figure 105**.

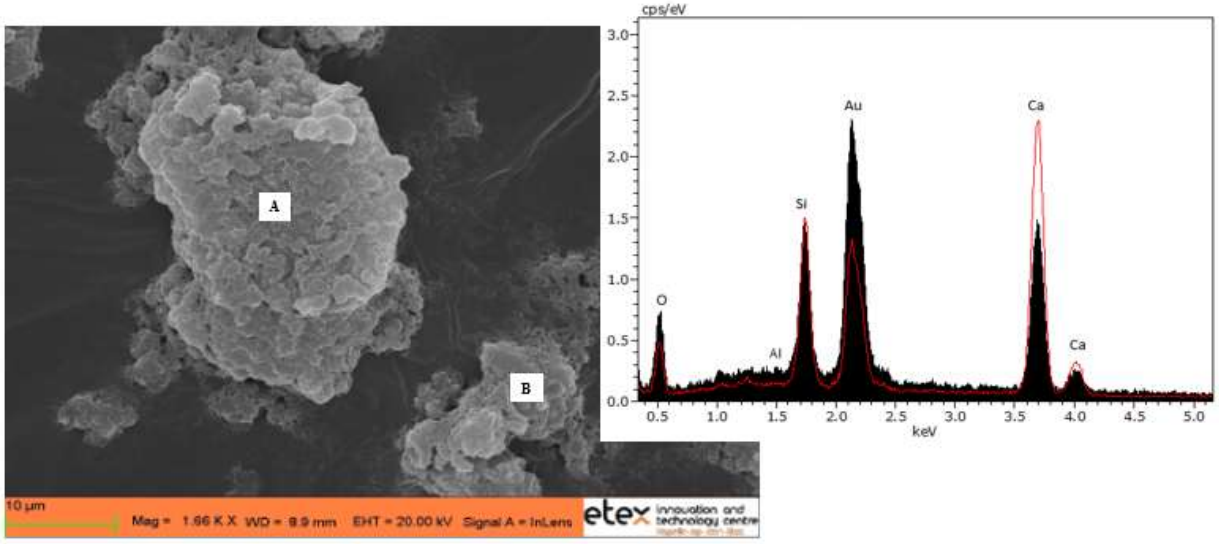

Figure 105. SEM image showing examples of C-S-H particles after the gel formation step with indications of compositional differences by EDX. (A): Big grain with a C-S-H gel composition given by the red spectrum; (B): Small grain with a C-S-H gel composition given by the black spectrum.

These differences in chemical composition of C-S-H particles are at least in part due to the impact of agglomeration on the rate of the micro-silica solubilization. In general, even after dispersion of micro-silica aggregates by mechanical shear forces, the tendency of this material to form agglomerates is very high and this phenomenon is permanently occurring. This tendency to agglomerate leads to a large spread in the particle size distribution and this contributes to a more difficult crystallization into xonotlite than in the case of quartz as silica source, because sand normally has a quite narrow particle size distribution and reacts more homogeneously. The same differences in degree of reaction with lime also have been found when using mixtures of silica fume and quartz (see **Figure**

106). Silica fume types such as Elkem Micro White have larger remaining aggregates after high shear mixing, and this results in lower consumption of $Ca(OH)_2$ than when using more reactive silicas such as Elkem MS 940 U.

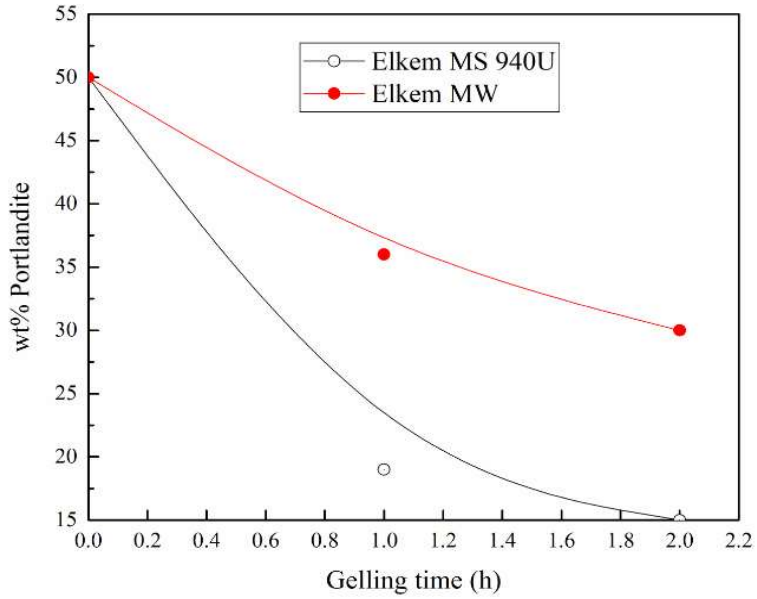

Figure 106. Contents of portlandite ($Ca(OH)_2$) over gelling time in GT549 and GT500 for two different microsilica combined with quartz (50% quartz/50% microsilica) at the starting formulation.

The autoclaved C-S-H gel preparations using initially these different microsilica qualities were also characterized by different techniques and tests. Here, the most relevant results are presented below.

The XRD-patterns as wells the results of the Rietveld analysis for the two GT-autoclaved samples, GT549/GT500, prepared previously via a C-S-H gel made with treated and non-treated silica are shown in **Figure 107** and **Table 24**. The black spectrum corresponding to the product made with non-treated microsilica shows hardly any conversion into xonotlite and the C-S-H broad peak is still clearly visible at $2\theta = 29.8^{\circ}C$. The blue spectrum presents the end product made with treated microsilica. A better re-crystallization of C-S-H into xonotlite is observed. It means that a treatment to break up the aggregates of microsphere silica fume is required in order to have the desired xonotlite crystallization in hydrothermal conditions.

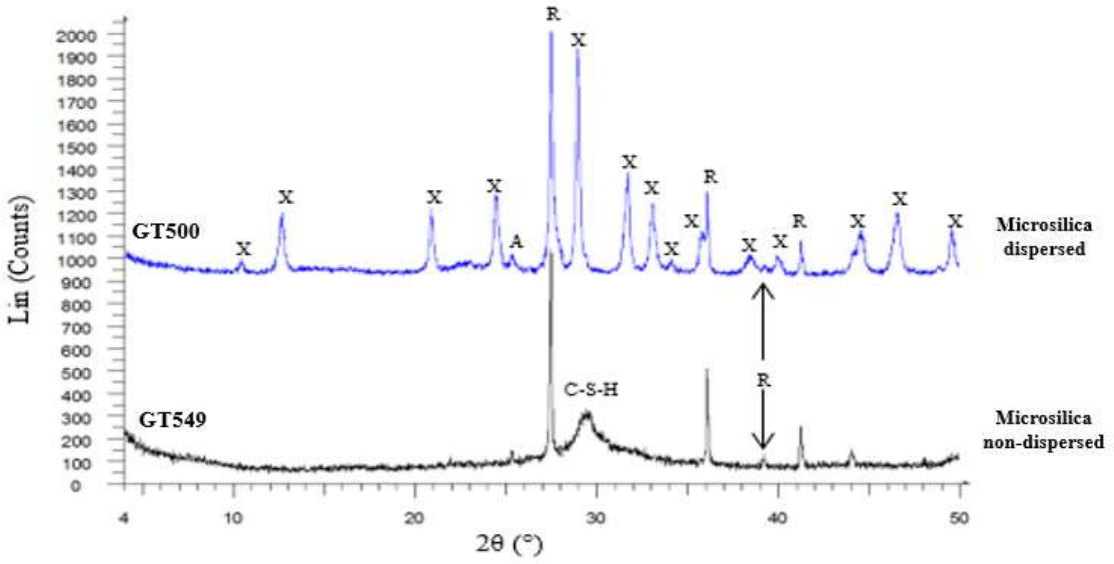

Figure 107. XRD spectra of GT-autoclaved samples. (Black) GT sample prepared via C-S-H gel with non-treated Elkem MS 940 U; (Blue) GT sample prepared via C-S-H gel with treated Elkem MS 940 U. X: Xonotlite; A: Anatase; C-S-H: Calcium silicate hydrate; R: Rutile (internal standard for Rietveld analysis).

Sample	Dispersion	Xonotlite (%)	Tobermorite (%)	Calcite (%)	Amorphous content (%)
GT549	No	29	9	3	59
GT500	Yes	84	0	1	15

Table 25. Rietveld analysis of final products after hydrothermal hardening step. (GT549) Non-treated Elkem MS 940 U; (500) treated Elkem MS 940 U.

The different C-S-H gel compositions formed in the gelling step (due to differences in particle size and distribution of the silica fume), lead to variations in the xonotlite and tobermorite during the hydrothermal hardening. Some of these variations are shown for the xonotlite content in the final product in **Figure 108**.

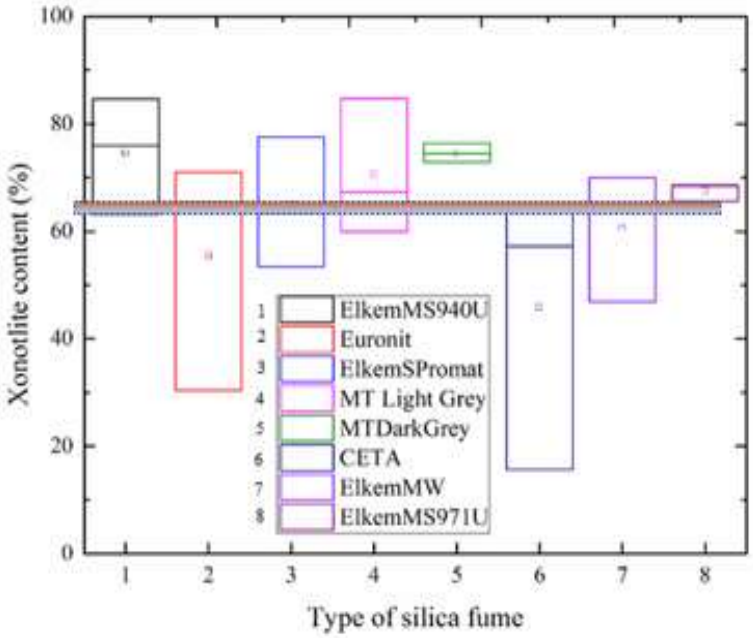

Figure 108. Xonotlite content in the GT-autoclaved samples prepared from C-S-H gel using different microsilica.

The horizontal bar in the graph of **Figure 108** represents the average value of the total population. The differences are not large, and more tests would be required for statistically significant conclusions. Nevertheless, some compositions showed higher contents of xonotlite than the average and others that are poorer in xonotlite. The main characteristics of the silica fume types that lead to higher xonotlite concentrations are the following: high purity (typically above 95wt%) and particle size distribution that consists of (after treatment) mostly of fine particles (sizes mostly below 1µm). On the other hand, less good crystallization was observed when the silica shows larger agglomerates after treatment, as for example Elkem Microwhite, Elkem Microsilica Slurry (ElkemS Promat), Emsac 500 (Euronit) due to their lower silica fume solubilization and low purity. Furthermore, the poor crystallization for less pure silicas might be due to the influence of impurities (e.g. K, Na...) on the C-S-H-structure and its ability to recrystallize **[14]**. The latter is for example the case for the products made with CETA silica fume. Some silica fume grades (Microsilica Trade Light Grey and Elkem Slurry Promat) contain small contents of Al_2O_3 (see table 22) and this favors the formation of tobermorite instead of xonotlite as can be seen in **Figure 109**.

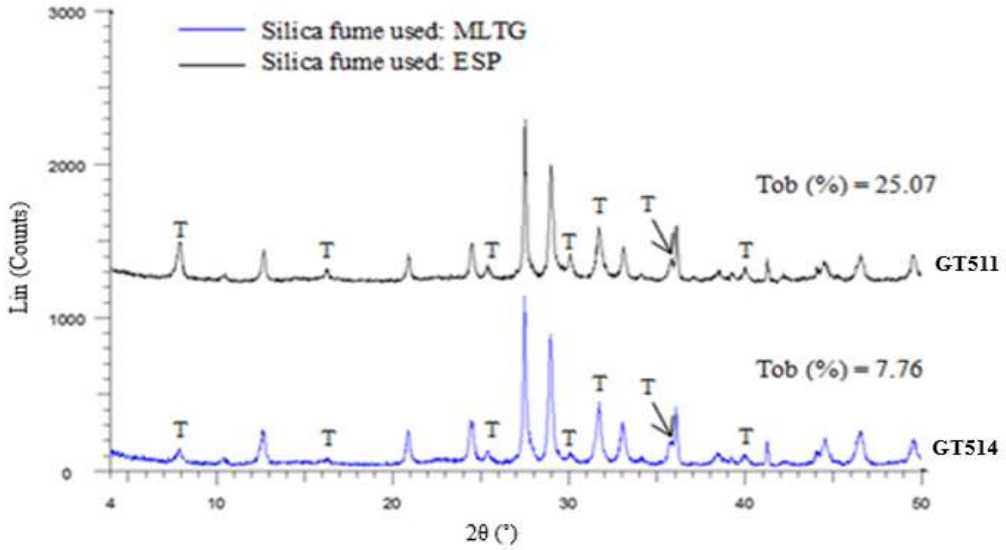

Figure 109. XRD spectra of GT-autoclaved samples. (Blue) GT514 sample prepared from C-S-H gel with Mikrosilika Trade Light Grey (MTLG); (Black) GT511 sample prepared from C-S-H gel with Elkem Microsilica Slurry (ESP). T: Tobermorite.

In spite of the scatter in the contents of xonotlite and tobermorite, the bending strength values of the final products made with different grades of silica fume are not too different and seem to be within the spread of error.

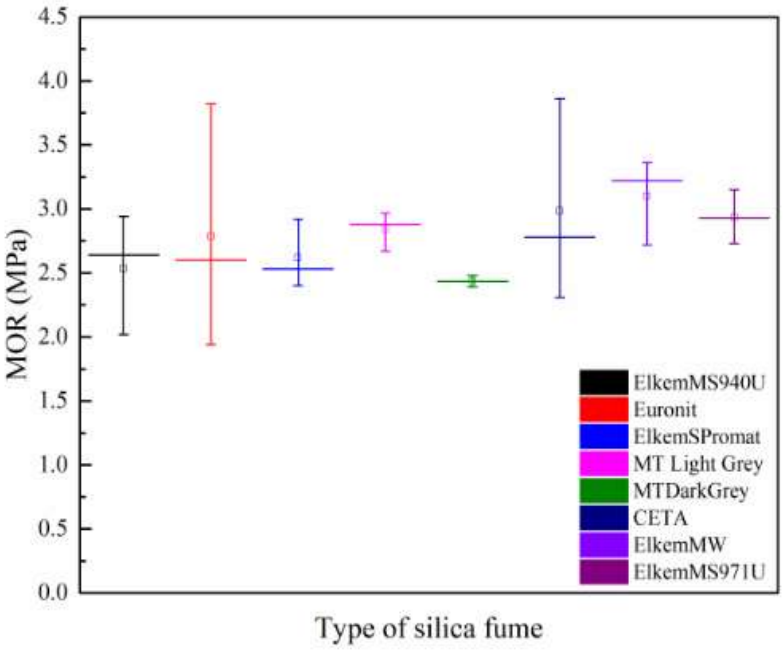

Figure 110. MOR values for GT-autoclaved samples made by different microsilica grades.

Silica fume sources with a wider particle size distribution tend to show a larger spread in the results, as it can be seen in the whisker-plot diagram represented on the **Figure 110**.

The differences in recrystallization into xonotlite or tobermorite for the GT C-S-H preparations made from initial compositions using different silica fume sources led to variations on the thermal stability. Products made with microsilicas of lower quality (lower SiO_2 %) and higher scatter such as Emsac 500 (Euronit), CETA and Elkem Microwhite also gave variations on the thermal shrinkage and tend to have lower thermal stability. Products made from microsilica with smaller particle size and less psd variation (for example Elkem MS 940 U, Elkem 971 U, Elkem Microsilica Slurry) showed lower and more stable thermal shrinkage values as a consequence of a better xonotlite crystallization. **Figure 111** illustrates the thermal shrinkage of the length-width (L-W) and thickness (T) of GT-autoclaved samples made by means of different microsilica.

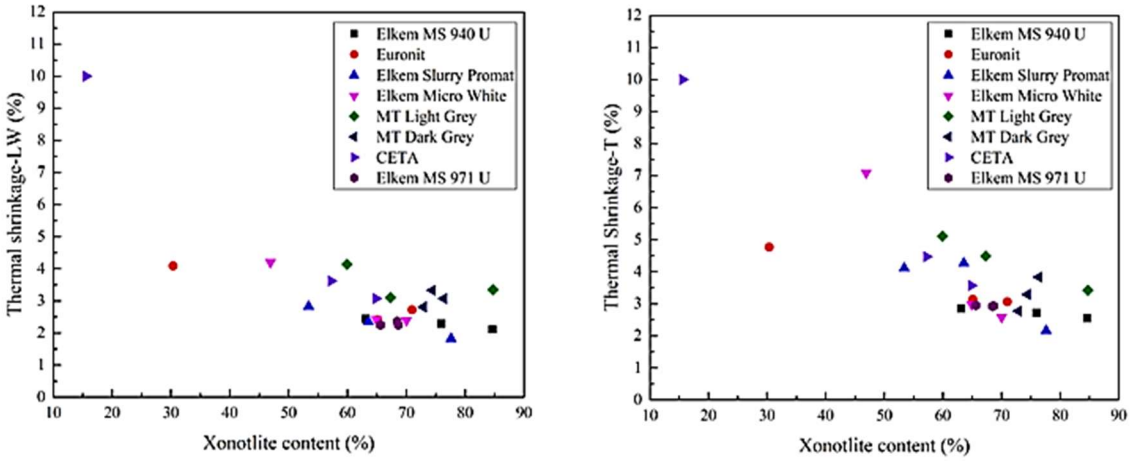

Figure 111. Thermal shrinkage values over xonotlite percentage of GT-autoclaved samples prepared from C-S-H gel with different silica fume sources.

The main aspects concerning the influence of the microsilica can be summarized as follows:

- In spite of its high specific surface, micro-silica as such is not highly reactive and the reaction between non-treated microsilica and $Ca(OH)_2$ is proceeding extremely poorly. This slow reaction is due to a high degree of agglomeration of microsilica in alkaline conditions leading to a limited reactive surface and high variability in C-S-H composition. This restricts the recrystallization into xonotlite.

- To have an acceptable reaction yield, the aggregates of microsilica need to be broken by mechanical or chemical dispersion. In this investigation, high shear mixing was usually applied.

- For different dispersed microsilica sources, variations in crystallinity and then in the final properties are observed. This is strongly linked to the purity and the particle size of microsilica.

4.1.2.5. Influence of silica sources: effect of microsilica/quartz ratio

In the previous section the influence of amorphous silica sources was investigated, but the effect of mixtures of this silica and quartz, as silica source, were also studied for gelling conditions of 1 h at 90ºC. The gel containing these mixes was afterwards pressed to form 450 Kg/m^3 density products and finally, autoclaved. Firstly, the corresponding characterization of the C-S-H gel preparations was performed.

The XRD curves and Rietveld refinement data are shown both in **Figure 112** and **Table 25**. They confirm what was observed in the previous sections. During the gelling step, portlandite and amorphous silica were reacted forming C-S-H gel (C-S-H (I) or C-S-H with C/S < 1.5)). Whereas that quartz hardly reacts (only amorphous rims present around the quartz-grains), meaning that high contents remain after the gelling step as it can be seen by Rietveld analysis and also in the SEM image in **Figure 113**.

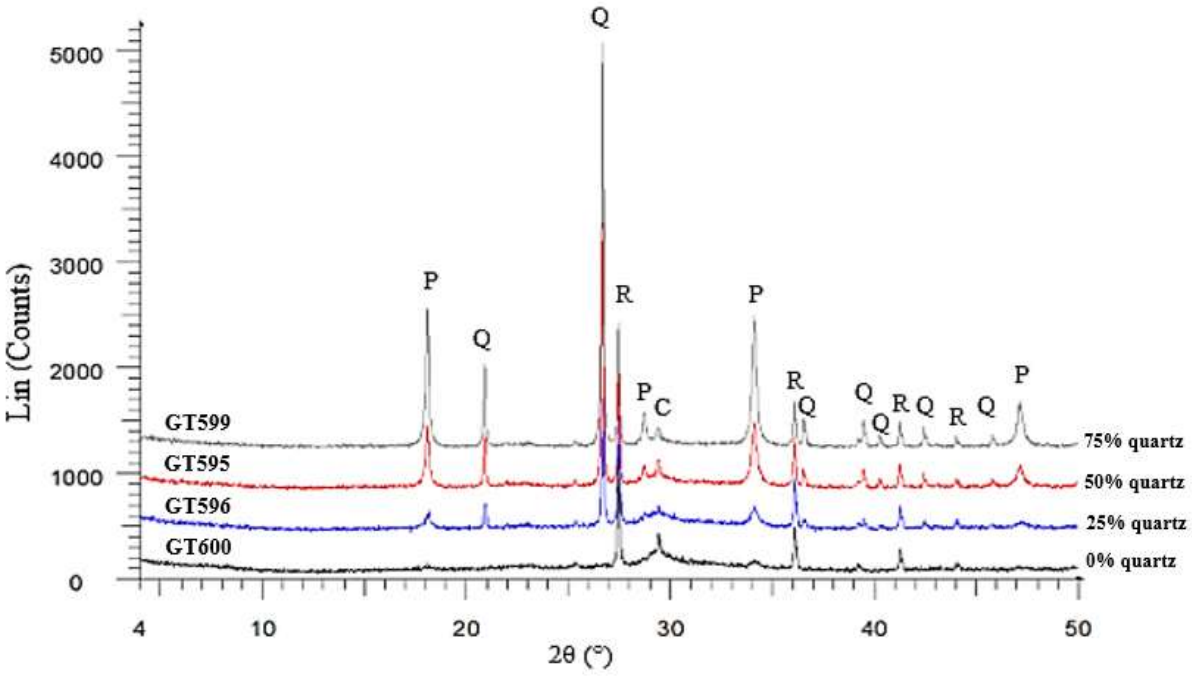

Figure 112. XRD spectra of C-S-H gel preparations made from different MS/Q ratios. P: Portlandite; Q: Quartz; R: Rutile as internal standard; C: Calcite.

Sample	Initial quartz/silica fume ratio (%)	Portlandite (%)	Quartz (%)	Calcite (%)	Amorphous content (%)
GT600	0%Q/100%MS	2.6	0	10.7	86.7
GT596	25%Q/75%MS	6.7	10.6	6.4	76.3
GT595	50%Q/50%MS	16.3	21.3	6.6	55.8
GT599	75%Q/25%MS	28.8	33.4	4.8	33

Table 26. Rietveld Refinement analysis of C-S-H gel preparations made from different MS/Q ratios.

The morphology of the C-S-H gel particles synthetized by means of quartz and microsilica mixtures was analyzed by SEM as shown in **Figure 113 (a/b/c)**. On one hand, **Figure 113.a** corresponds to a SEM micrography of a C-S-H gel-based sample prepared with an initial composition containing only silica fume as silica source and lime. In this case, the gel microstructure presents aggregates of flaky C-S-H particles. **Figure 113.b** and **Figure 113.c** correspond to C-S-H gel formed using silica mixtures based on 50% crystalline silica (quartz) and 50% of amorphous silica (microsilica). For these samples, the microstructure of C-S-H gel aggregates seem to be similar morphologically than the previous one; these samples contain unreacted or partially reacted quartz and portlandite particles. This is in line with the Rietveld analysis results shown above in **Table 25**.

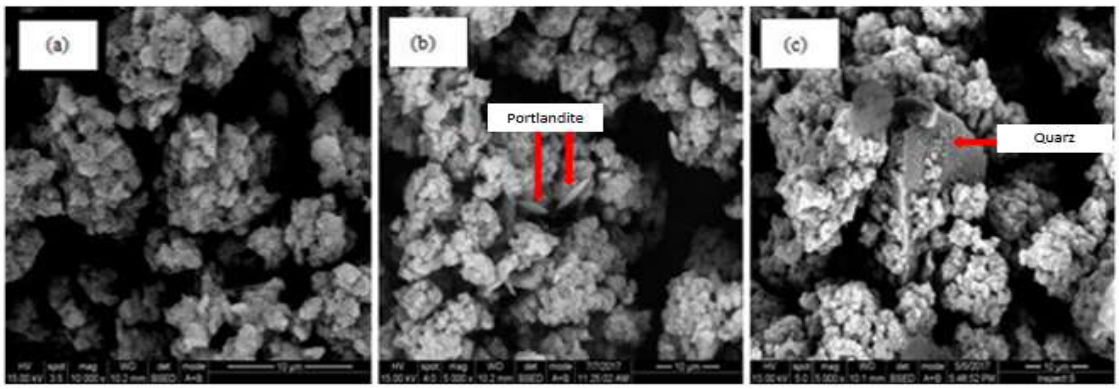

Figure 113. SEM images of particles formed during the 'gelling' step for a mixture of lime, quartz, and amorphous silica: (a) C-S-H gel particles made by 100% microsilica; (b) and (c) C-S-H gel particles made by 50% quartz-50% microsilica.

Sedimentation tests of C-S-H gel preparations obtained from mixtures with high and low initial quartz content were done in order to compare the formulations. **Figure 114** shows pictures of glass measuring cylinders containing different mixtures of C-S-H gel, residual SiO_2 (quartz and amorphous silica) and $Ca(OH)_2$. The slurries were sedimented for 1 hour. As it can be observed the volume of settled solid (C-S-H gel particles, quartz and microsilica) was significantly different depending on the initial composition of the mixture. Higher amounts of silica fume used at the starting formulation led to a faster C-S-H gel phase formation and lower sedimentation. This implies that a higher force was required to press the slurry to a given final density. Mixtures with an initially high amount of quartz, form less C-S-H , sediment more and develop less pressure during the molding to form certain densities.

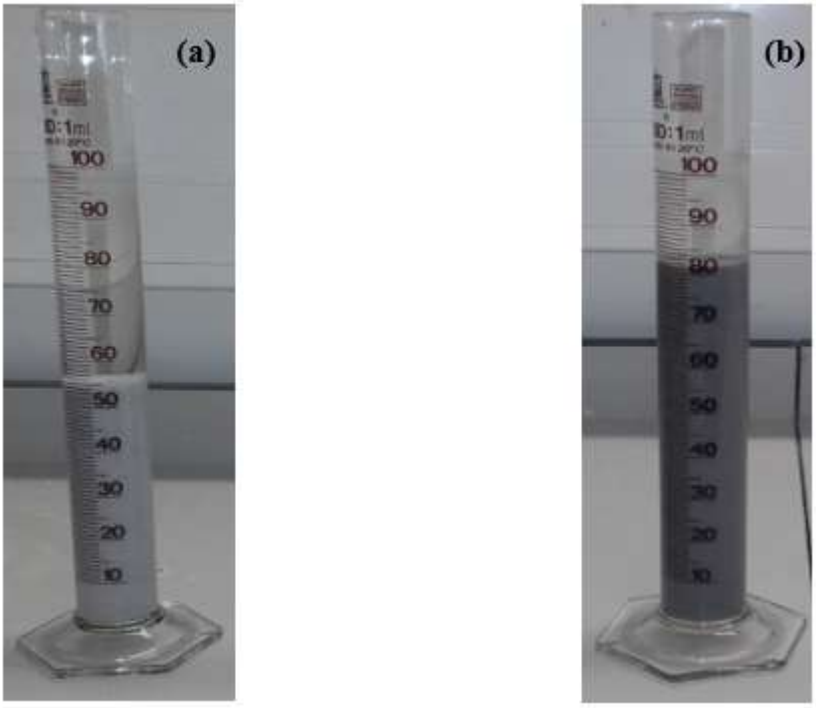

Figure 114. C-S-H gel-based samples after 1 hour of sedimentation. (a) GT595 sample made from 75% Q-25% MS; (b) GT596 sample made from 25% Q-75% MS.

The volume variation of settled solid as well as the force applied for pressing is noted in **Table 26**. On the other hand, these C-S-H gel samples (GT595 and GT596) were also characterized by BET method to obtain the adsorption isotherm curves.

Sample	Starting composition	Sedimentation/ΔV (ml)	Force F-P (kN)
GT596	25% Q – 75% MS	19	80
GT595	75% Q – 25% MS	45	12

Table 27. Results of sedimentation tests for GT596 and GT595 samples as C-S-H gel preparations and force values registered during filter-pressing step.

As expected, the C-S-H gel preparation (GT596) made from higher initial silica fume percentage (75% MS) presented greater nitrogen adsorption than the other one prepared from a higher initial quartz amount. Meaning that a more porous material was formed that occupies more volume and thus, it shows much less sedimentation as seen in **Figure 114**. As can be seen in **Figure 115**, the volume of N_2 adsorbed increases with initial % of microsilica used at the starting formulation (compared GT596-75% MS/25% Q and GT595-75% Q/25%MS).

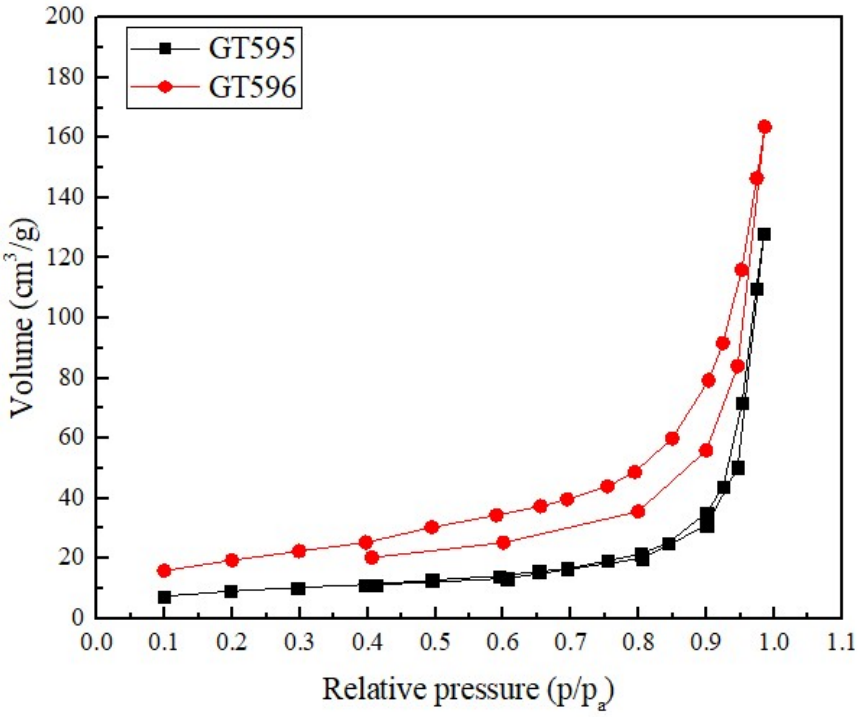

Figure 115. N_2 adsorption-desorption isotherms for gels pre-reacted from different initial ratio of MS and Q.

The XRD spectra for calcium silicate boards made from initial compositions with a different combination of quartz and silica fume, presented as main crystalline phases xonotlite and tobermorite as can be seen in **Figure 116**. Besides, it is also seen a trend in the increase of the tobermorite peaks as a higher initial quantity of quartz was used in the Geltank process.

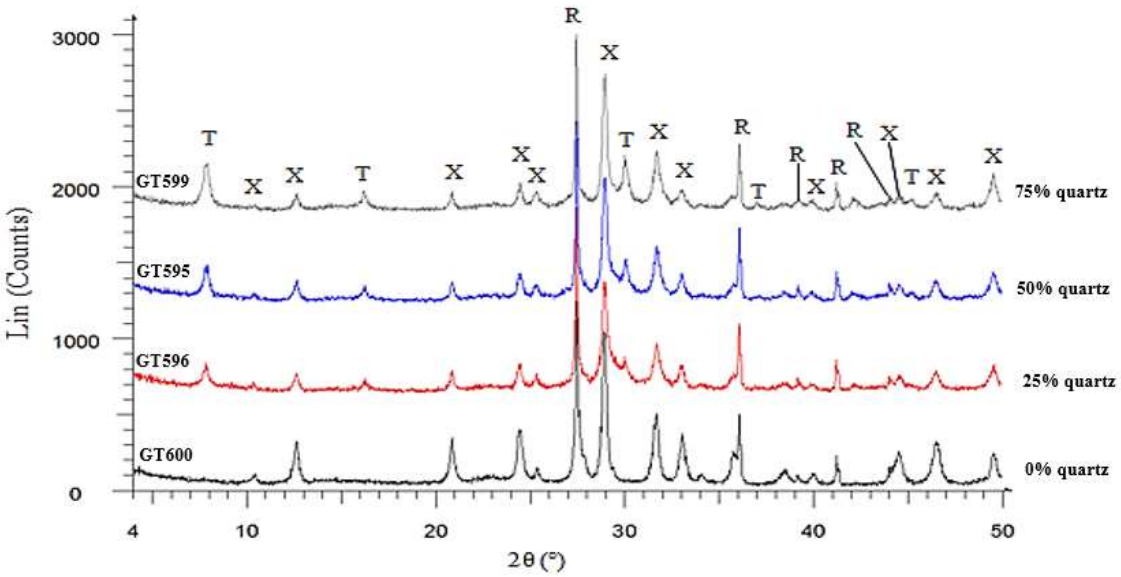

Figure 116. XRD spectra of GT-autoclaved samples made from C-S-H gel preparations with different initial MS/Q ratios. X: Xonotlite; T: Tobermorite; R: Rutile.

Sample	Initial Q/MS ratio (%)	Xonotlite (%)	Tobermorite (%)	Quartz (%)	Calcite (%)	Amorphous content (%)
GT600	0%Q/100% MS	57.3	4.4	0	0.6	37.7
GT596	25%Q/75% MS	44.2	13	5.7	6.5	30.6
GT595	50%Q/50% MS	35.4	25.8	0	3.8	35
GT599	75%Q/25% MS	31	36.4	0	2.4	30.2

Table 28. Rietveld Refinement analysis of calcium silicate boards made from different quartz and microsilica wt%.

It is important to remark that xonotlite mostly forms from C-S-H gel synthesized via microsilica. The recrystallization of a such C-S-H gel in hydrothermal conditions is directly into xonotlite. On the other hand, the C-S-H gel formed from a quartz-portlandite mixture does not transform immediately into xonotlite though occurs via intermediate tobermorite formation.

The degree of crystallinity for the GT boards was slightly higher for the quartz-rich samples as can be seen in the results of Rietveld analysis given in **Table 27**. The more efficient reaction of quartz compared to microsilica is at least in part related to its narrow particle size distribution, given a more constant composition of the initial C-S-H and also to the fact that the C-S-H around quartz forms at higher temperature and pressure.

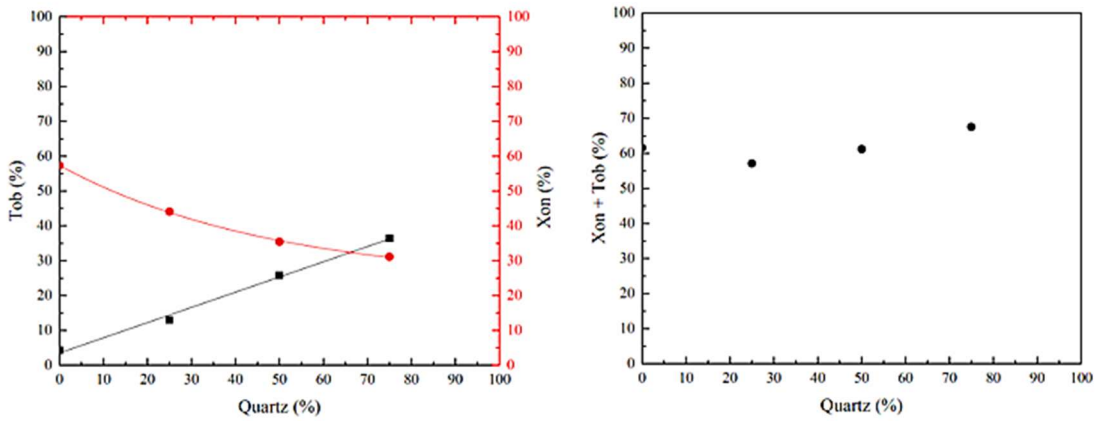

Figure 117. Evolution of tobermorite and xonotlite contents (left) and the total content of crystalline Ca-silicates (right) over the percentage of quartz used in the initial SiO_2 mixture.

There are differences in xonotlite crystallization between GT samples made with and without quartz as can be seen in **Figures 117-118**.

These differences are due to the formation of C-S-H phases with different structure and composition. In mixtures with quartz, the C-S-H gel forms around the quartz grains in the initial phases of the hydrothermal step. This C-S-H typically is Ca-rich due to the lower solubility of quartz compared to that of portlandite **[1]** and has a molar C/S ratio varying from 1.5 to 1.9, depending on the size of the quartz crystals . In advanced stages, when more crystalline silica is solubilized and diffuses in the formed C-S-H (II), the latter will convert into C-S-H (I) and transforms into tobermorite. And finally, tobermorite into xonotlite. So, the Ca-silicate-hydrate formation starting from quartz proceeds via the following reaction mechanism:

$Ca(OH)_2$ + quartz → CSH-II → CSH-I → Tobermorite

The differences between intermediate and final reaction products starting from quartz and amorphous silica have also studied by Mitsuda *et al.* and El-Hemaly **[50, 56]**, but for the stirred reactor autoclaving technology. The C-S-H phases synthesized from amorphous silica and calcium hydroxide in the gelation process seem to have a structure such that it does not convert easily into tobermorite, though immediately converts into xonotlite **[1, 6]**. The recrystallization is less complete when using amorphous silica than when using quartz as silica source and besides variable since it is depending on the nature and the processing of the amorphous silica. There is less diffusion involved than in the case of quartz and the reaction happens via nucleation on a large surface area of the dispersed silica fume particles. The differences in microstructure were visually observed from SEM analysis during the early stages of the hydrothermal hardening for mixtures containing both quartz and microsilica. Examples of this are shown in **Figure 118**.

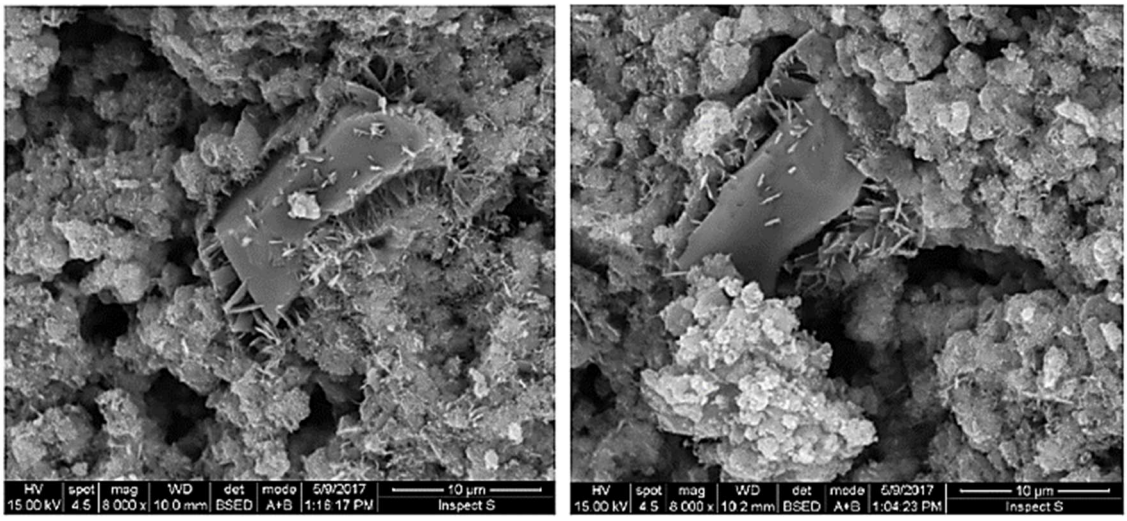

Figure 118. SEM images of GT-autoclaved samples prepared using mixtures of amorphous silica and quartz. Microstructure after 1h in hydrothermal conditions at 10bar.

Initial crystallization of semi-crystalline C-S-H particles are formed on the surface of quartz particles can be seen in the SEM images in **Figure 118**. Quartz needs higher temperature and pressure conditions to start reacting appropriately with calcium hydroxide-and in these conditions more crystalline products are formed. Meanwhile in the same sample, there are also C-S-H gel particles formed from silica fume.

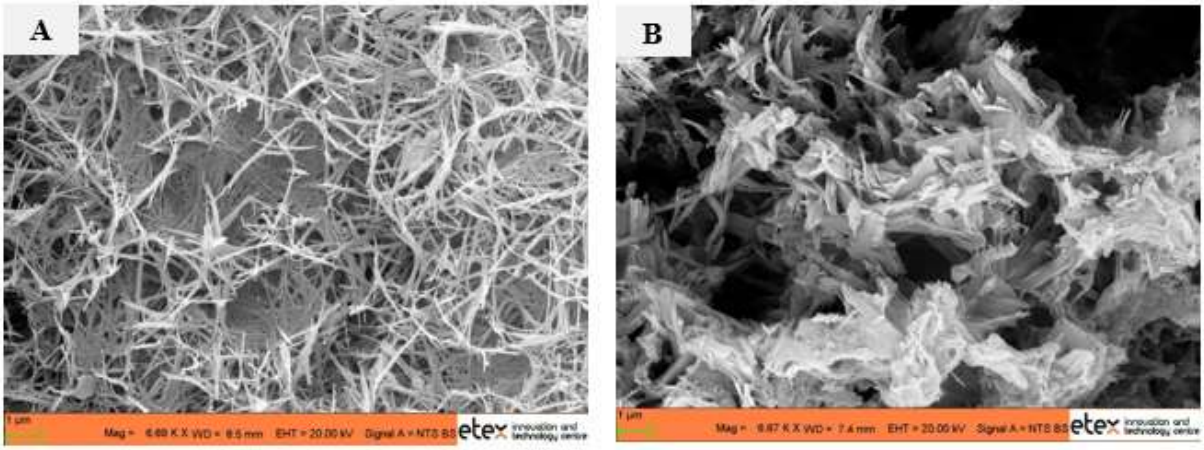

Figure 119. SEM micrographs of GT-autoclaved samples prepared from different silica sources. (A) GT600 sample prepared from an initial mix containing 100% amorphous SiO_2 and $Ca(OH)_2$. The morphology consists of long and thin needle-like xonotlite crystals forming a highly crystalline lattice. (B) GT599 sample prepared from 75% Q/25% MS and $Ca(OH)_2$. The morphology is based on a combination of short and thick xonotlite needles which are less defined and tobermorite lath- and plate-like crystals sticking together.

They have a less well crystallized flaky nature. After longer autoclaving times, a network of needles or a mixture of needles-plates were crystallized as can be appreciated in **Figure 119**. The microstructure of an end-product made with 100% amorphous silica seems to consist of finer xonotlite needles while the end-products made with quartz and amorphous silica are composed of platelets and thicker needles.

The flexural strength of final products for GT-autoclaved samples prepared via different wt.% of amorphous and crystalline silica in the initial composition shows important differences as can be seen in the whisker-plot of **Figure 120** A higher content of quartz in the initial composition seems to give higher flexural strength. This might be rather unexpected as the quartz containing C-S-H gel slurries were molded applying lower pressure (filter-pressing force) than those based upon microsilica only, though is probably related to the differences of the microstructure and degree of crystallization.

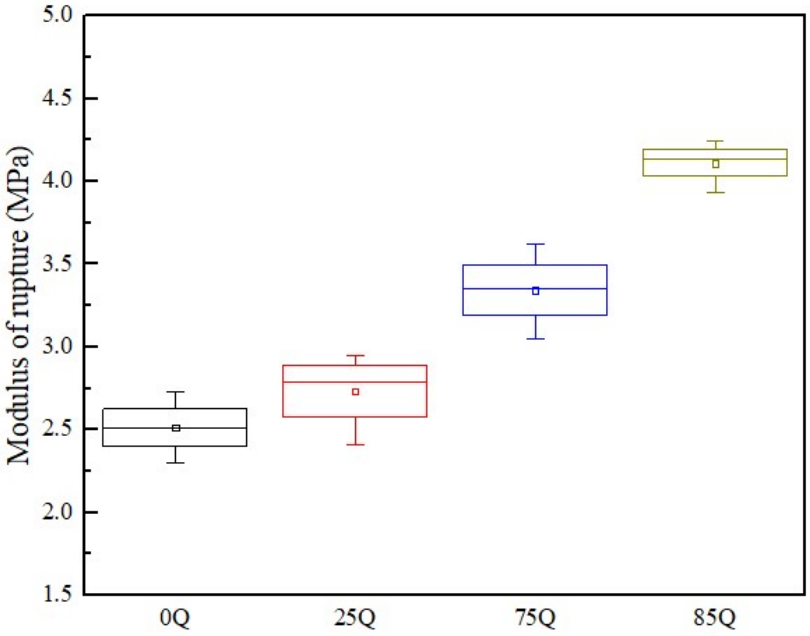

Figure 120. Whisker-plot diagrams comparing the Modulus of Rupture of GT-autoclaved samples prepared from different silica sources and combinations.

The thermal stability of highly crystalline calcium silicates obtained via a combined mixture of 50% quartz and 50% microsilica at starting formulation was somewhat lower than for crystalline calcium silicates prepared from only well dispersed microsilica.

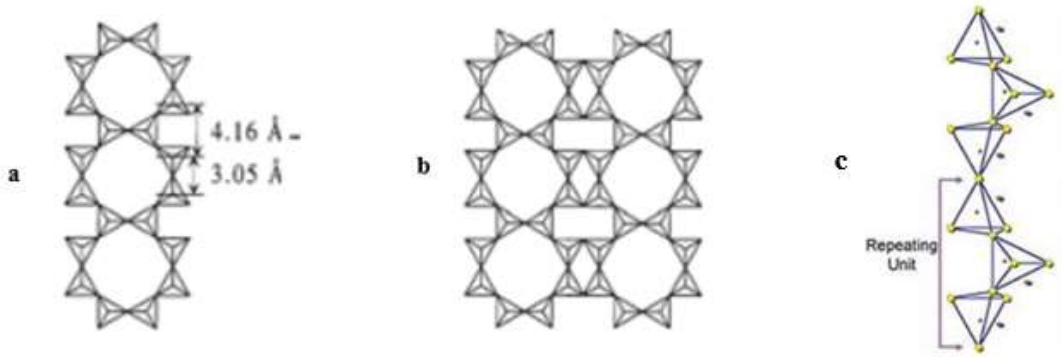

Figure 121. Type of ordering of SiO_4 tetrahedrons. a) Xonotlite structure; b) Tobermorite structure; c) Wollastonite structure **[135]**.

Anton, Opsommer et al. investigated the impact of the calcium silicates morphology on the thermal stability. So, they reported that xonotlite is the most stable structure **[135]**. This is due to the fact that the structure of xonotlite is very similar to that of wollastonite in which it does recrystallize at around 800°C. For tobermorite, the difference in structure is larger and also the dimensional changes during the recrystallization into wollastonite and this transformation involves also more transitions. The silicon-tetrahedron-structures of xonotlite, tobermorite and wollastonite are shown in **Figure 121.** Therefore, the presence of higher tobermorite contents in the calcium silicates matrix formed by means of starting compositions with 50% of quartz as crystalline SiO_2 source results into a less thermal stable material. The TMA curves are plotted in **Figure 122**, they confirm these results.

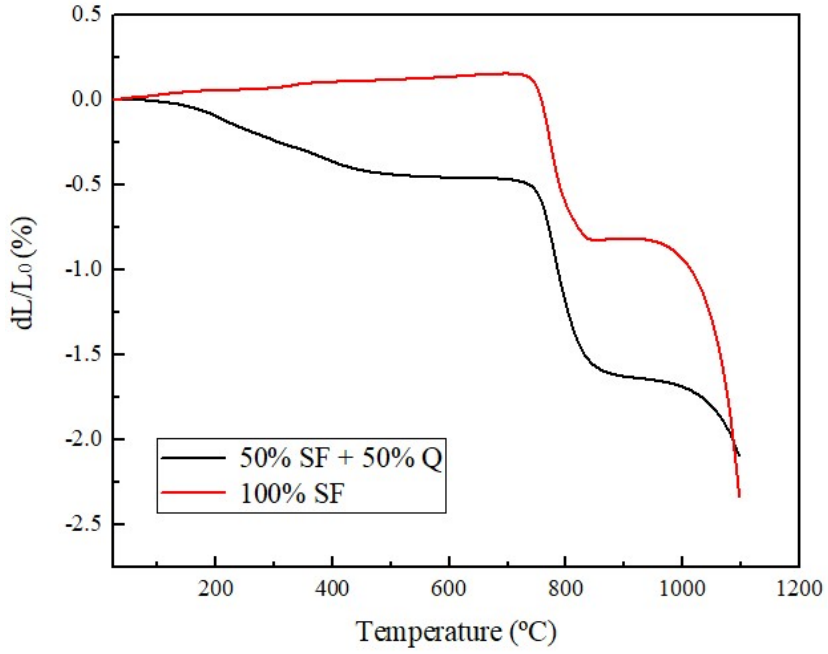

Figure 122. TMA curves of GT-autoclaved samples made from pure silica fume and a 50% quartz-silica fume mixture at the starting formulation.

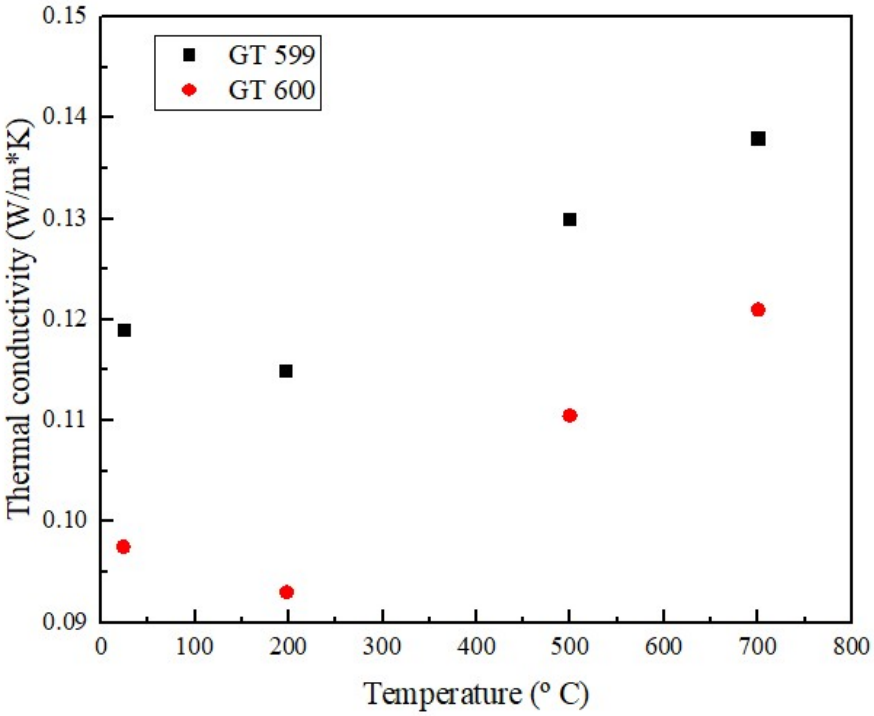

Figure 123. Evolution of thermal conductivity values for hydrothermally treated calcium silicates as a function of temperature. (Black dots) GT599 sample prepared from a silica mixture of 75% Q/25% MS; (Red dots) GT600 sample prepared from 100% MS as the only silica source.

The thermal conductivity (λ) of GT599 and GT600 samples was measured by the hot-wire technique and is shown in **Figure 123.** The thermal conductivity appears lower for the products based upon xonotlite made with 100% amorphous silica (GT600). The differences in cumulative pore volume for the samples GT599 and GT600 were determined and are shown in **Figure 124**. They do not explain the differences in the thermal conductivity as the pore volumes seemed higher in the sample GT600 than in GT599. The lower conductivity of the xonotlite based composition might be due the presence of more amorphous nature and the more regular pore-structure. The samples made using quartz showed a larger fraction of larger pores as can be seen in **Figure 119**.

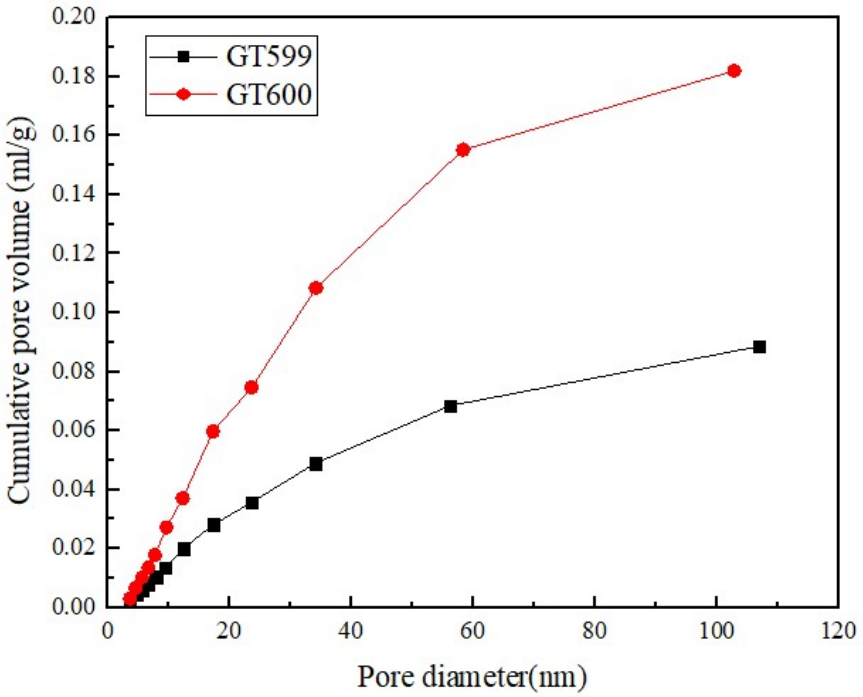

Figure 124. Curves of cumulative pore volume as a function of pore diameter. (Black curve) GT599 sample prepared from a silica mixture of 75% Q/25% MS; (Red curve) GT600 sample prepared from 100% MS as the only silica source.

It is known that the heat transfer in porous materials occurs by a combination of mechanisms, being the conduction by phonons in the solid state (λ_{solid}), the conduction by collision of gas-molecules in the pore-stem (λ_{gas}) and the transport by radiation (λ_{rad}). Because of the small pore-sizes in calcium silicate-based materials, the contribution of convection can be neglected. The overall thermal conductivity can be estimated by a summation of the above-mentioned processes. *Anton* and *Opsommer* further studied the factors of influence on different mechanism of heat transfer in relation to the type of calcium silicate-based mineral matrix. They affirmed that the conduction in the solid phase depends mainly on the density, the number of contact points and the phase composition **[135]**. The number of contact points can be controlled influencing the density and the structure of calcium silicate products. However, lowering of the density results in higher fractions of pores that increase the contributions of gas-conduction and radiation, especially at higher temperatures. It was shown in the research of Anton et al. that optimal densities exist for applications at different temperatures.

Formation of amorphous calcium silicate hydrates can allow to limit the conduction in the solid phase. Nevertheless, limiting the crystallization to C-S-H cannot be applied because it compromises the thermal stability. Then, the best way to control the solid

conduction seems to be the selection of an optimal density as a function of the application temperature and the use of additions that limit the radiation.

Concerning to the pore-size in the final autoclaved matrix, when they are small enough (typically below 100 μm), then a partial suppression of the gas-conduction occurs, meaning that the thermal conductivity in the pore-system is lower than that of free air. In calcium-silicates the pores-sizes can be 'engineered' by the control of crystals growth, though there is in general a fraction of pores below 100 μm, leading to a partial suppression of the gas conduction. This is especially the case at higher temperatures.

In their research work, *Anton* and *Opsommer* observed that the calcium silicate particles and crystals also contribute to the scattering of the photons **[135]**. The scattering efficiency is higher conforming the crystals are larger and is for plate-like tobermorite better than for needle-like xonotlite crystals. Nevertheless, the formation of tobermorite instead of xonotlite limits the thermal conductivity. The contribution of the particles or secondary aggregates depends on their size and is only important in the particle sizes of 10-20μm.

To summarize, the influence of silica sources and crystalline and amorphous ratio used at the starting formulation on Geltank technology can be summarized as follows:

- The use of amorphous silica or mixtures of amorphous silica and quartz in the gel tank process leads to products with different structure and properties. Products based upon quartz have better mechanical properties, though less good thermal stability, and also higher thermal conductivity.
- The differences in structure are mainly related to the reaction mechanisms and C-S-H-phases that form during the gelling reaction and the initial stages of the hydrothermal reactions.

4.1.2.6. Effect of additives: mineral fillers

The products made via the gel tank process have reasonably good strength though in general low fracture toughness. Several mineral fillers with specific physical and chemical properties were selected to be added at the starting formulation in order to study its influence on the mechanical and thermal behavior of xonotlite-type calcium silicate hydrate boards.

The mineral fillers used for a set of experiments were wollastonite, exfoliated vermiculite, and expanded perlite. They could be useful for increasing the fracture toughness by the mechanism of crack deviation.

Wollastonite is a naturally occurring mineral, although it can be also industrially processed. It is comprised chemically of calcium, silicon and oxygen. Its molecular formula is $CaSiO_3$, and its theoretical composition consists of 48.28% CaO and 51.72% SiO_2. Wollastonite has found application as a substitute for asbestos in fire-resistant building products used in the construction industry. As a functional additive, wollastonite improves flexural and impact strengths. Its low thermal conductivity and high aspect ratio structure also makes wollastonite an attractive addition for applications requiring fire resistance.

Vermiculite is a mica-derived mineral with shiny flakes and is one member of the phyllosilicate group. It can be expanded up to 30 times its original volume when heated at 650–950 °C. The exfoliated vermiculite exhibits interesting properties such as low thermal conductivity, low bulk density, endurance, chemical inertness and relatively high melting point. Exfoliated vermiculite has many applications in civil engineering. The flaky structure of vermiculite enables it to have high lubricating characteristics for wide ranges of applications and it is often used as in fire-protecting materials and as lightweight porous filler for heat insulating. Perlite is a material that can be also used for insulation in buildings. It is a porous, lightweight, fire resistant and moisture retaining material with sound and thermal insulation properties. A relatively high-water content of 2–5% distinguishes perlite from other hydrous volcanic glasses, such as obsidian, hydrated volcanic ash, and pumice. Upon rapid heating, the water in the structure converts into steam and this steam expands a softening glass matrix that constitutes the perlite and transforms it into a cellular material of low bulk-density. The formation of these bubbles allows perlite to expand up to 15–20 times of its original volume. Because of its favourable physical and chemical characteristics, expanded perlite is a potential mineral filler in thermal insulation construction materials.

These additives were added by 10% wt of the total solid mix at the starting composition before gelling step as they do not react with calcium hydroxide and microsilica. For the different preparations of GT samples, as silica source, silica fume was only used. As shown in the section **4.1.2.4.**, the xonotlite-based calcium silicate boards processed from silica fume presented a variable flexural strength, a low fracture toughness and a certain thermal shrinkage variation too. The GT samples containing additions of wollastonite, expanded vermiculite and expanded perlite were characterized by means of 3-Point Bending test. The mechanical properties of the autoclaved boards are given in **Table 28**.

Sample	Inorganic filler (%)	Density (Kg/m^3)	MOR (MPa)	MOE (MPa)	i.MOR (MPa)	i.Pl20 (J/m^2)
GT571-ref	0	548	2.3	716	47	59.7
GT562	10% W	541	2.5	695	78	133.4
GT561	10% V	529	2.3	539	111	186
GT560	10% P	534	2.8	900	53.8	0

Table 29. Mechanical properties of gel tank end-products containing additives to influence the fracture toughness. W: wollastonite; V: Vermiculite; P: Perlite.

Wollastonite and exfoliated vermiculite tended to reduce the pressure formed during the filter-pressing of C-S-H-based slurry as they behaved as inert materials. Therefore, this results in a reduction of the content of C-S-H gel that forms during the gelling step. After autoclaving, wollastonite and exfoliated vermiculite seemed to lead an improved fracture toughness in the calcium silicate matrix. This phenomenon is probably related to crack deflection around the additives. **Figure 125** shows the evolution of stress-strain curves for each GT sample containing additions of wollastonite, vermiculite and perlite, and for the GT reference. It is clearly seen that there was a considerable plastic part in of stress-strain curves for GT561 and GT562, and this was especially the case for the composition with vermiculite.

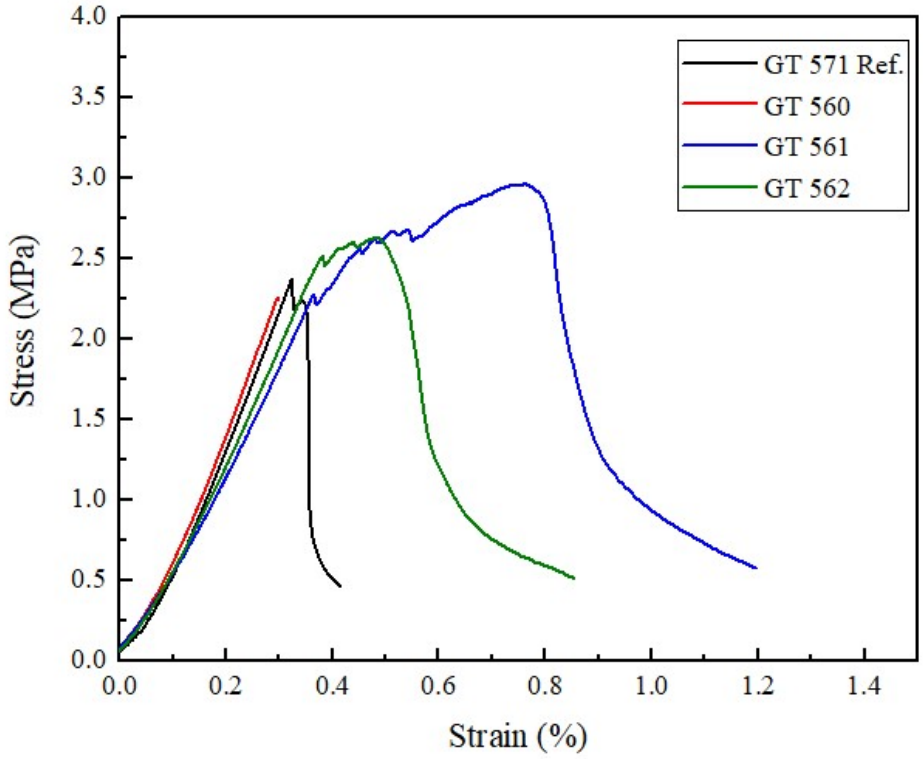

Figure 125. Stress -strain curves for GT-autoclaved samples with different additive compared to a GT-reference.

On the other hand, the expanded perlite addition to the starting formulation did not favour the fracture toughness of the calcium silicate matrix. Perlite is known to react in a calcium silicate formation process and leads to the development of a different C-S-H gel and the formation of an Al-tobermorite. Because of being involved in the C-S-H reaction, perlite forms strong bonds with the developing reaction products. Because of the strong interfaces, perlite did not favour crack deviation and hence had no positive impact on the fracture toughness.

The morphological analysis of the fracture surface of GT samples with mineral fillers was done by scanning electron microscopy. In the case of GT560, SEM analysis **(Figure 126)** shows that the fracture breaks up all the perlite particles, meaning the crack goes through the perlite and not around it as required for crack deflection.

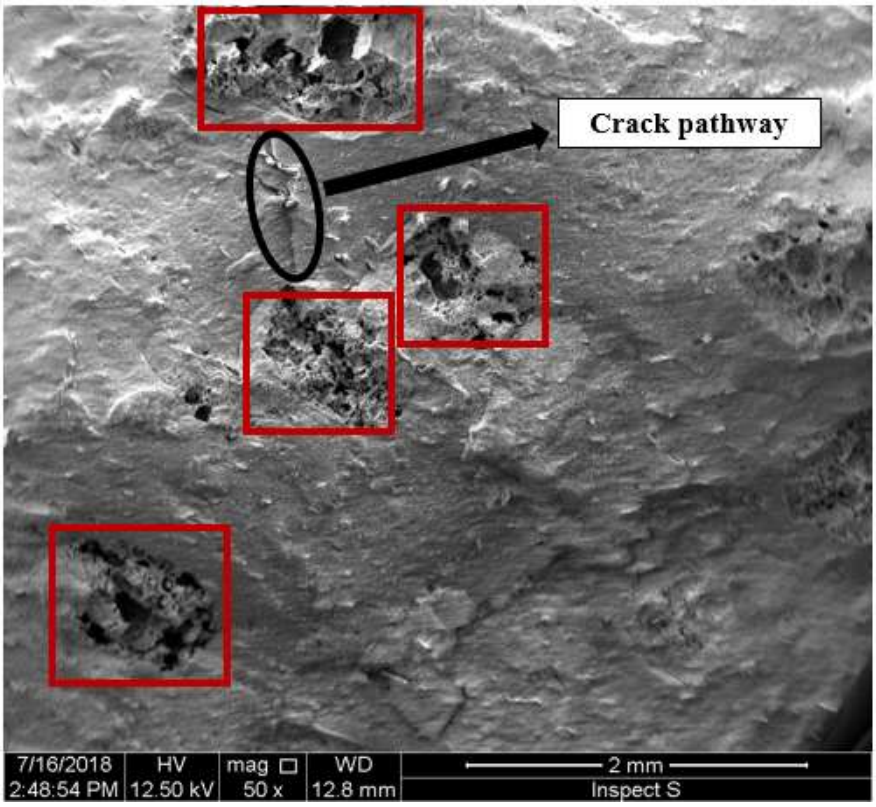

Figure 126. Scanning electron micrograph of fracture surface for GT560: Inclusions of expanded perlite particles in the matrix.

On the other hand, for GT samples containing additions of exfoliated vermiculite (GT 561) the mechanical behaviour is quite different. As observed in **Figure 127** by scanning electron microscopy, the crack gets around the vermiculite grains and this confirms the deviations of cracks by this mineral. The crack deviation due to a weak interface between the vermiculite and the Ca-silicate matrix and it results in an increased fracture toughness.

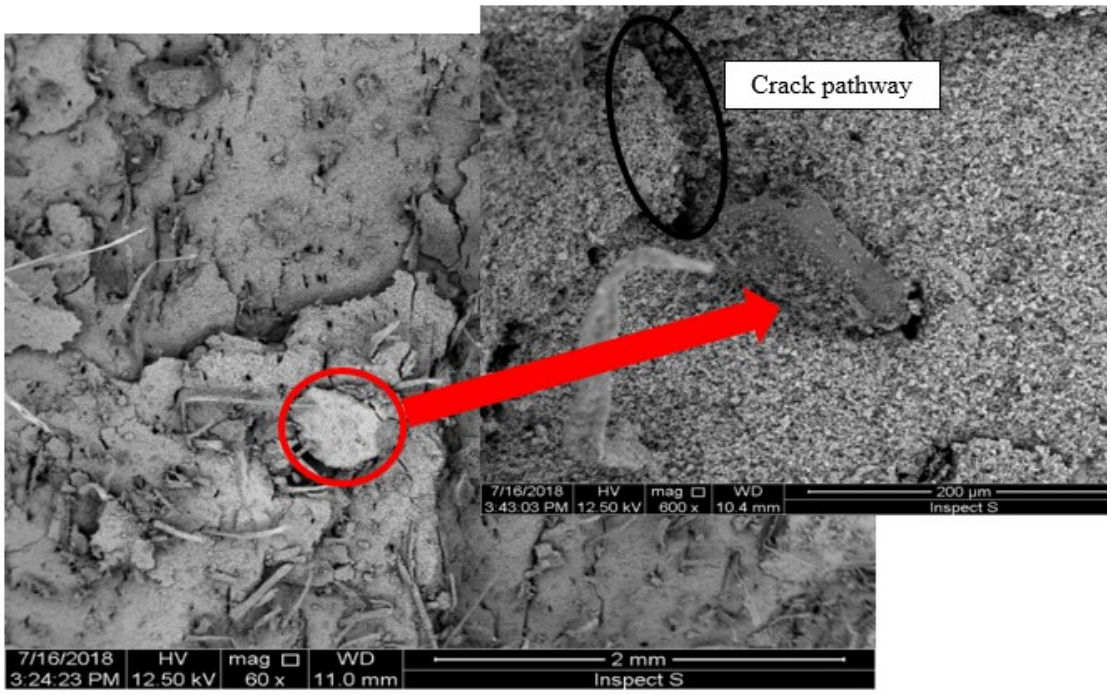

Figure 127. SEM micrography of fracture surface for GT 561: inclusion of exfoliated vermiculite grain in the matrix, which deviates the crack pathway.

For the GT samples that contain wollastonite (GT 562) the strain hardening was less than for the mixtures with vermiculite, though better than for the reference. In **Figure 128**, fracture surfaces of GT562, as observed by SEM, shows deviation and some pull-pout of the wollastonite. The interface is probably somewhat stronger than in case of vermiculite what could explain the intermediate behaviour for this additive.

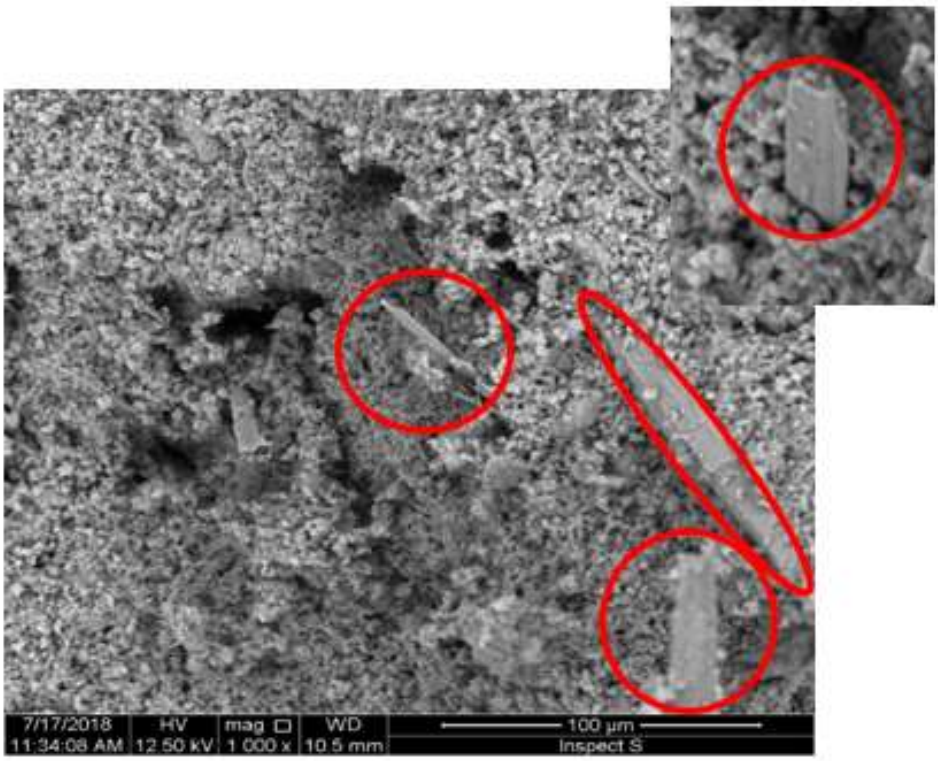

Figure 128. Scanning electron micrograph of fracture surface for GT562: Inclusions of wollastonite fibres in the matrix.

An indicative study of the contribution on the mechanical resistance of embedded wollastonite fibres in a calcium silicate matrix was requested to a modelling expert. So, a simple study based on a 2D mechanical linear elastic simulation was performed to understand the impact of wollastonite fibres on the mechanical behaviour of a calcium silicate board. The simulations were performed via outsourced services using COMSOL version 5.4 software. A simplified matrix of for a calcium silicate sample with vertical wollastonite fibres was simulated with details as shown in **Figure 129** and **Figure 130**.

Name	Expression	Description
h	150E-6[m]	height of element
w	2*h	width of element
f_w	8.69E-6[m]	width fiber wollastonite
f_sp	w/nn	spacing between fibers
nn	1 till 4 (10)	number of fibers

Number of fibers	Spacing between fibers
1	300 E-6 m
2	150 E-6 m
4	75 E-6 m
10	30 E-6 m

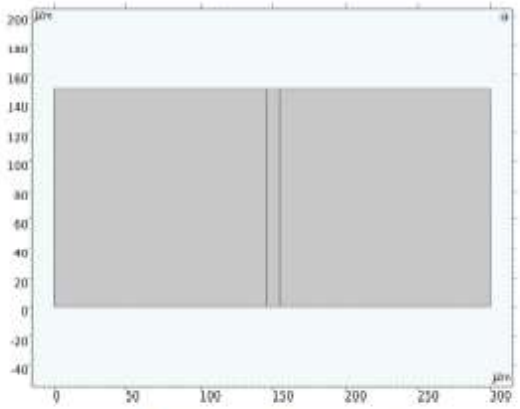

Example geometry for 1 fiber

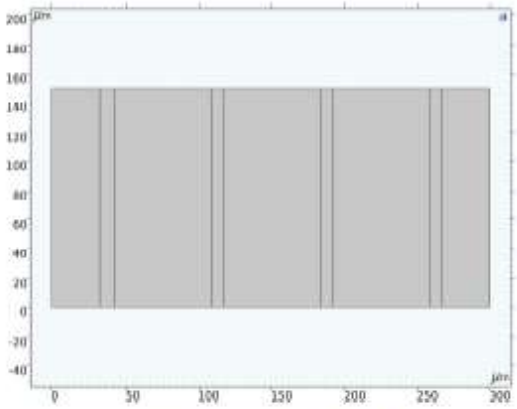

Example geometry for 4 fibers

Figure 129. Geometry of samples

Material	MOR (Max. stress), MPa	EMod, MPa	Poison coefficient
Calcium silicate hydrate	2.33 (not applied, linear material model)	716	0.2
Wollastonite fibers	416.5x10³ (Average value of literature range of 303-530 x10³), applied as bilinear plastic model	3400 (Average value of literature range of 2700-4100	0.2

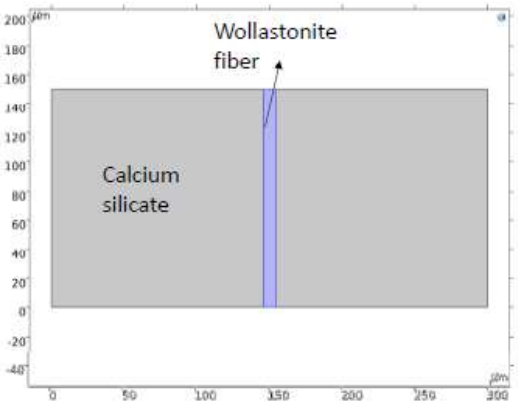

Figure 130. Mechanical properties of calcium silicate hydrate sample and wollastonite fibres.

Then, a set of 3 different tensile-stress tests were carried out. The first test was performed applying a load in y-direction to the sample as it can be observed in **Figure 131**.

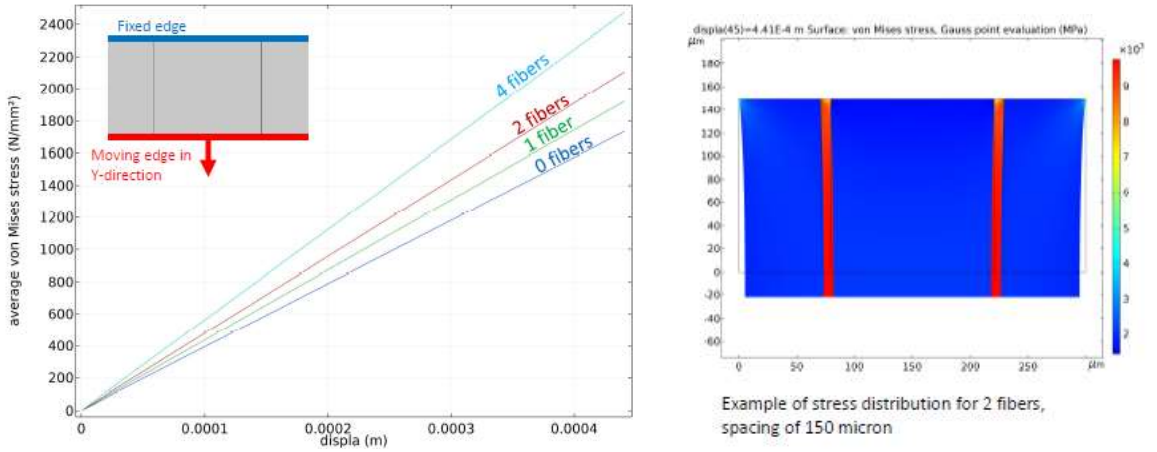

Figure 131. Tensile-stress test simulation for a load case in y-direction.

Here, it is clearly seen how increases the flexural strength in the sample as the number of wollastonite fibres are added in the matrix. In this case, as the loading force was in the same direction as the fibres were oriented the effect on the mechanical response was very positive. A second test was done applying a load in x-direction to the sample (see **Figure 132**).

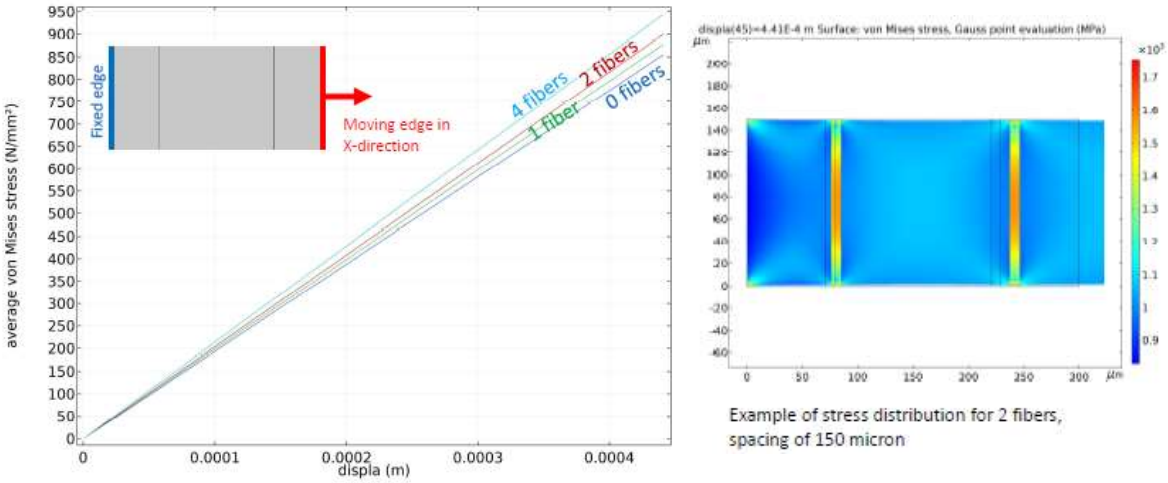

Figure 132. Tensile-stress test simulation for a load case in x-direction.

In this second simulation test, it seemed that the impact of the wollastonite fibres oriented vertically on the flexural strength was rather limited as expected. The third tensile-stress test applied a load in both x and y direction and the results are shown in **Figure 133.**

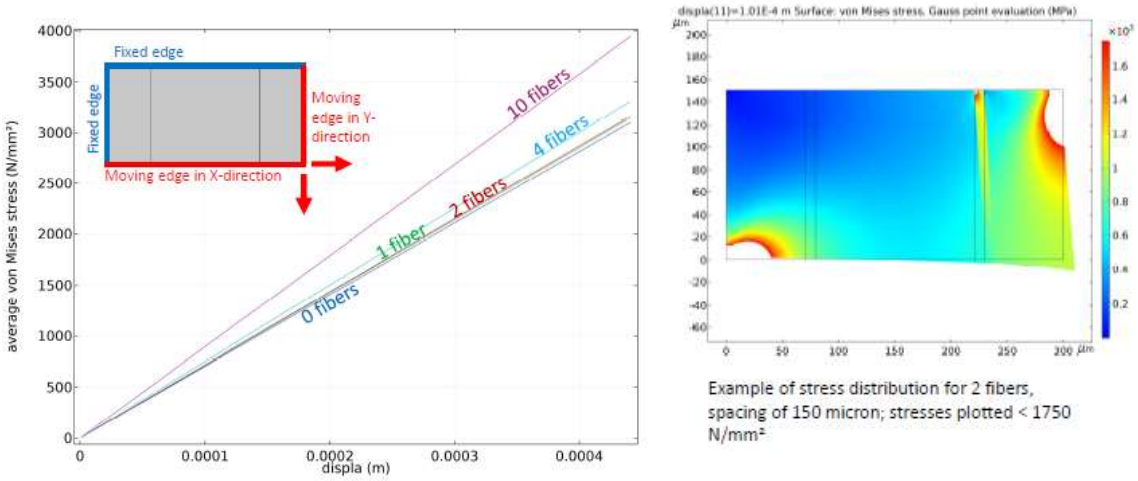

Figure 133. Tensile-stress test simulation for a load case in xy-direction.

When combining x- and y-direction the mechanical response was intermediate, and a clear positive effect was noted for a matrix with 10 wollastonite The positive impact of wollastonite on the E-modulus was confirmed experimentally with 3-bending point tests done on samples with different concentrations of wollastonite and this is shown in **Figure 134**. Due to the impact on the E-modulus, also the bending strength increases with the wollastonite-content.

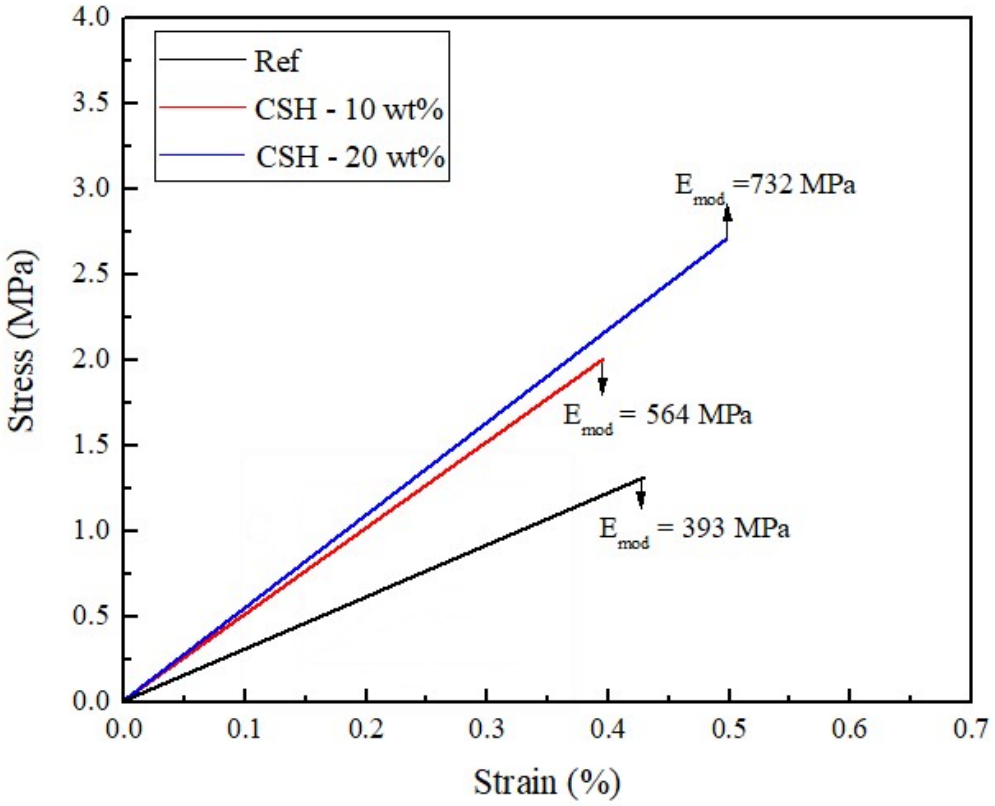

Figure 134. Elastic region of stress-strain curves for GT-autoclaved samples with different additions of wollastonite compared to a GT- autoclaved sample reference.

The thermal stability of Geltank samples containing different inorganic fillers is showed in **Figure 135**. A positive contribution when wollastonite and vermiculite are present in the matrix is observed. The positive effect of wollastonite on the thermal stability of Ca-silicate mased matrixes is well-known and is related to the high aspect ratio and the high thermal stability of wollastonite. Also, vermiculite in its exfoliated form limits the thermal shrinkage which is related to the refractory character of the mineral and the secondary expansion that compensates any shrinkage.

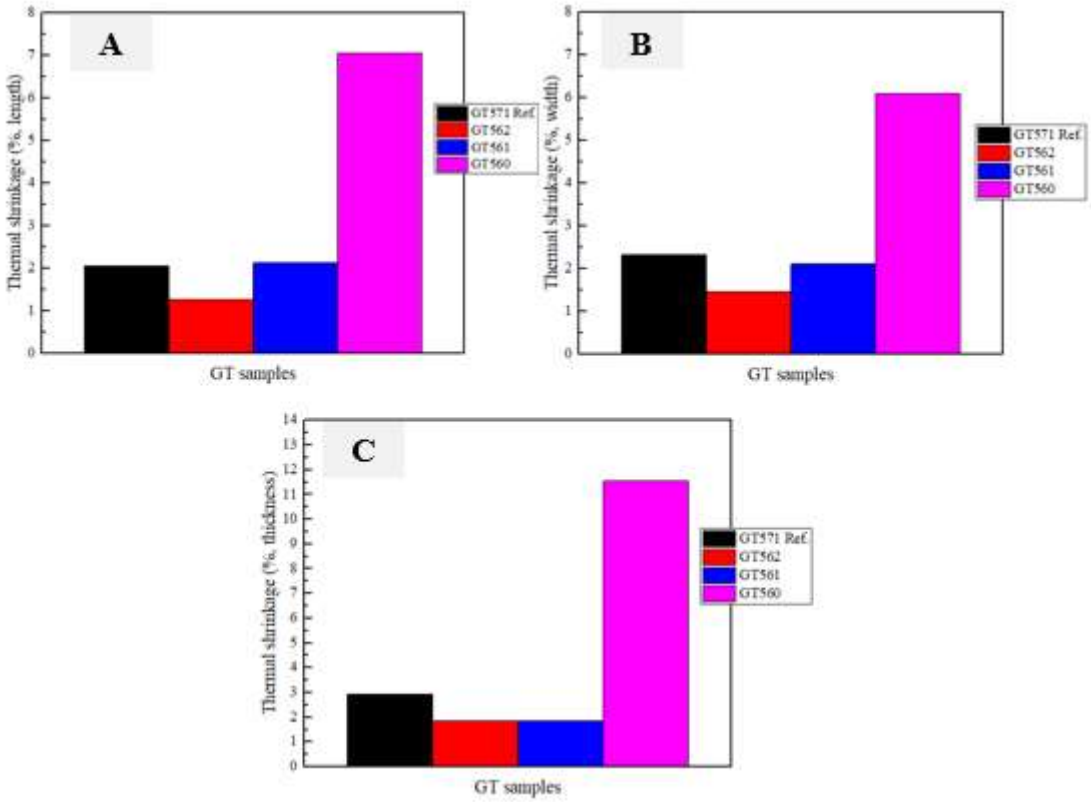

Figure 135. Thermal shrinkage values for length (A), width (B) and thickness (C) of Geltank samples.

The presence of perlite in the calcium silicate matrix does not favour the thermal resistance of the board. This is expected as perlite is a low melting phase that softens above 850°C and it also impacts the tobermorite formation. The effects of the mineral additives is clear from **Figures 136a, 136b, 137a** and **137b**.

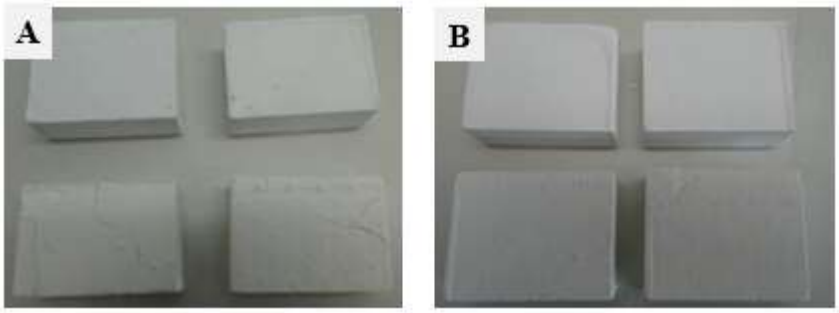

Figure 136. Images of GT specimens after thermal shrinkage tests at 950ºC and 1050ºC for 3 hours. (A) GT571-reference; (B) GT562-10wt% of wollastonite.

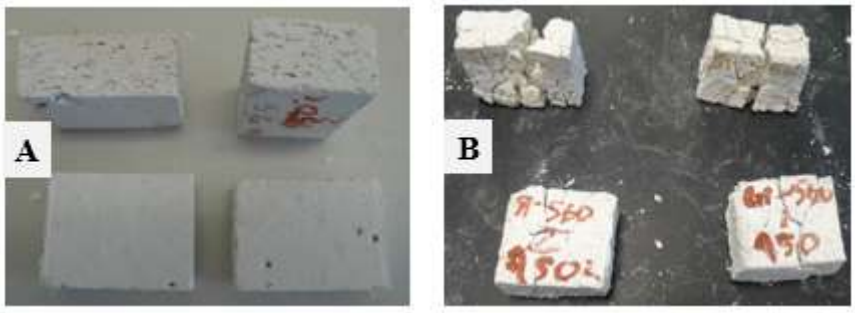

Figure 137. Images of GT specimens after thermal shrinkage tests at 950ºC and 1050ºC for 3 hours. (A) GT561-10 wt% vermiculite; (B) GT560-10 wt% of perlite.

The Rf-curves for the different compositions are given in **Figure 138**. The compositions with vermiculite and wollastonite have somewhat lower Rf values, which is due to the lower amount of C-S-H. For perlite this is less the case as it is also involved in C-S-H formation.

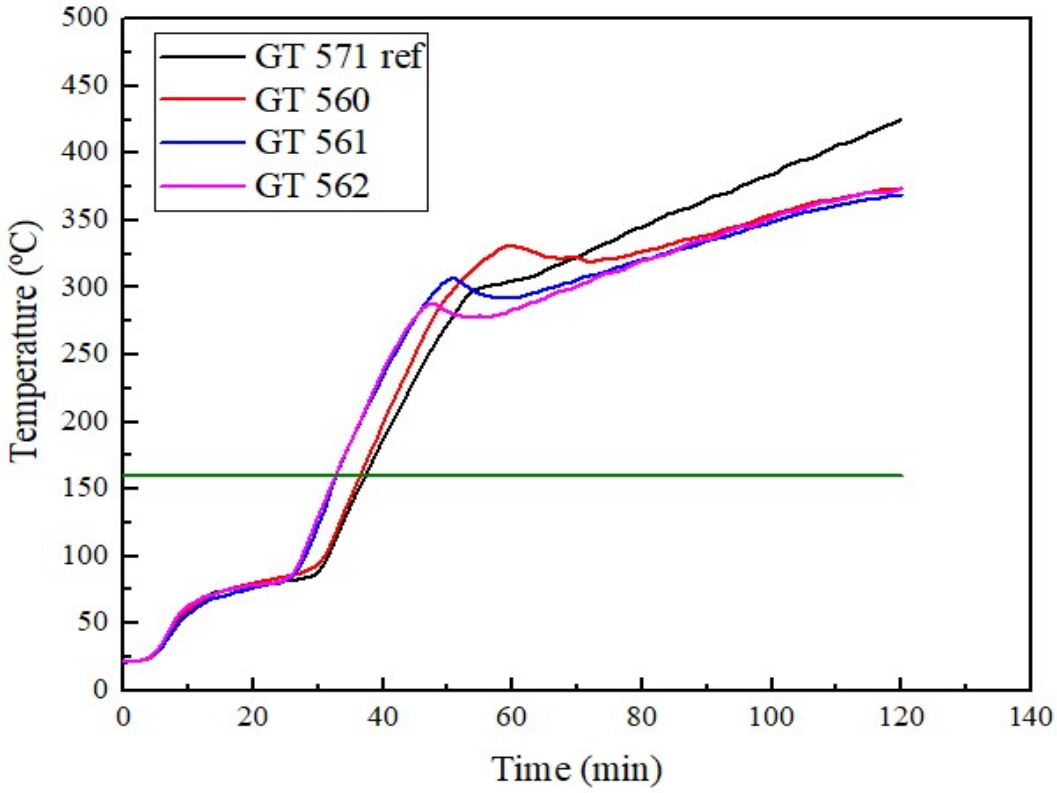

Figure 138. Comparison of RF-curves for gel tank end-products containing inorganic fillers compared with a reference.

The stabilization levels for all compositions with additives are somewhat better than for the reference. This could be due to effects on the thermal conductivity and is in the compositions with vermiculite and wollastonite also due to a better thermal integrity (lower degree of crack development).

Concluding it might be stated that the fracture toughness of the gel tank end-products can be improved using mineral inorganic fillers as additives that form a weak bond with the matrix and hence lead to crack deviation. Both vermiculite and wollastonite are additives that improve the fracture toughness. Besides, they also contribute to lowering of the thermal shrinkage.

4.1.3. Conditions to obtain different product densities

Geltank is a hydrothermal-based calcium silicate technology that allows to develop a quite wide range of low- and medium-density porous materials for use in insulation and passive fire protection. A scheme representing a scale of bulk densities product (150-750 Kg/m^3) which can be practically scanned by means of different starting formulations and working conditions is illustrated in **Figure 139**. Depending on the final bulk density desired, a specific mixture of amorphous and crystalline silica is used with the corresponding MS/Q ratio and the indicated gelling and autoclaving conditions. It is important to remark that very low densities (typically below 280 Kg/m^3) are difficult to reach with the Geltank technology. For these low densities, C-S-H gels of lower density than those obtained in this work would be needed.

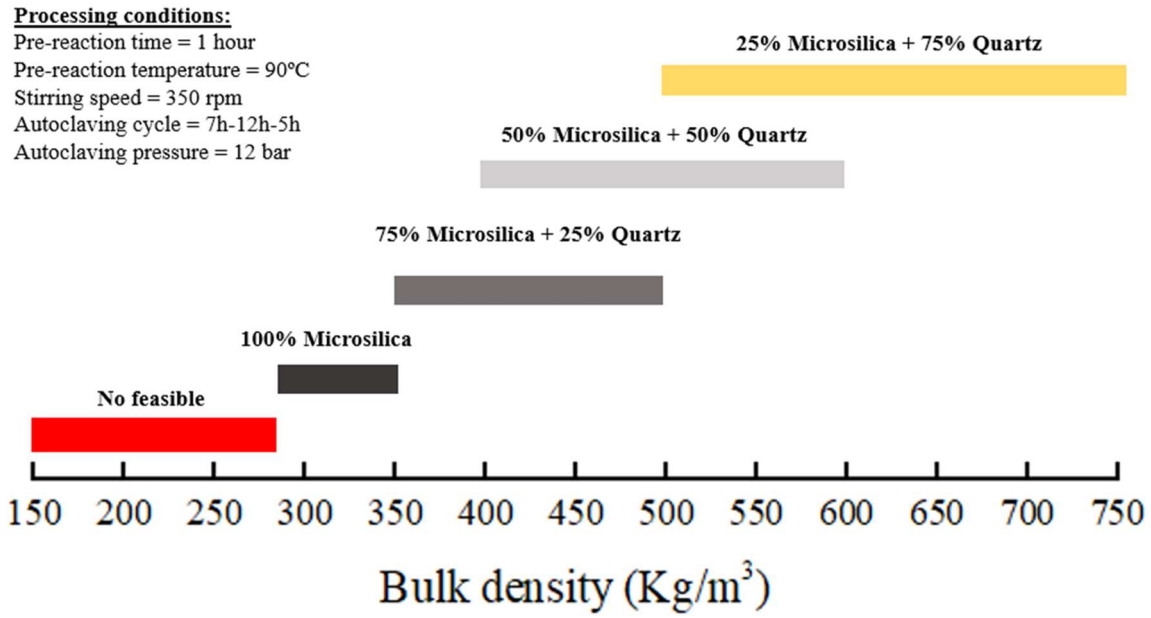

Figure 139. Scheme of bulk densities range covered by given compositions for the mentioned processing conditions in Geltank technology.

Summarizing the different options that Geltank technology provides, these are the following:

- Densities 280-350g/m^3 using 100% amorphous silica, 1 hour gel- reaction at 90°C.

- Densities 350- 500kg/m^3 using 50-75% amorphous silica, 1 hour gel- reaction at 90°C.

- Densities 500-750kg/m^3 using ≤ 25%amoprhous silica, 1 hour gel- reaction at 90°C.

4.2. Stirred autoclave reactor-filter pressing technology

4.2.1. Basics

Several of the most important Promat products are based upon the stirred autoclave technology. In this technology, low density particles are formed by reaction between lime and silica in stirred hydrothermal conditions. These particles have morphologies like shown in **Figure 140**. They are mixed with other ingredients like fibers, binders, endotherms and pressed into boards that are dried and ready for use. The exact reaction mechanisms are not fully understood. One of the targets of this PhD was to develop a better understanding by studying the reaction using different silica sources: quartz of different particle sizes, microsilica and mixtures of amorphous and crystalline silica. For this, several reactions were investigated as well as the end-products made with these different silica sources.

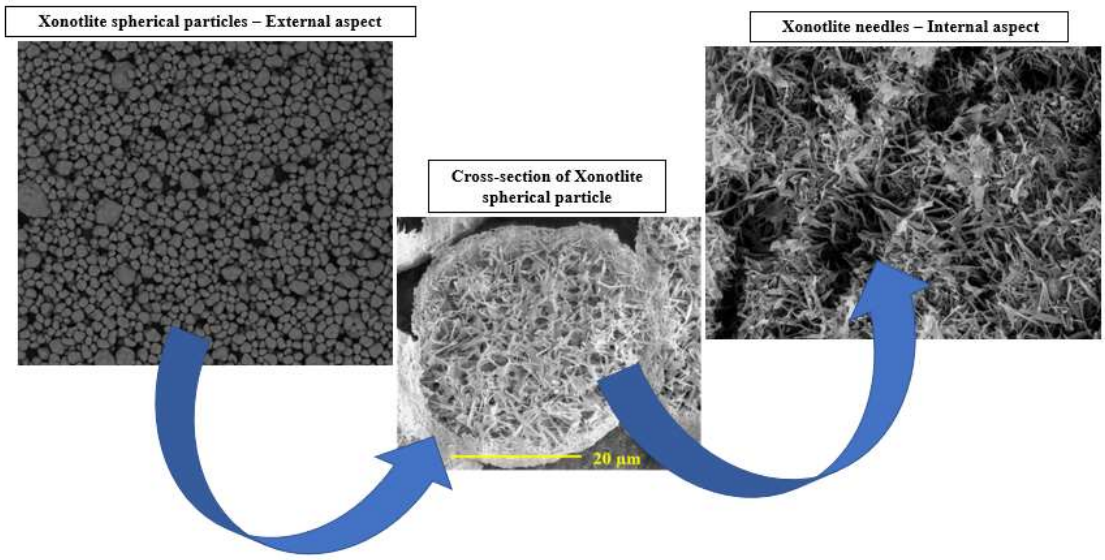

Figure 140. Scanning electron image of a porous xonotlite particle in a calcium silicate product.

On the other hand, 2 types of medium-density calcium silicate-based products developed by Promat Research and Technology Centre, PROMATECT-L and PROMATECT-LS. PROMATECT-LS contain ettringite as an endotherm agent to provide sufficient heat absorption capacity to the board when exposed to high temperature. The replacement of ettringite in the matrix by other chemical substances with endothermic properties was evaluated as well as the possibility of using opacifiers depending on the final application in passive fire protection and thermal insulation.

The main component of the calcium-silicate based products made upon the stirred autoclave reactor technology in the factory of Tisselt is so called xonotlite (Xo).

Xonotlite particles are spherical-like composite elements consisting of a denser skin composed of small xonotlite needles surrounding a less dense, more porous core of longer xonotlite needles that include around 95% of very small pores. The morphology and microstructure of these highly crystalline xonotlite particles are given in **Figure 140**.

PROMATECT-L product matrix contains besides the Xo-particles, glass fibers and cellulose as structure reinforcement components, OPC cement and bentonite clay. PROMATECT-LS contains Xo-particles, CFL-cement, bentonite clay, reinforcing fibers and ettringite which is added as an endotherm agent to increase the use of heat during a fire, limiting the temperature spread at the so-called cold side. **Figure 141** shows the morphology by scanning electron microscopy corresponding to the polished section of PROMATECT-L and PROMATECT-LS.

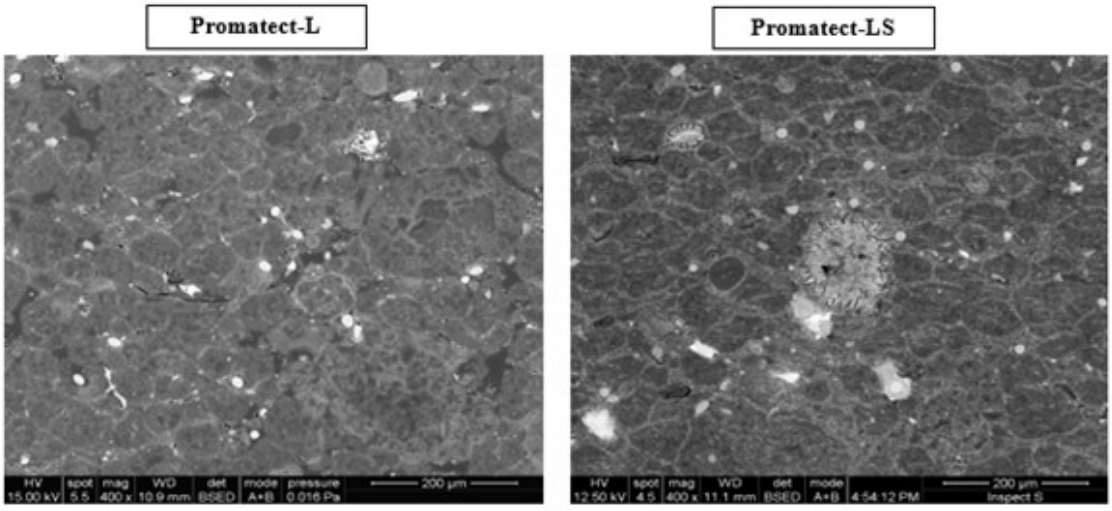

Figure 141. SEM micrographs of PROMATECT-L and PROMATECT-LS polished section microstructure.

4.2.2. Study of Xonotlite synthesis using different silica sources: quartz vs microsilica

To investigate the crystallization mechanisms of xonotlite from quartz (different particle sizes) and microsilica in combination with calcium oxide in hydrothermal conditions, a set of syntheses were done using a vertical stirred autoclave. The idea was to follow up the reaction sequence sampling at different dwell time to identify the new species formed as well as the unreacted phases. All the syntheses are listed below in **Table 29**. The aqueous slurries were characterized by means of x-ray diffraction and scanning electron microscopy to know the mineralogical composition and the morphological evolution.

Sample	Synthesis	Silica source	Lime source	Dwell time (h)
H1140-1	H1140	Quartz-M400	Lhoist Lime	1
H1140-2	H1140	“	“	2
H1140-3	H1140	“	“	3
H1140-4	H1140	“	“	4
H1135-1	H1135	Quartz-M500	Lhoist Lime	1
H1135-2	H1135	“	“	2
H1135-3	H1135	“	“	3
H1135-4	H1135	“	“	4
H1138-1	H1138	Quartz-M300	Lhoist Lime	1
H1138-2	H1138	“	“	2
H1138-3	H1138	“	“	3
H1138-4	H1138	“	“	4
H1136-1	H1136	Quartz -M8	Lhoist Lime	1
H1136-2	F1136	“	“	2
H1136-3	H1136	“	“	3
H1136-4	H1136	“	“	4
H1134-1	H1134	Suspension of non-dispersed microsilica-Elkem MS 940	Lhoist Lime	1
H1134-2	H1134	“	“	2
H1134-3	H1134	“	“	3
H1134-4	H1134	“	“	4
H1143-1	H1143	Suspension of dispersed microsilica-Elkem MS 940	Lhoist lime	1
H1143-2	H1143	“	“	2
H1143-3	H1143	“	“	3
H1143-4	H1143	“	“	4

Table 30. Experimental data for the hydrothermal reactions done in stirred autoclave reactor.

- ***Reactions with quartz***

Figure 142 shows the reaction sequences for Ca-silicate formation using crystalline silica M400 (example of fine sand) and M8 (example of coarse sand) based on XRD spectra. From these spectra it is clear that, depending on the particle size of quartz, two reactions ways can be distinguished. For fine sand the reaction goes via C-S-H whilst for coarse silica the reaction goes via α-C_2SH. On the other hand, **Figure 143** compares the phase composition after 3 hours of reaction with quartz of different particle size (M8/M300/M400/M500**)**. It is observed that with finer silica the reaction goes via the formation of tobermorite and higher contents of tobermorite are formed. In the synthesis done with M8, M300 and M400 almost no tobermorite is detected.

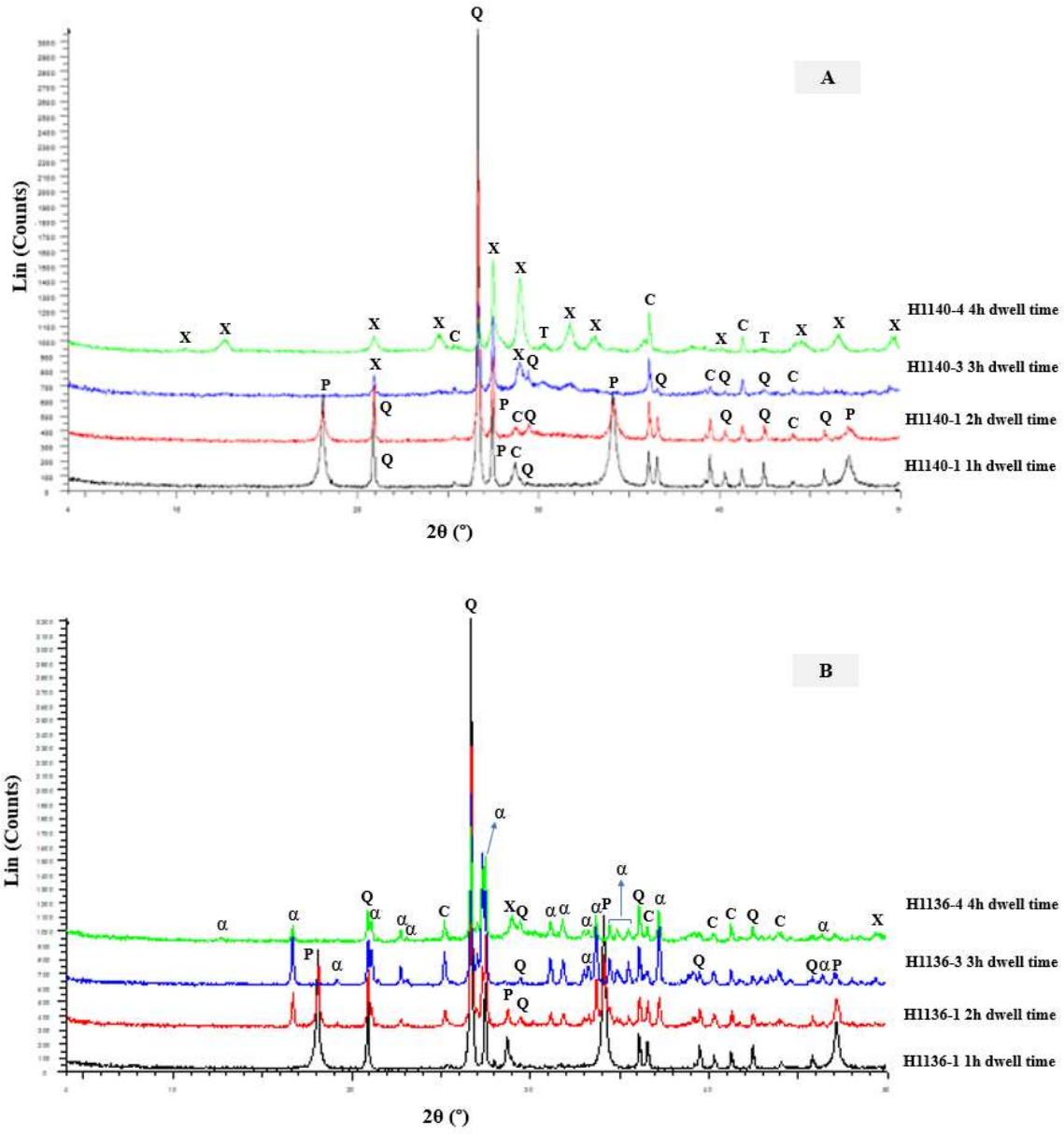

Figure 142. XRD-patterns showing the phases after different autoclaving time for reactions with quartz of different particle size. (A) XRD spectra of samples prepared via M400 quartz; (B) XRD spectra of samples prepared via M8 quartz. P: Portlandite, C: Calcite, α: α-C_2SH, Q: Quartz, X:Xonotlite, T: Tobermorite.

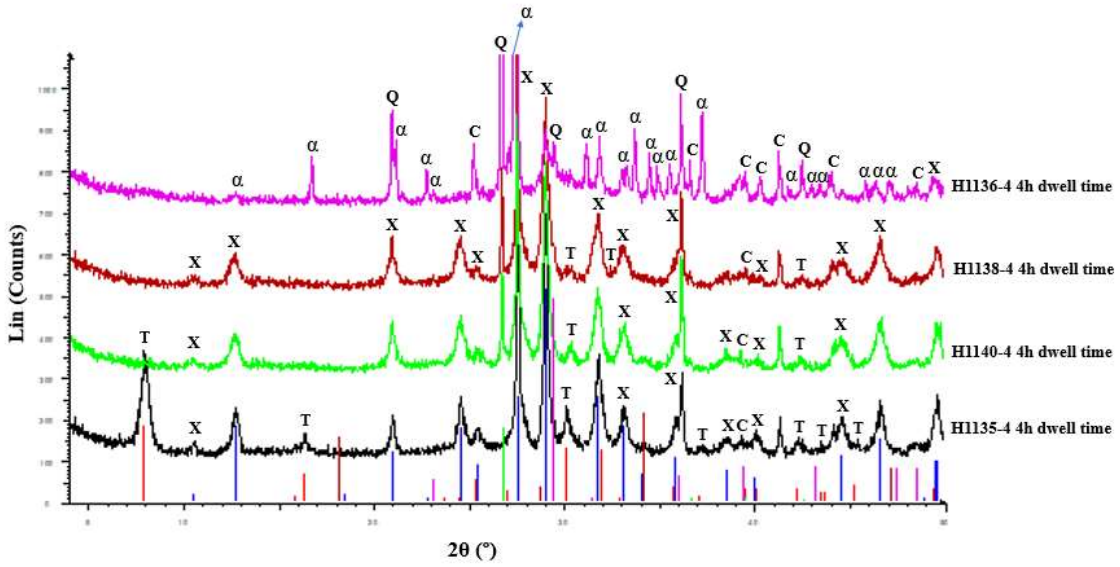

Figure 143. XRD-patterns showing the phases after 3h reaction for reactions with quartz of different particle size (M8/M300/M400/M500). X: Xonotlite, T: Tobermorite, C: Calcite, α: α-C_2SH, Q: Quartz.

From **Figure 142**, it is also clear that the formation of xonotlite via α-C_2SH is slow and incomplete, as seen on the x-ray diffraction spectra for the measured samples prepared initially with M8 silica. The crystallisation occurs faster in reactions with finer silica such as M500 and M400. This is visible in **Figure 144**, where XRD patterns of the phases are shown after different reaction times for reactions with M400 and M500. Here, there is already some xonotlite formation in the sample taken after 3 hours in the reaction with M500. In the reaction with M400, xonotlite formation is only present from the sample of the product and not after 3 hours. Tobermorite is not usually to be formed when using coarser silica. However, it was observed in the XRD spectra for the sample prepared with M500. Thus, the end-product of reactions with finer quartz contains a greater percentage of tobermorite than with coarser quartz. The reaction pathways for the reactions with M500, M400, M300 and M8 can be written as follows:

CaO + Q M500 → Ca-rich C-S-H + Q → C-S-H → To → To + Xo

CaO + Q M400 → Ca-rich C-S-H + Q → C-S-H → Xo

CaO + Q M300 → Ca-rich C-S-H + Q → C-S-H → Xo

CaO + Q M8 → α-C_2SH → C-S-H + α-C_2SH → C-S-H + α-C_2SH + Xo

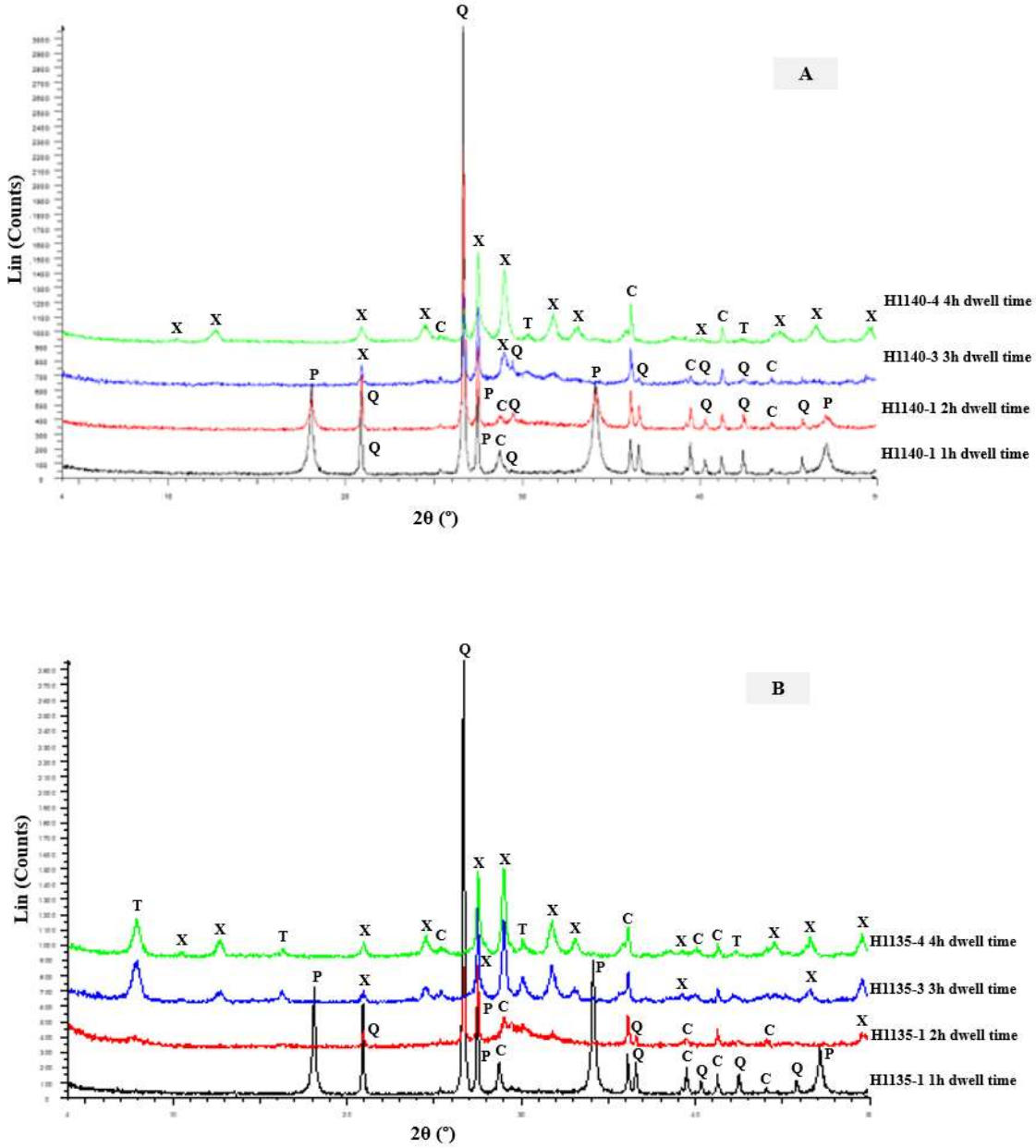

Figure 144. XRD-patterns showing the phases after different reaction times for reactions with M400 (A) and M500 (B). X: Xonotlite, T: Tobermorite, C: Calcite, P: Portlandite, Q: Quartz.

The above can be explained by the mechanism schematically represented in **Figure 145**. For fine quartz, the formation of calcium silicate hydrates proceeds via the following steps:

- Conversion of CaO in $Ca(OH)_2$, process called slaking. This recrystallization can be controlled by additions. In the process used in Promat, Ca_2SO_4 is added to make larger $Ca(OH)_2$-crystals and reduce the rate of solubilization.
- Partial dissolution of $Ca(OH)_2$ (according to its solubility in the considered conditions), leading to increase of the pH to above 11. Due to this higher pH and the effect of temperature, the quartz grains start to partially dissolve in the superficial layers (being amorphous).
- Reaction of Ca^{2+} with dissolved silica, and precipitation as Ca-rich CSH(II). The initial phases are Ca-rich as the solubility of $Ca(OH)_2$ is higher than that of quartz in the initial reaction conditions.
- Further diffusion of Si-ions in the CSH(II) and formation of a C-S-H that is less Ca-rich (CSH(I)) , while further CSH(II) is formed at the reaction/liquid interface.
- Reaction within these agglomerates, in a way that depends on the relative reactivity of CaO and SiO_2 leading to CSH-phases with different CaO/SiO_2 ratios that recrystallize as tobermorite and later into xonotlite or directly to xonotlite.

Several reacting quartz grains surrounded by the reaction rims can during the hydrothermal reaction meet and further react together and these reacting rims can also include $Ca(OH)_2$ forming composite particles.

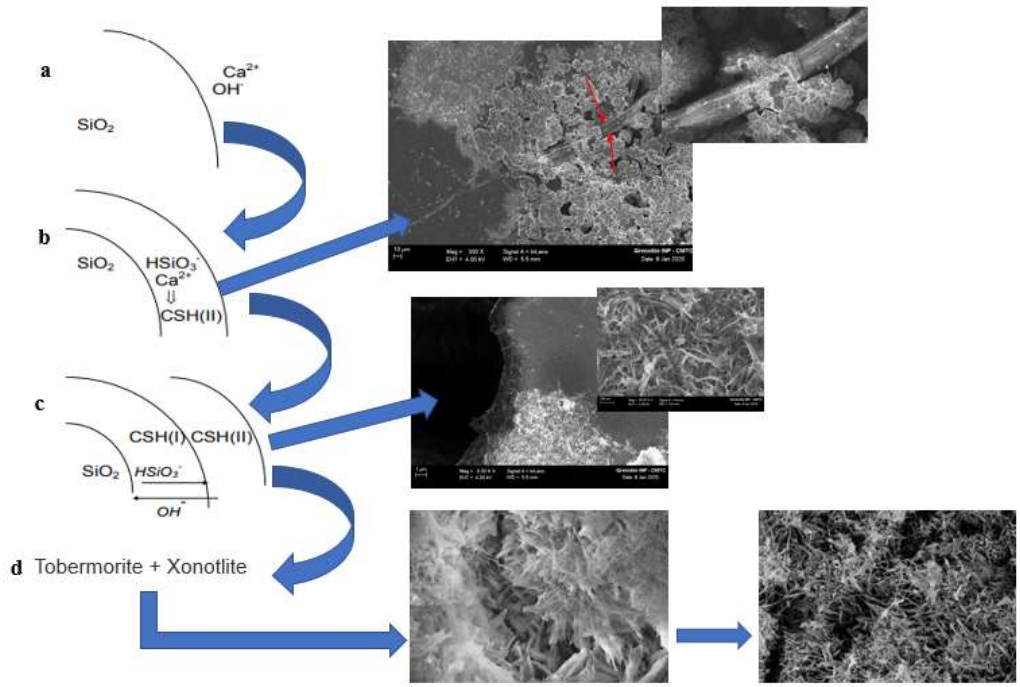

Figure 145. Schematic evolution (top to bottom) of calcium silicate synthesis.

The initial C-S-H composition depends on the solubilization rate of quartz and $Ca(OH)_2$. Conforming the silica is finer, there is more dissolved silica available and the C/S-ratio of the C-S-H decreases.

For coarser quartz, the rate of solubilisation is very low and therefore the C/S-ratio of the solution is high. This results in the precipitation of a Ca-richer phase instead of C-S-H. This phase is α-C_2SH. C-S-H gel forms in a later stage and acts again as a binder. This leads to agglomerates of quartz, C-S-H and α-C_2SH. As the dissolution of quartz proceeds, α-C_2SH transforms into C-S-H. The reaction is much slower, and the particles formed in this way tend to have a more pronounced 'cauliflower' morphology.

$$CaO + Q\ M8 \rightarrow \alpha\text{-}C_2SH \rightarrow C\text{-}S\text{-}H + \alpha\text{-}C_2SH \rightarrow C\text{-}S\text{-}H + \alpha\text{-}C_2SH + Xo$$

The morphology of H1140 samples (synthesis with M400) at the different dwell time was determined by SEM as shown in **Figure 146**. After 1h dwell time, we observe loose agglomerates of C-S-H, quartz and C-S-H formed on the Q-grains (see **Figure 146A**). The degree of agglomeration of the C-S-H particles increased over time.

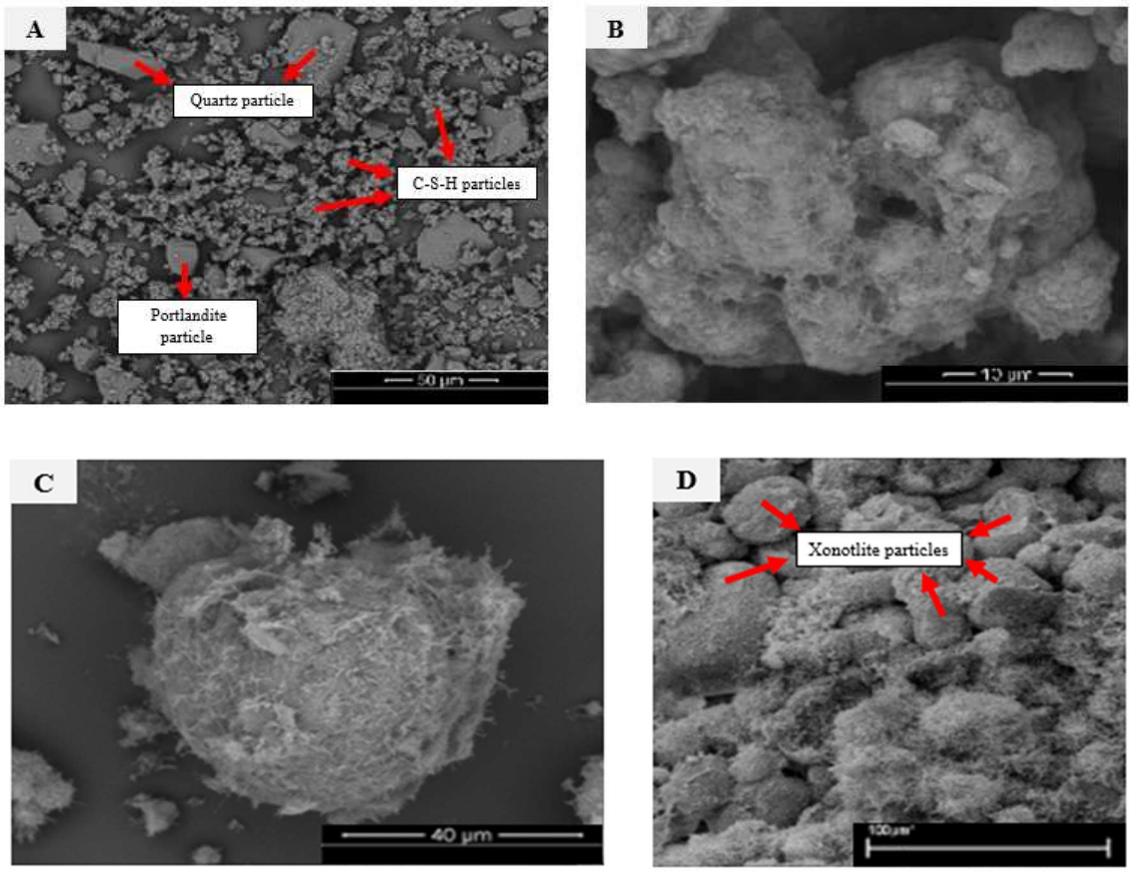

Figure 146. SEM micrographs of H1140 samples showing the microstructure of different crystalline and semicrystalline phases along the hydrothermal reaction.

In addition, the microstructure of the C-S-H particles appeared to be more developed, presenting a considerable porosity (see **Figure 146B**) and the particles get rounder (**Figure 146C**). Finally, after 4 hours of dwell time, quite well rounded xonotlite-based particles were formed at the end of the process as shown Figure **146D**. Whilst for coarse quartz, the reaction goes via α-C_2SH, and an example of the microstructure is shown in **Figure 147** as a SEM image.

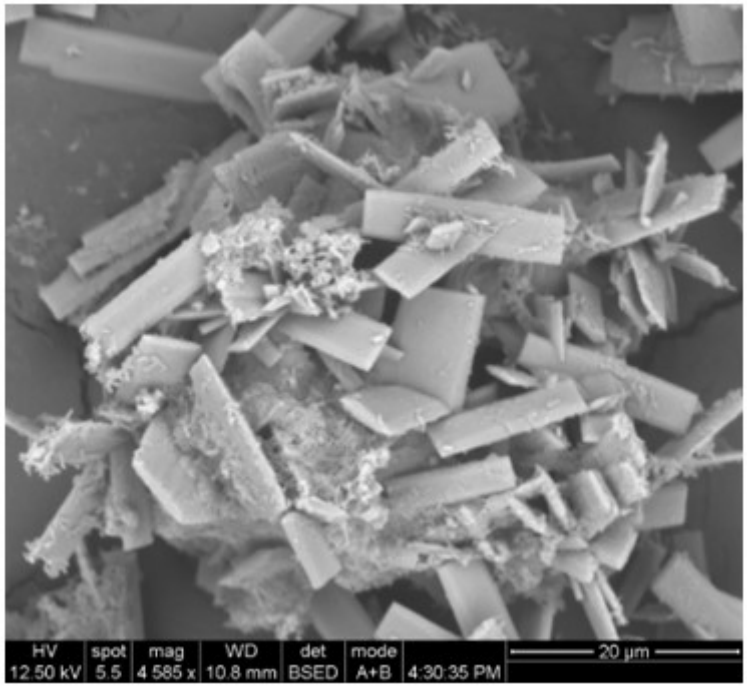

Figure 147. Aggregates containing α-C_2SH that form after 1-2 hours in reactions using M8 quartz.

- ***Reactions with amorphous silica***

As alternative silica source in the hydrothermal reaction with lime instead of quartz, an amorphous silica, Elkem MS 940 (as aqueous dispersion) was used for several syntheses to study its influence.

In **Figure 148**, the XRD patterns are shown with the results of the $Ca(OH)_2$-SiO_2 synthesis using Elkem MS940 slurry, sampled in function of time. It can be observed a fast development of C-S-H. This can be derived from the fact that portlandite ($Ca(OH)_2$) contents are much lower in the beginning of the reaction than in the initial reaction products of reactions with crystalline silica (see **Figure 142A**). All the portlandite is already reacted away after 1 hour of reaction with the amorphous silica slurry. In the reactions with crystalline silica there is always a portlandite peak in the sample taken after 1 hour. But nevertheless, this quickly formed C-S-H transforms very slowly into the end-

product. This end-product is xonotlite, whilst for finer quartz the reaction goes via tobermorite, and this seems not the case for the reaction between lime and amorphous silica.

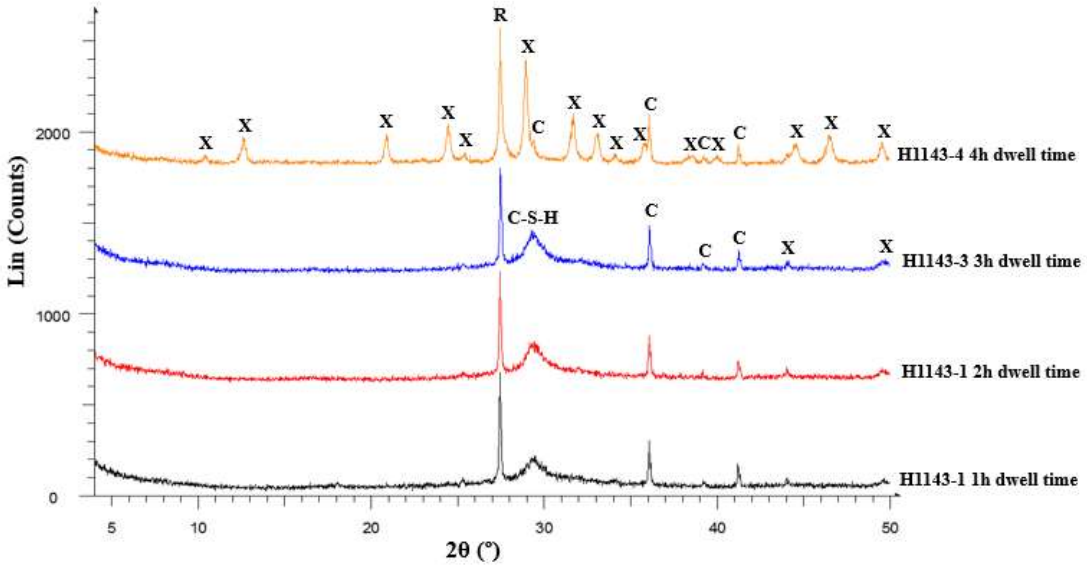

Figure 148. XRD spectra of autoclaved slurries at different dwell time made from starting lime-microsilica mixture. X: Xonotlite, C: Calcite, R: Rutile, C-S-H: Calcium silicate hydrate with C/S ratio ≤ 1.

By this way, the reaction pathway of xonotlite from amorphous silica and lime would be as follows:

$$CaO + MS\ Elkem\ MS\ 940\ (dispersed\ in\ water) \rightarrow C\text{-}S\text{-}H \rightarrow C\text{-}S\text{-}H + Xo \rightarrow Xo$$

Two possible reasons might explain the differences between the mechanism reactions of crystalline (quartz-fine) and amorphous silica:

- The rate of dissolution of these siliceous materials is totally different. The order of the rate of dissolution is considered in terms of solubility and specific surface area as follows: Elkem MS 940 (dispersed in water) >> Quartz-fine M500 > Quartz-fine M400. The reaction mechanism is highly dependent on the rate of dissolution of siliceous materials.
- A different composition and structure of the early C-S-H phases is most likely formed at the beginning of the reaction, then it influences on the recrystallization of C-S-H into xonotlite/tobermorite

In case of Elkem MS 940 (dispersed in water), the C-S-H phase formed is more stable and persists longer until that the temperature at which xonotlite crystallizes is reached

(~190ºC-200ºC). This C-S-H is expected to be silica-richer than the C-S-H formed when using quartz due to the higher solubility of the amorphous silica. Noma reported that this C-S-H synthesized from amorphous silica (Elkem MS 940) must be homogeneous and it contains relatively long silicate chains and non-distorted Ca-O layers, meaning a higher degree of polymerization **[79]**. A small study based on solid-state nuclear magnetic resonance was performed by the KU Leuven to reinforce the hypotheses concerning the different structure and composition of early the C-S-H phases formed by means of different silica sources. In **Figures 149** and **150**, it is shown the ^{29}Si HDPEC and CPMAS NMR spectra of samples taken during the hydrothermal reactions of xonotlite from quartz M400 and dispersed Elkem MS 940 at 1 and 2 hours of dwell time respectively.

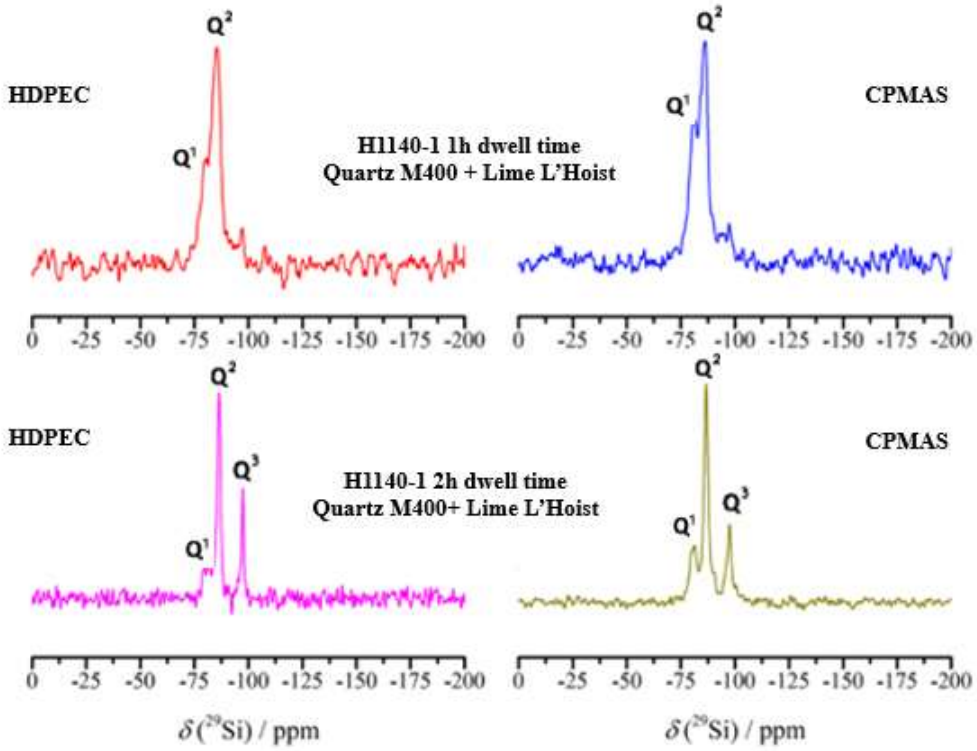

Figure 149. ^{29}Si HDPEC and CPMAS NMR spectra of the products hydrothermally synthesized from Quartz-fine (M400).

At the reaction time of 1h for the HDPEC and CPMAS spectra of H1140-1, a low signal intensity of Q^1 was observed at -79 ppm. Whereas that in the HDPEC spectra of H1143-1, the signal intensity of Q^1 is very low, becoming a smaller peak. In CPMAS is a bit more pronounced the Q^1 peak. A similar signal intensity of Q^2 at -85 ppm was found for both the HDPEC/CPMAS spectra of H1140-1 and the H1143-1. Although, in the HDPEC spectrum for H1143-1, Q^1 and Q^2 NMR peaks merged because the chemical shifts lie very close together, then a larger intensity of Q^2 was observed. At the reaction time of 2h, the HDPEC and CPMAS spectra of H1140-1 showed a larger signal intensity of Q^1 comparing to the HDPEC and CPMAS spectra of H1143-1. Q^2 peak becomes sharper with a higher signal intensity in both reaction systems. A sharp signal at -95 ppm was found as Q^3 peak in the HDPEC and CPMAS spectra of H1140-1 and H1143-1 respectively.

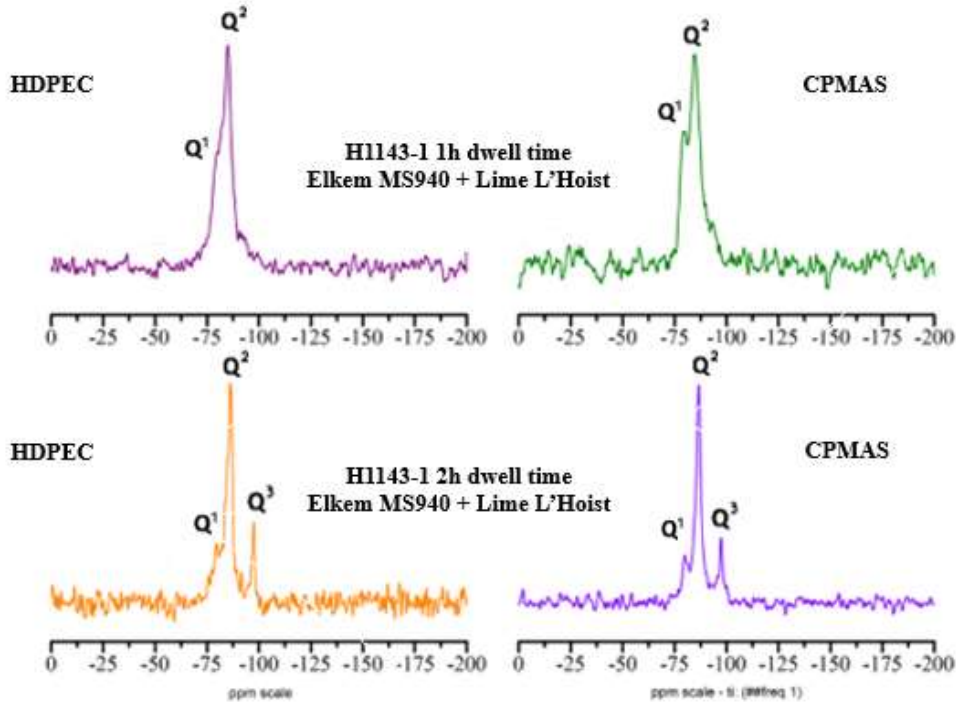

Figure 150. ^{29}Si HDPEC and CPMAS NMR spectra of the products hydrothermally synthesized from amorphous silica (aqueous suspension of Elkem MS 940).

It can be inferred from the NMR results that the silicate chains of the C-S-H formed from quartz-fine present a shorter polymerized structure than the C-S-H produced from amorphous silica as Q^2/Q^1 ratio increased at 1 and 2 hours of reaction. This also might explain an easier recrystallization from C-S-H synthesized by quartz-fine into tobermorite and later, into xonotlite, owing to the shorter silica chains in its structure. A shorter chain length indicates a higher C/S ratio, namely a calcium-richer C-S-H. On the other hand, the C-S-H produced from the used amorphous silica, contains longer silica chains (Q^2 – chain middle groups), meaning a higher degree of polymerization. Then, the chance to form tobermorite crystals was nearly non-existent due to the long and more complex C-S-H structure and morphology. By this was, xonotlite needles were directly formed from the C-S-H that evolves into a more order structure as hydrothermal reaction time increases.

For the non-dispersed microsilica (Elkem MS 940), the reactivity is very low, therefore the C-S-H formation when reacting this amorphous silica with lime occurs very slowly via α-C_2SH (same intermediate phase formed when using quartz-coarse) as intermediate phase and being incomplete as xonotlite is not crystallized. This may be clarified, since the aggregates of non-dispersed amorphous silica react mainly on the surface as higher reactive sites, meaning that the rate of solubilization is low. These agglomerates might react in the same way as coarse silica source (M8 quartz). But, if this kind of microsilica is well dispersed in water, a rapid formation of C-S-H is occurred and later, xonotlite crystallizes in a proper way.

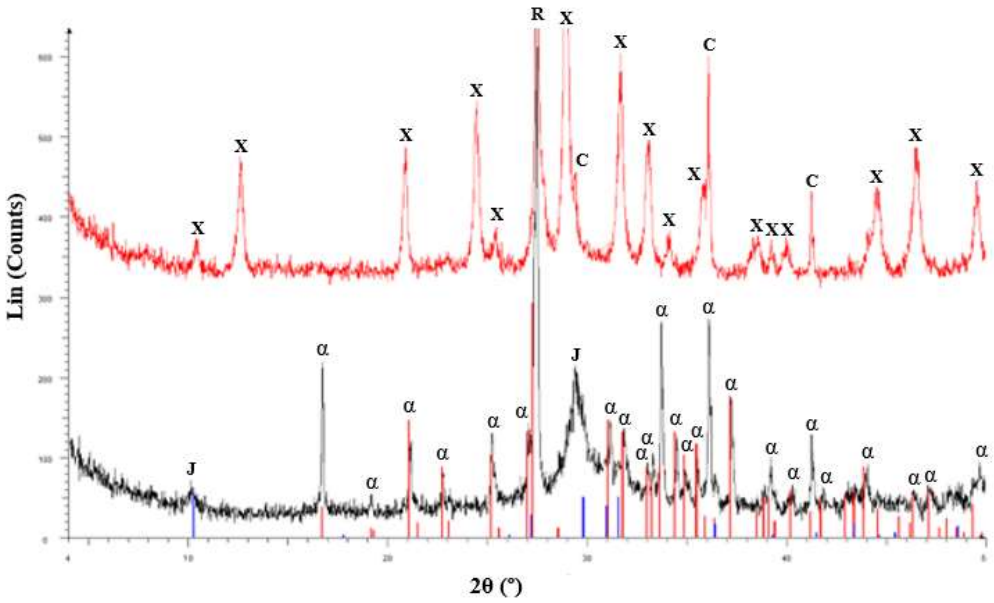

Figure 151. XRD spectra of H1134 and H1143 samples showing the phases formed after 3 hours reaction time when using non-dispersed silica fume (black curve) and dispersed silica fume (red curve). X: Xonotlite, C: Calcite, R: Rutile, J: Jaffeite, α: α-C_2SH.

This can be observed in **Figure 151**, where the mineral phases found after 3 hours of hydrothermal reaction time are shown when using Elkem MS 940 as such (powder without dispersion) and as aqueous suspension obtained by powder high shear mixing. In the XRD spectrum corresponding to the sample prepared from non-dispersed silica, there is no presence of xonotlite peaks and mostly peaks of α-C_2SH were found. Whereas that in the XRD spectrum corresponding to the sample prepared from a water suspension of dispersed Elkem MS 940 a large number of xonotlite peaks are recognisable.

The reaction products of synthesis with amorphous silica (H1143) samples were also characterized by SEM and STEM techniques. **Figure 152** shows some SEM and STEM micrographs of the microstructure of these samples at different dwell time. After 1 and 2 hours, a large amount of C-S-H gel phase agglomerates are formed as can be seen in **Figure 152A** and **152B**. In agreement with the XRD data, these are poorly crystalline phases. STEM shows some Xo-crystallites forming in the C-S-H-agglomerates formed after 3h. These are present as very fine needles as can be seen in **Figure 146C**.

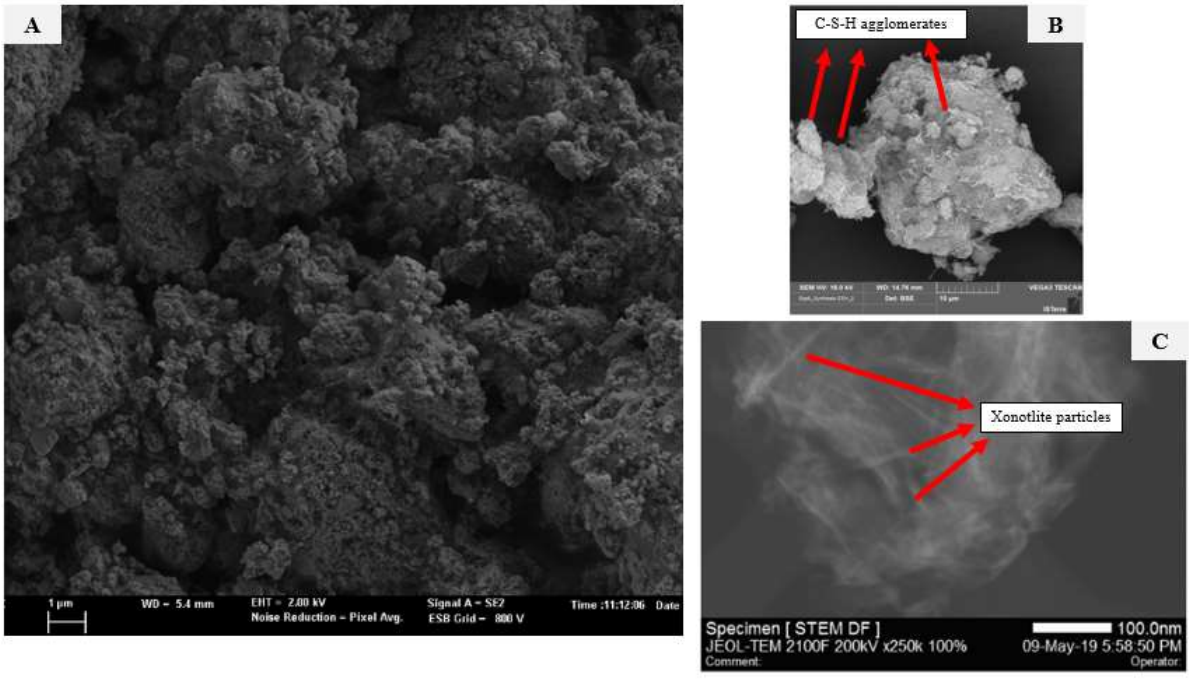

Figure 152. SEM/STEM micrographs of H1143 samples after 1h, 2h and 3h of hydrothermal treatment.

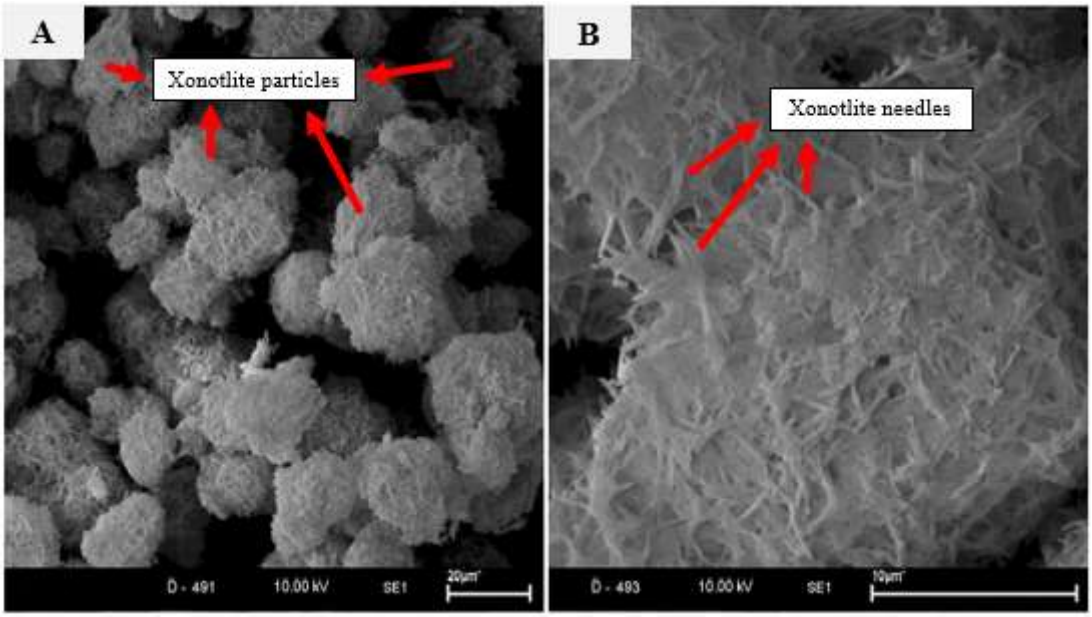

Figure 153. SEM micrograph of H1143 sample after 4h of hydrothermal treatment.

After 4 hours dwell time, quasi-spherical particles composed of needle-like xonotlite fibers were well observed by SEM as **Figure 153** shows. Unlike the particles synthesized via quartz-lime mixtures, in this case, the xonotlite needles are longer and thinner (see **Figure 153B**) , including more pores and the skin that normally is observed in the xonotlite particles made with quartz, is absent. When looking in an optical microscope, the xonotlite particles produced from quartz-fine are larger and denser than the ones synthesized by means of amorphous silica. In the latter, a few non-opened aggregates are also visible (see **Figure154**).

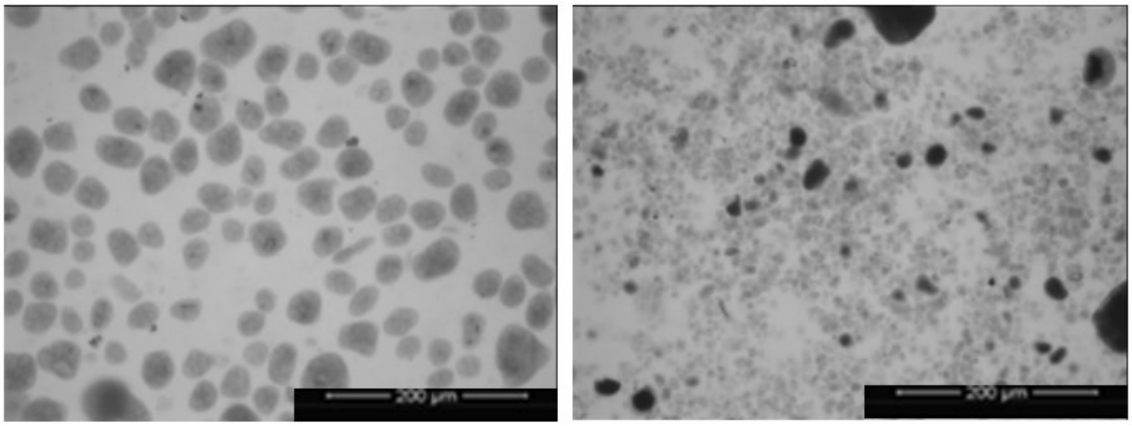

Figure 154. Ca-silicate reaction products based upon crystalline silica and amorphous silica as seen in an optical microscope. (Left) Xonotlite-based slurry made using M400 quartz; (Right) Xonotlite-based slurry made using M500 quartz (finer than M400).

Sample ID	Silica type	%P	% AP	% Q	% C	Ca^{2+} in the solution (mg/L)	Calculated molar ratio for CSH
H1140 1h	Quartz M400	37.3	14.4	47.6	0.7	353	>2
H1140 2h	Quartz M400	16.2	47.5	31.0	5.3	253	1.5
H1135 1h	Quartz M500	35.2	16.0	46.3	2.4	396	>2
H1135 2h	Quartz M500	0	78.1	3.6	11.6	348	1
H1143 1h	Elkem MS940 slurry	1.4	88.8	0	9.7	530	0.8
H1143 2h	Elkem MS940 slurry	0.7	87.9	0	11.4	142	0.7

Table 31. Phase compositions for reaction products using different silica-sources. P: portlandite, AP: amorphous phases, Q: quartz, C: calcite.

Table 30 presents the calculated Ca/Si ratio of the C-S-H obtained from different silica sources at 1- and 2-hours dwell time. On one hand, the content of portlandite, amorphous phases, quartz and calcite was obtained from XRD Rietveld analysis. On the other hand, the concentration of calcium in the solution was measured by ion chromatography. Thus, the final calculation of the corresponding molar C/S ratio was done based upon the mass-balance for $Ca(OH)_2$.

- ***Reactions with mixtures of quartz and amorphous silica***

In **Figure 155**, it is shown the XRD spectra of the reactions obtained from a mixture of quartz and amorphous silica without dispersion (H1145), quartz (H1140) and dispersed amorphous silica (H1143) respectively. The black spectrum belongs to H1140 sample, the red one to H1145 sample and the blue spectrum to H1143 sample. A larger crystallization resulted when using a starting mixture of quartz and amorphous silica than when using either quartz or amorphous silica alone as seen in **Figure 156**.

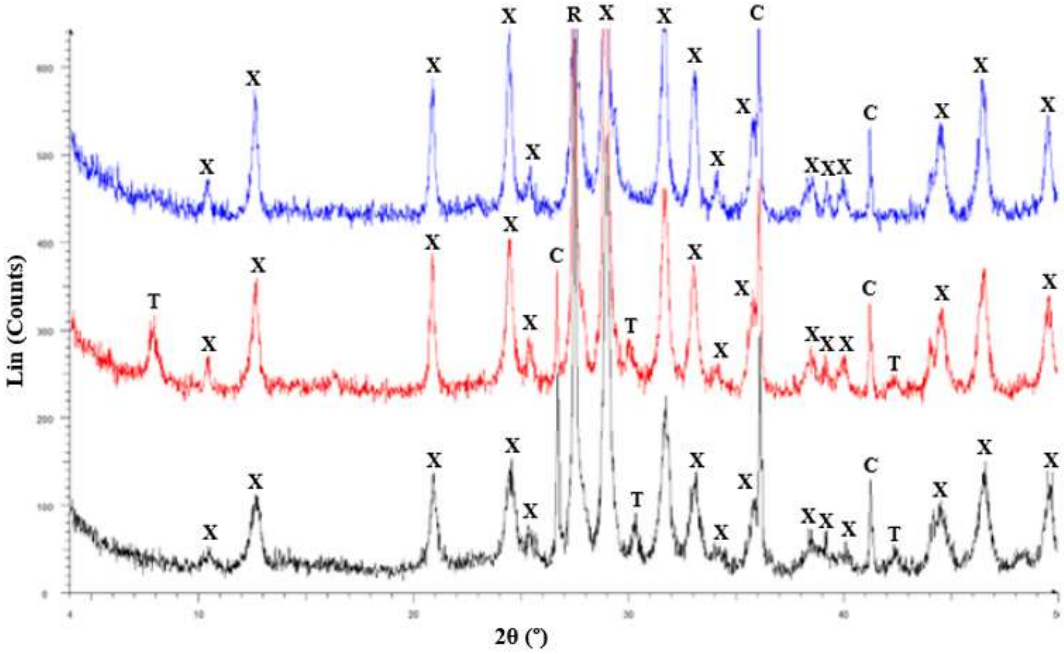

Figure 155. Reaction products for mixtures of quartz and amorphous silica compared with the those formed using amorphous silica and quartz (M400).

In the initial stages (at lower temperature range) of the reaction procedure between lime and the mixture of quartz and amorphous silica, the reaction occurs as C-S-H formation due to the presence of amorphous silica. Quartz hardly reacts in these lower temperature range. For that reason, all the available Ca^{2+} is available for the reacting amorphous silica and a Ca-rich CSH is formed (ratio $CaO/SiO_2 > 1$). These Ca-rich CSH-phases transform easily into xonotlite. In case of a reaction using 100% amorphous silica, the Ca/Si ratio for the C-S-H formation is around 1. **Table 31** gives an estimation of the Ca/Si ratio during C-S-H formation from amorphous silica. In later stages of the reaction, the quartz becomes reactive (at higher temperature and vapor pressure). At this moment, the Ca^{2+} concentration in solution is already low, due to the increase of temperature and the formation of Ca-rich C-S-H with the amorphous silica. This might explain the crystallization of tobermorite.

Starting composition of SiO_2 source	Approximate Calcium/reactive Silica ratio at the initial stages of the reaction when the amorphous silica is reacting: $Ca(OH)_2$ +amorphous $SiO_2 \rightarrow$ CSH	Facility to crystallize as xonotlite
100% amorphous SiO_2	1	Limited
50% amorphous SiO_2 50% quartz	>1 (1-2)	Better

Table 32. Estimated ratio of C/S in the initial part of the reaction when amorphous silica is reacting.

- ***Investigation in collaboration with ISTerre-University Grenoble Alpes***

A deeper investigation was carried out in collaboration with the geochemistry research group of ISTerre at the University Grenoble-Alpes (France) to explore the hydrothermal reactions from these two types of silica, quartz and microsilica. In order to understand better the structural evolution of those calcium silicate hydrates (C–S–H) as a function of its calcium to silicon (Ca/Si) ratio, Pair Distribution Function analysis of synchrotron-based high-energy X-ray scattering data of hydrothermal treated samples at different dwell time was performed.

In these trials the starting formulation was composed of very small additions of gypsum, calcium hydroxide instead of calcium oxide, and M400 quartz or dispersed Elkem MS 490 in acidic solution. The initial C/S ratio chosen to synthesize xonotlite was 0.98. Deionized water and argon were used to minimize the presence of impurities and keep an inert atmosphere. Besides, the stirred autoclave reactor used was different than the one used in Tisselt. In this case, a smaller electrical heater jacketed autoclave with paddle-based agitation mechanism was employed. Here, the set temperature for dwell time (200ºC) was reached faster than in the Tisselt's autoclave.

Powder (solid phase) of slurry samples probed at different reaction times were loaded into 1.5 mm diameter polyimide capillaries that were sealed on both sides using epoxy glue. High-energy X-ray scattering analyses were performed at beamline 11-ID-B of the Advanced Photon Source (APS, USA) using an energy of 58.62 keV and a Mar 2D image plate detector. For all images, a dark current subtraction and flatfield correction was applied. Samples were loaded onto a sample rack and exposed to the X-ray radiation for few seconds to obtain scattering patterns in a Q-range between 1 and 23 $Å^{-1}$. Pair Distribution Functions (PDFs) were obtained from the scattering patterns using the PDFGetX3 code **[136]**. The PDFs were analysed by linear combination fitting of different references, including a series of C-S-H samples with different C/S ratios from a previous experiment **[137]**, and the PDF of xonotlite, obtained at the end of the reaction.

Theoretical diffraction patterns of tobermorite and xonotlite were generated from published structures **[34, 72]**.

Firstly, high-energy X-ray scattering patterns and the obtained PDFs corresponding to the analyses for samples prepared from calcium hydroxide and microsilica (Elkem MS940) are shown in **Figure 156**. A qualitative comparison with theoretical diffraction patterns of tobermorite and xonotlite allows recognizing some features in the diffraction patterns, suggesting the very quick formation of a tobermorite-like solid, and ending with the formation of xonotlite. The scattering patterns of samples probed during the experiment presented broad peaks and the presence of diffuse scattering (background oscillating intensity) indicative of the presence of a poorly crystalline solid. The PDFs confirm this observation: the coherent domain size (spatial range up to which peaks in the PDF can be observed) is short at the initial times, with few peaks visible after 20 Å, and it increased with the experimental time. The comparison of the final scattering pattern with the theoretical pattern of xonotlite as well as the comparison between the final PDF and theoretical PDF patterns of xonotlite confirm the successful synthesis of xonotlite.

The theoretical diffraction patterns and PDFs of tobermorite and xonotlite are shown for comparison. The initial scattering pattern and PDF (0h as dwell time) are almost identical to those of a C-S-H sample with C/S = 1.04, also shown in the **Figure 156**. The last pattern and PDF are almost identical (except for the first neighbors in the PDF) to those of simulated for the xonotlite structure, confirming that the synthesis of xonotlite was successful.

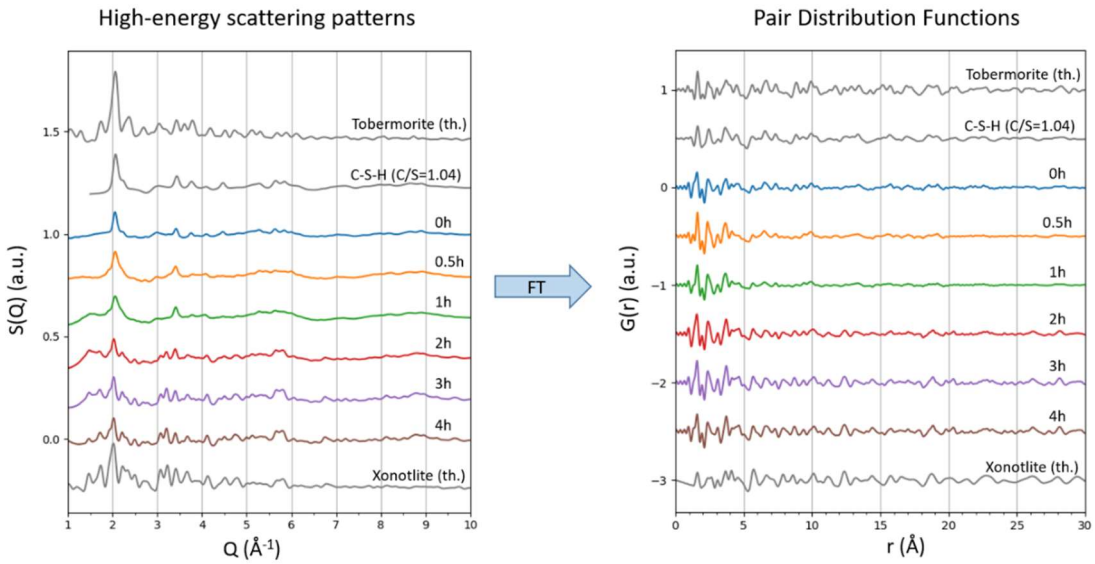

Figure 156. High-energy X-ray scattering patterns (left) and PDFs of samples obtained at different times throughout the hydrothermal reaction by microsilica-calcium hydroxide system.

A more detailed analysis of some features observed provides a better understanding of the xonotlite crystallization process in this case. The similarity of the initial scattering pattern and PDF with that of a C-S-H with C/S = 1/04 (**Figure 156**) led us to choose a lineal combination fitting approach as the method to obtain quantitative information from the data. Results of the fits are shown in **Figure 157**. All the intermediate PDFs were fitted as a linear combination of the PDF of C-S-H with a C/S ratio to 1.04 and the PDF of xonotlite. The fits were performed in two different regions: a first fit (left panel in **Figure 157**) was performed in the very short-range order region, from 0 to 10 Å, to identify the structural motifs of the growing phase. A second fit was performed in the medium-range order region, from 10 to 30 Å, to discern the ordering pattern of the above-mentioned structural motifs. The left panel (short-range order) shows that the short-range order of the initial precipitate (0h) can be explained by a combination of structural motifs of both C-S-H and xonotlite, a level of ~50% each. However, the right panel (medium-range order) of **Figure 157** is mostly that of C-S-H. Over time, the structure evolved and a clear evolution towards a pure xonotlite structure was observed after ~1.5h. The occurrence of a xonotlite-like C-S-H at the early stages is an interesting, unexpected observation – the first time to our knowledge that a different short-range order for C-S-H is reported- which reveals the effect of temperature on the local order.

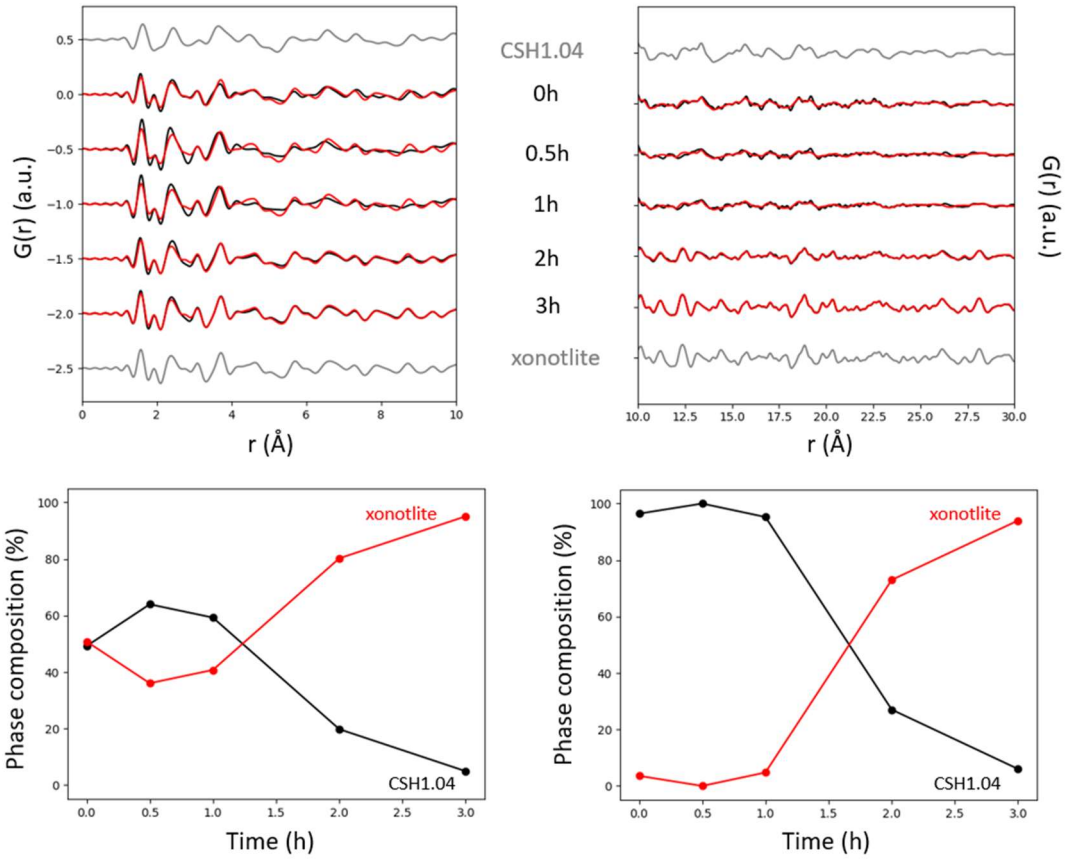

Figure 157. (Top) Pair Distribution Functions of samples obtained at different times throughout the hydrothermal reaction by microsilica-calcium hydroxide system. (Bottom) Linear combination fitting from PDF's data.

Secondly, high-energy X-ray scattering patterns and the obtained PDFs corresponding to the analyses for samples prepared from calcium hydroxide and quartz (M400) are shown in **Figure 158**. The scattering pattern at t = 0h shows that unreacted quartz and portlandite are present in the sample. A visual inspection of the scattering pattern allows also identifying an oscillating background, which amplifies over time (it starts to be clearly visible at t=0.5h), showing the presence of a disordered phase. The PDFs and the fits show that this disordered phase is a high Ca/Si C-S-H (C-S-H II), that is well fitted with the PDF of a Ca/Si = 1.47 C-S-H. Attempts to fit this disordered contribution with C-S-H of lower Ca/Si ratios yielded fits of lower quality. From time t = 0.5h and beyond, the quartz and portlandite reflections disappear, and the scattering patterns and PDF of xonotlite are clearly observed from t = 2h. It is shown in grey at the bottom of **Figure 158** the scattering pattern and PDF of the final xonotlite obtained in the experiment when used quartz as silica source for comparison, confirming that the synthesis results in single phase xonotlite.

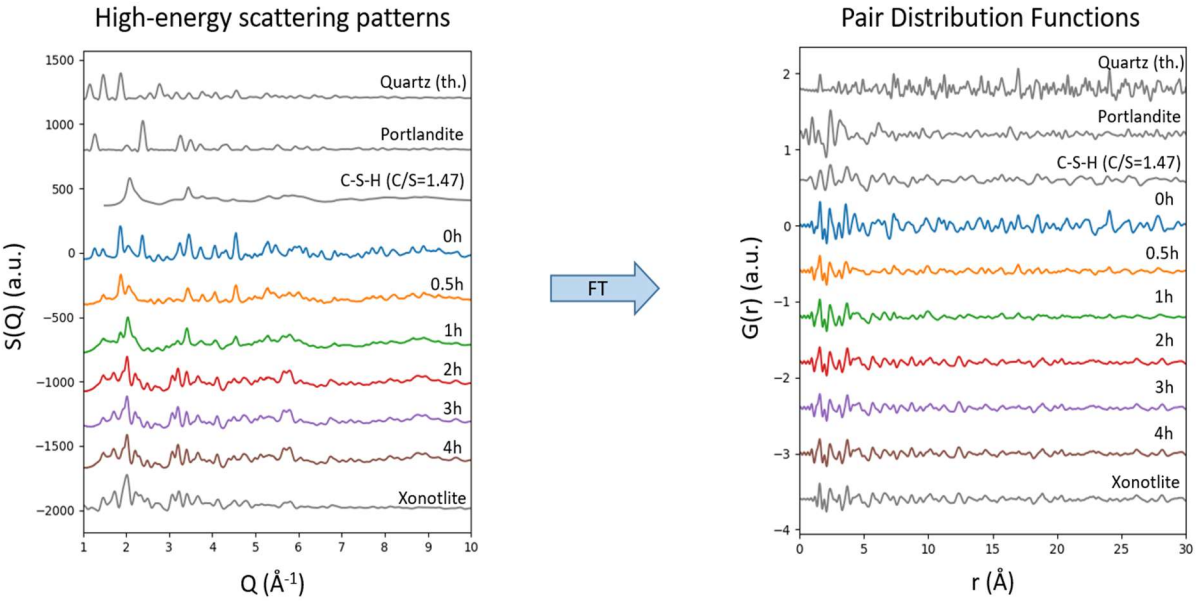

Figure 158. High-energy X-ray scattering patterns (left) and PDFs of samples obtained at different times throughout the experiment with quartz. The theoretical diffraction pattern and PDF of quartz, and the experimental ones of portlandite and xonotlite are shown for comparison (grey). The initial scattering pattern and PDF (0h) show a strong contribution of quartz and portlandite. The last pattern and PDF are almost identical (except for the first neighbors in the PDF) to those of xonotlite, confirming that the synthesis of xonotlite was successful.

A detailed analysis of the PDFs obtained allows following the phase distribution at each time point during the reaction. The results are shown in **Figure 159**. Four components are used: quartz, portlandite, C-S-H (C/S=1.47) and xonotlite. Quartz and portlandite are present at the early stages, but they react forming C-S-H and xonotlite. The C-S-H component is present from the beginning. It should be noted that the presence of a tobermorite component was considered, but it did not result in better fit of the data. Unlike the synthesis using amorphous silica, the presence of quartz and portlandite at the early stages prevents the detailed characterization of the short-range order of the obtained C-S-H. However, the presence of a xonotlite-like component from the t = 0h, even in the absence of clear diffraction peaks of xonotlite in the diffraction pattern, suggests that the disordered phase formed might share some structural characteristics with xonotlite, as shown in the case of the experiment with amorphous silica.

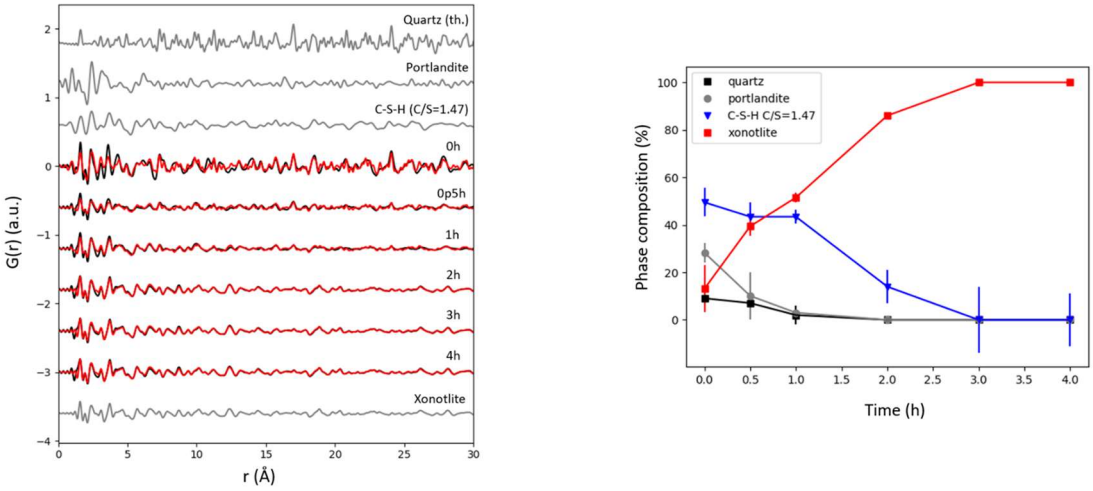

Figure 159. (Left) Linear combination fits of the PDFs using quartz, portlandite, C-S-H (C/S=1.47) and xonotlite standards. Red lines are the fit to the experimental data, in black. (Right) Resulting weight percentage of each phase.

4.2.3. Influence of xonotlite type particles on the properties of Promatect L500 product

The PROMATECT L500 product is composed mainly of the earlier described xonotlite-particles. They have excellent properties for use in passive fire protection and high temperature insulation. The most relevant characteristics for these applications are *a low thermal conductivity* due to the low density and the *well-engineered porosity* (large number of pores with dimensions below 1 micrometer) *and good thermal stability and mechanical stability* that is kept during/after heating. The good thermal stability is due to the fact that xonotlite converts at high temperature into wollastonite and this process hardly involves any dimensional change because of a high resemblance in crystal

structure. On laboratory scale 500 Kg/m^3 density boards were made with different xonotlite-particles and these were characterized and tested.

Polished sections analyzed by SEM for the PROMATECT-boards with xonotlite synthesized from M400 and Elkem MS 940 are shown in **Figure 161**. When using M400 (see **Figure 161A**), a structure is formed with xonotlite particles and some large pores between the particles. The pores are the darkest spots in the SEM images. When using amorphous silica, smaller and lighter xonotlite particles are formed that fill the complete space. Xonotlite particles are hardly distinguished in the SEM image of the amorphous silica because the particles are lighter and fill the complete space (see **Figure 161B**).

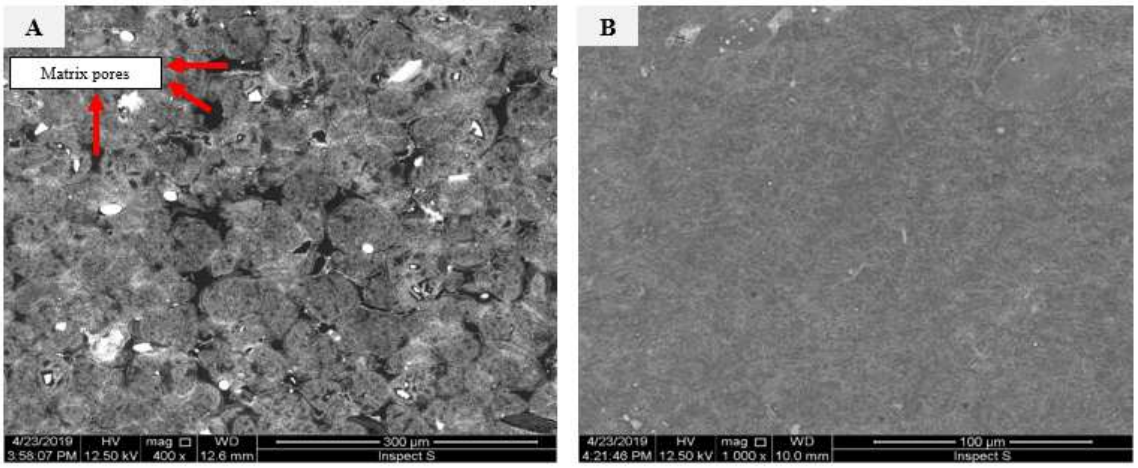

Figure 160. SEM micrographs of polished section of 2 calcium silicate boards matrix. (A) Matrix produced with xonotlite particles from M400 Quartz; (B) Matrix produced with xonotlite particles from Elkem MS 940.

SEM analysis of fracture surface of these samples are shown in **Figures 161** and **162**. The samples containing Xo prepared with M400 quartz and lime system have a structure consisting of spherical particles, most likely formed by coalescence of different reactive quartz particles with surrounding reaction rim, meeting one another and growing together (see **Figure 161**). The developed xonotlite crystals presented a lath- and occasional plate-like morphology typical for a crystallization via tobermorite as intermediate crystalline C-S-H phase.

Fracture surfaces of samples made with Xo by hydrothermal reaction between Elkem MS 940 and lime are shown in **Figure 162**. They did not show clearly individual xonotlite particles as such and the rims of the particles are presumably very thin or not existing so that crystallizing xonotlite needles interlock and form a more or less continuous network.

The crystals are more acicular and less lath- or plate-like compared to xonotlite formed from quartz-lime system and this might be due to other formation mechanism (nucleation and growth with less diffusion of Si and Ca ions in the reaction rims). Also,

when using mechanically dispersed microsilica, some agglomerated amorphous silica structures are present and the crystallization around them has a particular different structure resembling more typical C-S-H phases with low degree of crystallization (see **Figure 162**). This indicates the importance of the initial Ca/Si ratio for the forming C-S-H and the recrystallization into xonotlite.

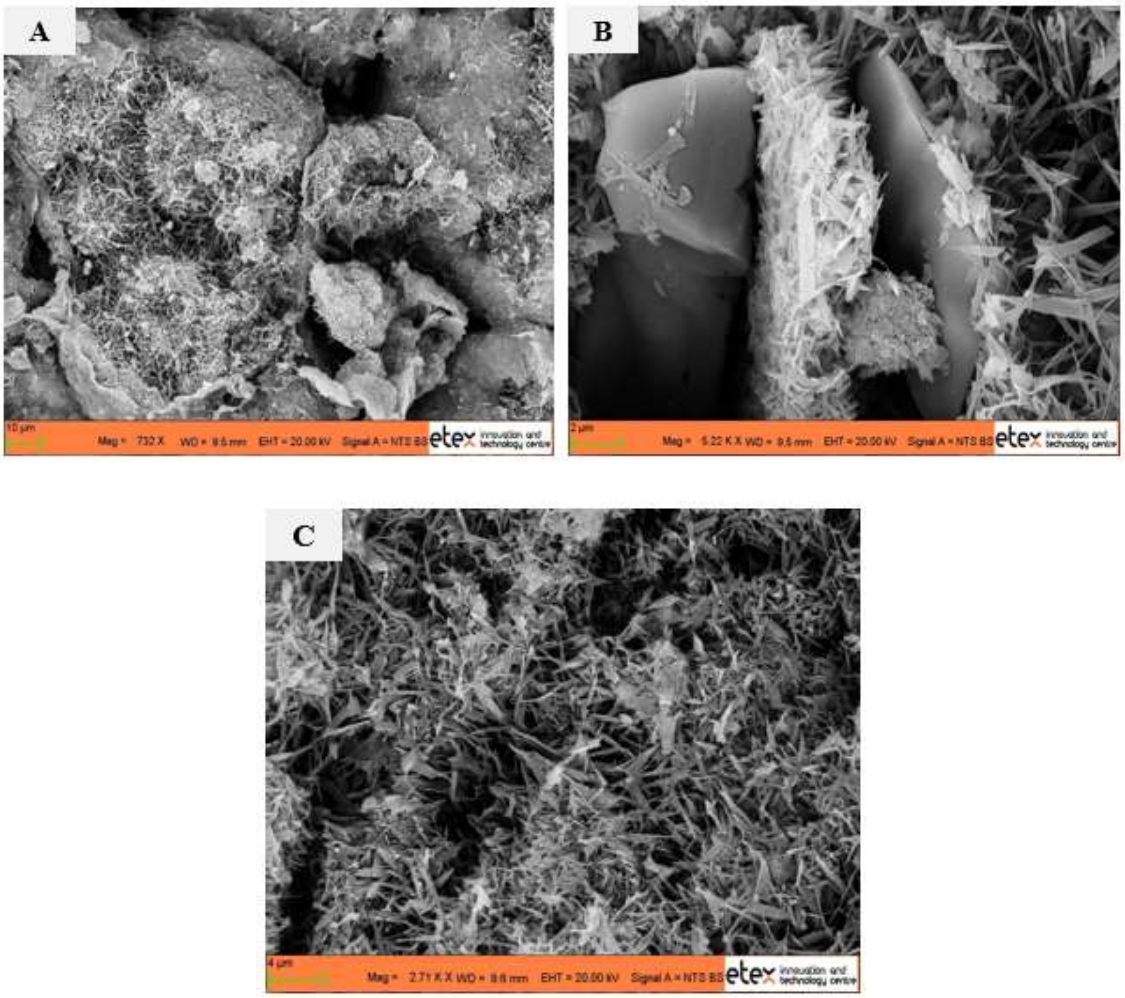

Figure 161. SEM micrographs of a calcium silicate board matrix composed of xonotlite particles formed through M400 Quartz and lime hydrothermal reaction. (A) Xonotlite particles formed by 'gluing' via C-S-H (I) phase of different reaction spheres around quartz grains; (B) Detail of crystallization around quartz; (C) Detail showing typical xonotlite short and thick needle-like crystals morphology.

Figure 163 also shows SEM images of the fracture surface that correspond to again samples containing xonotlite particles prepared by hydrothermal reaction between Elkem MS 940 and lime, where other details can be observed. For example, how the C-S-H and xonotlite needles are crystallized in different ways.

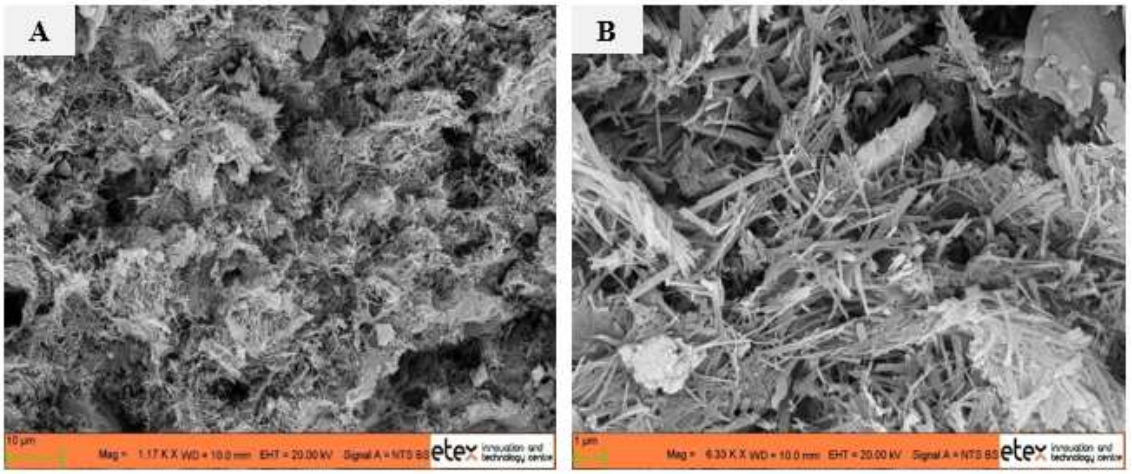

Figure 162. SEM micrographs of a calcium silicate board matrix consisting of xonotlite particles formed from Elkem MS 940 and lime hydrothermal reaction. (A) Typical xonotlite crystals morphology resulting from poorly crystalline C-S-H phase recrystallization with a C/S ratio ≈ 1 at hydrothermal conditions; (B) Detail of xonotlite long and thin needle-like crystals morphology.

One case, when these crystals grow on the surface of the amorphous silica aggregates acting as support. The other case, it is the C-S-H and xonotlite formation in the bulk solution. There is no crystal growing on the surface of microsilica aggregates, it occurs when calcium ions and silicate anions start nucleating in the solution and finally forming C-S-H phases which convert later into xonotlite.

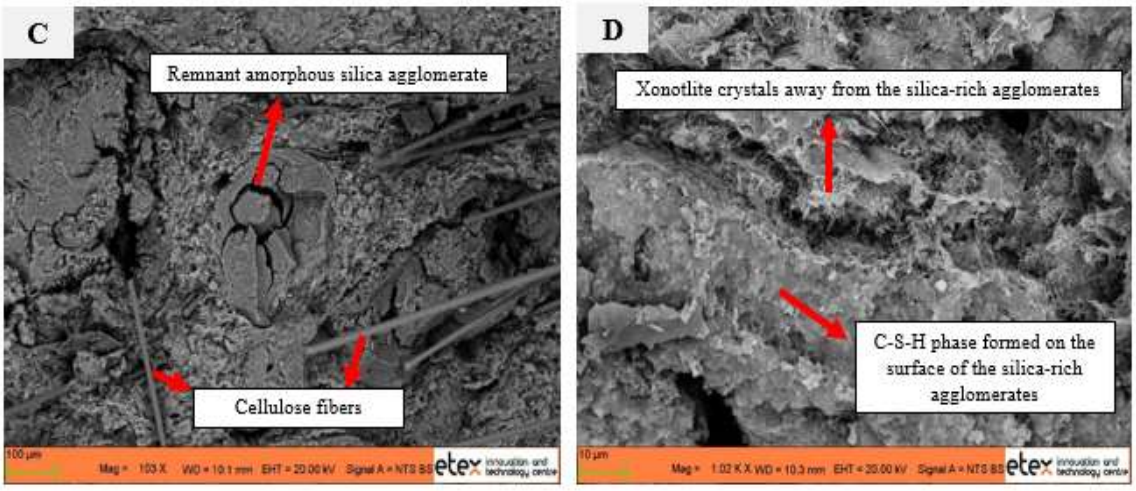

Figure 163. SEM micrographs of a calcium silicate board matrix containing cellulose fibers, xonotlite crystalline particles, C-S-H phases with C/S ≈ 1 and microsilica agglomerates. (C) Detail of microsilica unreacted agglomerates surrounded by poorly crystalline C-S-H phase and xonotlite crystallites; (D) Detail of C-S-H phase crystallization around the microsilica agglomerates as well as xonotlite needle-like crystals.

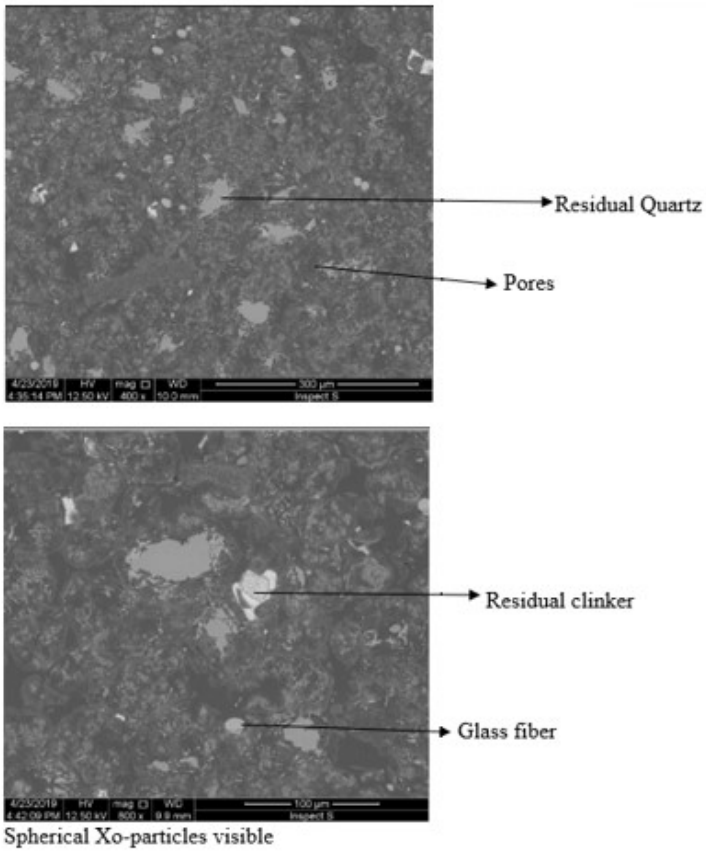

Figure 164. SEM-polished section of PROMATECT-boards using Xo made with M8-quartz.

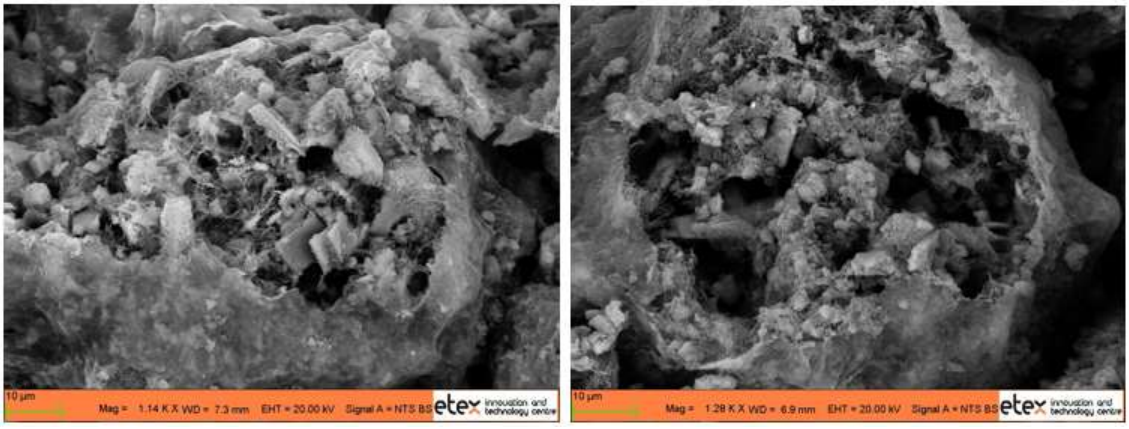

Figure 165. SEM images of a calcium silicate board containing xonotlite particles made with M8 quartz.

The porosity of the calcium silicate slabs was determined by Hg-porosimetry. It was requested in an external laboratory. The results are summarized in **Table 32**. The data confirm that there are significant differences in the pore size distribution for the tested samples as seen below in **Figure 166**. The sample prepared with synthetic xonotlite particles from Elkem MS 940 (H1143) as silica source, resulted to have the lowest pore volume and mostly fine pores (pores inside the xonotlite particles). Whilst the other sample consisting of spherical xonotlite particles formed from M400 sand (H1140) as crystalline silica source, presents fine pores inside the xonotlite particles (diameter smaller than 1 μm) and larger pores between them (1-10μm).

Sample ID	Larger Pores		Smaller Pores		Total pore volume (cm^3/g)
	Specific pore volume (cm^2/g)	Most frequent pore diameter (μm)	Specific pore volume (cm^2/g)	Most frequent pore diameter (μm)	
H1136	0,44	7,5	1,15	0,23	1,59
H1140	0,19	3,6	1,73	0,35	1,92
H1143	-	-	1,35	0,37	1,35

Table 33. Hg-Intrusion Porosimetry parameter data measurement for PROMATECT-boards made with Xo prepared with different silica sources.

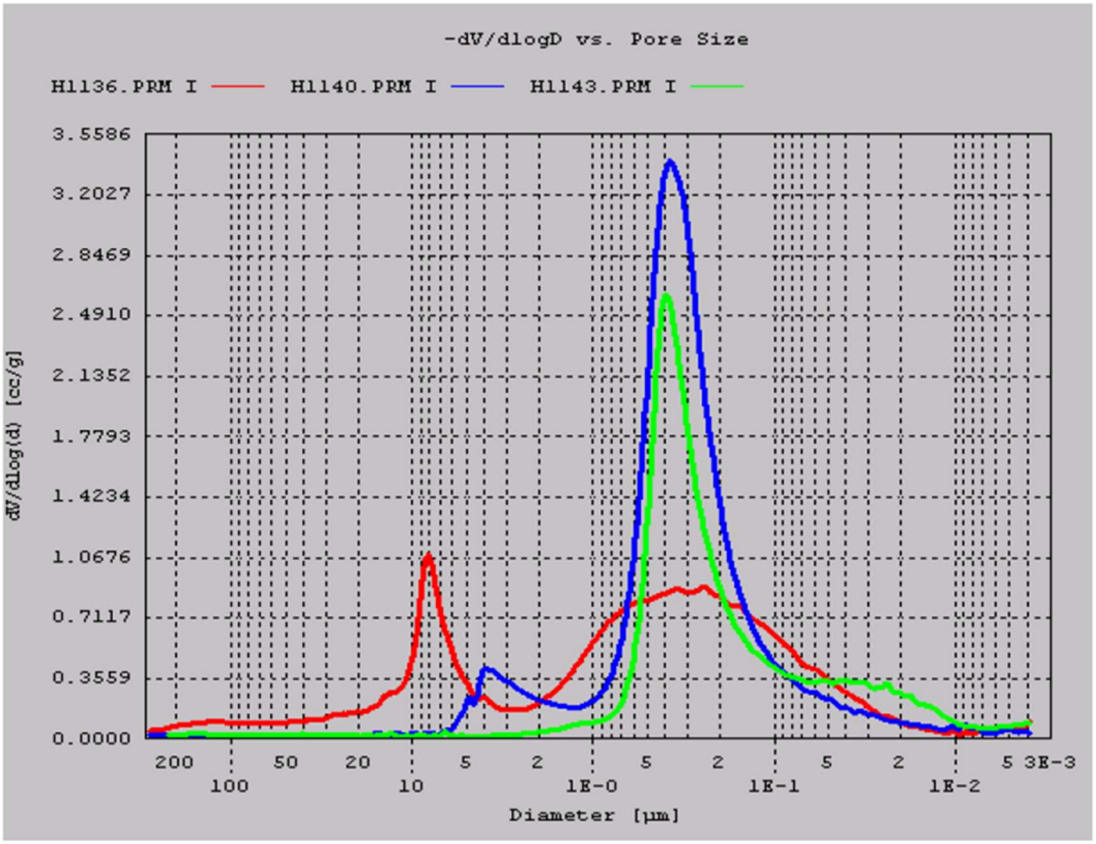

Figure 166. Pore size distribution of autoclaved xonotlite-based boards formulated from different xonotlite particles by Hg-Intrusion Porosimetry.

The boards that contain xonotlite particles formed from the reaction between $Ca(OH)_2$ and amorphous silica presented the best values in terms of mechanical properties. This is due to the fine interlocking structure and high content of binder, consisting of interlocking xonotlite needles. However, the boards made with xonotlite slurry produced from coarse quartz (M8) showed poor mechanical properties owing to the larger pore structure and low binder content. Whilst the boards made with xonotlite slurry synthesized from quartz fine (M400) had intermediate values of flexural strength. **Table 33** shows the mechanical strength (bending strength) and densities of these three types of boards.

Sample	Density (Kg/m^3)	Flexural strength (MPa)	Corrected flexural strength (MPa), ρ = 500 Kg/m^3
H1140 (M400)	413	2,4	2,9
H1143 (Elkem)	536	3,3	3,1
H1136 (M8)	491	1,2	1,2

Table 34. Data obtained from 3-Bending Point Test for PROMATECT boards made with Xonotlite prepared with different silica sources.

The results of thermal stability as measured by using Thermal Mechanical Analysis for the samples listed in **Table 33** are shown in **Figure 167.** From the graph, it can be seen that the highest thermal stability is given by the board made with well-dispersed amorphous silica (Elkem MS 940). Whereas that the lowest thermal stability is given by the board made with coarse quartz, (M8 quartz). The thermal stability is higher conforming there is more xonotlite present in the matrix. This is because xonotlite is the most stable phase in the $CaO\text{-}SiO_2\text{-}H_2O$ system, showing only a slight contraction corresponding with the wollastonite transition at 1100°C.

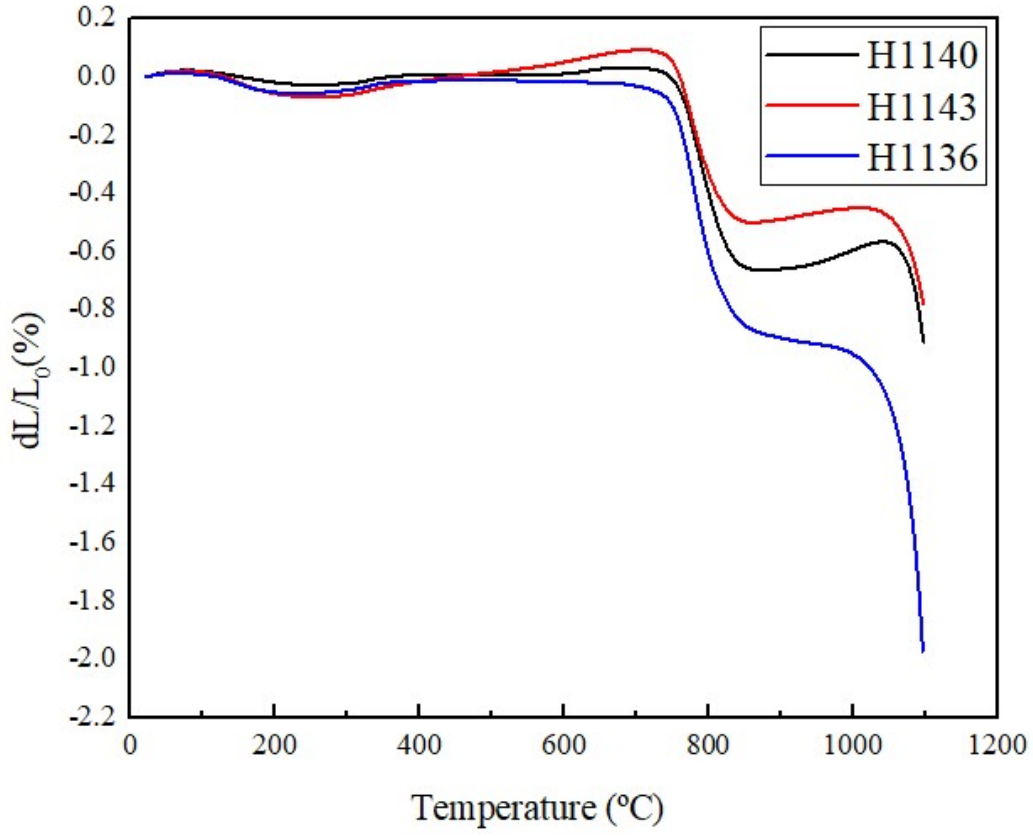

Figure 167. TMA curves of calcium silicate-based samples H1140, H1143 and H1134.

The thermal conductivity as a function of temperature was measured by using the 'Hot wire' method for PROMATECT L500 type large calcium silicate plates. In this case, the tested boards contain xonotlite particles synthesized from M400 quartz and Elkem MS 940, respectively. Therefore, **Figure 168** shows the data values recorded during the measurement of H1140 and H1143 plate-like specimens.

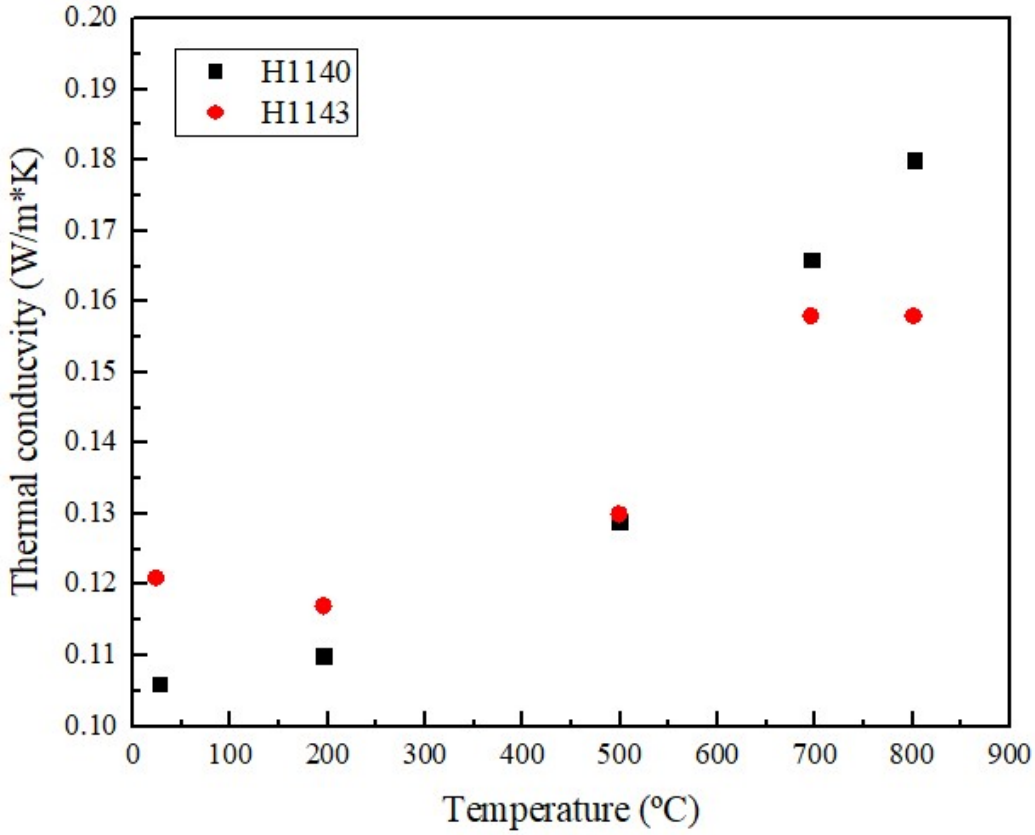

Figure 168. Thermal conductivity values by Hot wire technique for H1140 and H1143 specimens.

It is observed that the calcium silicate plate composed of xonotlite particles formed by the reaction between lime and Elkem MS940 slurry gave higher λ-values at low temperatures. The higher values for the thermal conductivity at low temperature are probably due to higher values for the λ_{solid} as a consequence of a higher degree of contact between xonotlite particles (particles are lighter and hence more compacted after filter-pressing). On the other hand, the calcium silicate plate containing xonotlite-based particles formed via microsilica as precursor, presented lower thermal conductivity values at high temperatures. The reason why the thermal conductivity decreased is due to smaller pore sizes which contributed to the reduction of radiation and thermal conduction in the gas phase. In literature is known that the thermal conductivity at high

temperatures is mostly dominated by radiation (**Figure 169)** and that small pore size result in lower contributions for λ_{gas} and $\lambda_{radiation}$ **[135]**.

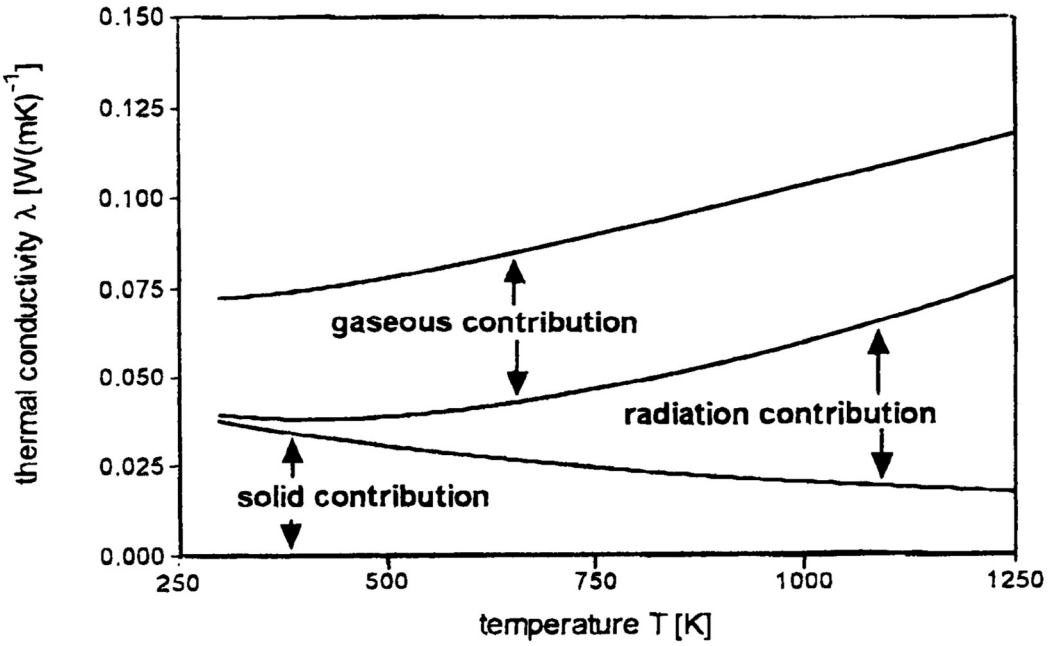

Figure 169. Typical example of contribution of different mechanisms of heat transfer on the total thermal conductivity vs. temperature **[135]**.

The main conclusions concerning the reaction pathways when different silica sources are used are summarized below:

- The formation of the main phases for calcium silicate-based products for use in passive fire protection and thermal insulation, being xonotlite and tobermorite, highly depends on the type and characteristics of the silica used for the synthesis.
- The particle size and nature of the silica used influences the solubility and rate of solubilization and hence influences the relative concentrations of Ca-and Si-ions in the solution in the beginning of the reaction. These determine whether the reaction goes via C-S-H or α-C_2SH as well as the composition of the C-S-H.
- Different C-S-H compositions have different structures (degree of polymerization) and recrystallize in different ways. Calcium-richer C-S-H phases have shorter silica-chains and have an easier recrystallisation than the silica-richer ones. The relative concentrations (for a given Ca^{2+}-concentration) depend on the silica solubility though also the solubilization rate and is hence dependent on the reactive surface of the silica (particle size of quartz, silica fume and degree of

aggregation (for silica fume). When using quartz, the initial C-S-H tends to have C/S around >1 while for amorphous silica the ratio of the initial C-S-H is around 1.

- When using crystalline silica, the dissolution of silica is the slowest step in the process as portlandite reacts faster than quartz. The reaction speed and ways as well as the properties of the end-product depend mainly on the particle size of the quartz used. In general, the reaction goes via calcium-rich initial phases due to the slow solubilization of quartz. For coarse quartz, the reaction proceeds via α-C_2SH that recrystallizes slowly and only partially into xonotlite, leading to products with poor mechanical and thermal properties. For fine quartz, the reaction goes via C-S-H. For a good reaction, there is an optimal particle size that enables a reaction via calcium-rich C-S-H phases that lead to a reasonable fast recrystallization into xonotlite, possibly via the intermediate formation of tobermorite. Too fine quartz results in an end-product that remaining tobermorite which is not optimal for the thermal stability. The reaction occurs on the quartz grains according to processes schematically represented in **Figure 145**, and quite a lot of diffusion is involved.

- When using amorphous silica, it is important to have a good dispersion of the silica particles to have a good reaction. For well dispersed silica, the reaction proceeds via fast formation of a C-S-H with C/S in nearly equivalent proportions and with a structure that seems such that it recrystallizes only slowly and at high temperature. While reactions with quartz involve an important contribution of diffusion, for silica-fume (well opened), there is a large reacting surface and hence, there is less diffusion and more crystal growth in solution than for reactions lime-quartz. This means longer xonotlite needles form by reaction of well dispersed silica fume with lime, and these include more pores and form xonotlite particles of lower apparent density. Then, this leads to different porosities and hence also thermal conductivity, thermal stability and mechanical properties. The use of amorphous silica allows to optimize the properties of low-density products. The reaction kinetics are not favoured using amorphous silica as they tend to form silica-richer C-S-H that recrystallize more difficultly in conditions where xonotlite is the stable phase. For good reactions, a special dispersion of the silica fume particles is required.
- The use of mixtures of amorphous and crystalline silica enables the optimization of the global content of crystalline phases and this is due to the formation of different C-S-H phases during the different stages of the reaction.

4.2.4. Enhancement approach for Promatect LS and Promatect L-500 thermal properties: use of new endotherms and opacifiers

One of the most important properties of materials applied on fire protection and high temperature insulation is a good resistance against the heat transfer. The main parameters influencing these features are the *thermal conductivity* and *specific heat*. As mentioned before, Promat Research and Technology Centre developed in the past an improved version for the standard product named PROMATECT L500 by integrating ettringite as an endothermic additive in the matrix. Ettringite, $Ca_6Al_2(SO_4)_3(OH)_{12}\cdot 26\text{-}32H_2O$, is a well-known endothermic inorganic compound owing to its high amount of chemical bound water in its structure (26-32 molecules of H_2O). Nevertheless, ettringite has the disadvantage that it has a low decomposition temperature and hence is difficult to dry in the production process of PROMATECT LS product. Ettringite begins to decompose around 80ºC, depending on the humidity. As PROMATECT LS-based board is dried industrially at ca. 140°C (air temperature which corresponds with a board temperature of ca. 80ºC), partial decomposition of ettringite occurs which in turn decreases the effectiveness of the board.

Within this section, alternatives to ettringite were looked for. In order to do so, an understanding is required of the desired properties for the endotherm additives in a number of different applications in passive fire protection.

Several factors influence the performance of the endotherm additive. These are:

- the decomposition temperature, T_{dec} (ºC)
- the enthalpy of endothermic reactions, ΔH (J/g).
- the solubility: PROMATECT-L500/LS are made in wet conditions, so the additives should be non-soluble otherwise they are lost in the process water
- they should be stable in alkaline environment as PROMATECT-products are alkaline
- they should have a limited impact on the HT-stability : the endotherm makes up a reasonable part of the fire protection boards, it is important that mechanical stability is maintained at high temperature , that the board has no cracking or deformation that would allow flames or radiation to pass in which case the board would fail by the integrity criterium.
- Particle size: must be high enough to avoid losses in the filter-pressing process or reducing the speed.
- the cost-price must such that they provide a viable solution. Promat International produces its own ettringite and it costs to the company about 0,15 euro per kilogram of ettringite manufactured.

A list of candidates as endothermic additives was derived from literature. They were chosen based on the decomposition temperature, (T_{dec}) and reaction enthalpy (ΔH). The first step was to characterize these inorganic compounds by Differential Scanning Calorimetry in order to determine the endothermic peaks, the decomposition temperature(s) as well as the enthalpy of the endothermic reaction.

Secondly, a set of new PROMATECT LS boards containing these additives were prepared and tested by ISO Fire Rate Assay for determination of the Rf values. **Tables 34**, **35** and **36** collect all the data related to the DSC and ISO Fire Rate Test measurements for endothermic compounds and the Rf-values for the PROMATECT LS boards.

Endothermic compound	**1st Endothermic Peak (DSC diagrams)**			
	T_0 (ºC)	**T_f (ºC)**	**T_{dec} (ºC)**	**ΔH (J/g)**
Ettringite	55.32	223.62	138.67	672.79
Gypsum	67.69	256.71	151.40	477.51
Hydrotalcite (hydrophobic grade)	121.93	292.82	264.20	344.77
Aluminum hydroxide SH-300	212.48	399.04	318.59	769.70
Aluminum hydroxide SH-150	216.54	401.32	314.42	765.48
Zeolite-Y	55.07	338.03	148.11	507.90
Magnesium hydroxide	289.48	455.98	403.60	1055.49
Calcite	503.42	914.11	869.20	1809.27
Silica gel orange	54.93	201.62	116.20	222.80
Silica gel 60Å	55.65	162.71	92.60	65.10

Table 35. Differential Scanning Calorimetry data corresponding to the first endothermic peak of chemical compounds listed.

Endothermic compound	**2nd Endothermic Peak (DSC diagrams)**			
	T_0 (ºC)	**T_f (ºC)**	**T_{dec} (ºC)**	**ΔH (J/g)**
Ettringite	----------	----------	----------	----------
Gypsum	----------	----------	----------	----------
Hydrotalcite (hydrophobic grade)	295.76	521.84	418.89	500.93
Aluminum hydroxide SH-300	446.38	577.88	532.20	77.93
Aluminum hydroxide SH-150	436.85	580.15	528.88	75.25
Zeolite-Y	868.61	1058.87	1006.71	-145
Magnesium hydroxide	----------	----------	----------	----------
Calcite	----------	----------	----------	----------
Silica gel orange	----------	----------	----------	----------
Silica gel 60Å	364.66	413.24	393	-6

Table 36. Differential Scanning Calorimetry data corresponding to the second endothermic peak of chemical compounds listed.

- ***Partitioning protection by ISO conditions***

PROMATECT boards with different endotherm additions were tested in partition conditions submitted to an ISO-curve (cellulosic fire). The fire resistance or fire rate in ISO-partition conditions is defined as the time that it takes the cold side of a calcium silicate board to reach 160°C, whilst the other side, the so-called hot side is exposed to an ISO-type of heating source.

The results are given in **Table 36.** Ettringite and gypsum are the best endotherms to optimize the Rf in ISO-partition conditions. The compounds with higher decomposition temperature range values such as calcite, magnesium hydroxide and aluminum hydroxide have higher enthalpy values, though they will only work in a section of the thickness and therefore do not result in high Rf-values. Other additives like silica gel have lower decomposition temperatures, though they have lower enthalpy values.

Endothermic compound	Rf (min)
Ettringite	40
Gypsum	42
Hydrotalcite (hydrophobic grade)	30
Aluminum hydroxide SH-300	28
Aluminum hydroxide SH-150	27.5
Zeolite-Y	27
Magnesium hydroxide	27
Calcite	26
Silica gel orange	26.7
Silica gel 60Å	24.4

Table 37. Fire rate tests data of the PROMATECT LS boards containing at the starting formulation different endothermic compounds

The decomposition temperature determines the temperature-time when an endotherm will be effectively contributing to the storage of heat. During a fire exposure in partition conditions, the material is submitted to a fire on one side, meaning that across the thickness, there is a temperature gradient, and each section is submitted to a given temperature range that varies over time. Once the decomposition temperature is reached in a section of the fire protection board, the endotherm becomes active. This means that it will start to uptake energy from its surroundings. Doing so, it will slow down the heat that is flowing from the hot side (where the fire is) to the cold side of the board.

For endothermic chemical agents with decomposition temperatures above 160°C, there will be sections in which the endotherm will not be active as the temperature is at any time lower than its decomposition temperature. The number of non-active sections (endotherm not active) will be higher conforming the decompositions occur at higher

temperatures. So, for ISO-partition conditions, it is preferred to have a decomposition temperature around 160°C, as in this case the endotherm will be active in all sections.

This is schematically shown in **Figure 170** where an example of a temperature gradient simulation throughout the cross-section of a board is shown at a late stage in the process where the temperature at the hot side in 1050°C (90' in ISO-fire) and 160°C is reached at the cold side. Endotherms like gypsum or ettringite would work in the whole section of a calcium silicate board (zone 1, 2 and 3) whereas that additives like $CaCO_3$ would work only in zone 1 and $Al(OH)_3$ would work in zone 1 and 2 as their decomposition temperature is higher.

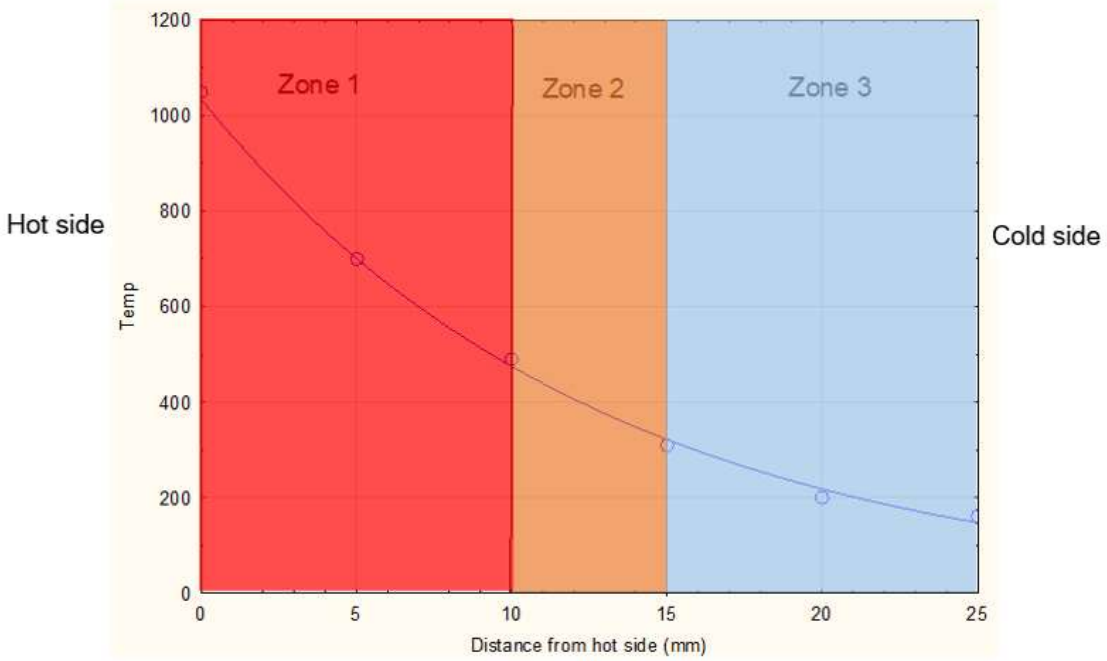

Figure 170. Temperature profile in a calcium silicate board section at the end of an ISO-fire test.

Nevertheless, in the ideal case, the decomposition temperature is higher than for ettringite as this makes the industrial drying difficult. On the other hand, the enthalpy of endothermal reaction (ΔH) means the required energy for decomposition which is a quantity of how much energy the endotherm can extract from the system and the higher this value, the more energy from the heat flow related to the fire is stored in the system.

When plotting the Fire rate (Rf) values of PROMATECT LS boards with additions of endothermic compounds (see **Table 34**) over the 2 mentioned key parameters, T_{dec} and ΔH, and making some simplifying assumptions, a 3D graph shown in **Figure 171** was drawn using a statistical software.

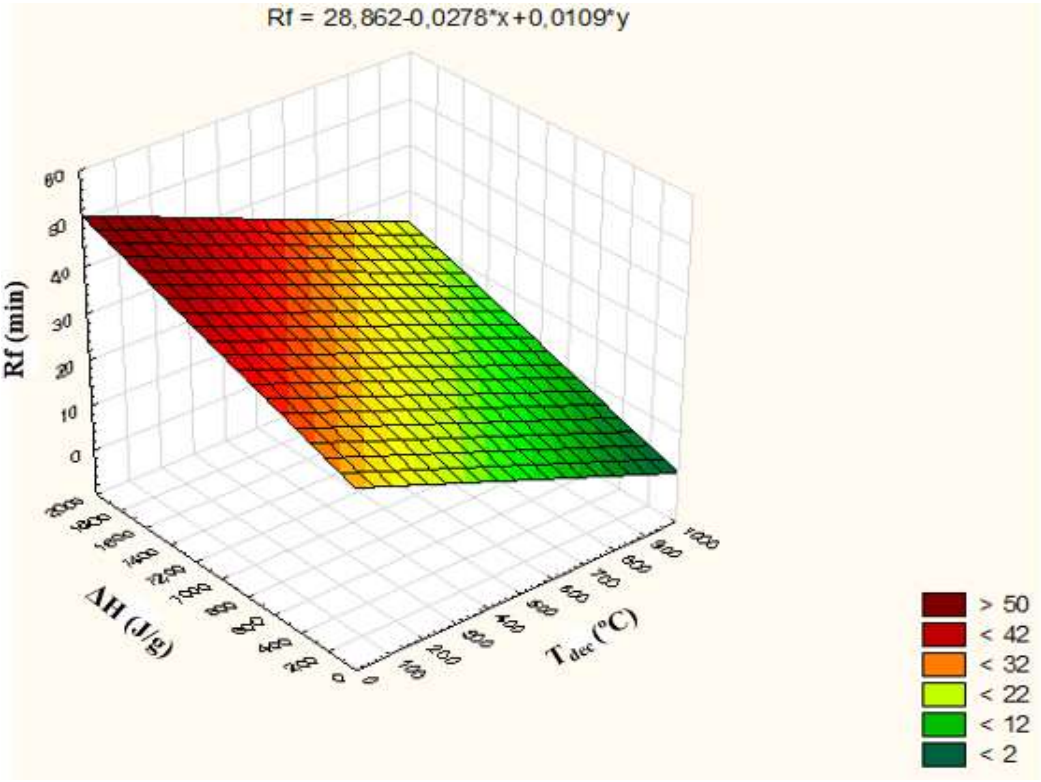

Figure 171. 3D Surface Diagram plotting the fire rate values (axes Y) over temperature decomposition (axes X), considering the first endothermic peak in DSC curves as the main peak, and enthalpy of endothermic reaction (axes Z) for all the endothermic compounds used at PROMATECT-LS formulation.

In order to know the influence of the temperature decomposition as well as the enthalpy of endothermic reactions on the fire rate values, a multiple regression was done. Therefore, the relative importance of these 2 factors was derived from this type of calculation. **Table 37** gives the main parameters obtained by means of a multiple regression. From the multiple regression analysis, it appears that both parameters T_{dec} and ΔH are almost equally important. There is still a considerable amount of unexplained variability. Various factors can explain this such as the simplification (it was considered only the most important decomposition temperature, that is the first endothermic peak for the endotherms showed 2 peaks) applied, the statistical errors for each measurement, the influence of the thermal conductivity and the influence of the gases formed during the decomposition on the thermal conductivity and other possible contributing factors.

Dependent variable	Rf
Multiple R	6.19
F value	2.18
R^2 value	3.83
Df value	2.70
Nr. Of cases	10
Adjusted R^2	2.07
p value	0.18
Std Error of estimation	5.39
Intercept value	30.17
Std Error	2.98
t(7) value	10.12
T_{dec}(REDCO) b*	-1.70
ΔH(REDCO) b*	1.53

Table 38. Multiple Regression results of 3D Surface Diagram for Rf vs. T_{dec} and ΔH.

An alternative way to look at the mentioned variables is illustrated by **Figure 172**. It is plotted a graph where considering the Fire rate values over the decomposition temperature uniquely. The spread around the regression line is related to the enthalpy, though also other factors such as the impact of the endotherm on the thermal conductivity.

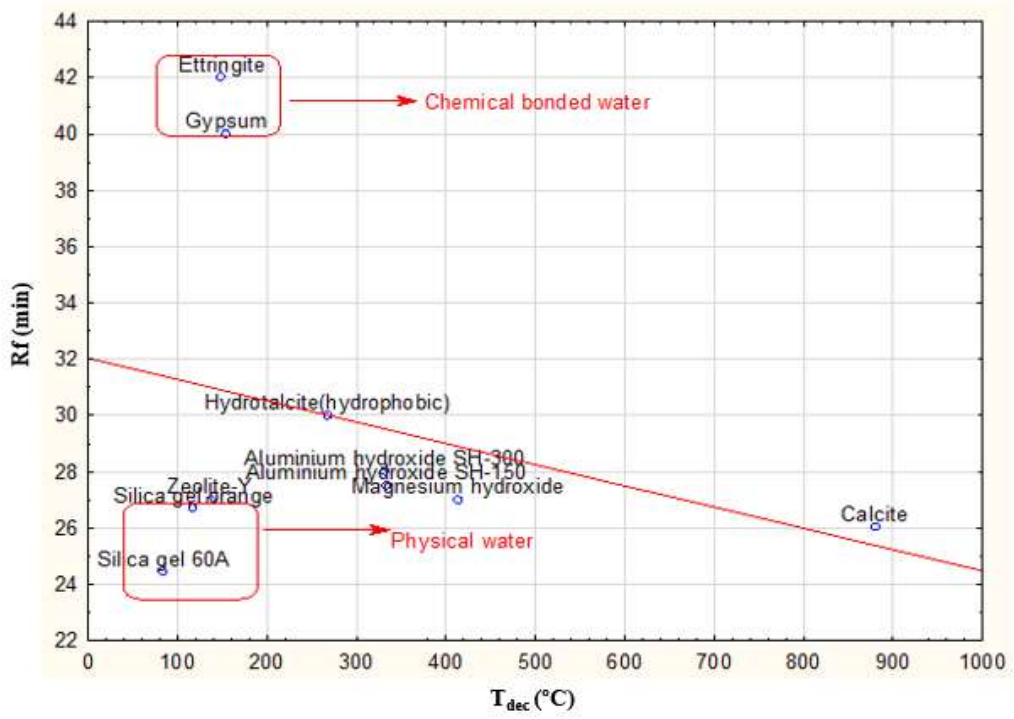

Figure 172. Diagram representing Fire rate values over Decomposition temperature to the endothermic agents listed in **Tables 34**, **35** and **36**.

- ***Steel-protection***

Fire protection of steel involves heat transfer in higher temperature zones to ensure that the temperatures reached on steel-based structures do not exceed 500-550°C. In this higher temperature range, the thermal conductivity is the most influencing parameter, whereas that the influence of the Cp and endotherms is less important. For that reason, it makes sense to use calcium silicate boards containing additions of opacifiers instead of any endothermic compound proposed above for these applications. These opacifiers scatter the heat radiation and hence reduce the contribution of this radiation in the transfer of heat. **Figure 173** compares the effects of 20% endothermic compound addition with the effect of 10% rutile as opacifier (replacing xonotlite content or Portland Ordinary Cement, OPC) in the total composition of PROMATECT-L500 and PROMATECT-LS boards. Rutile (in an optimal particle size of around 4-5 micron) is one of the most effective opacifiers and it is already used for some existing Promat products for high temperature insulation. When using 10% of rutile, an improvement over the reference product of at least 19% was reached for the time to attain 500°C and for higher temperatures, the benefit is even higher.

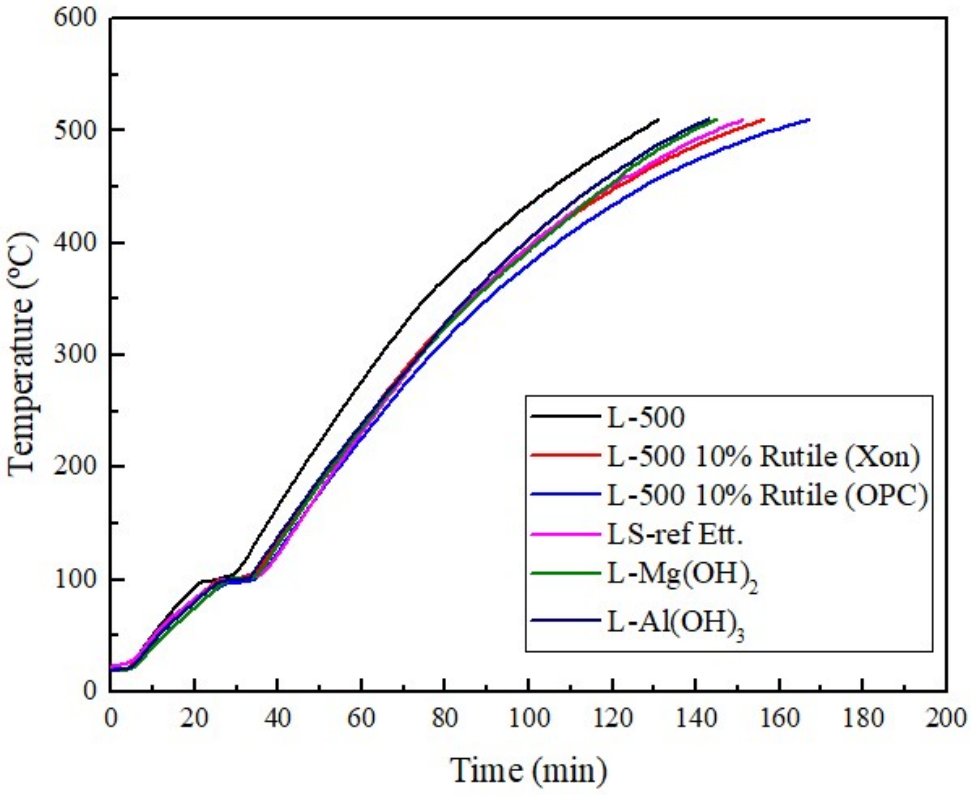

Figure 173. ISO Fire Rate curves of PROMATECT-L500 boards applied for steel protection conditions.

Concerning the endotherms, their effect is less (ca. 10%) and ettringite marginally remains better than $Mg(OH)_2$ and $Al(OH)_3$ which is also due to the effects of the endotherms on the thermal conductivity (Figure164). The difference between the different endotherms is clearly lower than for partition conditions which is logic as the 3 endotherms work now in most of the sections as they all reach at least 500°C, meaning that for steel protection, $Mg(OH)_2$ and $Al(OH)_3$ can be used.

As it was mentioned before, thermal conductivity (λ) plays a relevant role in case of steel structure passive fire protection applications since the unexposed side of the calcium silicate board use to reach ~500ºC. Therefore, the thermal conductivity was measured vs. temperature for the reference sample (PROMATECT L500) and samples containing endotherms in their matrix such as ettringite, magnesium hydroxide and aluminum hydroxide. **Figure 174** shows that the different endotherms lower the thermal conductivity, and this is especially the case for ettringite. The lower lambda values are possibly related to the porosity induced by the endotherm materials. It contributes to the better Rf-values.

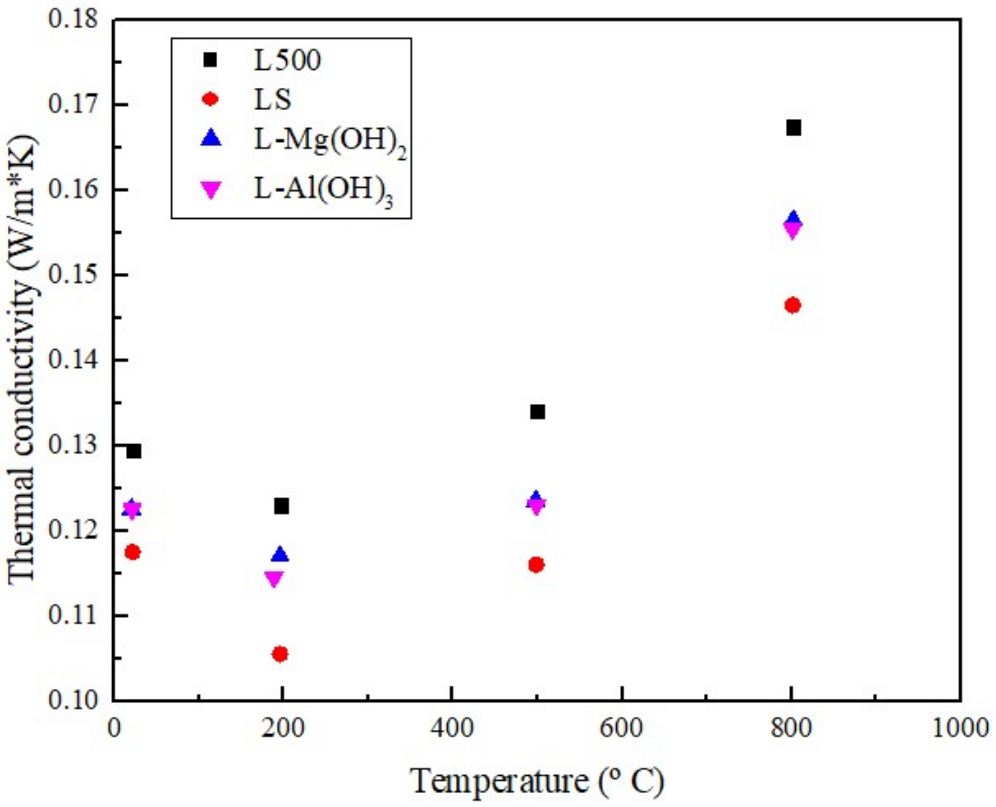

Figure 174. Thermal conductivity values at different temperatures for sample reference (L-500) and samples with endotherm additions.

- ***Concrete protection by Hydrocarbon conditions***

Other passive fire protection application where calcium silicates are employed is the protection of concrete structures for Hydrocarbon types of fire. **Figure 175** shows the Hydrocarbon Fire rate curves corresponding to the sample reference, (LS board with ettringite), and other two samples containing $Mg(OH)_2$ and $Al(OH)_3$ as endotherms. Here, it was determined the fire rate for calcium silicate boards in concrete protection conditions. In these conditions, a temperature range of 200-300°C, is considered (in order to avoid the spalling of concrete and in order to protect the embedded steel reinforcement). These Rf-curves show that all the endotherms performed reasonably well. This is related to the more severe heating curve (hydrocarbon compared to cellulosic fire) and the higher temperature of the application (200-300°C). More tests would be needed to establish the spread of the results before concluding on the best additive for this application.

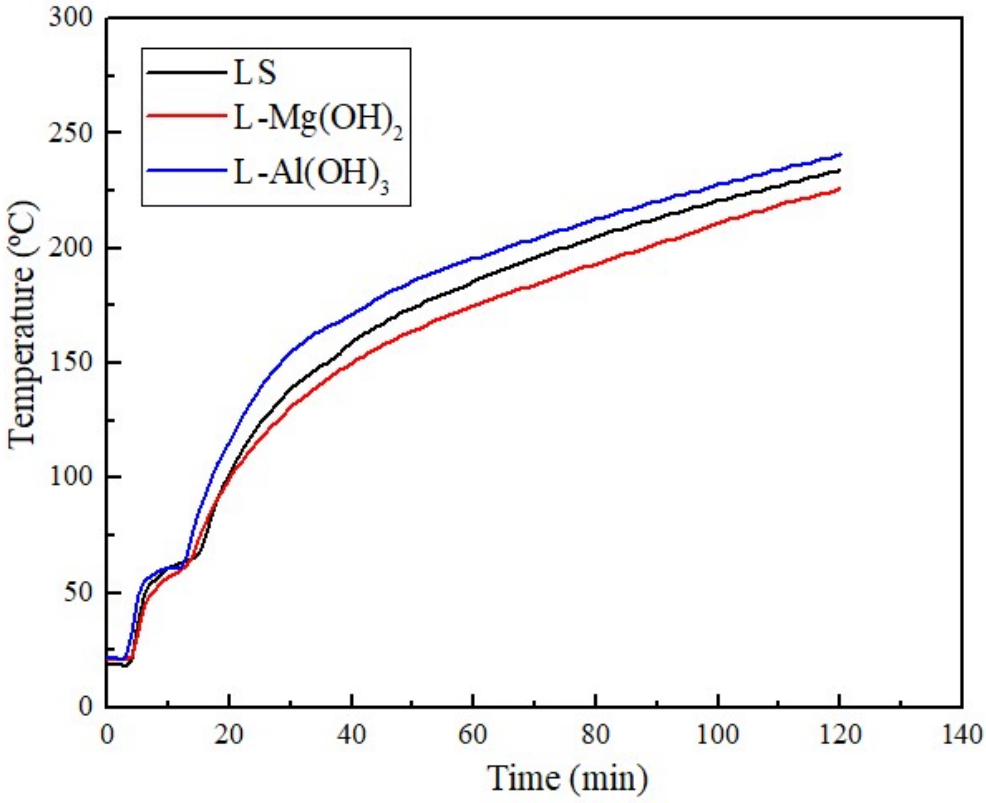

Figure 175. Hydrocarbon Fire Rate curves for PROMATECT- LS boards applied for concrete protection conditions.

Reviewing the results of section **4.2.4**, it can be summarized the following:

- The endotherms have to be chosen as a function of their application. They have decomposition temperatures below or near to the temperature to protect, being 160°C for ISO-partition, below 500C for steel, 300°C for concrete in hydrocarbon fire.
- For ISO-partition, no better alternatives than ettringite could be found as most of the possible additives have too high decomposition temperatures. Gypsum seems the best choice after ettringite, though is more soluble meaning that there will be loss of material and contamination of the water-circuit. The decomposition temperatures for gypsum are in the same range as for ettringite and drying is expected to be difficult.
- The use of rutile as opacifier in PROMATECT-L-500 board replacing a low percentage of Ordinary Portland Cement is a promising solution to achieve better Rf values for steel protection applications. Ettringite might be an alternative as endothermic additive for steel-protection applications because of its low thermal conductivity.
- For concrete protection in hydrocarbon fires, Magnesium hydroxide is a potential candidate to be an endothermic additive, though also other endotherms and opacifiers could be considered and are recommended for further study.

4.2.5. Conditions to obtain different product densities

Stirred autoclave reactor/filter pressing technology is a hydrothermal-based processing methodology to make industrially medium-density calcium silicate boards for high temperature insulation and passive fire protection in compartmentation, concrete, steel protection structures, etc. Within Etex, the technology is mainly used for medium density products in the range 400-550 Kg/m^3. For lower densities (240-300 Kg/m^3), the cheaper casting technology is used or the previously gel tank technology would be a good option. Lower densities can also be made using this technology although they are not economical in Europe. For very low densities, the use of amorphous silica would be required as it forms lighter Xonotlite particles, though this would further increase the cost.

Higher densities than 600 Kg/m^3 can be made by means of stirred reactor/filter pressing technology. But this would only make sense when there are specific demands for higher mechanical properties.

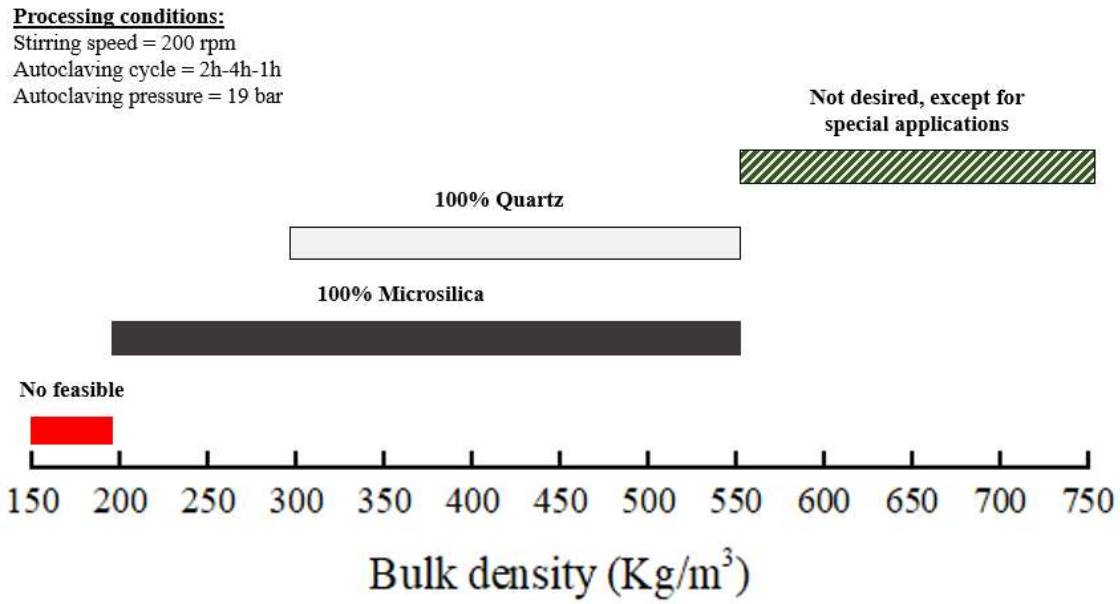

Figure 176. Scheme of bulk densities range covered by the type of silica as precursor for the mentioned processing conditions in Stirred Autoclave Reactor technology.

4.3. Double autoclaving technology

4.3.1. Basics

Promat has in its calcium silicate product portfolio a kind of calcium silicate boards called PROMARINE-450T or PROMATECT-MLT. These boards are autoclaved calcium silicates with excellent fire performance, ideal for application in fire dampers and for application in the marine market as compartmentation materials and non-combustible furniture. This product is manufactured by means of double autoclaving technology. The density range that can be covered using this type of hydrothermal-based process is 400-1200 Kg/m^3. Double autoclaving technology is a combination of the following processing steps:

- Formation of a green board by means of filter-pressing that contains primary xonotlite /tobermorite particles as lightening agents (formed in stirred reactors), Ordinary Portland Cement (OPC) as binder, cellulose fibers as reinforcement agents, wollastonite as mineral filler and quartz as silica source to react with hydrated OPC-cement formed during the curing step.
- Curing step: hardening of the board at low temperature (20ºC/24hours) by the following reactions:

  Alite + water → C-S-H phase + calcium hydroxide (portlandite):

$2(3CaO{\cdot}SiO_2) + 6H_2O \rightarrow 3CaO{\cdot}2SiO_2{\cdot}3H_2O + 3Ca(OH)_2$

Belite + water → C-S-H phase + calcium hydroxide (portlandite):

$2(2CaO{\cdot}SiO_2) + 4H_2O \rightarrow 3CaO{\cdot}2SiO_2{\cdot}3H_2O + Ca(OH)_2$

The target of the curing step is to form a product with a certain green strength, high enough to withstand the subsequent processing.

- Autoclaving step: converting C-S-H phases formed (binder) into tobermorite and additional tobermorite formation by reaction of $Ca(OH)_2$-SiO_2 in hydrothermal conditions (P_{vapour} = 12bar / T ≈ 180-190ºC):

$6\ SiO_2 + 5\ Ca(OH)_2 \longrightarrow 5CaO{\cdot}6SiO_2{\cdot}5H_2O$
Quartz + portlandite 11.3Å tobermorite

$13\ SiO_2 + 5\ (3CaO{\cdot}SiO_2{\cdot}H_2O) \longrightarrow 5CaO{\cdot}6SiO_2{\cdot}5H_2O$
Quartz + tri-C-S-H 11.3Å tobermorite

The microstructure obtained by SEM examination of such a calcium silicate-based board is shown in **Figure 177**. The first two SEM micrographs show a general view of the matrix formed after filter-pressing the mixture of components and the last two SEM images show the matrix after curing and hydrothermal treatment of the board. The sphere-like particles are xonotlite particles formed previously in the vertical stirred reactor that are used as lightening agents at the starting formulation (see **Figure 177A**). Besides, both cellulose and wollastonite fibers are visible in the fracture surface of the board (**Figure 177B**). The other SEM images (**Figure 177C** and **177D**) show the presence of C-S-H/tobermorite phases that are binding the different ingredients (spherical xonotlite particles, cellulose fibers, wollastonite crystals) together. In this way, a matrix with very good mechanical properties and good thermal stability is developed.

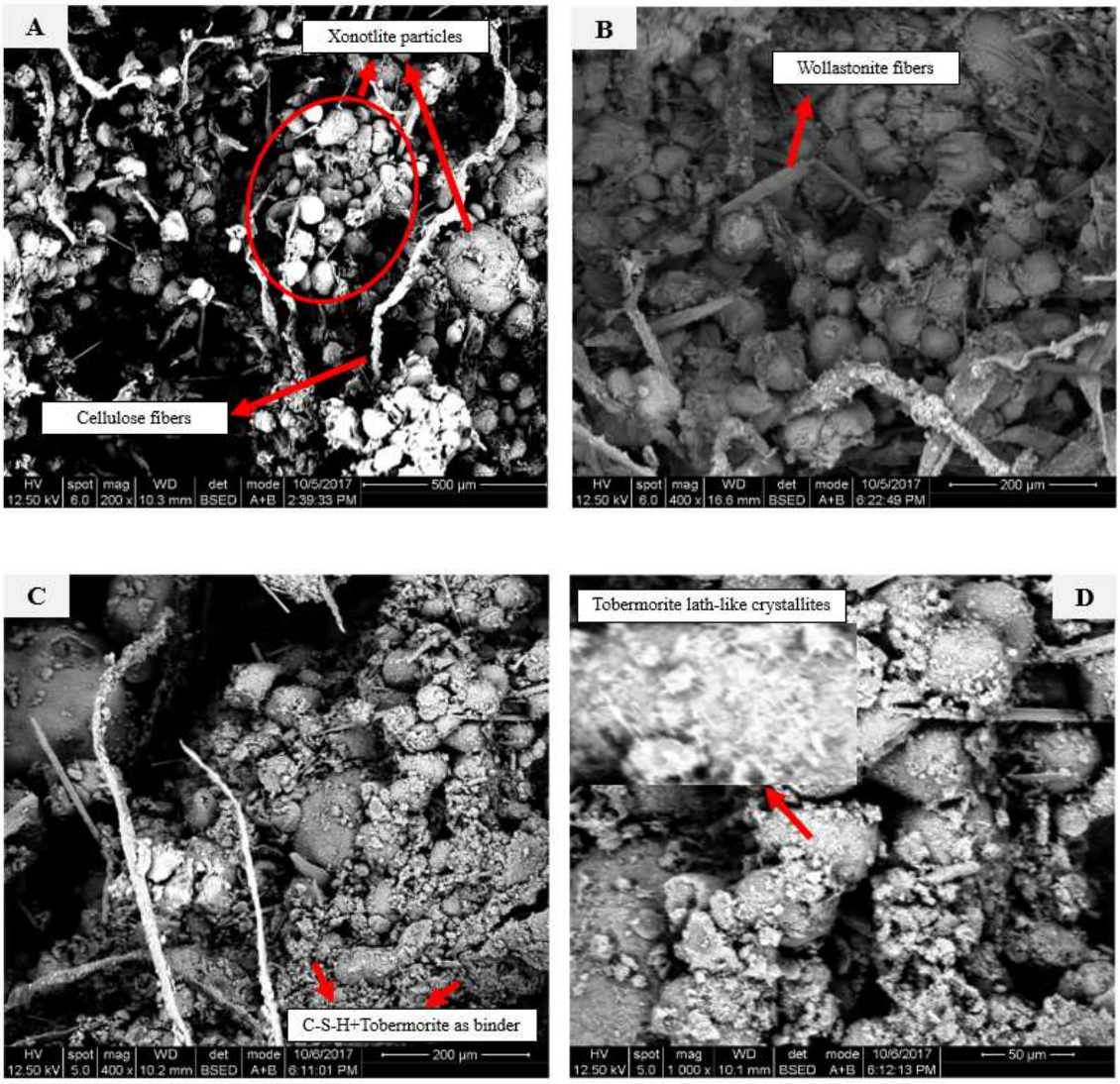

Figure 177. SEM micrographs of fracture surface corresponding to PROMARINE-450 board.

On the other hand, an image of the final product as seen in a polished section by means of SEM is shown in **Figure 178**.

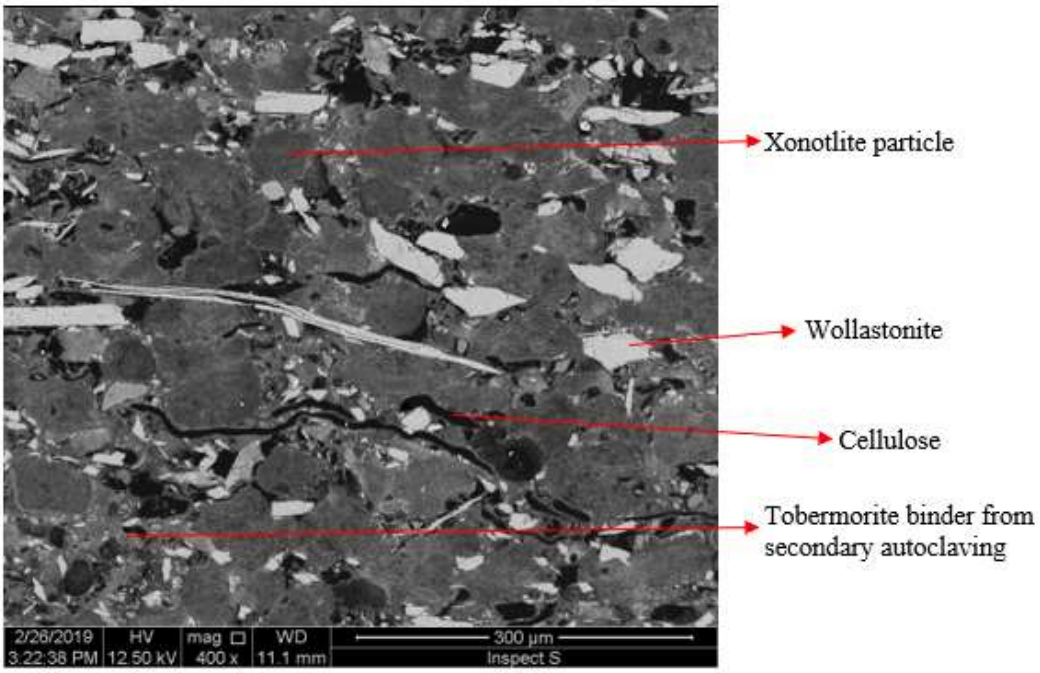

Figure 178. SEM structure as seen in polished section of a typical product formed via double autoclaving.

Compared to the single autoclaved products (stirred autoclave reactor technology), the double autoclaved products have a few advantages and disadvantages as summarized below in **Table 38**. The double autoclaved products are used at Promat in specific conditions, for example when high and specific mechanical and thermal properties are required such as high E-modulus and very low thermal shrinkage for fire dampers. One of the disadvantages of the double autoclaved products is that they contain residual quartz and that is considered as a health hazard in certain conditions of long exposure times. The residual quartz comes from three main sources, being :

- The hydrothermal reaction of quartz with lime or hydrated cement
- Presence of quartz in wollastonite.
- The presence of residual quartz in the xonotlite particles formed in the reactors.

Key Parameters	Single autoclaved	Secondary autoclaved
Bending strength	Lower	Higher E-modulus
Delamination strength	Lower	Higher
Compatibility with special additives	Use of glass fibers is possible (increase of mechanical properties)	Use of only cellulose fibers
Fire resistance	Use of endotherms is possible (increase of Rf-values)	No possibility to use additions of endotherms

Table 39. List of strong and weak points for both stirred autoclave technology (single autoclaved calcium silicate boards) and double autoclaving (secondary autoclaved calcium silicate boards).

In the case of remaining quartz in the wollastonite fibers added to these kind of calcium silicates, it must be remarked that wollastonite is a Ca-silicate existing in nature often used to limit the thermal shrinkage or hygric/hydric movement in Ca-silicate based products. Because of its high thermal stability and specific morphology, it is frequently added to Promat products in order to reduce the thermal shrinkage and it is very effective for this purpose. However, wollastonite crystals often include at the same time quartz crystals.

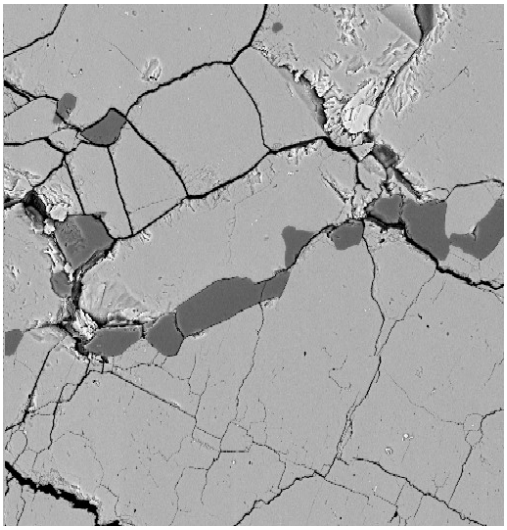

Figure 179. Section through a wollastonite rock. Dark grey particles are quartz; Lighter grey matrix is the wollastonite.

An example of this can be observed in **Figure 179**. As these quartz particles (dark grey particles) are of larger size and they are normally not in contact with the alkaline reactive medium, they tend to be present after the reaction. For that reason, in some tested formulations wollastonite was omitted from the starting recipe.

On the other hand, residual quartz may be also commonly found in the xonotlite particles synthesized by stirred autoclave reactor. In order to avoid residual quartz in the xonotlite particles, a special xonotlite-based slurry synthesized initially with KOH addition in the vertical stirred reactor, was used.

One of the targets of the present thesis, has been the development of a quartz-free calcium silicate product processed by means of double autoclaving technology as a non-hazardous calcium silicate board. The reference product as mentioned above is composed from the following components: primary xonotlite particles, OPC, sand, cellulose fibers, and wollastonite. Therefore, the research was focused on the development of a quartz-free alternative for the product sold in the market as PROMATECT-MLT or PROMARINE-450T, depending on the application. The goal established was to achieve similar properties as for the existing quartz containing product PROMARINE-450T. So, to prevent the presence of residual quartz, the following changes were applied to the starting formulation of PROMARINE-450 board:

- Replacement of quartz by ***amorphous silica (Elkem MS 940)***
- Replacement of wollastonite by **xonotlite/** ***vermiculite***.
- Use of a special xonotlite-based slurry (xonotlite synthesized with KOH addition).

4.3.2. Development of quartz-free PROMATECT-MLT boards

- **General composition and properties of products based upon microsilica and special xonotlite.**

A set of PROMATECT-MLT boards prepared from different formulations and processed via double autoclaving technology were made and the main properties such as flexural strength, thermal shrinkage and fire rate were determined. The first set of formulations is given in **Table 39**. In these trials M400 quartz was replaced by Elkem MS 940 for every sample. Furthermore, wollastonite was also removed from the formulation for most of samples, being replaced by an extra xonotlite-based slurry content (MLT-14/ MLT-15/ MLT-16) and by crude vermiculite in a few additional formulations (MLT-15/MLT-16). In these samples, two different concentrations of vermiculite were used (0.5- 1%). Besides, a number of extra formulations were proposed to influence mechanical and thermal properties, and these will be discussed in the next sections.

Sample	Composition								
	M400	OPC	$Ca(OH)_2$	X	Elkem MS940	W	Cel.	Additives	Remark
MLT-12 ref	Yes	Yes	No	Yes	No	Yes	Yes	No	Reference 450 g/l
MLT-29 ref	Yes	Yes	No	Yes	No	Yes	Yes	No	Reference 400 g/l
MLT-13	No	Yes	No	Yes	Yes	Yes	Yes	No	Q-free
MLT-14	No	Yes	No	Yes	Yes	No	Yes	No	Q-free
MLT-15	No	Yes	No	Yes	Yes	No	Yes	Micron vermiculite (0.25 μm)	Q-free
MLT-16	No	Yes	No	Yes	Yes	No	Yes	Micron vermiculite (0.5 μm)	Q-free
MLT-20	No	Yes	No	Yes	Yes	No	Yes	$Al(OH)_3$	Q-free
MLT-31	No	Yes	Yes	Yes	Yes	No	Yes	No	Q-free/Partial replacement of OPC by lime
MLT-69	No	Yes	No	Yes	Yes	No	Yes	No	Q-free/Use of surfactant

Table 40. List of starting raw materials and additives of PROMATECT-MLT samples composition. M400: quartz M400, OPC: ordinary Portland cement, X: xonotlite slurry, Cel: cellulose fibers. ***Note:** The composition of PROMATECT-MLT samples is indicated qualitatively instead of quantitively owing to be confidential.

During the filter-pressing of PROMATECT-MLT slurry-based mixture, the force needed to shape a green board was recorded. So, these values are listed below in the **Table 40,** and they correspond to the samples MLT-12 ref, MLT-13/-14/-15/-16.

Sample	Pressing Force (kN)
MLT-12 ref	20
MLT-13	40
MLT-14	50
MLT-15	60
MLT-16	70

Table 41. Pressing force values of the first set of test samples of PROMATECT-MLT samples in the filter-pressing process.

Looking at the force-values reached during the pressing of the different mixtures, there is a clear upward trend as quartz is replaced by microsilica, and wollastonite by an extra amount of xonotlite slurry and by crude vermiculite in a few trials. This can be explained based upon the lower apparent density of silica fume compared to quartz, the possible formation of CSH with silica fume already during the preparation and the lower density of xonotlite and vermiculite compared to wollastonite. A greater compaction of the solids leads to stronger interfaces and hence a more brittle microstructure and products with lower fracture toughness. SEM images of fracture surface of these two samples are presented in **Figure 180**.

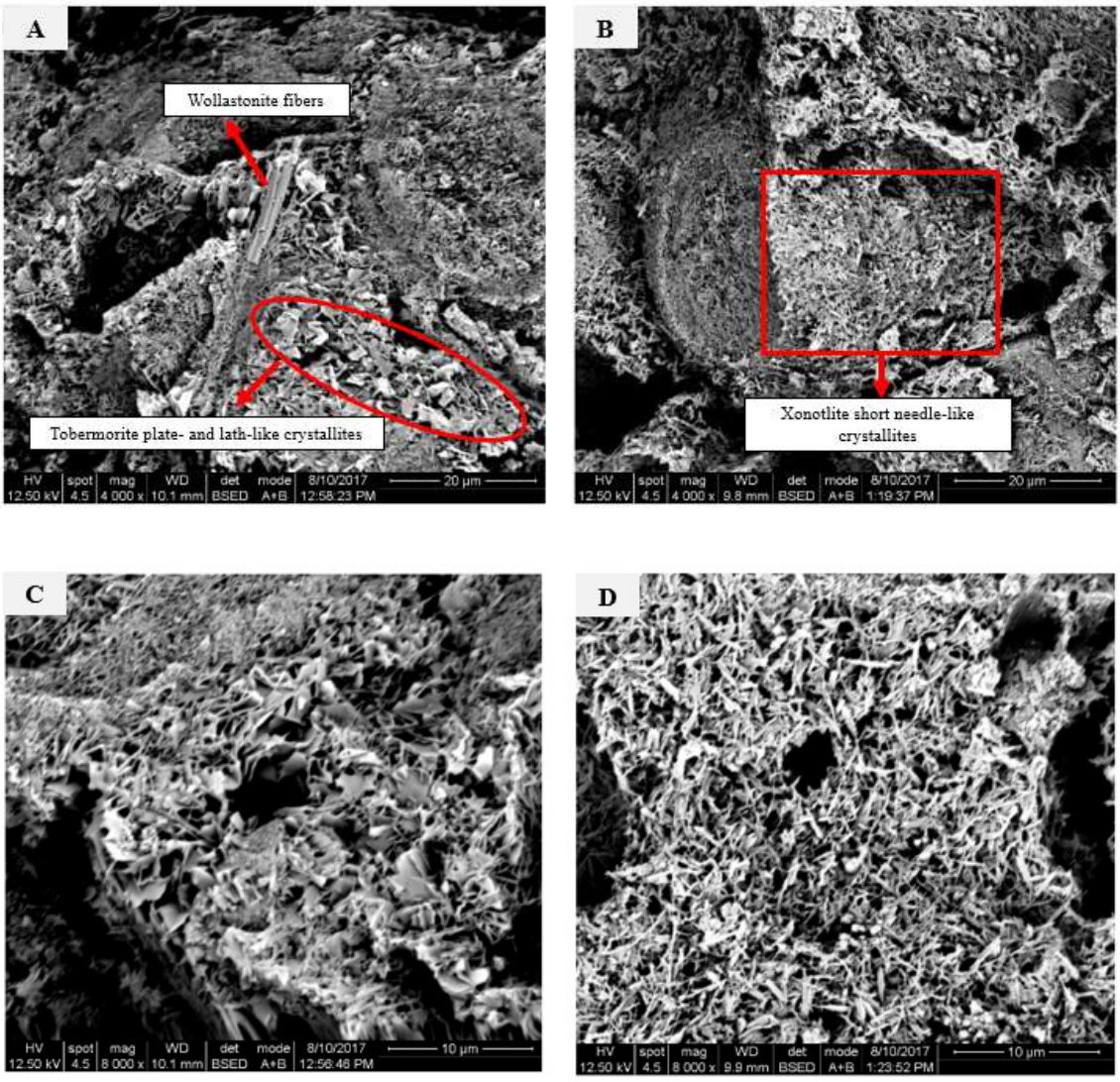

Figure 180. SEM micrographs of PROMATECT-MLT boards fracture surface. (A/C) MLT-12 Ref sample; (B/D) MLT-14 sample.

The structure in all cases is composed of xonotlite-particles bonded by tobermorite crystals. For the reference, the binding tobermorite occurs mainly as plate-like crystals. For the Q-free product, the tobermorite appears with a more needle like structure. From the XRD diagrams in **Figure 181**, it is seen that the products made with amorphous silica are composed of a tobermorite-binder that is less crystalline compared to the binder in the Q-containing reference board. This could be due to the formation of an initial CSH with lower C/S-ratio compared to the reference and a higher degree of variability in the composition (larger spread of reacting surface due to variable agglomeration).

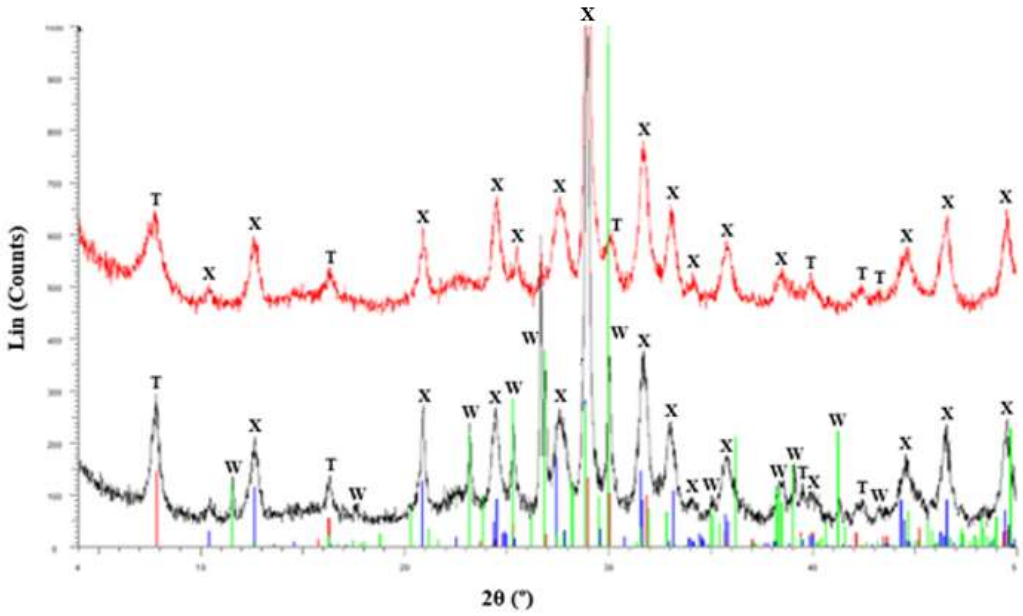

Figure 181. XRD spectra overlay comparing the reference sample MLT-12 (black spectrum) and the MLT-15 sample (red spectrum).

The results of the corresponding tests performed at the laboratory to determine the mechanical and thermal properties of the quartz-free MLT samples, are displayed in the **Figures 182-185**. In general, the laboratory products showed the following changes compared to the reference:

- Comparable mechanical properties (SMOR, E-modulus) , though lower IMOR /IPL20 due to a more fragile character.
- Somewhat higher thermal shrinkage.
- Similar Rf-values

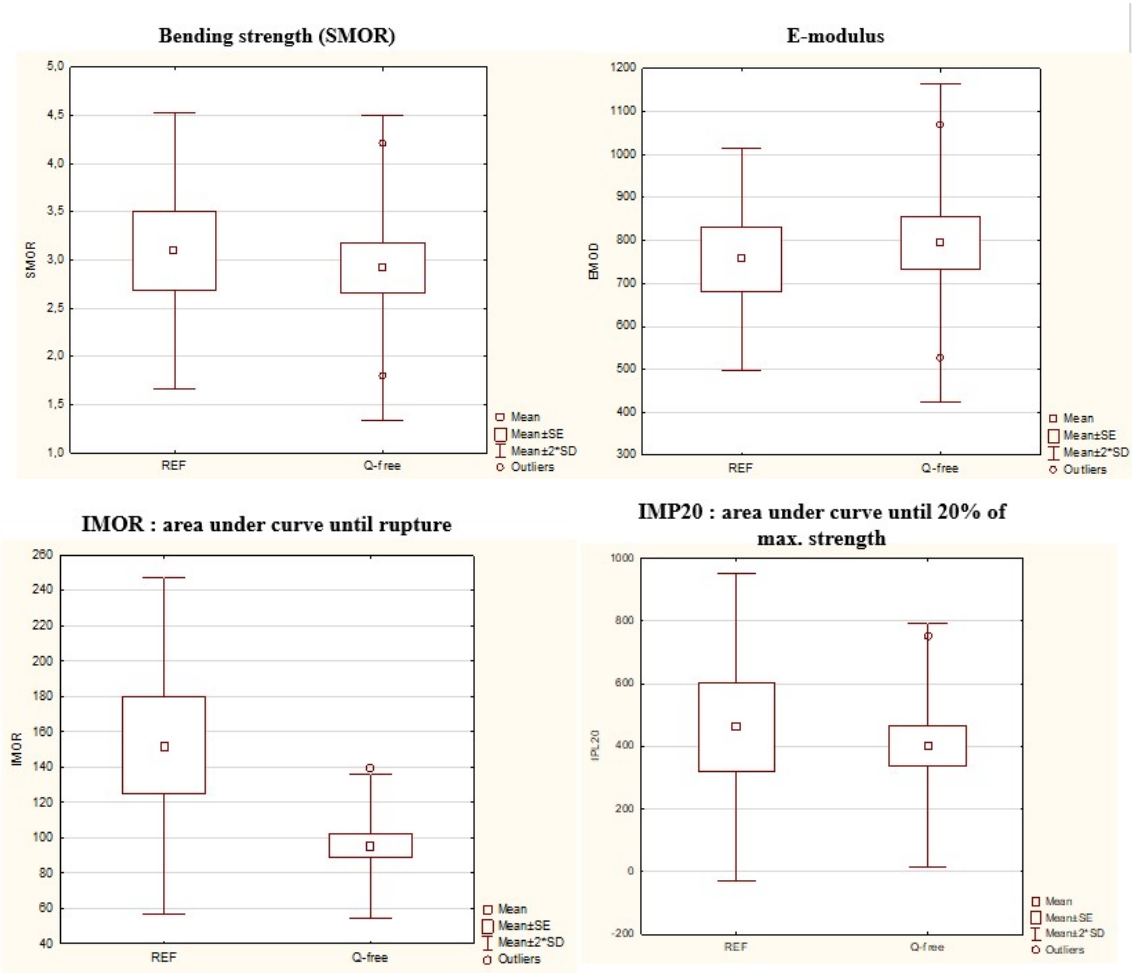

Figure 182. Whisker-plot comparing the mechanical properties of MLT-12 as reference with the quartz-free MLT samples.

The more fragile character appears in **Figure 182** and in the stress-strain diagrams shown in **Figure 183**. The more fragile character is linked to the high pressures developed during the pressing of the boards. The PROMATECT-MLT-products using Elkem MS 940 as silica source have slightly thermal higher shrinkage than the reference boards. This is visible in the whisker-plot in **Figure 184**.

The less good thermal stability is due to:

- The well less crystallized tobermorite binder
- The finer crystal-size of the binder.
- The fact that no wollastonite was used. Wollastonite has lower thermal shrinkage than xonotlite because it is an anhydrous compound and present as large crystals.

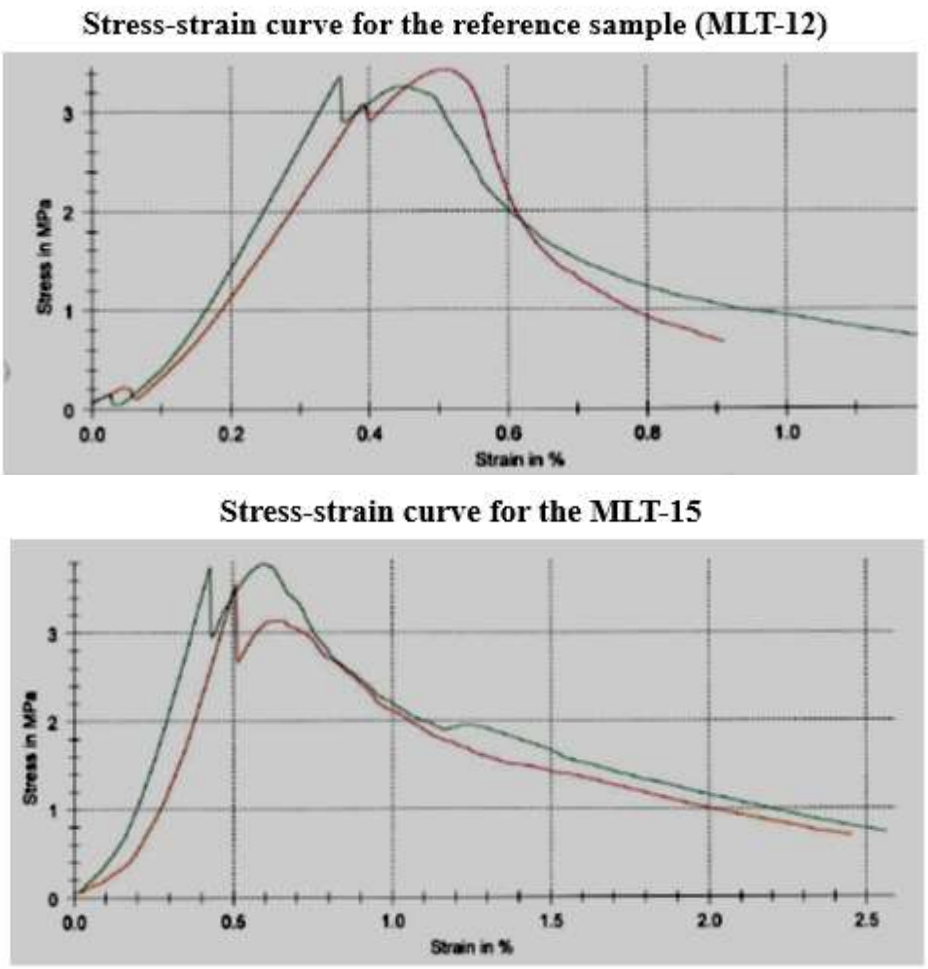

Figure 183. Comparison between the strain-stress curves of the reference sample (MLT-12) and MLT-15 sample.

Concerning to the Fire Rate (Rf) values obtained for the specimens: MLT-12 (ref), MLT-13/-14/-16; they seem quite comparable to the reference as it can be observed in **Figure 185**. The small differences are due to variations in thickness, density and humidity percentage during chamber conditioning. An overlay of the temperature vs. time curves was plotted for these samples as **Figure 185** shows. At 160ºC (horizontal red line), the time recorded for each specimen tested indicates the Rf value. These Rf values are shown in the chart legend for all the specimens as well as the density, thickness and humidity percentage of the board.

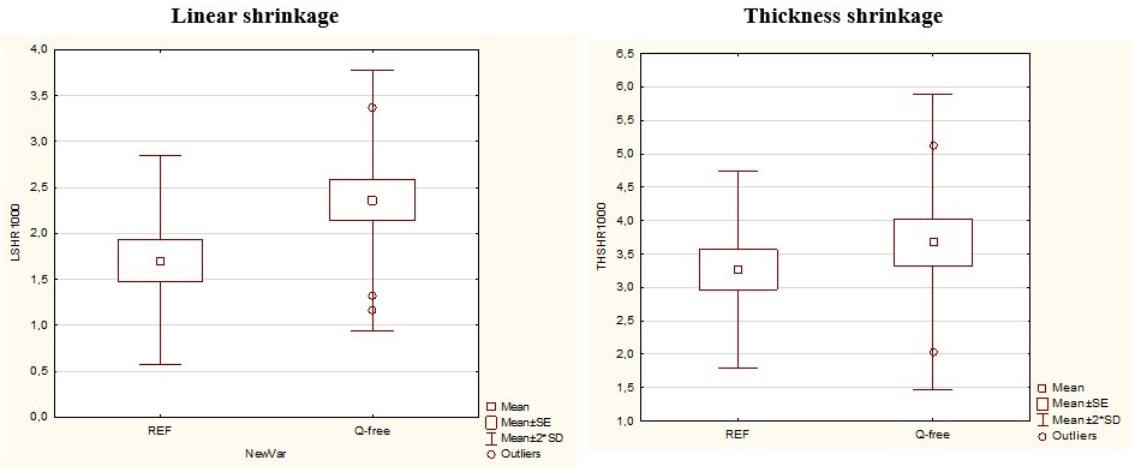

Figure 184. Whisker-plot comparing the thermal shrinkage values of MLT-12 as reference with the quartz-free MLT samples, on the length (left diagram) and on the thickness.at 1000°C.

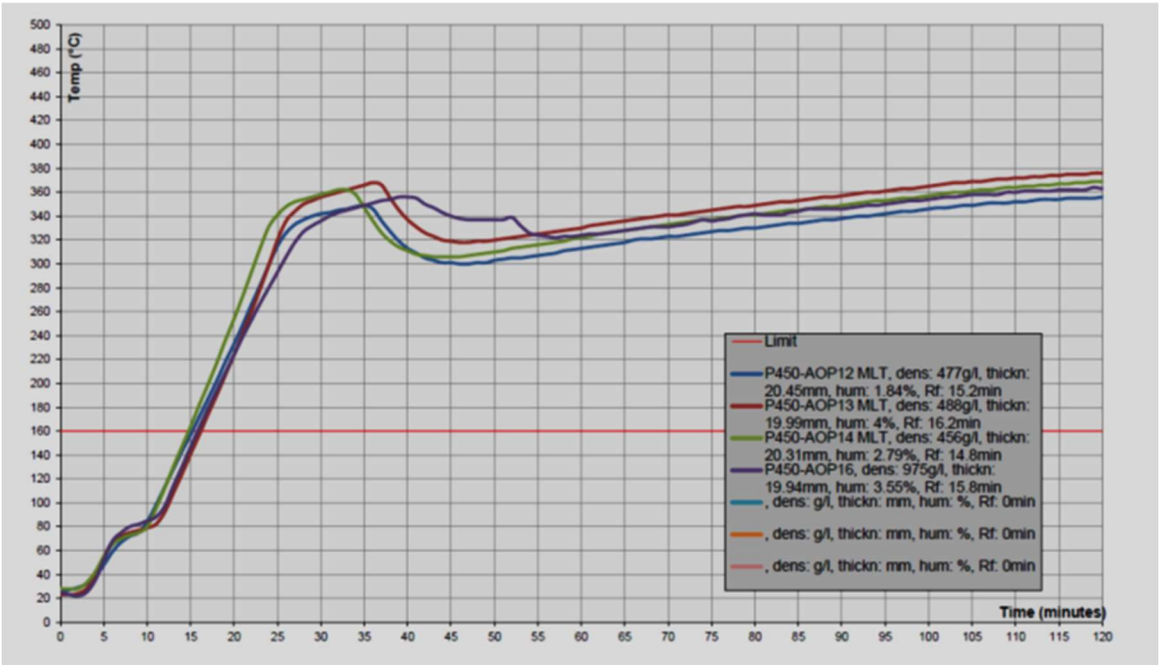

Figure 185. ISO Fire Rate curves of MLT-12 as reference quartz-free MLT samples.

- **Methods to correct the brittleness**

In order to try to correct for the higher brittleness of calcium silicate boards produced via double autoclaving in the previous trials, the following approaches were tested:

- Lowering the density/Increasing the content of xonotlite particles
- Use of vermiculite
- Changing the binder-type: replace OPC/SiO_2 by lime + OPC /SiO_2
- Use of surfactants

The effects of the some of the tested variables can be visible in the whisker-plot diagrams shown in **Figure 186**.

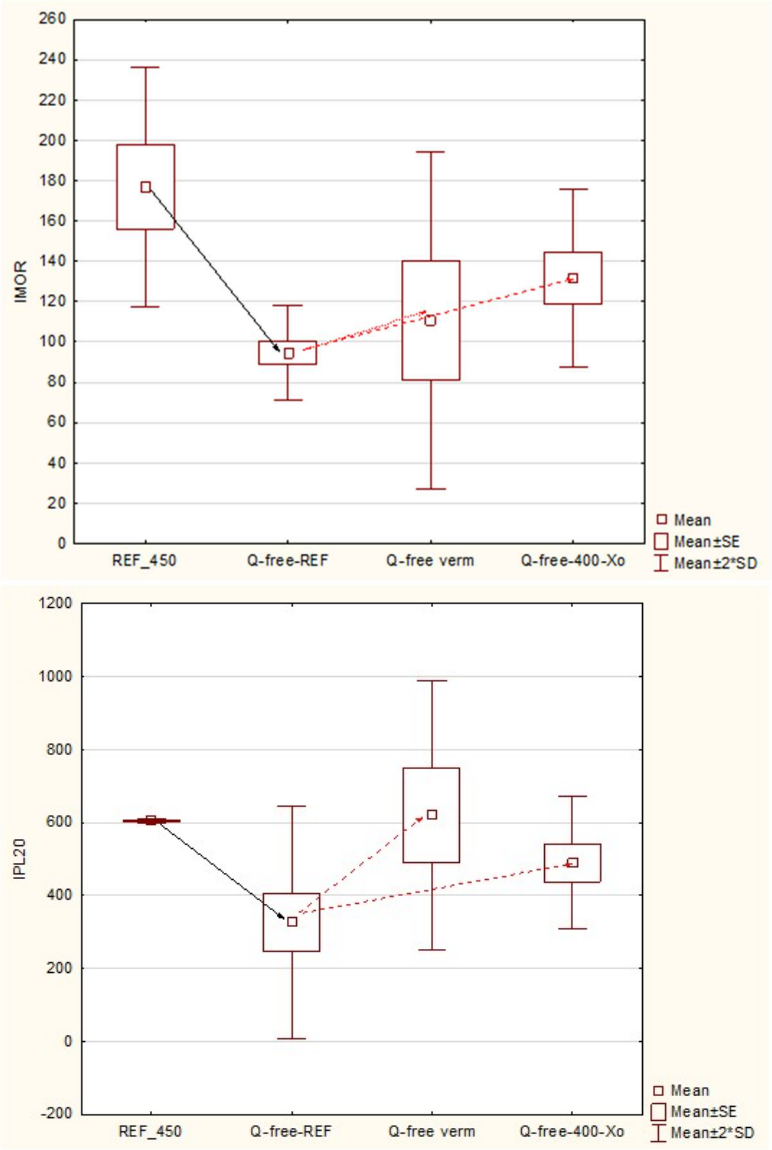

Figure 186. Whisker-plot diagrams showing IMOR and IPL20 for different formulations. Black arrow: effect of Q-free changes; Red arrows: effects of extra changes to reduce the brittleness.

On the other hand, the effects of the density, xonotlite content and presence of vermiculite on the fragility of the MLT samples are observed in the stress strain-stress curves shown in **Figure 187**.

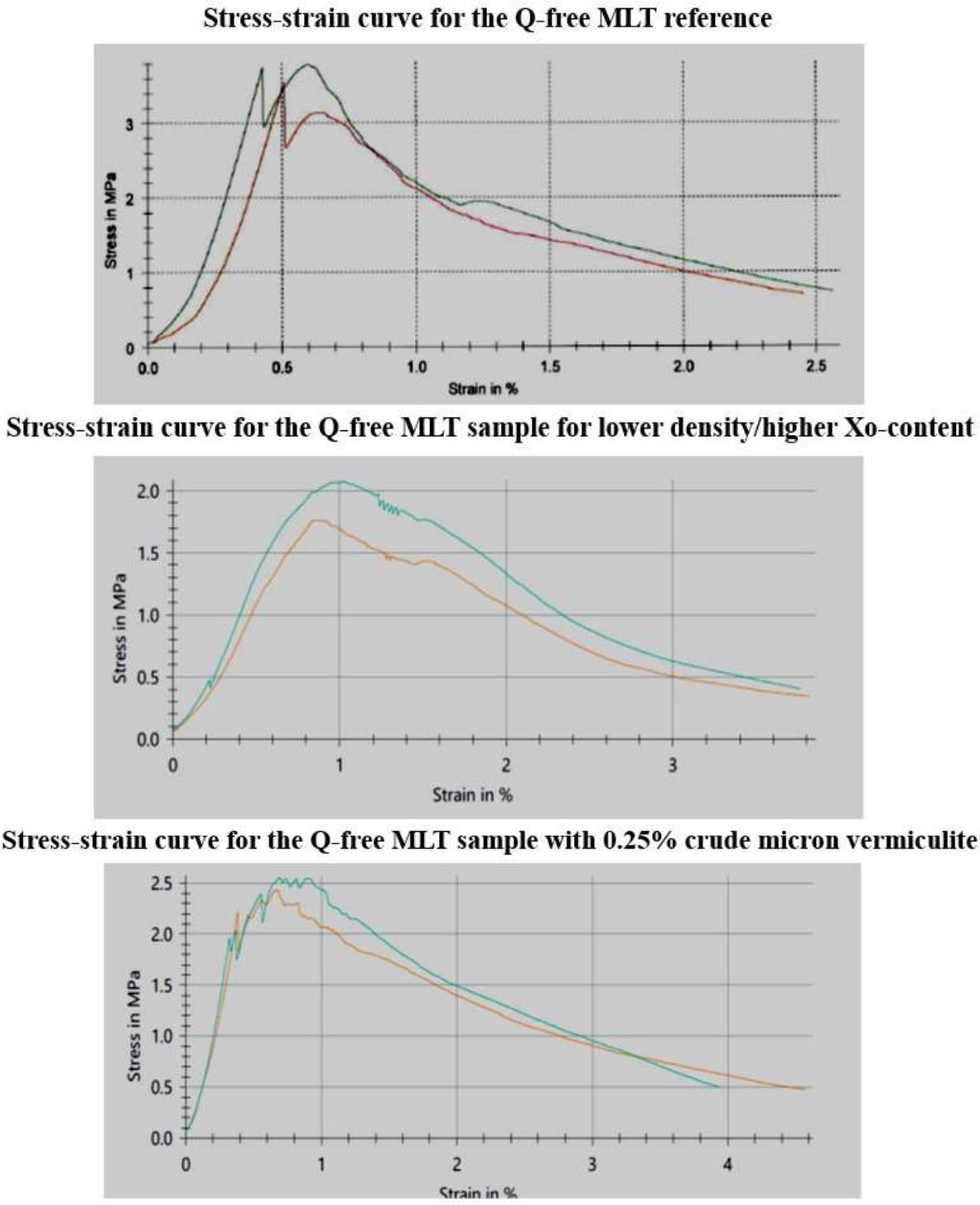

Figure 187. Comparison between the strain-stress curves of reference composition and the new, quartz-free composition based upon amorphous silica to replace quartz and xonotlite replacing wollastonite.

Figure 188. Aspect of MLT-boards made with lime instead of OPC.

Ordinary Portland Cement (OPC) is used in the double autoclaved products to introduce enough green strength, so that calcium silicate boards can better withstand the stresses during the hardening in the autoclave. When using only lime as lime source, the boards tend to have some delamination cracks (see **Figure 188**). Stresses can appear during autoclaving owing to slight pressure variations and expansion of the water in the boards (due to temperature variations/boiling of water).

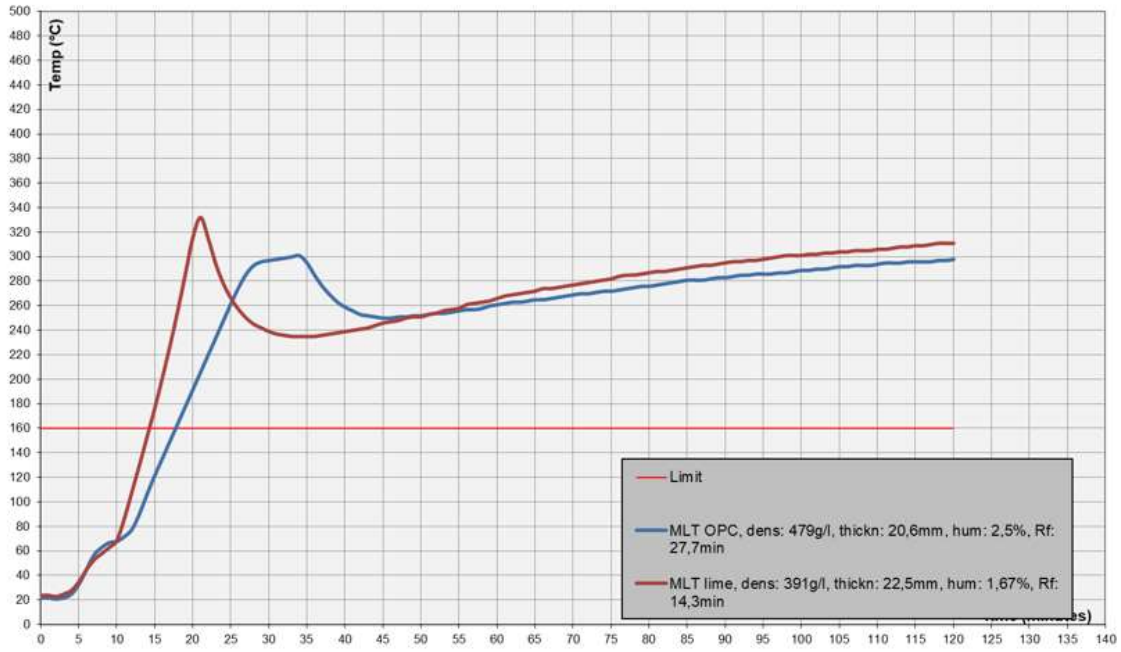

Figure 189. ISO Fire Rate curves of MLT samples using lime and OPC as CaO-source respectively.

Due to the expansion, the boards made with additions of Ca(OH) have lower density and less good Rf-values. This is illustrated by **Figure 189**. However, the use of a partial replacement of OPC by lime seems to lead to higher IMOR/IPL20 values, as it can be seen in **Table 41**.

Sample	Bending strength				Density (g/l)	Comments
	S.MOR (MPa)	E.MOD (MPa)	i.MOR (J/m^2)	i.pl20 (J/m^2)		
MLT-29 ref	1,85	526	115	384	397	400 density-sample as reference
MLT-31	1,69	392	149	634	400	Partial replacement of OPC by $Ca(OH)_2$

Table 42. Mechanical properties for samples made with OPC as Ca-source (MLT-29) or a mixture of OPC/$Ca(OH)_2$ (MLT-31).

These differences in mechanical properties might be due to differences in content of tobermorite binder and/or to differences in morphology of the tobermorite crystals. This was also observed in other matrixes studied by Etex (Fibre-cement-products) and a few examples of differences in morphology are given below (see **Figures 190** and **191**).

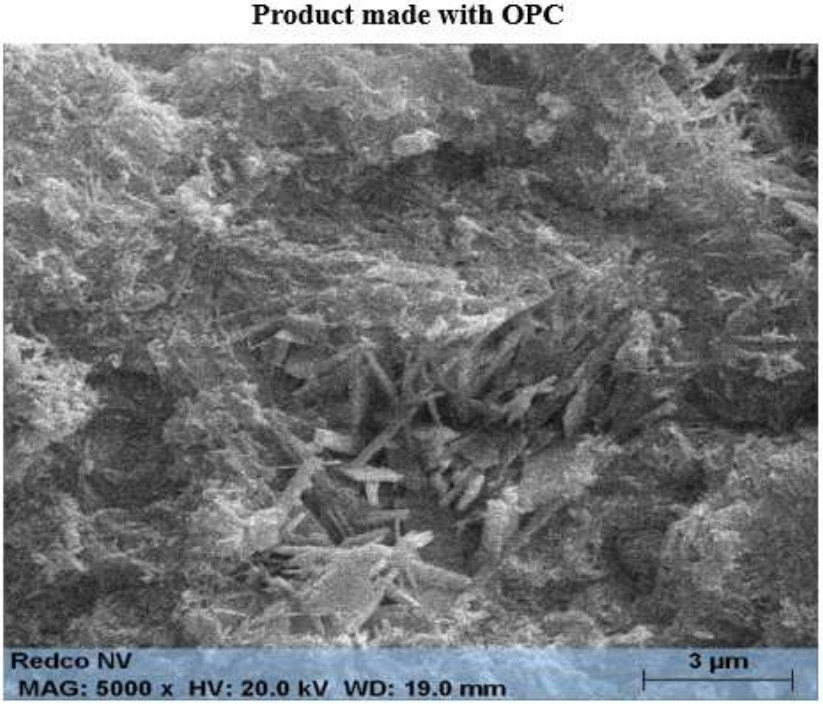

Figure 190. Fracture surfaces showing differences in tobermorite crystals when using OPC.

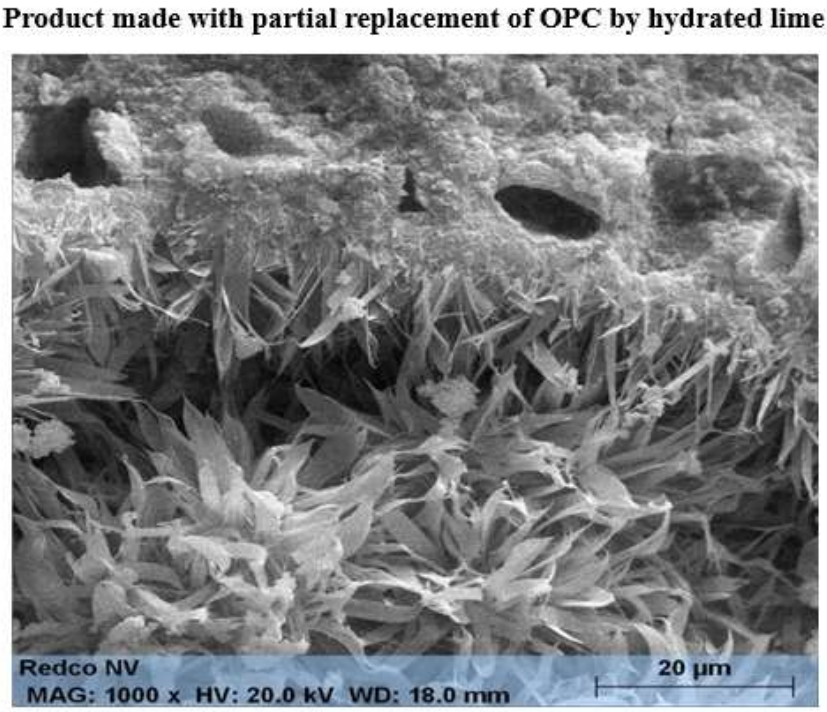

Figure 191. Fracture surfaces showing differences in tobermorite crystals when using mixtures of OPC/hydrated lime.

The morphological differences are not fully explained tough they could be related to differences in the CSH compositions. In OPC compositions at least part of the CSH has high C/S ratio whilst for CSH formed from reactions with lime, the CSH/tobermorite formation occurs during the thermal hardening at high temperatures. In these conditions, the CSH is expected to have lower C/S ratios (lower solubility of lime at higher temperatures), meaning CSH with a low CaO/SiO_2 ratio. The CSH that forms via OPC will also integrate Al^{3+} and hence have a different structure.
The XRD-patterns in **Figure 192** show the mineralogical phases present in MLT-29 ref sample and MLT-31 sample respectively. The black spectrum belongs to MLT-29 sample and the red spectrum corresponds to MLT-31. In addition, XRD Rietveld analysis was done to determine quantitively the content of mineralogical phases for each sample (see **Table 42**). Both the XRD spectra and Rietveld analysis reveal that the differences specially in the tobermorite content are clear.

Sample	T (%)	X (%)	W (%)	Q (%)	C (%)	AMC (%)
MLT-31	0	73,3	7,6	0,6	2,8	15,7
MLT-29 ref	14,2	53	6,3	1,7	0,8	24

Table 43. Results of XRD Rietveld analysis of MLT-29 ref and MLT-31. T: tobermorite; X: xonotlite; W: wollastonite; Q: quartz; C: calcite; AMC: amorphous content.

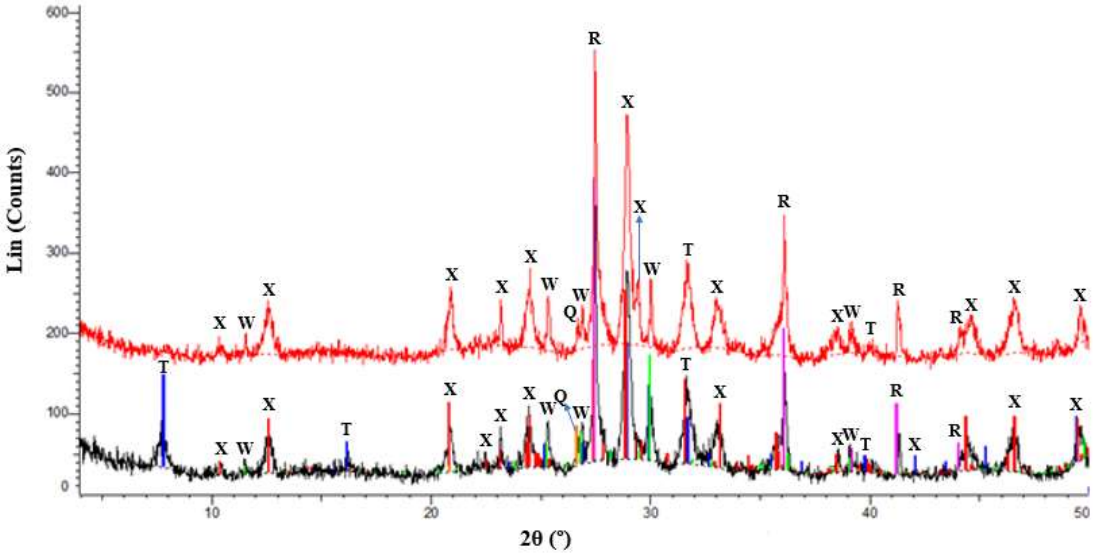

Figure 192. XRD spectra corresponding to MLT-29 reference (black curve) and MLT-31 (red curve).

Another possibility to modify the fracture toughness was to add a surfactant as alternative at the starting formulation. A commercial existing product (Micropol) was added in the mixture before filter-pressing step. This was only tested for the quartz containing MLT reference sample. It seems likely that the bubbles introduced by the surfactant can lead to crack-arrest and crack-deflection. Hence, it makes a positive impact on the fracture toughness of the product. **Table 43** collects the mechanical features of the MLT products based on the reference composition and the Micropol addition.

Sample	Bending strength				Density (g/l)
	S.MOR (MPa)	E.MOD (MPa)	i.MOR (J/m^2)	i.pl20 (J/m^2)	
MLT-29 ref	2,25	307	257	980	448
MLT-69	2,96	352	462	1513	468

Table 44. Mechanical properties for samples made with and without the use of surfactant.

- **Methods to correct the thermal shrinkage**

The methods used to reduce the thermal shrinkage were the following:

- Use of small fractions of crude micron vermiculite
- Use of $Al(OH)_3$ to influence the tobermorite structure

An alternative way to reduce the shrinkage is by means of using mica instead of wollastonite at the starting formulation. But this was not tested as mica tends to hinder the water evacuation during the filter pressing. The use of crude micron vermiculite is known from gypsum-based products where small amounts of crude vermiculite are added to compensate for the shrinkage of gypsum on heating. During heating, the crude vermiculite expands, and this counterbalances the shrinkage effects. On the other hand, the addition of $Al(OH)_3$ is used to favour the formation of Al-tobermorite which is morphologically a bit different to the tobermorite. This crystalline mineral phase has special properties, and it is added in fibre-cement-based products to reduce the hydric movement. In our applications, the addition of $Al(OH)_3$ enables a better tobermorite crystallization hence it can correct the effects of silica fume addition which is added instead of quartz (lower content and less crystalline tobermorite). Some XRD spectra of different formulations are plotted in **Figure 193**.

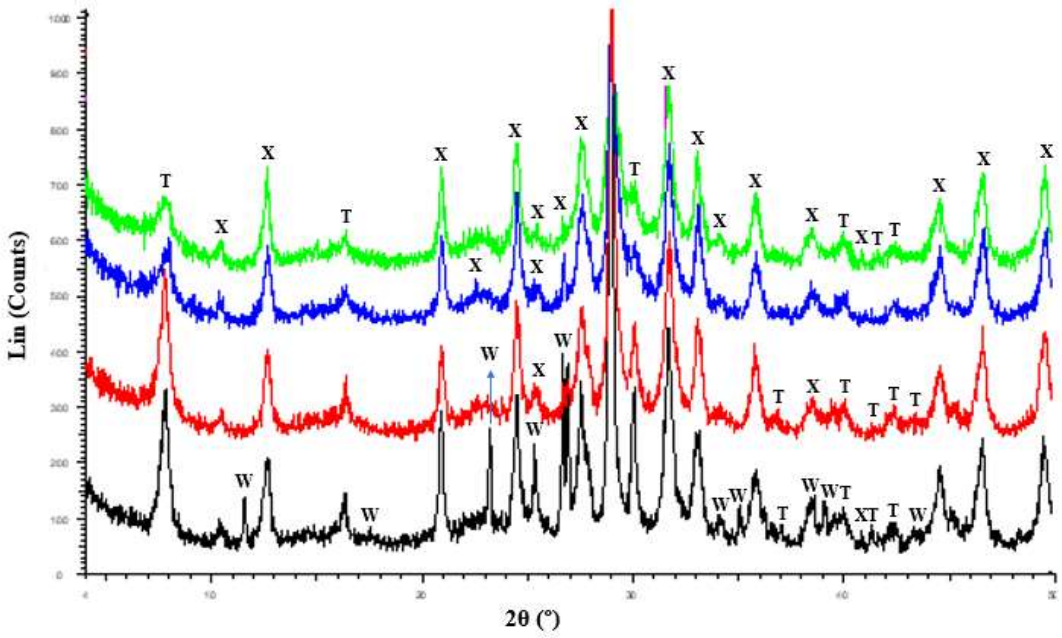

Figure 193. XRD spectra of MLT samples with different composition (black curve: MLT-12 reference/red curve: MLT-20 with $Al(OH)_3$ addition/ blue curve: MLT-14/green curve: MLT-15).

The red spectrum corresponding to the MLT-20 presents a considerable content of tobermorite as well as the MLT-12 reference. This is reflected by the high intensity of some x-ray diffraction peaks that belong to 11-Å tobermorite/Al-tobermorite. In literature is reported that aluminium element can enter into the structure of tobermorite and result in an increasing interlayer space. With aluminium incorporated, the ratio of Ca/(Si + Al) increases and the content of Si decreases. Besides, the morphology of tobermorite changes with aluminium incorporated, which has a larger arrangement of foils.

Due to the increased tobermorite concentration when adding $Al(OH)_3$, the thermal shrinkage of the $Al(OH)_3$-containing Q-free MLT samples is lower than for the Q-free MLT without $Al(OH)_3$. The differences in thermal shrinkage for the different formulations are summarized in the graph presented below in **Figure 194**.

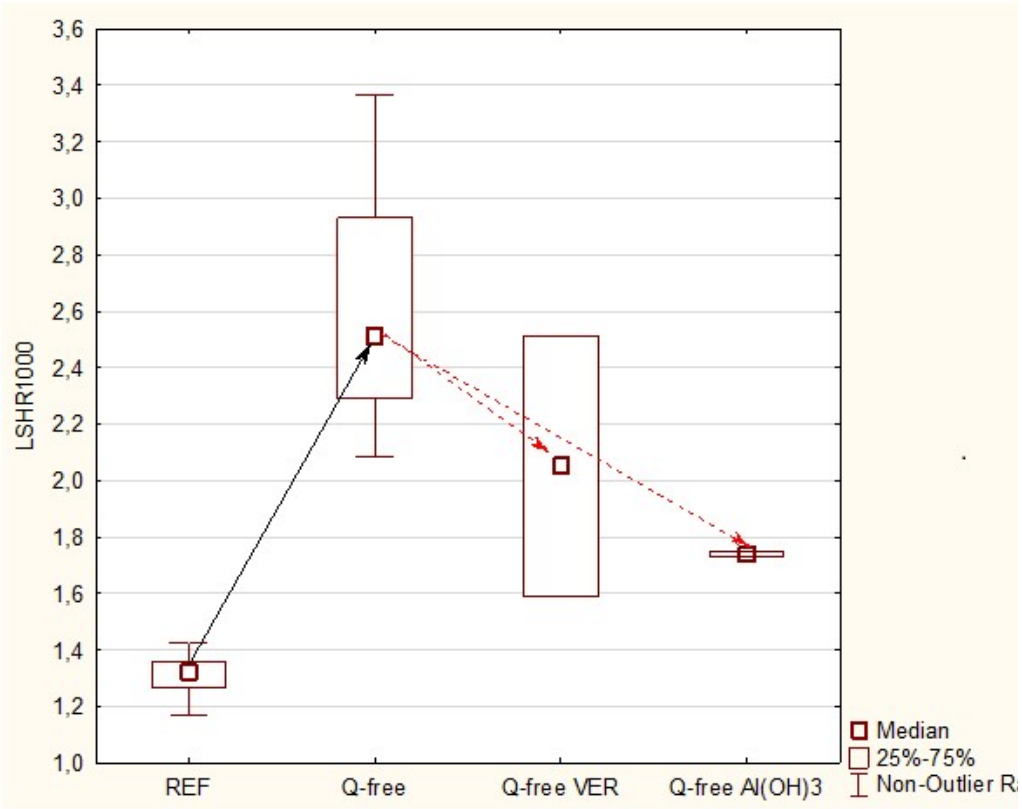

Figure 194. Whisker-plot comparing thermal stability of Q-free products, the MLT-12 reference and Q-free MLT-20 (with improved thermal stability).

The target of this part of the investigation was to make quartz-free version of the double autoclaved products for Promat to mitigate the occupational risks. So, the approaches used to avoid the presence of quartz in the final product at laboratory scale were the following:

- Use of PROMAXON-type of xonotlite
- Replace M400 quartz by Elkem MS 940 and replace wollastonite by xonotlite
- Use of special xonotlite synthesized from KOH addition.

These approaches were tested for the products known as PROMATECT-MLT or PROMARINE 450.

- Use of extra xonotlite-based slurry and Elkem MS 940 to replace both wollastonite and sand respectively, always leads to higher pressure and thus higher fragility. This can be improved by addition of small amounts of crude micron vermiculite, mixtures of lime and OPC, use of surfactants and finally by reducing the density and decreasing the content of tobermorite formed as secondary binder during the hydrothermal treatment of the board. Compositions with very low content of secondary binder tend to have lower values for the delamination strength.
- The replacement of wollastonite and quartz in the quartz-free formulations leads to lower crystallinity and hence higher thermal shrinkage. But this can be compensated by addition of vermiculite or $Al(OH)_3$.

CHAPTER 5

CONCLUSIONS AND FUTURE RESEARCH

CHAPTER 5. Conclusions and Future Research

This PhD thesis is focused on three main goals, being in the first place establish a new and lower energy-consuming process to make calcium silicate-based products for high-temperature applications; in the second place, to develop a better understanding of some of the actual used processes; and in the third place, to propose methods to improve some of the existing technologies.

In order to optimize heat transfer in products used for high-temperature applications such as passive fire protection and thermal insulation, a reasonably high content of pores with very small diameters is required. In the current process, the high porosity is obtained via xonotlite particles that are formed by means of hydrothermal treatment with agitation and that typically use water/solid ratios to 10 or higher. This implies a high energy-consumption. For that reason, as first target, an alternative process with lower energy-consumption was investigated. This process is called 'Geltank' by Promat, and it is thought that some of the competitors are using this technology. In this process, a C-S-H gel is synthesized at pressure-less conditions, after that this gel is mixed with other ingredients. Then, filter-pressed and finally hardened at non-stirring hydrothermal conditions (secondary autoclaving). The water-content used is typically at least 20-30% lower than in the current used processes. The target was to find the suitable reaction conditions and raw materials to make the desired C-S-H gels as well as the starting formulations for the end-products. The C-S-H gels were characterized by XRD, FTIR, SEM and BET-BJH surface area analysis. To make C-S-H gel of the desired low-density in a reasonable time and with the desired recrystallization into xonotlite during the hydrothermal hardening, mixtures of a pre-treated amorphous silica (opened microsilica by mechanical high shearing) and lime need to be stirred at ca. 90°C, for one hour. Along this process, $Ca(OH)_2$ and micro-silica react, forming a C-S-H with enough pore-volume and a suitable composition (C/S-ratio). Therefore, this C-S-H gel converts into the desired content of xonotlite during the hydrothermal hardening of the pressed calcium silicate boards. This is required to obtain low-density end-products with the desired thermal stability (no cracking, low thermal shrinkage).

As the amorphous silica tends to agglomerate to a high degree (as influenced by sintering during its formation), a mechanical or chemical pre-treatment is required because of its reactivity is on the one hand hardly linked to the particle size. On the other hand, the microsilica must fulfill certain specifications concerning the chemical composition. This parameter is also very relevant in terms of microsilica reactivity.

Several mixing conditions were investigated. Suitable conditions for low-density C-S-H gels are those that avoid sedimentation of components and that minimally break-up the earlier formed C-S-H gel particles. Minimal shearing by mechanical agitation of the matrix results in lower density C-S-H gel.

Mixtures of amorphous silica and quartz should be used to produce medium-density products by using 'Gel Tank' technology. Quartz will only react during the hydrothermal hardening, and it impacts on the phase composition and on the properties of the final product. The ratio of amorphous silica/quartz depends on the desired density for the end-product, and it decreases conforming the final product density increases. The ratio is chosen such that the product formed after the filter-pressing, has a certain green strength

(the associated pressure during filter-pressing). This green strength needs to be high enough to avoid delamination cracks during the secondary autoclaving. On the other hand, too high pressure loads during pressing lead to more fragile products which is also not desired. When comparing the products formed by the 'Gel Tank' process with those prepared by double autoclaving process used by Promat, it was observed that the former products are more fragile and have lower fracture toughness. It was found out that this issue can be improved using special functional additives that introduce crack-deflection or crack arrest in the calcium silicate matrix. For this purposed, wollastonite or exfoliated vermiculite can be used.

As second goal for this PhD thesis, it was performed the development of a better understanding of the formation of xonotlite particles by stirred autoclave reactor technology via reactions with different silica sources (quartz of different particle size distribution, amorphous silica, and mixtures of crystalline and amorphous silica). When using quartz as silica source, the initial phases formed depend highly on the particle size distribution of quartz as this influences the rate of silica solubilization and hence also the C/S ratio of the initial phases in the hydrothermal reaction between $Ca(OH)_2$ and SiO_2. In general, the reaction goes via calcium-rich initial phases due to the slow solubilization of quartz. For coarse quartz, the first phase formed tends to be α-C_2SH and this phase only partially converts into xonotlite. But the xonotlite crystals formed present poor structures leading to a matrix of low quality. Good reactions proceed via formation of C-S-H round the quartz grains that later take up more silica in the structure and convert into tobermorite, xonotlite and/or mixtures depending on the C/S ratio and autoclaving conditions. The mineral phases obtained as well as the structure of the xonotlite particles depend highly on the Ca/Si-ratio of the initial C-S-H. For a good reaction, there is an optimal particle size that enables a reaction via calcium-rich C-S-H phases. These phases have a less polymerized structure and have a reasonable fast recrystallization into xonotlite via the intermediate formation of tobermorite. Too fine quartz gives silica-richer C-S-H with higher degree of polymerization and this results in an end-product with remaining tobermorite which is not optimal for the thermal stability. Reactions with fine quartz or opened amorphous microsilica tend to quickly form C-S-H gel, though the recrystallization of this C-S-H gel is taking more time than for the optimal quartz sizes (around 10 micron).

When using amorphous silica, it is important to have a good dispersion of the silica particles for a desired reaction. For well dispersed silica, the reaction proceeds via fast formation of a C-S-H gel with C/S ratio in nearly equivalent proportions (C/S = 1.04) and with a structure that seems such that it recrystallizes only slowly and at high temperature (due to higher degree of polymerization). This crystallization occurs as long xonotlite needles that include a considerable number of small pores, meaning xonotlite particles with low apparent density are formed. This results in end-products with good mechanical and thermal properties. The reaction between lime and amorphous silica occurs more in the liquid/solution and hence crystal growth is more pronounced. Whereas that in the reaction between lime and quartz, it occurs mainly on the quartz surface (solid surface). The overall reaction is more controlled by quartz itself (lower reacting surface and more diffusion-controlled process). The different compositions and structures of the C-S-H formed by reaction of lime and different silica sources were characterized by classical techniques such as XRD, FTIR, SEM and BET-BJH analysis and slightly studied by advanced techniques such as NMR and high energy synchrotron-based X-ray-scattering.

The use of mixtures of amorphous and crystalline silica tends to give products with high degree of crystallization and consisting of xonotlite and tobermorite. This is due to the formation of different C-S-H phases in different parts of the synthesis and the impact of the initial C-S-H composition on the later reaction.

Different xonotlite particles formed when using different silica sources were used as lightening agents in the matrix of calcium silicate-based products to test the mechanical and thermal properties. It was found that the calcium silicate boards containing xonotlite-based particles formed via microsilica as precursor, showed a better mechanical performance, a higher thermal stability and lower thermal conductivity values at high temperatures.

To optimize the heat transfer values of the single-autoclaved products, it is typically to use endotherm additives. The endotherms need to have a high decomposition energy and the optimal decomposition temperatures depend on the application. For partition applications, it is required that the endotherm additives present thermal decomposition temperatures near to 160°C to optimize the energy storage in the board. Ettringite and gypsum gave the best results in these conditions. For passive fire protection in which higher temperatures are reached such as steel protection, tunnel-fires or hydrocarbon fires, endotherm additives with higher decomposition temperatures need to be used. $Al(OH)_3$ and $Mg(OH)_2$ were the ideal candidates as endotherms in this case. For these higher temperature applications, also opacifiers lead to desired improvements of the fire rate.

Xonotlite particles are also used to control the density of the so called double autoclaved products. These xonotlite particles are mixed with fibres, OPC and quartz. This is filter-pressed and submitted subsequently to a curing phase in which the cement-hydration develops enough C-S-H for a good green strength. Later, it is hydrothermally hardened. So, the C-S-H recrystallizes into tobermorite crystals that bind the different ingredients together and provide products with high mechanical properties. These double autoclaved products tend to have residual quartz, and this is not ideal from health point of view. Within this PhD, a third target, a method was developed to make quartz-free double autoclaved products. For this, a special xonotlite was developed , the quartz was replaced by microsilica, and wollastonite was omitted from the starting composition. To reach the required thermal stability without the use of wollastonite, the addition of micron vermiculite and addition of $Al(OH)_3$ were tested. Both were found to be effective. The replacement of quartz by microsilica was resulted in more fragile end-products due to the development of high pressure during the filter-pressing. Investigation into methods to mitigate this, showed that this can be solved adding exfoliated vermiculite or surfactants in the mixture. Both bubbles from surfactant as vermiculite, can act as crack-arresting or crack-deviating structures and so contributing to better fracture toughness. Also, the use of lime as CaO-source (or at least a partial replacement of OPC by $Ca(OH)_2$) seemed to enable higher fracture toughness due to an impact on the tobermorite development (content and morphology).

The PhD showed that the ‘Geltank process’ might be an interesting technology to make new Promat products, as good products with lower energy consumption can be formed. This is for Etex Group a completely new process that needs to be further studied via larger scale testing. The process requires more expensive silica (microsilica) and so, the location of possible production sites must take in consideration the local availability of this type

of amorphous silica at reasonable costs. The minimal densities reached within this research work were around 300kg/m^3 which is the optimal density for use at high temperatures. For even lower densities (of possible interest for building applications), the density of the C-S-H needs to be further reduced and this will require further investigation. Some parameters such as the lime properties and the water/solid ratio were not considered in this study and would need to be further investigated. The higher densities (>500kg/m^3) could also be interesting as they could represent possible alternatives for some double-autoclaved products having better LCA-values.

The study on the understanding of the formation of xonotlite will help the company to better control and optimize the xonotlite formation process. Also here, a deeper study is needed, especially the specific aspects of the industrial process need to be further looked at (heating via steam injection, impact of flow patterns induced by the stirrers). The use of certain endotherms in steel and concrete protection applications is already under consideration. So, broader search to extend the list of suitable additives for partitions also could be useful for the company.

The possibility of making quartz-free double autoclaved products is important in case the market demands for these kinds of products are such that more expensive silica can be considered. This study showed that different results are obtained, depending on the lime source (hydrated lime or OPC cement). The optimal ratios of these components in the existing range of double autoclaved products will be more exhaustively studied in the company.

REFERENCES

1. Chen, J.J., et al., *Solubility and structure of calcium silicate hydrate.* Cement and Concrete Research, 2004. **34**(9): p. 1499-1519.

2. Richardson, I.G., *The calcium silicate hydrates.* Cement and Concrete Research, 2008. **38**(2): p. 137-158.

3. Díez-García, M., *Synthesis by supercritical fluids methods of advanced additions for cementitious materials*, 2017. Universidad del País Vasco.

4. Nonat, A., *The structure and stoichiometry of C-S-H.* Cement and Concrete Research, 2004. **34**(9): p. 1521-1528.

5. Richardson, I.G., *The nature of C-S-H in hardened cements.* Cement and Concrete Research, 1999. **29**(8): p. 1131-1147.

6. Richardson, I.G., *Tobermorite/jennite- and tobermorite/calcium hydroxide-based models for the structure of C-S-H: applicability to hardened pastes of tricalcium silicate, beta-dicalcium silicate, Portland cement, and blends of Portland cement with blast-fumace slag, metakaolin, or silica fume.* Cement and Concrete Research, 2004. **34**(9): p. 1733-1777.

7. Taylor, H.F.W., *Nanostructure of C-S-H - Current Status.* Advanced Cement Based Materials, 1993. **1**(1): p. 38-46.

8. Shpynova, L.G., Nabitovi, I., Belov, N.V., *Microstructure of alite cement stone (hydrated tricalcium silicate).* Soviet Physics Crystallography, Ussr, 1967. **11**(6): p. 747-754.

9. Grudemo, A., *The crystal structures of cement hydration – A review and a new gel structure model*. 4th Interantional Symposium on the Chemistry of Cement, 1960. Washington.

10. Megaw, H.D., Kelsey, C.H., *Crystal structure of tobermorite.* Nature, 1956. **177**(4504): p. 390-391.

11. Taylor, H.F.W., *Relationships between calcium silicates and clay minerals.* Clay Minerals Bulletin, 1956. **3**(16): p. 98-111.

12. Kurczyk, H.G., Schwiete, H.E., *Electronenmikroskopische und thermochemische Untersuchungen über die Hydratation der Calciumsilikate $3CaO{\cdot}SiO_2$ und β-$2CaO{\cdot}SiO_2$ und den Einfluß von Calciumchlorid und Gips auf den Hydratationsvorgang.* Tonindustrie-Zeitung und Keramische Rundschau: Zentralblatt für das Gesamtgebiet der Steine und Erden, 1960. **84**: p. 585-598.

13. Kurczyk, H.G., Schwiete, H.E., *Concerning the hydration products of C_3S and β-C_2S.* 4th International Symposium on the Chemistry of Cement, 1960. Washington.

14. Kantro, D.L., Brunauer, S., Weise, C.H., *Development of surface in the hydration of calcium silicates. II. Extension of investigations to earlier and later stages of hydration.* Journal of Physical Chemistry, 1962. **66**: p. 1804-1809.

15. Stade, H., *On the structure of ill-crystallized calcium hydrogen silicates.II. A phase consisting of poly- and disilicate.* Zeitschrift für Anorganische und Allgemeine Chemie, 1980. **470**: p. 69-83.

16. Taylor, H.F.W., *Proposed structure for calcium silicate hydrate gel.* Journal of the American Ceramic Society, 1986. **69**(6): p. 464-467.

17. Klur, I., Pollet, B., Virlet, J., Nonat, A., *C-S-H structure evolution with calcium content by multinuclear NMR*. Second international conference on the Nuclear Magnetic Resonance Spectroscopy of Cement-Based Materials, 1996. Bergamo. p. 119-141.

18. Richardson, I.G., Groves, G.W., *Models for the composition and structure of calcium silicate hydrate (C-S-H) gel in hardened tricalcium silicate pastes.* Cement and Concrete Research, 1992. **22**(6): p. 1001-1010.

19. Pellenq, R.J.M., et al., *A realistic molecular model of cement hydrates.* Proceedings of the National Academy of Sciences of the United States of America, 2009. **106**(38): p. 16102-16107.

20. Richardson, I.G., Brough, A.R., Brydson, R.M.D., Groves, G.W., Dobson, C.M., *Location of Aluminum in Substituted Calcium Silicate Hydrate (C-S-H) Gels as Determined by ^{29}Si and ^{27}Al NMR and EELS.* Journal of the American Ceramic Society, 1993. **76**(9): p. 2285-2288.

21. Cong, X., Kirkpatrick, R.J., *^{29}Si MAS NMR study of the structure of calcium silicate hydrate.* Advanced Cement Based Materials, 1996. **3**(3-4): p. 144-156.

22. Cong, X., Kirkpatrick, R.J., *^{17}O MAS NMR Investigation of the Structure of Calcium Silicate Hydrate Gel.* Journal of the American Ceramic Society, 1996. **79**(6): p. 1585-1592.

23. Nonat, A., Lecoq, X., *The structure, stoichiometry and properties of C-S-H prepared by C_3S hydration under controlled conditions*, Second international conference on the Nuclear Magnetic Resonance Spectroscopy of Cement-Based Materials, 1996: Bergamo. p. 197-207.

24. Glasser, F.P., Lachowski, E.E., Macphee, D.E., *Compositional model for calcium silicate hydrate (C-S-H) gels, their solubilities and free-energies of formation.* Journal of the American Ceramic Society, 1987. **70**(7): p. 481-485.

25. Fujii, W., Kondo, K., *Heterogeneous equilibrium of calcium silicate hydrate in water at 30 °C.* Journal of the Chemical Society, 1981: p. 645-651.

26. Grutzeck, M.W., *A new model for the formation of calcium silicate hydrate (C-S-H).* Materials Research Innovations, 1999. **3**(3): p. 160-170.

27. Powers, T.C., Brownyard, T.L., *Studies of the physical properties of hardened portland cement paste.* Journal of the American Concrete Institute, 1947. **43**: p. 101-132, 249-336, 469-505, 549-602, 669-712, 845-880, 933-992.

28. Feldman, R.F., Sereda, P.J., *A new model for hydrated Portland cement and its practical implications.* Engineering Journal of Canada, 1970. **53**: p. 53-59.

29. Wittmann, F., *Grundlagen eines Modells zur Beschreibung charakteristischer Eigenshcaften des Betons*, 1977. Deutscher Ausschuss für Stahlbeton: Berlin.

30. Jennings, H.M., Tennis, P.D., *Model for the developing structure in Portland cement pastes.* Journal of the American Ceramic Society, 1994. **77**(12): p. 3161-3172.

31. Jennings, H.M., J., *A model for the microstructure of calcium silicate hydrate in cement paste.* Cement and Concrete Research, 2000. **30**: p. 101-116.

32. Tajuelo Rodríguez, E., Richardson, I.G., Black, L., Boehm-Courjault, E., Nonat, A., Skibsted, J., *Composition, silicate anion structure and morphology of calcium silicate hydrates (C-S-H) synthesized by silica-lime reation and by controlled hydration of tricalcium silicate (C_3S).* Advances in Applied Ceramics, 2015(114): p. 362-371.

33. Taplin, J.H., *A method to following the hydrate reaction in Portland Cement Paste.* Australian Journal Application of Science, 1959. **10**(3): p. 329-345.

34. Merlino, S., Bonaccorsi, E., Armbruster, T., *The real structure of tobermorite 11 angstrom: normal and anomalous forms, OD character and polytypic modifications.* European Journal of Mineralogy, 2001. **13**(3): p. 577-590.

35. Shaw, S., Clark, S.M., Henderson, C.M.B., *Hydrothermal formation of the calcium silicate hydrates, tobermorite ($Ca_5Si_6O_{16}(OH)_2 \cdot 4H_2O$) and xonotlite ($Ca_6Si_6O_{17}(OH)_2$): an in situ synchrotron study.* Chemical Geology, 2000. **167**(1-2): p. 129-140.

36. Bell, N.S., et al., *Morphological forms of tobermorite in hydrothermally treated calcium silicate hydrate gels.* Journal of the American Ceramic Society, 1996. **79**(8): p. 2175-2178.

37. Black, L., Garbev, K., Stumm, A., *Structure, bonding and morphology of hydrothermally synthesised xonotlite.* Advances in Applied Ceramics, 2009. **108**(3): p. 137-144.

38. Vidmer, A., Sclauzero, G., Pasquarello, A., *Infrared spectra of jennite and tobermorite from first-principles.* Cement and Concrete Research, 2014. **60**: p. 11-23.

39. Bonaccorsi, E., Merlino, S., *Modular microporous minerals: Cancrinite-Davyne group and C-S-H phases*, in *Micro- and Mesoporous Mineral Phases*, Reviews in Mineralogy & Geochemistry, 2005. **57:** p. 241-290.

40. Bonaccorsi, E., Merlino, S., Kampf, A.R., *The crystal structure of tobermorite 14Å (plombierite), a C-S-H phase.* Journal of the American Ceramic Society, 2005. **88**(3): p. 505-512.

41. Myers, R.J., et al., *Effect of temperature and aluminium on calcium (alumino)silicate hydrate chemistry under equilibrium conditions.* Cement and Concrete Research, 2015. **68**: p. 83-93.

42. Berg, U., et al., *Phosphorus removal and recovery from wastewater by tobermorite-seeded crystallisation of calcium phosphate.* Water Science and Technology, 2006. **53**(3): p. 131-138.

43. Land, G., Stephan, D., *Controlling cement hydration with nanoparticles.* Cement & Concrete Composites, 2015. **57**: p. 64-67.

44. Shrivastava, O.P., Shrivastava, R., *Cation exchange applications of synthetic tobermorite for the immobilization and solidification of cesium and strontium in cement matrix.* Bulletin of Materials Science, 2000. **23**(6): p. 515-520.

45. McConnell, J.D.C., *The hydrated calcium silicates riversideite, tobermorite and plombierite*. *Mineralogical Magazine*, 1954. p. 293-305.

46. Maeshima, T., Noma, H., Sakiyama, M., Mitsuda T., *Natural 1.1 and 1.4 nm tobermorites from Fuka, Okayama, Japan: Chemical analysis, cell dimensions, ^{29}Si NMR and thermal behaviour.* Cement and Concrete Research, 2003. **33**: p. 1515-1523.

47. Merlino S., Bonaccorsi, .E., Armbruster, T., *The real structures of clinotobermorite and tobermorite 9Å: OD character, polytypes, and structural relationships.* European Journal of Mineralogy, 2000. **12**(2): p. 411-429.

48. Yu P., Kirkpatrick, R.J., *Thermal dehydration of tobermorite and jennite.* Concrete Science and Engineering, 1999. **1**: p. 185-191.

49. Taylor, H.F.W., *The dehydration of tobermorite*, 6th National Conference on Clays and Minerals, 1957. p. 101-109.

50. Mitsuda T., Taylor, H.F.W., *Normal and anomalous tobermorites*, Mineralogical Magazine, 1978. p. 229-235.

51. Merlino, S., Bonaccorsi, E., Armbruster, T., *Tobermorites: Their real structure and order-disorder (OD) character.* American Mineralogist, 1999. **84**(10): p. 1613-1621.

52. Jakobsson, S.P., Moore, J.G., *Hydrothermal minerals and alteration rates at Surtsey Volcano, Iceland.* Geological Society of America Bulletin, 1986. **97**(5): p. 648-659.

53. Guarino, B., *Ancient Romans made world's 'most durable' concrete. We might use it to stop rising seas*, The Washington Post, 2017.

54. Destefani, J., *Ancient lessons: Roman concrete durable, green.* American Ceramic Society Bulletin, 2013. **92**(6): p. 17-17.

55. Jackson, M.D., et al., *Phillipsite and Al-tobermorite mineral cements produced through low-temperature water-rock reactions in Roman marine concrete.* American Mineralogist, 2017. **102**(7): p. 1435-1450.

56. Elhemaly, S.A.S., Mitsuda, T., Taylor, H.F.W., *Synthesis of normal and anomalous tobermorites.* Cement and Concrete Research, 1977. **7**(4): p. 429-438.

57. Gabrovsek, R., et al., *Tobermorite formation in the system CaO,C_3S-SiO_2-Al_2O_3-NaOH-H_2O under hydrothermal conditions.* Cement and Concrete Research, 1993. **23**(2): p. 321-328.

58. Mitsuda, T., Taylor, H.F.W., *Influence of the aluminium on the conversion of calcium silicate hydrate gels into 11Å tobermorite at 90ºC and 120ºC.* Cement and Concrete Research, 1975. **5**: p. 203-210.

59. Sakiyama, M., Mitsuda, T., *Hydrothermal reaction between C-S-H and kaolinite for the formation of tobermorite at 180ºC.* Cement and Concrete Research, 1977. **7**(6): p. 681-685.

60. Kalousek, G.L., *Crystal chemistry of hydrous calcium silicates: I, substitution of aluminium in lattice of tobermorite.* Journal of the American Ceramic Society, 1957. **40**(3): p. 74-80.

61. Diamond, S., *Coordination of substituted aluminum in tobermorite.* Journal of the American Ceramic Society, 1964. **47**(11): p. 593-594.

62. Pardal, X., et al., *^{27}Al and ^{29}Si Solid-State NMR Characterization of Calcium-Aluminosilicate-Hydrate.* Inorganic Chemistry, 2012. **51**(3): p. 1827-1836.

63. Wang, Z., et al., *Incorporation of Al and Na in Hydrothermally Synthesized Tobermorite.* Journal of the American Ceramic Society, 2017. **100**(2): p. 792-799.

64. Barnes, M.W., Scheetz, B.E., *The chemistry of Al-tobermorite and its coexisting phases at 175ºC*. Symposium on Specialty Cements with Advanced Properties, 1989. Boston.

65. Diamond, S., White, J.L., Dolch, W.L., *Effects of isomorphous substitution in hydrothermally-synthesized tobermorite.* American Mineralogist, 1966. **51**(3-4): p. 388-396.

66. Komarneni, S., et al., *Cation-exchange properties of (Al + Na)-substituted synthetic tobermorites.* Clays and Clay Minerals, 1987. **35**(5): p. 385-390.

67. Ma, W.P., Brown, P.W., Komarneni, S., *Sequestration of cesium and strontium by tobermorite synthesized from fly ashes.* Journal of the American Ceramic Society, 1996. **79**(6): p. 1707-1710.

68. Coleman, N.J., *11Å ion exchanger from recycled container glass.* International Journal of Environment and Waste Management, 2011. **8**: p. 366-382.

69. Coleman, N.J., Li, Q., Raza, A., *Synthesis, structure and performance of calcium silicate ion exchangers from recycled conatiner glass.* Physicochemical Problems of Mineral Processing, 2014. **50**(1): p. 5-16.

70. Komarneni, S., et al., *Reactions of some calcium silicates with metal-cations.* Cement and Concrete Research, 1988. **18**(2): p. 204-220.

71. Taylor, H.F.W., *Torbermorite, jennite and cement gel.* Zeitschrift Für Kristallographie, 1992. **202**(1-2): p. 41-50.

72. Hejny, C., Armbruster, T., *Polytypism in xonotlite $Ca_6Si_6O_{17}(OH)_2$.* Zeitschrift Fur Kristallographie, 2001. **216**(7): p. 396-408.

73. Qian, G.R., et al., *Mg-xonotlite and its coexisting phases.* Cement and Concrete Research, 1997. **27**(3): p. 315-320.

74. Mamedov, K.S., Belov, N.V., *Structure of xonotlite $Ca_6Si_6O_{17}(OH)_2$.* Doklady Akademii Nauk SSSR, 1955. **104**: p. 615-618.

75. Eberhart, E., Hamid, S., Röttger, B., *Strukturverfeinerung und Polytypie von Xonotlite.* Zeitschrift für Kristallographie, 1981. **174**: p. 271-272.

76. Liebau, F., *Bemerkungen zur Systematik der Kristallstrukturen von Silikaten mit hochkondensierten Anionen.* Zeitschrift für Physikalische Chemie, 1956. **206**: p. 73-92.

77. Lequeux, N., et al., *Extended X-ray absorption fine structure investigation of calcium silicate hydrates.* Journal of the American Ceramic Society, 1999. **82**(5): p. 1299-1306.

78. Cong, X., Kirkpatrick R.J., *^{29}Si and ^{17}O NMR investigation of the structure of some crystalline calcium silicate hydrates.* Advanced Cement Based Materials, 1996. **3**: p. 133-143.

79. Noma, H., Adachi, Y., Matsuda, Y., Yokohama, T., *^{29}Si and ^{1}H NMR of natural and synthetic xonotlite.* Chemistry Letters, 1998. **3**: p. 219-220.

80. Gard, J.A., *A system of nomenclature for the fibrous calcium silicates, and a study of xonotlite polytypes.* Nature, 1966. **211**: p. 1078-1079.

81. Kudoh Y., Tackeuchi, Y., *Polytypism of xonotlite: 1 structures of an A-1 polytype.* Mineralogy Journal, 1979. **9**: p. 349-373.

82. Grimmer, A.R., Wieker, W., *Bestimmung der Art der Wasserbindung im Xonotlit $6CaO\text{-}6SiO_2\ H_2O$.* Zeitschrift für anorganische und allgemeine Chemie, 1971. **384**: p. 34-42.

83. Kalousek, G.L., Roy, R., *Crystal chemistry of hydrous calcium silicates: II, characterization of interlayer water.* Journal of the American Ceramic Society, 1957. **40**(3): p. 236-239.

84. Shaw, S., Henderson, C.M.B., Komanschek, B.U., *Dehydration/recrystallization mechanisms, energetics, and kinetics of hydrated calcium silicate minerals: an in situ TGA/DSC and synchrotron radiation SAXS/WAXS study.* Chemical Geology, 2000. **167**(1-2): p. 141-159.

85. Kalousek, G.L., Mitsuda, T., Taylor, H.F.W., *Xonotlite - cell parameters, thermogravimetry and analytical electron-microscopy.* Cement and Concrete Research, 1977. **7**(3): p. 305-312.

86. Roy R., Roy, D.M., *Pseudomorphism in xonotlite and tobermorite with Co^{2+} and Ni^{2+} exchange for Ca^{2+} at 25°C.* Cement and Concrete Research, 1986. **16**(1): p. 47-58.

87. Shrivastava, O.P., Komarneni, S., Breval, E., *Mg^{2+} uptake by synthetic tobermorite and xonotlite.* Cement and Concrete Research, 1991. **21**(1): p. 83-90.

88. Milestone, N.B., Ahari, K.G., *Hydrothermal processing of xonotlite based compositions.* Advances in Applied Ceramics, 2007. **106**(6): p. 302-308.

89. Anton, O., Eckert, A., *Asbestos-free phenolic brake linings with improved properties,* 1991. Redco Nv.

90. Low, N.M.P., Beaudoin, J.J., *Mechanical-properties and microstructure of cement binders reinforced with synthesized xonotlite micro-fibers.* Cement and Concrete Research, 1993. **23**(5): p. 1016-1028.

91. Li, X.K., Chang, J., *Synthesis of wollastonite single crystal nanowires by a novel hydrothermal route.* Chemistry Letters, 2004. **33**(11): p. 1458-1459.

92. Li, X., Chang, J., *A novel hydrothermal route to the synthesis of xonotlite nanofibers and investigation on their bioactivity.* Journal of Materials Science, 2006. **41**(15): p. 4944-4947.

93. Byrappa, K., Yoshimura, M., *Handbook of Hydrothermal technology*, 2013. Norwich, New York, U.S.A.: WILLIAM ANDREW PUBLISHING, LLC.

94. Brunner, G., *Hydrothermal and Supercritical Water Processes*, Hydrothermal and Supercritical Water Processes. 2014. p. 1-666.

95. Schubert, U., Hüsing, N., *Synthesis of Inorganic Materials*. 4th edition, 2019: WILEY.

96. Snell, D.S., *Review of synthesis and properties of tobermorite, C-S-H(I), and C-S-H gel.* Journal of the American Ceramic Society, 1975. **58**(7-8): p. 292-295.

97. Kurdowski W., *Cement and Concrete Chemistry*. 1st edition, 2014. Kraków, Poland: Springer Dordrecht. 700.

98. Hou, D., et al., *Calcium silicate hydrate from dry to saturated state: Structure, dynamics and mechanical properties.* Acta Materialia, 2014. **67**: p. 81-94.

99. Harker, R.I., *Dehydration series in the system $CaSiO_3$-SiO_2-H_2O.* Journal of the American Ceramic Society, 1964. **47**(10): p. 521-529.

100. Hamid, S.A., *Electron microscopic characterization of the hydrothermal growth of synthetic 11Åtobermorite ($Ca_6Si_6O_{18} \cdot 4\ H_2O$) crystals.* Journal of Crystal Growth, 1979. **46**(3): p. 421-426.

101. Meller, N., Kyritsis, K., Hall, C., *The mineralogy of the CaO-Al_2O_3-SiO_2-H_2O(CASH) hydroceramic system from 200 to 350 degrees C.* Cement and Concrete Research, 2009. **39**(1): p. 45-53.

102. Hong, S.Y., Glasser, F.P., *Phase relations in the CaO-SiO_2-H_2O system to 200ºC at saturated steam pressure.* Cement and Concrete Research, 2004. **34**(9): p. 1529-1534.

103. Black, L., et al., *Characterisation of crystalline C-S-H phases by X-ray photoelectron spectroscopy.* Cement and Concrete Research, 2003. **33**(6): p. 899-911.

104. Buckner, D.A., Roy, D.M., Roy, R., *Studies in the system CaO-SiO_2-Al_2O_3-H_2O Part 2, The system $CaSiO_3$-H2O.* American Journal of Science, 1960. **258**(2): p. 132-147.

105. Taylor, H.F.W., *Hydrated calcium silicates. Part II. Hydrothermal reactions: Lime: Silica Ratio 1:1.* Journal of the Society, 1951: p. 2397-2401.

106. Speakman, K., *The stability of tobermorite in the system CaO-SiO_2-H_2O at elevated temperatures and pressures.* Mineralogical Magazine and Journal of the Mineralogical Society, 1968. **36**(284): p. 1090-1103.

107. Hartmann, A., Buhl, J.C., *The influence of sucrose on the crystallization behaviour in the system CaO-SiO_2-$C_{12}H_{22}O_{11}$-H_2O under hydrothermal conditions.* Materials Research Bulletin, 2010. **45**(4): p. 396-402.

108. Hartmann, A., Khakhutov, M., Buhl, J.C., *Hydrothermal synthesis of CSH-phases (tobermorite) under influence of Ca-formate.* Materials Research Bulletin, 2014. **51**: p. 389-396.

109. Huang, X.A., Jiang, D.L., Tan, S.H., *Novel hydrothermal synthesis of tobermorite fibers using Ca(II)-EDTA complex precursor.* Journal of the European Ceramic Society, 2003. **23**(1): p. 123-126.

110. Reinik, J., et al., *Alkaline modified oil shale fly ash: Optimal synthesis conditions and preliminary tests on CO_2 adsorption.* Journal of Hazardous Materials, 2011. **196**: p. 180-186.

111. Flint, E.P., McMurdie, H.F., Wells, L.S., *Formation of hydrated calcium silicates at elevated temperatures and pressures.* Journal of Research of the National Bureau of Standards, 1938. **21**(5): p. 617-638.

112. Sato, H., Grutzeck, M., *Effect of starting materials on the synthesis of tobermorite*. *Symposium on Advanced Cementitious Systems: Mechanisms and Properties, at the Meeting of the Materials Research Soc*, 1991. Boston.

113. Cao, J., et al., *Hydrothermal synthesis of xonotlite from carbide slag.* Progress in Natural Science-Materials International, 2008. **18**(9): p. 1147-1153.

114. Lin, K., Chang, J., *A Simple Method to Synthesize Single-Crystalline β-Wollastonite Nanowires.* Journal of Crystal Growth 2007. **300**(2): p. 267-271.

115. Cooke, T., *Formation of Films on Hatschek Machines*, B.M.a.T.P.L. Australia, Editor. 2007.

116. Domone, P., Illston, J., *Construction Materials: Their Nature and Behaviour*. 4th edition, 2010. 587.

117. Harries, K.A., Sharma, B., *Nonconventional and Vernacular Construction Materials Characterisation, Properties and Applications*. 2nd edition, 2019. 716.

118. Coutts, R.S.P., *From forest to factory fabrication*. in 4th *RILEM International Symposium on Fibre Reinforced Cement and Concrete*, 1992. Sheffiled, UK: Taylor & Francis.

119. Bragg, W.H., *The nature of gamma and X-rays.* Nature, 1908. **77**: p. 270-271.

120. Bragg, W.L., Thomson, J.J., *The diffraction of short electromagnetic waves by a crystal.* Proceedings of the Cambridge Philosophical Society, 1914. **17**: p. 43-57.

121. Hewat, A., David, W. I. F., van Eijck, L., *Hugo Rietveld (1932–2016).* Journal of Applied Crystallography, 2016. **49**: p. 1394-1395.

122. Beckhoff, B., Kanngießer, B., Langhoff, N., Wedell, R., Wolff, H., *Handbook of Practical X-Ray Fluorescence Analysis*. 2006: Springer.

123. Tinke, A.P., et al., *A review of underlying fundamentals in a wet dispersion size analysis of powders.* Powder Technology, 2009. **196**(2): p. 102-114.

124. Brunauer, S., Emmett, P.H., Teller, E., *Adsorption of gases in multimolecular layers.* Journal of the American Chemical Society, 1938. **60**: p. 309-319.

125. Barrett, E.P., Joyner, L.G., Halenda, P.P., *The determination of pore volume and area distributions in porous substances.1. Computations from nitrogen isotherms.* Journal of the American Chemical Society, 1951. **73**(1): p. 373-380.

126. Rigby, S.P., Edler, K.J., *The influence of mercury contact angle, surface tension, and retraction mechanism on the interpretation of mercury porosimetry data.* Journal of Colloid and Interface Science, 2002. **250**(1): p. 175-190.

127. Venables, J.A., Smith, D.J., Cowley, J.M., *HREM, STEM, REM, SEM - and STM.* Surface Science, 1987. **181**(1-2): p. 235-249.

128. Griffiths, P.R., *Fourier-transform infrared spectrometry.* Science, 1983. **222**(4621): p. 297-302.

129. Sherma, J., *Fourier transform infrared (FT-IR) spectrometry.* Journal of Aoac International, 2004. **87**(4): p. 113A-118A.

130. Thompson, M., Walsh, J.N., *Handbook of Inductively Coupled Plasma Spectrometry*. 2nd edition. Springer. 1989: Blackie and Son Ltd.

131. Mlynárik, V.,, *Introduction to nuclear magnetic resonance.* Analytical Biochemistry, 2017. **529**(15): p. 4-9.

132. Engelhardt, G., Michel, D., *High-resolution solid-state NMR of silicates and zeolites*, in *Angewandte Chemie*. 1988. p. 1464-1465.

133. Coats, A.W., Redfern, J. P., *Thermogravimetric Analysis - A Review.* Analyst, 1963. **88**(1053): p. 906–924.

134. Davis, W.R., *Hot-Wire Method for the Measurement of the Thermal Conductivity of Refractory Materials*, Compendium of Thermophysical Property Measurement Methods, P. Press, Editor. 1984. p. 161.

135. Anton O., Opsommer, A., Krasselt, V., Tonnesen T., Schickle B., *Matrix Engineered Insulation Material for Usage in Refractory Linings*, UNITECR, 2009: Salvador, Brazil.

136. Juhás P., Davis,T., Farrow, C.L., Billinge, S. J. L. , *PDFgetX3: a rapid and highly automatable program for processing powder diffraction data into total scattering pair distribution functions.* Journal of Applied Crystallography, 2013. **46**(2): p. 560-5666.

137. Grangeon, S., Fernández-Martínez, A., Baronnet A., Marty N., Poulain A., Elkaïm E., Roosz C., Gaboreau S., Henoc P., Clare, F., *Quantitative X-ray pair distribution function analysis of nanocrystalline calcium silicate hydrates: a contribution to the understanding of cement chemistry.* Journal of Applied Crystallography, 2017. **50**: p. 14-21.

LIST OF PUBLICATIONS

Publications in peer-reviewed journals:

1. Martí-Montava, F., Opsommer A., García-Sanoguera D., *Influence of silica fume source on crystallization of xonotlite in a new process making medium density Ca-silicate based products.* Key Engineering Materials, 2018. **788**: p. 3-12.

Publications in conference proceedings:

1. Martí-Montava, F., Opsommer A., García-Sanoguera D., *New method for making medium density Ca-silicate based products and influence of the used raw materials*. 60th International Colloquium on Refractories (ICR), 2017.Aachen, Germany. p:230-235.
2. Martí-Montava, F., Opsommer A., García-Sanoguera D., *Influence of silica fume source on crystallization of xonotlite in a new process making medium density Ca-silicate based products.* Key Engineering Materials, 2018. **788**: p. 3-12.

Oral presentations at conferences:

1. Martí-Montava, F., Opsommer A., García-Sanoguera D., *New method for making medium density Ca-silicate based products and influence of the used raw materials*. 60th International Colloquium on Refractories, 2017.Aachen, Germany.
2. Martí-Montava, F., Opsommer A., García-Sanoguera D., *Influence of silica fume source on crystallization of xonotlite in a new process making medium density Ca-silicate based products.* 8th International Conference on Silicate Materials (BaltSilica), 2018. Riga, Latvia.